Imperial College London

Medical Robotics for use in MRI Guided Endoscopy

by Oliver John North

Submitted for the degree of Doctor of Philosophy

London, August 2013

DEPARTMENT OF MECHANICAL ENGINEERING

Abstract

Interventional Magnetic Resonance Imaging (MRI) is a developing field that aims to provide intra-operative MRI to a clinician to guide diagnostic or therapeutic medical procedures. MRI provides excellent soft tissue contrast at sub-millimetre resolution in both 2D and 3D without the need for ionizing radiation. Images can be acquired in near real-time for guidance purposes.

Operating in the MR environment brings challenges due to the high static magnetic field, switching magnetic field gradients and RF excitation pulses. In addition high field closed bore scanners have spatial constraints that severely limit access to the patient.

This thesis presents a system for MRI-guided Endoscopic Retrograde Cholangio-pancreatography (ERCP). This includes a remote actuation system that enables an MRI-compatible endoscope to be controlled whilst the patient is inside the MRI scanner, overcoming the spatial and procedural constraints imposed by the closed scanner bore. The modular system utilises non-magnetic ultrasonic motors and is designed for image-guided user-in-the-loop control. A novel miniature MRI compatible clutch has been incorporated into the design to reduce the need for multiple parallel motors.

The actuation system is MRI compatible does not degrade the MR images below acceptable levels. User testing showed that the actuation system requires some degree of training but enables completion of a simulated ERCP procedure with no loss of performance. This was demonstrated using a tailored ERCP simulator and kinematic assessment tool, which was validated with users from a range of skill levels to ensure that it provides an objective measurement of endoscopic skill.

Methods of tracking the endoscope in real-time using the MRI scanner are explored and presented here. Use of the MRI-guided ERCP system was shown to improve the operator's ability to position the endoscope in an experimental environment compared with a standard fluoroscopic-guided system.

Copyright Declaration

‘The copyright of this thesis rests with the author and is made available under a Creative Commons Attribution Non-Commercial No Derivatives licence. Researchers are free to copy, distribute or transmit the thesis on the condition that they attribute it, that they do not use it for commercial purposes and that they do not alter, transform or build upon it. For any reuse or redistribution, researchers must make clear to others the licence terms of this work.

Declaration of Originality

I declare that this thesis constitutes original research that I produced during the period January 2010 to August 2013. All works contained herein are my own; exceptions to this are referenced appropriately.

Oliver North
London, August 2013

Acknowledgements

This work wouldn't have been possible without funding from the Wellcome Trust and Imperial College. All those involved in the MRI guided endoscopy funded project were very supportive, notably Mike Ristic, Richard Syms and Djordje Brujic. Colin Besant in particular provided much needed perspective and encouragement throughout. A special mention must go to Marc Rea, who put aside endless evenings for testing and answering questions.

Throughout my studies I leant heavily on and was supported by a network of fellow PhD sufferers. Stef Glassford, Diogo Geraldes and Will Ferguson joined me in the ideal distraction that is sub-wardening while Francesca Galassi and Enrico Franco provided an unmistakeably Latin flavour to proceedings in the department. The many gallons of coffee drunk and hours spent in discussion with Nick Lambert were instrumental to the research process and I don't think either of us would have made it through this without the other.

Last but not least, I am lucky to have had the tireless encouragement and patience of my family every day of my life. Nettie, Robin, Judith and John; you have all been fundamental to this in every way, and I dedicate this thesis to you all.

Contents

Abstract **1**

Copyright Declaration **2**

Declaration of Originality **3**

Acknowledgements **4**

Contents **5**

List of Figures **9**

List of Tables **22**

Abbreviations **24**

Nomenclature **26**

1. Introduction **28**

1.1 Motivation for Research 28

1.2 Research Objectives 29

1.3 Structure of the Thesis 30

2. Magnetic Resonance Imaging **32**

2.1 Introduction 32

2.2 MRI Background 32

2.2.1 Image Acquisition 35

2.2.2 Auxiliary Imaging Coils 40

2.2.3 Effects of Motion during MRI 40

2.3 MRI Compatibility 46

2.4 Conclusions 51

3. Interventional MRI Systems **53**

3.1 Introduction 53

3.2 Actuators 53

3.3 Sensors 60

3.4 Tool tracking in interventional MRI 63

3.5 MRI Compatible Endoscopy 67

3.6 Robotic Endoscopy 69

3.7 Conclusions 73

4. MRI Guided ERCP System 74

4.1 Introduction 74

4.2 Techniques for diagnosis of biliary tumours 74

4.2.1 Background 74

4.2.2 Endoscopic Investigation of the Bile Duct 75

4.2.3 Diagnostic Imaging of the Bile Duct 77

4.2.4 Limitations of Existing Techniques 78

4.3 MRI-guided ERCP Procedure 80

4.3.1 Objectives 80

4.3.2 Procedure Outline 81

4.3.3 System Requirements 82

4.3.4 System Overview 85

4.4 Enabling Technologies 86

4.4.1 MRI Compatible Duodenoscope 86

4.4.2 Intra-Luminal MR Receiver Coils 93

4.5 Conclusions 99

5. Endoscope Remote Actuation System Design 100

5.1 Introduction 100

5.2 Design Overview 100

5.3 Actuator Module Designs 104

5.3.1 Right Hand Module 104

5.3.2 Left-Hand Module 108

5.3.3 Catheter Feed Module 110

5.3.4 Docking Procedure 113

5.4 Miniature Pneumatic Clutch 114

5.4.1 Design Requirements 114

5.4.2 Clutch Theory 116

5.4.3 Prototype Design 118

5.4.4 Performance Testing 120

5.4.5 Results 122

5.4.6 Discussion 125

5.5 User Interface Handle Design 127

5.6 Control Unit 128

5.7 MRI Compatibility 131

5.7.1 Materials and construction 131
5.7.2 Shielding 132
5.7.3 Filtering 133
5.8 Conclusions 135

6. Remote Actuation System Validation 137
6.1 Introduction 137
6.2 Performance Criteria 137
6.2.1 MRI Compatibility Criteria 138
6.2.2 Functional Criteria 140
6.3 MRI Compatibility Testing 140
6.3.1 Introduction 140
6.3.2 Initial Component Evaluation 141
6.3.3 System Evaluation 142
6.3.4 System Evaluation Results and Discussion 146
6.4 Functional Testing 150
6.4.1 Introduction 150
6.4.2 Background 150
6.4.3 Study Design 153
6.4.4 Biliary Cannulation Simulator 155
6.4.5 Kinematic Performance Analysis 160
6.4.6 Training Simulator Validation 166
6.4.7 Remote Actuation System Testing 169
6.5 Conclusions 178

7. Duodenoscope Tip Tracking in MRI 179
7.1 Introduction 179
7.2 Background 179
7.3 Materials and Methods 181
7.3.1 Coil Position Measurement Method 181
7.3.2 Experimental Procedure 186
7.4 Results 188
7.5 Discussion 192
7.6 Conclusions 196

8. System Concept Testing 197
8.1 Introduction 197
8.2 Background 197

8.3 Materials and Methods 199
8.4 Results 204
8.5 Discussion 208
8.6 Conclusions 211

9. Conclusions and Future Work 212
9.1 Summary of Thesis 212
9.2 Contributions 213
9.2.1 Endoscope Remote Actuation System 213
9.2.2 Duodenoscope tip tracking 214
9.2.3 MRI-guided ERCP System and Procedure 215
9.2.4 Other Research 216
9.3 Future Work 216
9.3.1 Endoscope Remote Actuation System 216
9.3.2 Duodenoscope tip tracking 217
9.3.3 MRI-guided ERCP System and Procedure 218
9.3.4 Other Research 219
9.4 Publications to Date 219

Bibliography 221

List of Figures

2.2.1. Cutaway diagram of a closed MRI scanner [Tse, 2008] 33
2.2.2. MRI scanner with coordinate system and imaging planes. Showing (red) Axial plane, (green) Sagittal plane and (blue) Coronal plane. 33
2.2.3. Examples of closed (l) and open (r) MRI scanners [Tse, 2008] 34
2.2.4. Dimensions of a typical closed bore MRI scanner [Tse, 2008]..... 34
2.2.5. Precession of atomic spin about the main magnetic field (B_0). 35
2.2.6. Example of a simplified gradient echo MR imaging sequence. Each horizontal line represent activity of one of the scanner components: the radio frequency excitation coil (RF), the magnetic gradient coils in the scanner X, Y and Z directions (G_x, G_y and G_z respectively) and the scanner analogue to digital converter for signal recording (ADC). The time between the RF pulse and the signal recording is known as the echo time (TE), while the time between successive RF pulses is the repetition time (TR). 36
2.2.7. MR images are constructed by repeating image sequences with phase encoding gradient changing on each repetition (top). Received signals are used to construct a 2 dimensional (2D) k-space matrix, with each sequence repetition corresponding to a horizontal line of k-space (bottom left). The image is generated by applying a 2D Fourier transform (FT) to the k-space matrix (bottom right). 37
2.2.8. Auxiliary imaging coils, showing (l) head and chest coils and (r) peripheral angiography coils [Brown, 2003]..... 39
2.2.9. Solid endorectal coil for prostate imaging, developed by DeSouza et al [DeSouza, 1996]..... 39
2.2.10. Illustration of the effect of acquiring an incomplete k-space matrix. If slightly more than half of k-space is filled, the resulting image is still relatively high quality (r) when compared with the original image (l) despite blurring in the phase encoding direction. 41
2.2.11. Respiratory signal used for image gating. Data acquisition is triggered by the signal passing above a threshold value (arrows), which can result in delays due to inconsistent breathing patterns [McRobbie, 2007]. 42

2.2.12. Navigator respiratory measurement, showing (l) columnar volume positioned across the diaphragm and (r) Navigator signal changes during respiration. Reproduced from [McRobbie, 2007]. 42
2.2.13. A standard image (left) is composed of different regions of k-space. The outer region contains high frequency information at the edges of regions of high contrast (right), while the majority of the image signal is contained in the centre of k-space (centre). 43
2.2.14. ROPE motion compensation strategy. Data is acquired over several breathing cycles, with the order of phase encoding rearranged to match the diaphragm position (left). When the image is reconstructed, the effect is as if the data have been acquired over a single, slower breathing cycle (right). Reproduced from [McRobbie, 2007]. 44
2.3.1. MR images of identical cylindrical samples of Macor® (l) and brass (r) suspended by Nylon in a liquid phantom. The susceptibility artefact of the brass cylinder can be clearly seen [Tse, 2011]. 47
2.3.2. Comparison of MR images taken when electronic components inside the MRI scanner room are not powered (l) and powered (r). 49
2.3.3. Method of SNR calculation using a pair of images. A high signal region of the first image (left) is used to determine the image signal (red). The second image is then subtracted from the first to generate a difference image (right). The same region of the difference image is then used to calculate the image noise (red). 50
2.3.4. Calculation of SNR using a single image, showing a region of high signal (red) and a background region (green). 51
3.2.1. Early prototype of the Invivo MRI-guided prostate biopsy positioning arm. Each degree of freedom (DOF) is directly actuated by the operator when the mechanism is outside the scanner [Beyersdorff, 2004]. 54
3.2.2. Prostate biopsy mechanisms directly actuated by flexible phosphor bronze shafts [Lambert, 2012; Susil, 2006]. 55
3.2.3. MRI-guided needle insertion device actuated by manually controlled timing belts. Due to it's height, this system is designed for use in a vertical open-bore scanner [Oura, 2006]. 55
3.2.4. Pneumatically operated MRI-guided prostate biopsy mechanism. The coloured tubes supply air to four horizontal cylinders at the base of the mechanism [Song, 2010]. 56

3.2.5. Innomotion MRI-guided needle insertion arm with pneumatically actuated DOF shown [Melzer, 2008]. 57
3.2.6 Diagram of the Pneustep motor [Stoianovici, 2007a] 58
3.2.7. Cross-sectional view of an ultrasonic USR-60 non-magnetic motor [Shinsei, 2005]. 58
3.3.1. Schematic showing the operating principle of a wavelength-encoded fibre optic rotary encoder [Maghoo, 1994]. 61
3.3.2. Fibre optic force sensor systems, showing (top) direct and (bottom) reflected light transmission [Gassert, 2008]. 62
3.4.1. Image voids in tissue surrounding inserted needles, with (l) needle in image plane and (r) cross sectional image. The true location of the needle centres and axes are shown in yellow [DiMaio, 2005]. 64
3.4.2. (l) MR contrast gel-filled needle guide with biopsy needle gun and (r) planar MR image of needle guide [Beyersdorff, 2004; Oliveira, 2007]. 64
3.4.3. Active device tracking using a miniature solenoidal microcoil mounted on a vascular catheter (l). A 1D projection enables the position of the coil to be determined accurately due to the presence of a single, well defined signal peak (r) [Dumoulin, 1997]. 65
3.4.4. Passive resonant microcoil fiducial, showing inductor coil (red) and capacitors (white) soldered to a circuit board [Rea, 2010]. 66
3.5.1. MR images of identical phantoms. When a standard endoscope is inserted into the phantom (l) the image is degraded to the point of uselessness. If the endoscope is modified to remove the CCD chip to the proximal end and replace it with fibre optics (r) the image improves significantly [Gross, 2001]. 68
3.5.2. MRI compatible endoscopes manufactured by Endsocan Ltd (l, with removable tip receiver coil) and Olympus (r, with inflatable latex balloon for positioning stability) [Gilderdale, 2003; Ichikawa, 2001]. 68
3.5.3. Spatial constraints posed by flexible endoscopy inside closed-bore MRI scanners [Naka, 2012]. 69
3.6.1. Flexible tools for NOTES interventional procedures [Abbott, 2007; Phee, 2009; Shang, 2011]. 70
3.6.2. NOTES user interfaces, showing (l) master user-controlled device that transmits control signals to (r) slave motor driven device [Abbott, 2007]. 70
3.6.3. Colonoscope remote actuation device, showing (1) optical encoders, (2) Bowden cables and (3) force sensors [Ruiter, 2012]. 72

3.6.4. Alternative colonoscope remote actuator user interfaces, showing (1) joystick, (2) buttons for auxiliary controls, (3) programmable switches, (4) connection to drive unit, (5) touchpad and (6) safety switch [Ruiter, 2012]. 72
4.2.1. Anatomy of the duodenum, pancreas and common bile duct, showing (a) oesophagus, (b) stomach, (c) duodenum, (d) sphincter of Oddi, (e) bile duct and (f) liver. 75
4.2.2. Side viewing duodenoscope tip, showing (A) camera lens, (B) light source and (C) catheter deflection bridge. 76
4.2.3. ERCP procedure, showing duodenoscope optical image of sphincter and catheter (left) and fluoroscopic image of duodenoscope and bile duct structure (right) [Padda, 2010]. 76
4.2.4. Malignant stricture identified from MRCP images [Yeh, 2009]. 77
4.2.5. Bile duct stone identified by MRCP images. The stone appears as hypo-intense on a T_2-weighted MR image (l), but is hyper-intense on a T_1-weighted image [Yeh, 2009]. 78
4.2.6. During ERCP training operators are taught to approach the papilla (raised central feature on duodenum wall) in the direction of 10 or 11 on a clock face (red arrow). 79
4.3.1. Working in closed-bore MRI scanners limits access to endoscopy patients. Sketch shows an average-sized patient with their abdomen at the scanner isocenter. 83
4.3.2. Schematic of the MRI-guided ERCP system. The 'MRI scanner' in this diagram includes the scanner itself as well as the image processing computers and graphical user interface. The nature of the connections between subsystems is labelled. 85
4.3.3. MRI compatible duodenoscope manufactured by Endoscan Ltd., showing (1) control handle, (2) distal tip, (3) flexible section and (4) light guide attachment.... 86
4.4.1. Duodenoscope degrees of freedom (DOF): (1) flexible section insertion and retraction, (2) flexible section rotation, (3) distal tip steering up and down (U-D), (4) distal tip steering left and right (L-R), (5) catheter deflection bridge and (6) catheter insertion and retraction. 87
4.4.2. The duodenoscope handle is designed to be held and operated by the user's left hand, while the right hand controls the flexible section. 88
4.4.3. Duodenoscope optics, showing (1) external camera, (2) lens attachment, (3) liquid light guide and (4) light source 88

4.4.4. Sagital (l) and Axial (r) MRI of duodenoscope tip immersed in water. Limited susceptibility artefacts are visible (arrow); the dark areas behind the tip are due to the tip coil (arrowheads)..... 89
4.4.5 Duodenoscope force and torque measurements. Tip steering (left), flexible section feed and twist (centre) and catheter feed (right). Red arrows indicate the DOF measured in each case. 90
4.4.6. Results from Duodenoscope tip steering up-down (U-D) backlash test (top) and tip steering left-right (L-R) backlash test (bottom)..... 91
4.4.7. Duodenoscope catheter deflection lever backlash (top) and flexible section torsional stiffness (bottom), where l indicates length of flexible section over which deflection was measured 92
4.4.8. Duodenoscope tip receiver coil (l) layout sketch and (r) completed instrument with window for catheter and optics (arrow)..... 94
4.4.9. Schematics of duodenoscope tip coil system showing (a) overall equivalent circuit, (b) equivalent circuit when PIN diode is open and (c) equivalent circuit when PIN diode is closed..... 94
4.4.10. Arrangement for comparison of cardiac array surface coil and duodenoscope tip coil [Syms, In Press]..... 95
4.4.11. Comparison of (l) surface array coil and (r) duodenoscope tip coil images (160mm field of view (FOV), number of excitations (NEX) 4)..... 95
4.4.12. Catheter coil (l) distal tip deflected through 90° by the duodenoscope, and (r) inductive tap connector at proximal end..... 97
4.4.13. Construction of the catheter-mounted receiver coil (top) and circuit board layout of figure of eight inductive loops with printed film capacitors (bottom). 97
4.4.14. Catheter coil imaging, with (l) experimental arrangement and (r) coronal MR image. The MR image labels correspond to the labels in 4.4.10 (b) above. 98
4.4.15. Comparison of (l) surface array coil and (r) catheter coil images (80mm FOV, 4 NEX). Phase wrap is visible as ghosting in the surface coil image (arrow)..... 98
5.2.1. Schematic of MRI compatible endoscope remote actuation system showing (1) MRI scanner, (2) Remote actuator modules, (3) Control box, (4) User input handle in either (a) the scanner room or (b) the control room, (5) Ground connection between control box and MRI scanner room shield and (6) Endoscope video visualisation device..... 101
5.2.2. Experimentally measured torque and output power curve for USR-30-NM motor at maximum input power..... 102

5.3.1. Complete endoscope remote actuation modules with duodenoscope handle docked, with (a) right hand module, (B) catheter feed module and (C) left hand module shown [North, 2012]. 104
5.3.2. Prototype right hand module based on angled friction rollers, showing (l) actuator prototype and (r) contact patches between rollers and duodenoscope... 104
5.3.3. Duodenoscope flexible section actuation is achieved via a quick-release collar (left) with gear attached. A dedicated motor is used to rotate the flexible section via the quick-release collar and a 3 stage gear train (right). 105
5.3.4. A dedicated motor is used to translate the endoscope flexible section via a leadscrew (left). Prototype actuator module is shown (right). 105
Fig.5.3.5. Top view of left hand module prototype, showing large helical gear with central cutouts for endoscope tip steering wheels 106
5.3.6. Endoscope tip steering wheel drivetrains. Three idler gears (arrows, left) and a drive gear (arrowhead, left) are used to mount the large central gears concentrically. Each tip steering wheel is actuated by a dedicated motor via a two stage drivetrain (right). 107
Fig.5.3.7. Left hand module design, highlighting catheter bridge deflection lever actuator drivetrain (green parts) and retractable yoke (arrowhead). 107
5.3.8. Left hand module prototype showing (a) lower circular housing, (b) contact points between duodenoscope handle and actuator module, (c) upper, removable circular housing parts and (d) duodenoscope umbilical. 108
5.3.9. Duodenoscope handle prior to docking, with region covered by operator's left hand shown in magenta. ..... **Error! Bookmark not defined.**
5.3.10. Catheter feed module showing internal load transfer parts and geartrain (left) and prototype mounted on duodenoscope handle (right). 110
5.3.11. Catheter follower designs (a) solid, (b) with cutouts to reduce parasitic friction but without taking into account the force required to deflect the catheter, and (c) final configuration. 111
5.3.12. Catheter feed pulley friction coating, with arrows indicating direction of force applied to catheter. 111
5.3.13. Endoscope remote actuation system docking procedure. The action performed in each step is highlighted blue. 113
5.4.1. Excerpt from time series of control inputs during simulated biliary cannulation (see Section 6.4). Positive and negative motor inputs correspond to clockwise and counter-clockwise motion respectively. Each coloured line represents one motor input. 115

5.4.2. Cross-sectional drawing of miniature pneumatic clutch showing 1) Input shaft; 2) Casing; 3) Input Friction Plate; 4) Output Friction Plate; 5) Load Transfer Plate; 6) Pneumatic Actuator; 7) Output Shaft. The parasitic friction contacts (A) and contact between the friction plates (B) are shown. Dimensions are in mm. 117
5.4.3. Prototype clutch, with (l) and without (r) outer casing. 118
5.4.4. Alternatives to flat friction plate design, with crenellations at 90° (l) and 35° (r). 119
5.4.5. Alternative pneumatic actuator designs. Two designs (left and middle) are intended to preferentially expand in one direction when inflated, which causes particular stress on the areas arrowed. The third (right) is moulded oversized and is compressed on assembly. Wall thicknesses in these sketches are indicative – multiple variants of all designs were tested. 119
5.4.6. Clutch performance testing rig, showing (a) motor; (b) clutch, (c) pulley with friction belt; (d) force sensors and (e) optical encoder. 121
5.4.7. Chart showing calculated pneumatic force using A = 308mm^2 (the cross-sectional area available for the balloon), compared with measured pneumatic actuator output force. 122
5.4.8. Chart showing parasitic torque calculated using □ = 0.115 compared with experimentally measured parasitic torque. 122
5.4.9. Time taken for clutch to engage, as a function of pneumatic pressure and hose length (H). 123
5.4.10. Time taken for clutch to disengage, as a function of pneumatic pressure and hose length. 123
5.4.11. Effect of repeated activation cycling on clutch output torque and clutch efficiency for material A (top) and material B (bottom). 124
5.4.12. Maximum torque that can be applied to clutch before slipping, as a function of pneumatic pressure for material A (top) and material B (bottom). Data displayed from the clutch before and after durability cycling, and compared with calculated values. 125
5.4.13. Friction coating material A is severely worn after 12,500 clutch activation cycles. 126
5.4.14. 2-DOF modified right hand module. A single motor drives the rotation DOF (l) via a clutch (yellow) and splined shaft (red). Activation of the second clutch (r) drives the translation DOF via a leadscrew (purple). 126
5.5.1. User interface handle, showing locations of controls for all 6 DOF (arrows) and trimmer resistors for speed control (arrowheads). Controls are in

ergonomically similar locations to the standard duodenoscope controls (see 4.4.1). 128
5.5.2. User input controls for right hand module (left) and catheter deflection bridge (right) with covers exposed. Showing (1) control input rod/lever, (2) speed control resistor, (3) microswitches for direction control, (4) control input rod/lever feature that depresses microswitch and (5) return spring. 128
5.6.1. Schematic of control box wiring for original actuator module designs presented in Section 5.3. 129
5.6.2. Control box, opened to show batteries (1), voltage regulator (2), motor control electronics (3), motor driver units (4) and external connections to the motors, user interface and camera (5). 130
5.7.1. Monel mesh shield for motor connection to control box (l) and removable external camera shield (r). 133
5.7.2. Motor shielding, showing the motor encased in insulation (left) prior to shielding with a continuous layer of copper tape (right). 133
5.7.3. Example of composite video encoding, with the chart (r) showing the waveform for a single scan line of the test image (l). Pixel luminance is defined by the magnitude of the waveform mean at the corresponding horizontal position. Pixel colour saturation is defined by the amplitude of the 3-5 MHz oscillation, while hue is defined by the phase difference between the waveform and the colour burst in the backpatch to the left of the screen. 134
5.7.4. Band stop filter constructed for video feed filtering at 3.0T, showing schematic of circuit (top) and signal attenuation (in dB) as a function of frequency (bottom) measured using a network analyser. 135
6.2.1. MRI of a quality assurance phantom with a reference SNR (l) and a SNR 5% below reference (r). 138
6.2.2. Histograms showing variation in reference image SNR for GE sequence (top), FSE sequence (middle) and TrueFISP sequence (bottom). 139
6.3.1 Susceptibility artefact of a single USR-30-NM motor immersed in water and imaged at 1.5T using a FSE sequence. The approximate motor position is outlined in red. 141
6.3.2: Mean change in image SNR due to presence of an unshielded motor placed at varying distances from the scanner isocentre. 141
6.3.3. Effect on image SNR of shielding motor driver, cable and motor when a single motor is placed in the scanner isocenter (see Table 6.3.2). Mean SNR plotted, with error bars representing maximum and minimum results. 146

6.3.4. Effect on image SNR of moving motor controls and changing power source when a single motor is placed in the scanner isocenter (see Table 6.3.2). Mean SNR plotted, with error bars representing maximum and minimum results. 146
6.3.5 Effect on image SNR of changing position of motor controls and battery grounding for complete actuation system (see Table 6.3.2). Mean SNR plotted, with error bars representing maximum and minimum results. 147
6.3.6. Effect on image SNR of changing the shielding, grounding and monitor location of the camera subsystem (see Table 6.3.3). Mean SNR plotted, with error bars representing maximum and minimum results.....147
6.3.7. Effect on image SNR of increasing clutch hose length and therefore moving the clutch actuation valve away from the scanner isocenter. Mean SNR plotted, with error bars representing maximum and minimum results.....148
6.3.8. Effect on image SNR of complete endoscope actuation system.....148
6.4.1 ERCP training simulators (clockwise from top left) AC4 OGI Phantom (Adam Rouilly, Kent, UK); Hands-on simulator [Grund, 2012]; ERCP Training Model LM-022 (Koken Ltd, Tokyo, Japan); and ERCP Mechanical Simulator [Leung, 2007]. See also 6.4.4. 151
6.4.2. Internal views of ERCP training simulators (clockwise from top left) AC4 OGI Phantom (Adam Rouilly, Kent, UK); ERCP Trainer (The Chamberlain Group, MA, USA); ERCP Training Model LM-022 (Koken Ltd, Tokyo, Japan); and Hands-on simulator [Grund, 2012]. 152
6.4.3 Duodenoscope tip showing catheter and tip mounted electromagnetic tracking sensors (arrows).....155
6.4.4. ERCP Trainer manufactured by The Chamberlain Group, showing (a) simplified upper GI tract, (b) rubber duodenum part, (c) location of ampulla part and (d) biliary tract. 156
6.4.5. Original rubber parts of the ERCP Trainer. Duodenum part shown (l) with recess for ampulla (arrowhead) and collar for locating within simulator frame (arrow). Ampulla part shown from the top (top right) and side (bottom right). ...156
6.4.6. Modified duodenum part. Rapid prototyped mould for the duodenum part shown (l), with endoscopic views of the inner surface of the modified duodenum (r). The modified ampulla part can be seen in the top right image.....157
6.4.7 Modified duodenum part mounted on training simulator, showing plate to compress duodenum against biliary tract (arrow) and void that allows duodenum wall to remain flexible despite the additional compression force (arrowhead). 158

6.4.8. Modified ampulla part (l) moulded from silicone rubber and (r) cross sectional view of part CAD model. The hole piercing the top surface of the ampulla is not visible in this image. 159
6.4.9. Endoscopic image series showing cannulation of the modified ampulla part: (l) catheter is advanced towards papilla, (m) incorrect catheter positioning results in papilla deforming and catheter failing to access the ampulla, and (r) catheter cannulated correctly through the papilla into the ampulla. 160
6.4.10. Experimental setup showing (a) training simulator, (b) electromagnetic field generator, (c) remote actuator modules, (d) duodenoscope, (e) remote actuation system user interface and (f) monitor for duodenoscope video visualisation. 162
6.4.11. CAD model of modified ERCP training simulator with a trace of the catheter electromagnetic tracking sensor (orange) and planes designating test start and end (blue). 162
6.4.12. Example 2D trajectories to illustrate scoring system. Trajectory (a) covers the least distance and has zero corrections so will score the highest. Trajectories (b) and (c) cover the same distance, but because trajectory (c) has a major correction it will score less than trajectory (b). 163
6.4.13. Total performance score (Z) plotted against number of ERCPs completed for operators in experience categories 1, 2 and 3. R^2 of trendline = 0.396 164
6.4.14. Total performance score (Z)plotted against operator experience category, with significance values (P) displayed. 164
6.4.15. Box plots showing measured values plotted against operator experience category for parameters 1, 2 and 3 (top, middle and bottom respectively). 167
6.4.16. Box plots showing measured values plotted against operator experience category for parameters 4, 5 and 6 (top, middle and bottom respectively). 168
6.4.17. Subjects' score for the manually operated test plotted against score for remotely actuated test score. The black line represents an equal score on both tests. 170
6.4.18. Box plot of all operators scores for manually actuated test (M) and remotely actuated test (R). 170
6.4.19. Box plots of all operators' scores for parameters 1-3 (top, middle, bottom respectively), separated by manual actuation (M) and remote actuation (R). 172
6.4.20. Box plots of all operators' scores for parameters 4-6 (top, middle, bottom respectively), separated by manual actuation (M) and remote actuation (R). 173

6.4.21. Comparison between test runs for operators that completed a second remotely actuated test run. 174
6.4.22. Excerpt from a test run to cannulate the simulated bile duct using the remote actuation system. The black line corresponds to the speed of the duodenoscope tip sensor speed. Coloured lines indicate user inputs, with +2 corresponding to the motor rotating clockwise (CW) and −2 corresponding to the motor rotating counter clockwise (CCW). 176
7.3.1. Simplified timing diagram of the MRI sequence used to acquire 1D projections. No magnetic gradient is applied during RF excitation and there is no phase encoding. The only gradient applied is frequency encoding (in this case in the Z direction) during scanner ADC signal acquisition. 182
7.3.2. Each point on the 1D projection (left) corresponds to the sum of the signal acquired from a plane orthogonal to the projection direction (right). 182
7.3.3. Axial image of the tip coil immersed in water shown in top right. Peaks on the 1D projections (blue lines) correspond to the centre of the coil, which is dark on the image due to the plastic mandrel. 183
7.3.4. Mexican Hat wavelet at position b = 0 and scales a = 0.5, 1.0 and 1.5. 183
7.3.5 Procedure for smoothing 1D projection, showing the original projection (a). This is followed by a coefficient map of the CWT function applied to projection (Eq. 7.1), with an outline around the coefficient peak at low wavelet scales due to the projection peak (b). The sum of the coefficients in the highlighted peak is shown in (c), which is then multiplied by the original projection to produce a smoothed result (d). It is then simple to determine the edges of the filtered peak (blue dots). 185
7.3.6. Experimental setup, showing (a) plastic container filled with liquid, (b) duodenoscope tip coil, (c) plastic mandrel to rigidly mount the tip coil and (d) coil connection to MRI scanner. 186
7.3.7. Axial MRI of duodenoscope tip coil showing alternative signal loading cases (SLC): Case 1 (left) idealised with coil surrounded by liquid; Case 2 (centre) plastic block placed adjacent to coil and; Case 3 (right) coil wrapped in air-filled plastic packing material. 187
7.3.8. Reference method of measuring the true coil position and orientation. Axial image slices (left and centre) were processed to determine the centre of the image void due to the coil mandrel (magenta dot). The centre of the coil was then defined as a distance from the tip of the coil along this axis using a coronal image slice (right). 188

7.4.1. Magnitude of coil measurement errors plotted against angle between coil and MRI scanner Z axis, with alternative signal loading cases (SLC) identified. Showing position error (top) and angular error (bottom). 189
7.4.2. Position measurment error in the X, Y and Z axes of the coil coordinate system (top, middle and bottom respectively) as a function of coil angle to MRI scanner Z axis, with separate signal loading cases (SLC) identified. 190
7.4.3. Position measurment error in the X, Y and Z axes of the scanner coordinate system (top, middle and bottom respectively) as a function of coil angle to MRI scanner Z axis, with separate signal loading cases (SLC) identified. 191
7.4.4 Magnitude of coil measurement errors (as 192
7.5.1. Axial image of coil (left) showing four evenly spaced radial signal lobes. These cause the signal sum (right, blue) and projection (red) to exhibit a distinctive peak pattern, which is clearly lower and more truncated on the right of the projection. 193
7.5.2. The 9 projections were all acquired at each of 13 test points. These 117 projections were each repeated 10 times. This chart shows the interquartile range, maximum and minimum peak centre measurements for each projection set, normalised to the median of the projection set measurement. 193
7.5.3. Variation in measured projection peak width as a function of the angle between projection and coil Z axis. Only a weak correlation is observed, which contributes to the instability of the coil orientation detection method. 195
8.2.1. Fluoroscopic image acquired during ERCP after the injection of contrast medium. The duodenoscope (arrowhead) and biliary tree (arrow) are indicated. 198
8.3.1. Biliary cannulation test rig, showing (A) duodenoscope clamp, (B) duodenum plate, (C) bile duct tube and (D) digital camera and mounting arm. 200
8.3.2. Setup for simulated fluoroscopic guided test runs (l) and simulated fluoroscopic guidance image (r). Showing (A) digital camera mounted on repositionable arm, (B) duodenum plate and (C) clear bile duct tube. 201
8.3.3. Setup for MRI guided test runs, with test rig immersed in liquid-filled plastic container (arrow). 201
8.3.4. MRI guidance image showing (A) bile duct tube, (B) duodenum plate, (C) catheter and (D) duodenum with imaging coil. 202
8.3.5. Positions of bile duct and catheter after a test run, as recorded using the vertical (left) and horizontal (right) camera mount. The central axis of the catheter (red) and bile duct (green) has been displayed. The black features on the

duodenum plate on either side of the bile duct are used to determine the image scale. 203

8.4.1. Histograms showing angular alignment errors measured with different guidance image types. Plots (a)-(d) show results measured using the vertical digital camera mount, while plots (e)-(h) show results measured using the horizontal digital camera mount. 205

8.4.2. Histograms showing linear alignment errors measured with different guidance image types. Plots (a)-(d) show results measured using the vertical digital camera mount, while plots (e)-(h) show results measured using the horizontal digital camera mount. 206

8.5.1. MRI guidance series, with the six images (A-F) displayed in the order that they were acquired during the alignment test. On the left the image is displayed with increased contrast (WC = 240, WW = 560) to visualise the catheter, while the right image display is brighter (WC = 80, WW = 220) to visualise the bile duct. .. 208

8.5.2. Image acquired from the horizontal camera mount showing the position of the MR guidance image slice (red lines). The thickness of the catheter means that it can remain within the slice despite a significant misalignment. 209

8.5.3. Image acquired from the vertical camera mount showing the direction and limits of the duodenoscope camera lens (red lines). In this position, the operator is unable to see the catheter tip or the papilla. 210

List of Tables

2.2.1. Relaxation times (T1 and T2) of different biological tissues as a function of magnetic field strength. Reproduced from [McRobbie, 2007]..... 38
2.3.1. Spatial and temporal zones of MRI compatibility. Reproduced from [Chinzei, 1999]..... 46
2.3.2. Magnetic susceptibility of various materials. Reproduced from [Schenck, 1996]..... 47
3.2.1. Comparison between actuation methods for interventional MRI systems. 60
3.4.1. Comparison between tracking methods for interventional MRI systems..... 67
4.4.1. Results of duodenoscope force and torque measurements 90
4.4.2. Acquisition time, signal and noise results for images acquired with the surface array coil and duodenoscope tip coil..... 96
4.4.3. Acquisition time, signal and noise results for images acquired with the surface array coil and catheter coil. 99
5.2.1. Predicted output speed and force or torque (F/T) for each endoscope actuation system DOF based on gear ratios and motor performance. Maximum and peak power (PP) values shown. 102
5.3.1. Maximum driving force of catheter feed module with different pulley friction coatings. Synthetic rubber was supplied by Plasti-Dip Ltd, UK while the silicone rubbers were from Mouldlife UK Ltd. 112
5.6.1. Control and power consumption for endoscope remote actuator system.....131
5.7.1. Materials used to manufacture endoscope remote actuator system.....132
6.2.1. Variation in reference image SNR. 139
6.3.1. Parameters of imaging sequences used for MRI compatibility testing, including repetition time (TR), echo time (TE), field of view (FOV) and number of excitations (NEX). Matrix size referes to the number of pixels in the image 142
6.3.2. Motor and actuation system MRI compatibility test variables. 143
6.3.3. Camera MRI compatibility test variables. 144
6.4.1. Categories of study participants. 154
6.4.2. Parameters used to assess operator performance.....161
6.4.3. Results for each subject (manual test). Measured values for each parameter are displayed, with the score given to that measurement in brackets. The final column is the sum of the six score parameters. 165

6.4.4. Remotely actuated test results for each subject. Measured values for each parameter are displayed, with the score given to that measurement in brackets. The final column is the sum of the six score parameters. 171
7.3.1. List of X, Y and Z components of the projection unit vectors. 187
7.3.2. List of orthogonal projection sets. 187
8.4.1. P values calculated using Levene's test to assess the differences in variance between two sets of angular alignment errors. Each cell shows the P value for the vertical digital camera mount results followed by the P value for the horizontal digital camera mount results. Significant (P <= 0.05) results are highlighted red. 207
8.4.2. P values calculated using Levene's test to assess the differences in variance between two sets of linear alignment errors. Each cell shows the P value for the vertical digital camera mount results followed by the P value for the horizontal digital camera mount results. Significant (P <= 0.05) results are highlighted red. 207

Abbreviations

1D	1 Dimensional
2D	2 Dimensional
ADC	Analogue to Digital Converter
bSSFP	balanced Steady State with Free Precession
CC	Cholangiocarcinoma
CCD	Charge Coupled Device
CT	Computed Tomography
DOF	Degrees of Freedom
EMI	Electromagnetic Interference
ERCP	Endoscopic Retrograde Cholangio-pancreatography
FDM	Fused Deposition Modelling
FOV	Field of View
FSE	Fast Spin Echo
FT	Fourier Transform
GRE	Gradient Recalled Echo
H/C	High Contrast
L/C	Low Contrast
L-R	Duodenoscope Left-Right steering direction
MRCP	Magnetic Resonance Cholangio-Pancreatography
MRI	Magnetic Resonance Imaging
NEMA	National Electrical Manufacturers Association
NEX	Number of Excitations
NMR	Nuclear Magnetic Resonance
PP	Peak Power
PSU	Power Supply Unit
RF	Radio Frequency
ROI	Region of Interest
ROPE	Respiratory Ordered Phase Encoding
SD	Standard Deviation
SLC	Signal Loading Case
SNR	Signal to Noise Ratio
T1	Longitudinal Relaxation Time

T2	Transverse Relaxation Time
TE	Time to Echo
TR	Time to Repeat
TrueFISP	True Fast Imaging with Steady-state Precession
U-D	Duodenoscope Up-Down steering direction

Nomenclature

a	Waveform scaling parameter
A	Area
b	Waveform position parameter
B_0	Main magnetic field
D_o	Outer diameter
D_i	Inner diameter
F_N	Normal (clamping) force
F_P	Pneumatic force
F_{RS}	Return spring force
F_{act}	Actuator force
G	Shear modulus
G_x	Gradient magnetic field in MRI scanner x direction
G_y	Gradient magnetic field in MRI scanner y direction
G_z	Gradient magnetic field in MRI scanner z direction
H	Applied magnetic field
i	Pixel position in horizontal direction
j	Pixel position in vertical direction
J_T	Second moment of area
k	Spring constant
l	Length
L_f	Free length
L_e	Engaged length
m	Number of pixels in vertical direction of an image
M	Magnetic dipole moment
M_0	Inherent magnetization
n	Number of pixels in horizontal direction of an image
N	Noise
p	Pressure
P	Significance value calculated using Student's T-Test
Q_i	Normalised parameter measurement
R^2	Coefficient of determination
S	Signal
t	Time

T	Torque
T_{motor}	Motor torque
T_{out}	Output torque
$T_{parasitic}$	Parasitic torque
$x(t)$	Original projection data
X_i	Parameter measurement
$y(t)$	Filtered projection data
Y_i	Parameter score
Z	Operator performance score
γ	Gyromagnetic ratio
η	Efficiency
θ	Angular deflection
[illegible]	Coefficient of friction
ν_L	Larmor frequency
ψ	Mexican Hat function
χ	Mmagnetic susceptibility
$\mathbf{I}$	Moment of inertia tensor
$\mathbf{n_k}$	Unit vector of a projection in MRI coordinates
$\mathbf{x}$	Matrix defining the coordinates of a point of intersection between planes
$\mathbf{x_k}$	MRI coordinates of the edges of a projection peak
$\mathbf{X_i}$	Vector from point i to median of all points

Chapter 1

Introduction

The use of Magnetic Resonance Imaging (MRI) as a tool to guide medical procedures offers many potential benefits and is currently an active area of research. There has been a parallel increase in robotic and computer assistance for interventional procedures, including in the fields of laparoscopic surgery and flexible endoscopy.

MRI-guided endoscopy offers the potential for an improvement in clinical outcomes by combining the strengths of both procedures. Intra-operative MRI can be used to guide the operator when attempting technically challenging interventional endoscopic procedures that are traditionally performed with fluoroscopic guidance or none at all. In addition, Intra-luminal MR receiver coils mounted on and positioned by the endoscope can be used to enhance diagnostic MRI in the region around the endoscope.

This chapter describes the motivation for the research presented in this thesis as well as outlining the research objectives. A brief overview of the structure of the thesis is presented at the end of the chapter.

1.1 Motivation for Research

MRI has become one of the most widely used radiographic techniques for the diagnosis of pathologies. MR images have excellent and adjustable soft-tissue contrast, can be generated at high temporal and spatial resolutions in a variety of cross sectional image planes and do not expose the patient to any ionising radiation. These features make MR images ideal for the guidance of interventional procedures in addition to its diagnostic capabilities.

However, operating in the MR environment is challenging due to the high magnetic fields and the sensitivity of the scanner to electromagnetic interference (EMI). In addition, the most common and highest-quality MRI scanners are of a closed-bore configuration, which significantly limits the available space for interventional tools.

Endoscopic procedures enable clinicians to directly view the inner surface of lumens such as the oesophagus and large intestine. They are minimally invasive since

access to the lumen is gained through natural orifices with a camera mounted on a steerable and flexible instrument. While endoscopy provides excellent images of the lumen inner wall, it is not capable of assisting diagnosis of pathology inside the lumen walls or in other body cavities. Techniques such as fluoroscopic-guided endoscopy aim to combine radiographic techniques with endoscopy, but they are limited by the relatively poor quality of the diagnostic imaging.

The desire to achieve combined MRI and endoscopy has led to the development of intra-luminal MR receiver coils that can be mounted on endoscopes and catheters. The use of these coils has been limited due to a lack of space available to operate the endoscope controls, which necessitates the removal of the patient from the MRI scanner before the endoscope can be moved and precludes real-time MRI guidance. However, research has demonstrated that intra-luminal coils are capable of significantly improving the diagnostic quality of MR images in the surrounding area.

Endoscopic retrograde cholangio-pancreatography (ERCP) is a technique for treating disorders and obtaining fluoroscopic images of the biliary system that would benefit greatly from the use of MRI guidance. The biliary system is a network of thin ducts located between the liver, gall bladder and pancreas which drain bile into the upper part of the small intestine (known as the duodenum). ERCP is a technically challenging procedure with a high failure rate due to the difficulty of controlling the endoscope and interventional tools.

Malignant tumours of the bile ducts are known as cholangiocarcinoma, which is associated with a very high mortality rate due to the difficulty in identifying and staging cancerous growths. The size and location of cholangiocarcinoma within the abdomen makes it very challenging to obtain high quality diagnostic images from MRI in the early stages of the disease.

This work is motivated by a desire to improve the diagnosis and treatment of biliary disorders, in particular cholangiocarcinoma, by overcoming the limitations of both traditional ERCP and MRI of the biliary system.

1.2 Research Objectives

The objective of this research is to develop a system that enables MRI-guided ERCP to be performed as a clinically viable procedure. This system is designed to enable high-quality MR images of the bile ducts to be acquired using intra-luminal MR receiver coils. The use of intra-operative MRI also facilitates an improvement in the technical success rate of ERCP through the use of intra-operative MR guidance images.

Development of the MRI-guided ERCP system involved the following research activities:

- Investigation into methods of controlling and actuating the duodenoscope during MRI scanning of the patient's abdomen. A prototype system that makes this possible was designed and constructed.

- The MRI compatibility of the duodenoscope actuation system was investigated to determine the extent to which it reduces the diagnostic value of intra-operative MRI. Testing to confirm the capability of the remote actuation system to achieve the complex movements required for ERCP was also performed.

- A method of duodenoscope tip tracking to facilitate high quality motion corrected MRI and intra-operative MRI guidance was developed. Following this the clinical benefits of MRI-guided ERCP over traditional fluoroscopic-guided ERCP were investigated within a simulated environment.

This research has resulted in a system which facilitates a complex endoscopic procedure to be performed under real-time MRI guidance, a result which has not previously been published. This is achieved by novel use of a hybrid manual / remotely actuated system and supported by a novel method of tracking the endoscope within the MRI environment. This system is readily adaptable to a range of similar procedures, as is the objective performance assessment method used to determine the system's effect on operator skill.

For clarification, the intra-luminal MR receiver coils and MRI compatible duodenoscope that the system presented in this thesis utilises are the products of collaborating research groups. The MR receiver coils mounted on the duodenoscope tip and catheter were developed by Professor Richard Syms and his research group based in the Department of Electrical and Electronic Engineering at Imperial College. The MRI compatible duodenoscope was developed by Tony Duncan and Tony Grantham of Endoscan Ltd. (West Sussex, UK) with support from the collaborating research groups. A description of these technologies is included in Chapter 4 for completeness.

1.3 Structure of the Thesis

Chapter 2 consists of an introduction to MRI scanners and the techniques involved in acquiring MR images. The hardware used to generate the images is introduced along with

an explanation of a simplified imaging sequence. The chapter concludes with a discussion of the effects motion and interventional devices on MRI.

Chapter 3 presents a review of the published literature on interventional MRI systems, including a discussion of the options for actuation, sensing and device tracking. A review of existing robotic and MRI compatible endoscopes is also presented.

Chapter 4 describes disorders of the biliary system and the ERCP technique in greater detail before presenting a detailed outline of the MRI-guided ERCP procedure. The requirements of an MRI-guided ERCP system are discussed along with a description and characterisation of the MRI compatible endoscope and intraluminal MR receiver coils that have been developed by collaborating research groups.

Chapter 5 focuses on the design of the endoscope remote actuation system that was developed to enable the MRI compatible endoscope to be operated during MR image acquisition. The development and final design of each module of the system, including the user interface and control box, is presented. The development of a novel MRI compatible pneumatic clutch that facilitates a significant system cost reduction is included in this chapter.

Chapter 6 details the testing performed to validate the performance of the endoscope remote actuation system. This chapter is split into two parts, with testing of the MRI compatibility of the system described first. This is followed by a user study that demonstrates the functionality of the system using an endoscopic training simulator and objective performance assessment.

Chapter 7 describes the development of a method to enable the position of the duodenoscope tip and imaging catheter to be measured in real-time by the MRI scanner.

Chapter 8 covers an experiment designed to demonstrate that the MRI-guided ERCP system developed in this thesis is capable of improving clinical outcomes. The benefit that MRI guidance can provide to the ERCP procedure when compared with fluoroscopic guidance is quantified in a simulated cannulation task.

Chapter 9 concludes the thesis by summarising the work completed and identifying areas of future development.

Chapter 2

Magnetic Resonance Imaging

2.1 Introduction

The technique of magnetic resonance imaging (MRI) was first developed in the 1970s, and has become an important radiographic tool for diagnostic imaging [McRobbie, 2007]. MRI scanners have changed significantly during this time, but the underlying physics of the imaging technique has remained consistent. MRI offers an unmatched combination of excellent soft-tissue contrast and flexible cross-sectional imaging without the harmful ionising radiation that characterises X-ray based imaging techniques such as Computed Tomography (CT). MRI is primarily a diagnostic technique, but the use of intra-operative images to guide interventional procedures has been investigated at length in recent years.

This chapter begins with an introduction into MRI scanner hardware and the principles of MRI. The impact of the MR environment on the design of interventional tools is explored along with a description of how patient motion affects MR imaging. These concepts are presented to provide context to the following chapters of this thesis and areas which have a direct bearing on later work have been identified.

2.2 MRI Background

The basic components of an MRI scanner are the main magnet, gradient coils and radio frequency (RF) coils (Fig. 2.2.1). The main magnet is used to create a high strength (commonly up to 3T for clinical use) homogenous, static magnetic field, while the gradient coils are used to generate a controlled magnetic field gradient in addition to the main magnetic field. The magnitude and direction of this gradient constantly changes throughout the image acquisition period to spatially encode the data from which the MR image is generated. Images are acquired as cross sectional planar slices, usually in contiguous sets that enable the operator to view a volume of the patient's anatomy (Fig. 2.2.2).

RF coils are used both to excite the protons within the scanner bore by emitting pulses of energy and to receive energy emitted by the excited protons as they relax back

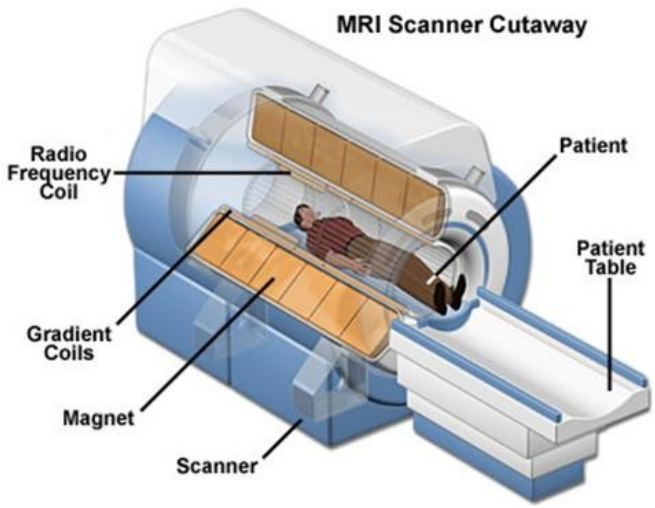

Fig. 2.2.1. Cutaway diagram of a closed MRI scanner [Tse, 2008]

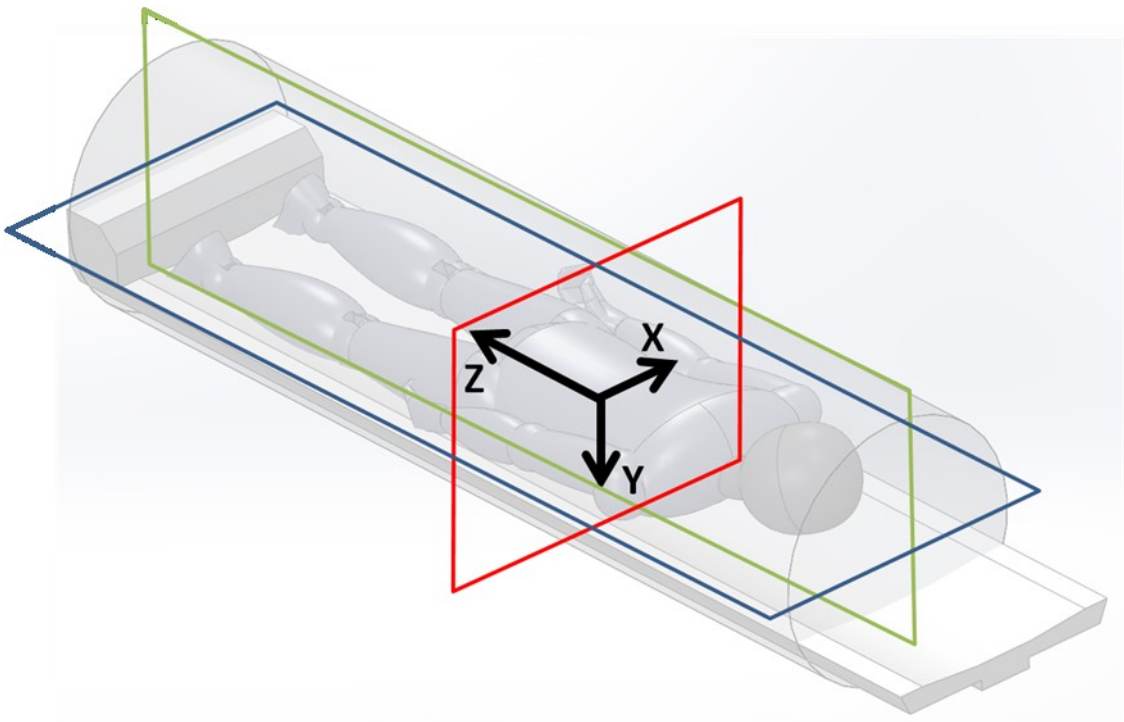

Fig. 2.2.2. MRI scanner with coordinate system and imaging planes. Showing (red) Axial plane, (green) Sagittal plane and (blue) Coronal plane.

to their equilibrium state. The strength of the signal received is heavily dependent on the distance between the coil and the excited tissue, so to maximise signal, additional receiver coils can be introduced into the scanner and placed closer to the region of interest. Since the excited signals are in the μT range [Elhawary, 2008b], MRI scanners are very sensitive to Electromagnetic Interference (EMI) and are usually placed within a shielded enclosure (Faraday cage) with all control electronics outside the shield.

Clinical MRI scanners fall into two main categories: closed and open (Fig. 2.2.3). Closed scanners consist of cylindrical magnets – they generally have stronger and more

Fig. 2.2.3. Examples of closed (l) and open (r) MRI scanners [Tse, 2008]

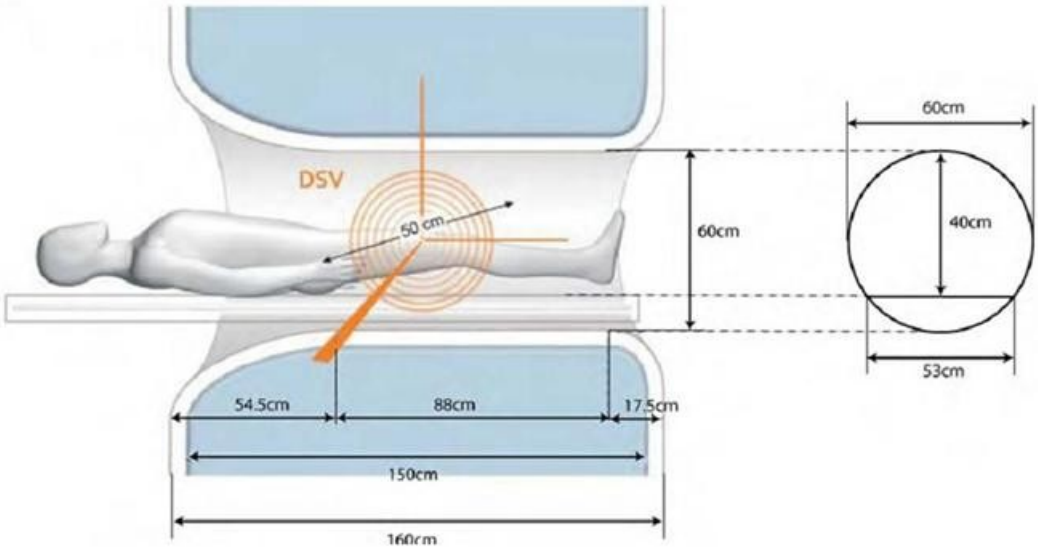

Fig. 2.2.4. Dimensions of a typical closed bore MRI scanner [Tse, 2008]

homogenous static magnetic fields and are therefore able to produce higher quality images. For this reason they are far more common in hospitals and are extensively used for diagnostic imaging. Open scanners come in many configurations and are far less common due to their relatively limited image quality and higher cost.

However, open scanners do not suffer from a major issue that afflicts closed scanners – that of limited access to the patient. Fig. 2.2.4 shows the dimensions of a typical 60cm bore closed MRI scanner, which demonstrates the challenge of patient access during Interventional MRI. When imaging the patient's abdomen in particular, the long bore and narrow diameter make it challenging for a clinician to access any part of the patient other than the top of their head, which makes fine control of an endoscope almost impossible. Closed scanners with shorter and wider bores exist, but suffer from some of the imaging issues outlined above for open bore scanners.

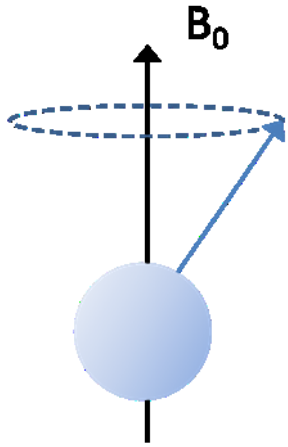

Fig. 2.2.5. Precession of atomic spin about the main magnetic field (B_0).

2.2.1 Image Acquisition

The following section describes the theory of Magnetic Resonance Imaging using a generalised example. The interaction between various physical phenomena is complex and there are many modifications to this general case which can alter the acquired image. While a full description of these factors lies outside the scope of this work, some of the concepts presented in this section are exploited in Chapter 7 to enable the duodenoscope tip to be tracked using the MRI scanner.

MRI utilises the principle of nuclear magnetic resonance (NMR) to generate images of biological tissues. Atoms with a non-zero nuclear spin generate a magnetic moment which aligns predominantly with the main static magnetic field when placed inside the MRI scanner [Brown, 2003]. Hydrogen is such an atom, and clinical MR imaging is commonly targeted at the Hydrogen atoms present in water. The atomic spins do not align perfectly with the field, but instead precess around the main axis of the field (Fig. 2.2.5). The frequency of this precession is known as the Larmor frequency (ν_L) and is calculated using the formula:

$$\nu_L = \gamma B_0$$

(Eq. 2.1)

Where B_0 is the magnetic field strength and γ is the gyromagnetic ratio, which is a constant value for a particular atom. For Hydrogen the gyromagnetic ratio is 42.58 MHz/T resulting in a Larmor frequency of 63.86 MHz for a magnetic field strength of 1.5 T [Brown, 2003].

An electromagnetic excitation pulse is applied to atoms within the imaging volume to generate an NMR signal. This excitation is at the Larmor frequency of the atoms and

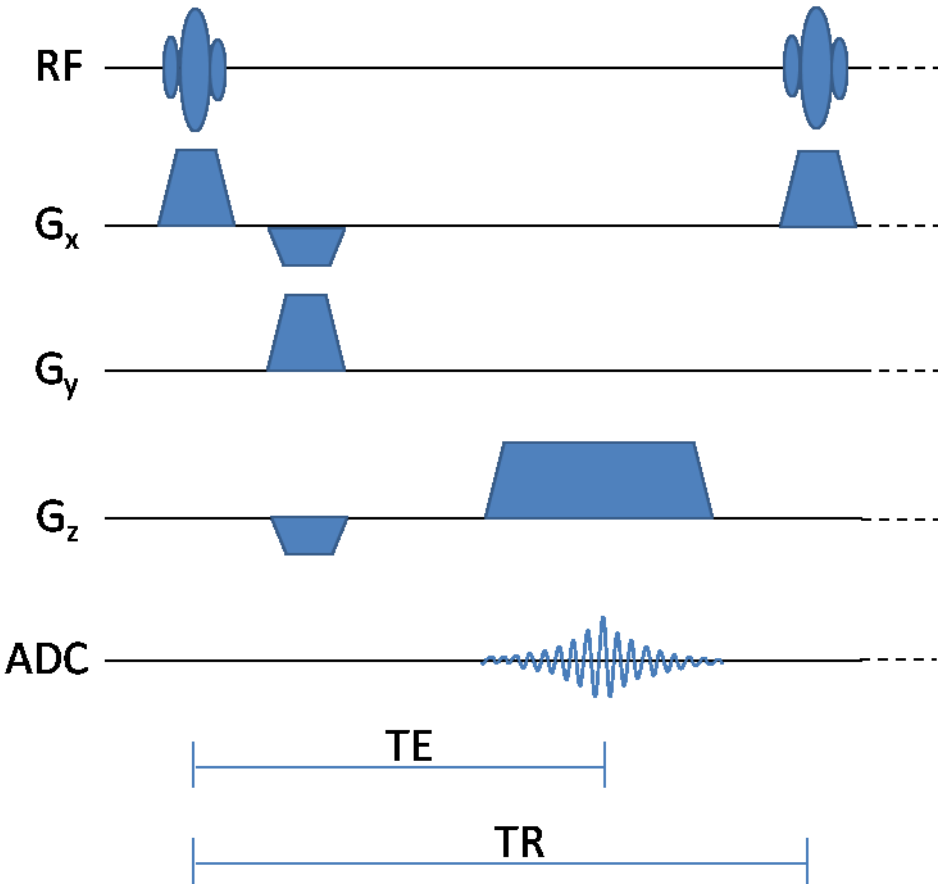

Fig. 2.2.6. Example of a simplified gradient echo MR imaging sequence. Each horizontal line represent activity of one of the scanner components: the radio frequency excitation coil (RF), the magnetic gradient coils in the scanner X, Y and Z directions (G_x, G_y and G_z respectively) and the scanner analogue to digital converter for signal recording (ADC). The time between the RF pulse and the signal recording is known as the echo time (TE), while the time between successive RF pulses is the repetition time (TR).

forces the atomic spin out of alignment with the main magnetic field. When the excitation pulse is complete the magnetic dipoles of the atoms relax back to their equilibrium position releasing energy in the form of an electromagnetic wave at the Larmor frequency as they do so.

Magnetic resonance images are generated by spatially encoding the NMR signals produced by objects within the scanner. Spatial encoding is achieved by applying an additional magnetic field to the main field that varies with position within the scanner. These additional fields are known as gradient fields and are applied both during excitation and acquisition of signals. The sequence in which the magnetic field gradients are applied has a significant effect on the image properties.

To illustrate this, a simple imaging sequence is shown in Fig. 2.2.6. The magnetic field gradient applied during the radiofrequency excitation pulse is known as the slice

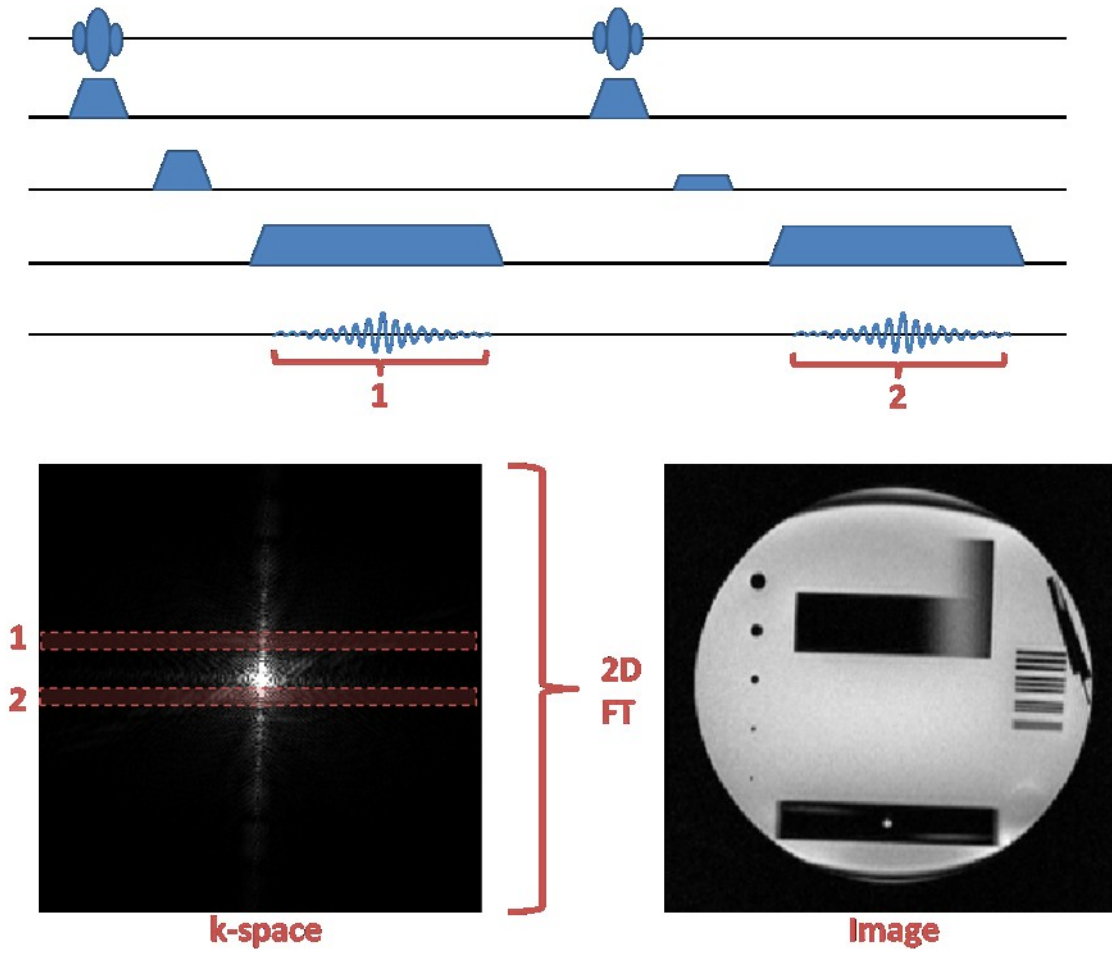

Fig. 2.2.7. MR images are constructed by repeating image sequences with phase encoding gradient changing on each repetition (top). Received signals are used to construct a 2 dimensional (2D) k-space matrix, with each sequence repetition corresponding to a horizontal line of k-space (bottom left). The image is generated by applying a 2D Fourier transform (FT) to the k-space matrix (bottom right).

selection gradient and it ensures that the Larmor frequency corresponding to the excitation pulse is only experienced by atoms within a specified region of space. All other atoms will have a Larmor frequency of above or below the pulse frequency and will therefore not be excited.

Once the excitation pulse is complete, a second magnetic field gradient is applied in an orthogonal direction to the slice selection gradient. Whilst this gradient is applied the excited atoms precess at varying frequencies dependent on their position. Once the gradient is removed there will be a difference in precession phase between atoms from different regions, which changes the sum of the transverse component of the NMR signal produced by the atoms as they relax to equilibrium.

After this, a third orthogonal gradient is applied at the same time as the scanner analogue to digital converter (ADC) is activated to receive the excited NMR signal via the

	T1 (ms)			T2 (ms)		
Tissue	**0.5T**	**1.5T**	**3T**	**0.5T**	**1.5T**	**3T**
White Matter	520	560	832	107	82	110
Grey Matter	780	1100	1331	110	92	80
Muscle	560	1075	898	34	33	29
Fat	192	200	382	108	-	68
Liver	395	570	809	96	-	34
Spleen	760	1025	1328	140	-	61

Table 2.2.1. Relaxation times (T1 and T2) of different biological tissues as a function of magnetic field strength. Reproduced from [McRobbie, 2007].

RF coil. The third gradient is known as the frequency encoding gradient and causes the Larmor frequency and therefore the frequency of the atom's NMR signal to vary dependent on the position of the atom.

Once the sequence in Fig. 2.2.6 is complete, an NMR signal will be received that is a combination of many frequencies and amplitudes. The signal has been acquired from atoms within a single region, in this case a slice of space in the Y, Z plane of the scanner. The signal has a particular phase encoding in one direction (scanner Y direction in this case) and a frequency encoding in the orthogonal direction. This signal can be thought of as a single horizontal line of a 2 dimensional (2D) matrix (Fig. 2.2.7) with frequency on the x axis and phase on the y axis. By repeating the sequence in Fig. 2.2.6 many times with different phase encoding gradients the 2D matrix (known as k-space) can be filled. The nature of the spatial encoding applied during the scanning sequence means that this matrix is the inverse Fourier transform (FT) of an image of the selected region of space. Applying a 2D FT to the matrix results in an image in which bright pixels correspond to regions of high NMR signal in the object being imaged.

The rate at which an atom relaxes back to equilibrium and the way in which it interacts with surrounding atoms is described by two time constants (known as T_1 and T_2 respectively). The molecular structure of a material determines the value of these time constants, which can vary widely and are dependent on the main magnetic field strength (Table 2.2.1). Since the NMR signal is produced by relaxation of the atoms, the signal strength measured by the MRI scanner is dependent on the T1 and T2 time constants, the length of time between excitation and signal acquisition (time to echo, or TE) and the length of time between successive excitation pulses (time to repetition, or TR. See Fig. 2.2.6). For a given sequence the TE and TR parameters can be adjusted to produce a

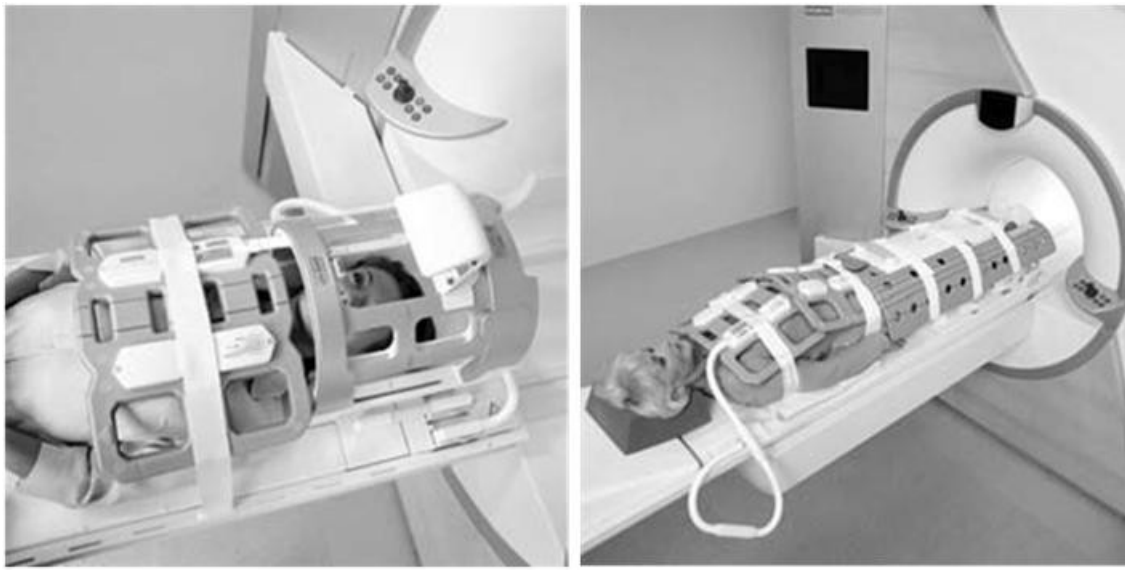

Fig. 2.2.8. Auxiliary imaging coils, showing (l) head and chest coils and (r) peripheral angiography coils [Brown, 2003].

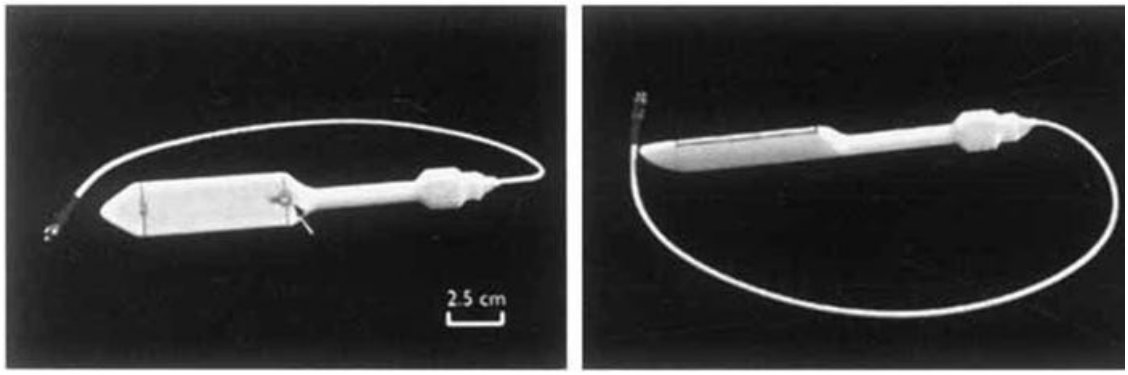

Fig. 2.2.9. Solid endorectal coil for prostate imaging, developed by DeSouza et al [DeSouza, 1996].

different level of signal from different materials, and therefore select the contrast of the MR image.

The simplified gradient echo sequence shown in Fig. 2.2.6 is only one of many different types. Image quality can be improved by repeated acquisition of the same volume and averaging the results. The order and magnitude of excitation pulses and field gradients as well as the timing of signal acquisition periods can be adjusted to produce images with different characteristics. Truncated imaging sequences are used to provide more information about the patient and interventional tools, as described further in Section 3.4 and Chapter 7.

2.2.2 Auxiliary Imaging Coils

The strength of the signal received by the MRI scanner is heavily influenced by the distance between the object being imaged and the RF receiver coil, as well as the size of the coil [Brown, 2003]. The scanner main coil (often referred to as the 'Body coil') is large and mounted on the inside surface of the scanner bore. It is therefore is a relatively long way from the centre of the imaging volume, but is capable of imaging a large volume. Imaging of specific anatomic regions is improved by the use of auxiliary coils, which reduce the imaging volume but increase the signal strength within this volume. These are designed to tightly enclose the region of interest, reducing the distance between the tissue and coil and dramatically improving the image quality. Most clinical systems include coils for the head, spine and chest as standard and other designs are available (Fig. 2.2.8).

An extension of this principle has led to the development of internal coils for targeted imaging of individual organs. Endorectal coils for imaging of the prostate (Fig. 2.2.9) and similar designs for vaginal imaging [Gilderdale, 1999] are in common clinical use. More recently, much smaller microcoils mounted on catheters and endoscopes have been developed for intraluminal imaging of the vascular and gastro-intestinal systems [Ahmad, 2008; Arepally, 2004; Rivas, 2002]. The improvement in image quality due to the use of internal coils is well established and as they become more common the benefit in diagnostic yield is beginning to outweigh their increased cost and complexity.

2.2.3 Effects of Motion during MRI

If the object to be imaged is moving, then it can be seen from the description above that there will be a significant impact on the resulting MR image. With the gradient echo sequence structure described above the time between successive excitations (TR) may be in the order of 500 ms [Brown, 2003], which means that and a typical image resolution of 128 k-space lines the time between acquisition of the first and last lines of k-space would be over 1 minute. If the object being imaged moves during this time then different k-space lines will be acquired from different regions within the object, and the resulting image will not be a faithful reproduction of the object. This is known as motion artefact.

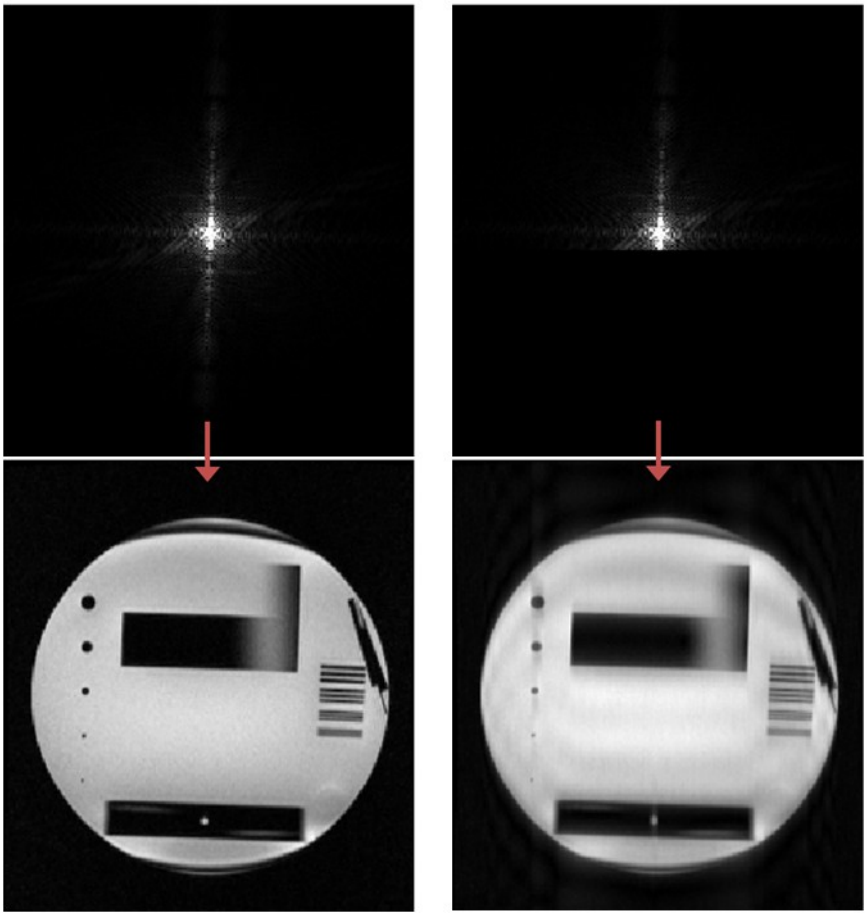

Fig. 2.2.10. Illustration of the effect of acquiring an incomplete k-space matrix. If slightly more than half of k-space is filled, the resulting image is still relatively high quality (r) when compared with the original image (l) despite blurring in the phase encoding direction.

The appearance of motion artefacts varies depending on whether the motion is in-plane or out-of-plane and is affected by the type of imaging sequence used. In anatomic imaging, motion is typically due to either gross patient movement, involuntary irregular movement (such as gut peristalsis) or involuntary regular movement (such as respiration and cardiac output). Gross movement and involuntary irregular movement are difficult to compensate for due to their inconsistent nature, so if they occur the image is typically re-acquired.

Respiration typically occurs at 12-18 breaths per minute, and various studies have suggested that the liver moves between 10 and 25 mm from the peak of inspiration to the peak of expiration during normal breathing [Clifford, 2002]. The motion is predominantly in the head-foot direction with some components in the anterior-posterior and left-right directions. Some studies [Brandner, 2006; Ito, 2012] suggest that abdominal organs move differently from each other, suggesting that the distance between them changes and that the motion of smaller structures such as the biliary system is more complex.

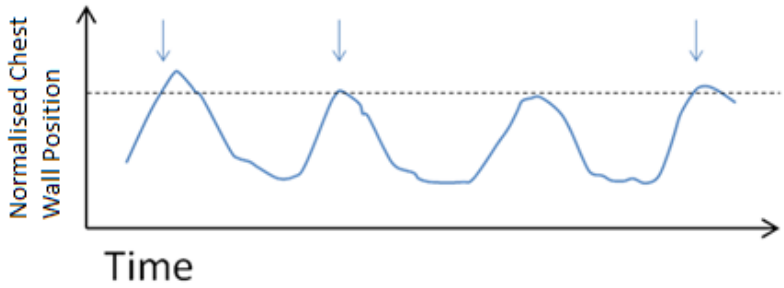

Fig. 2.2.11. Respiratory signal used for image gating. Data acquisition is triggered by the signal passing above a threshold value (arrows), which can result in delays due to inconsistent breathing patterns [McRobbie, 2007].

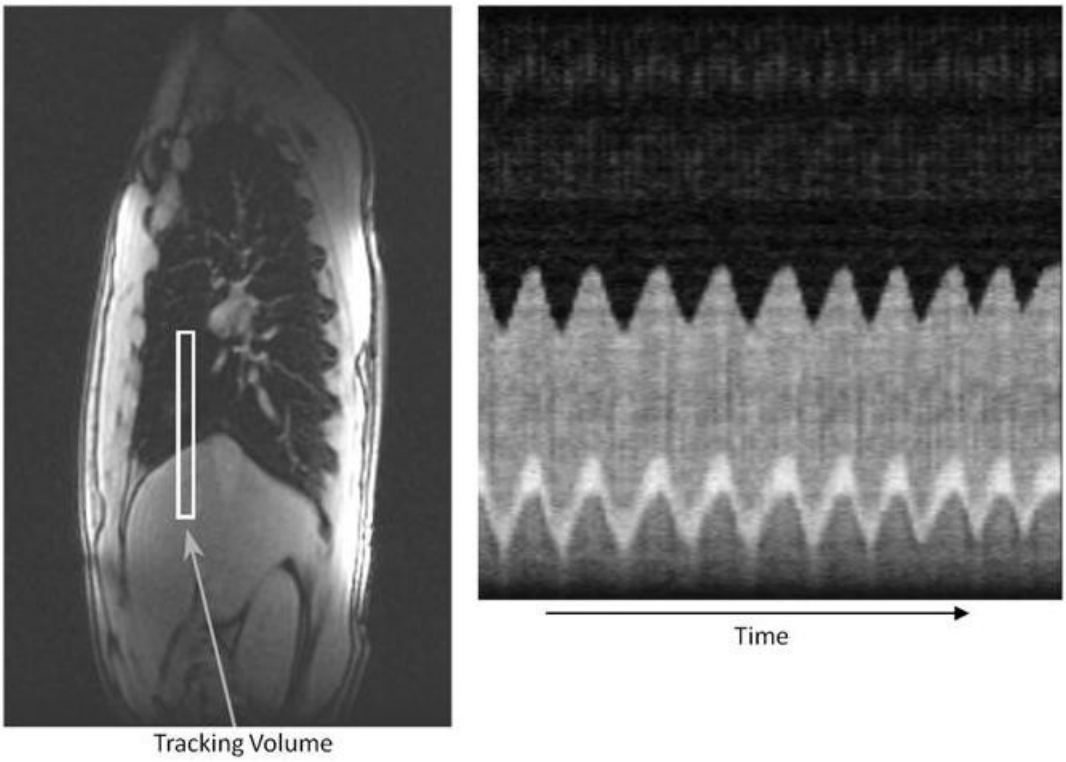

Fig. 2.2.12. Navigator respiratory measurement, showing (l) columnar volume positioned across the diaphragm and (r) Navigator signal changes during respiration. Reproduced from [McRobbie, 2007].

In all cases a reduction in the acquisition time will limit motion artefacts, either by reducing the magnitude of motion during the sequence or by enabling the sequence to be completed within a single breath-hold. Due to the desire to generate a specific image contrast it may not be desirable to reduce the TR and TE to reduce the acquisition time, however advanced sequences (such as Fast Spin Echo or FSE) enable a significant reduction in overall acquisition time without reducing the effective TR by modifying the excitation pulse and interleaving the signal acquisition periods. This can lead to blurring

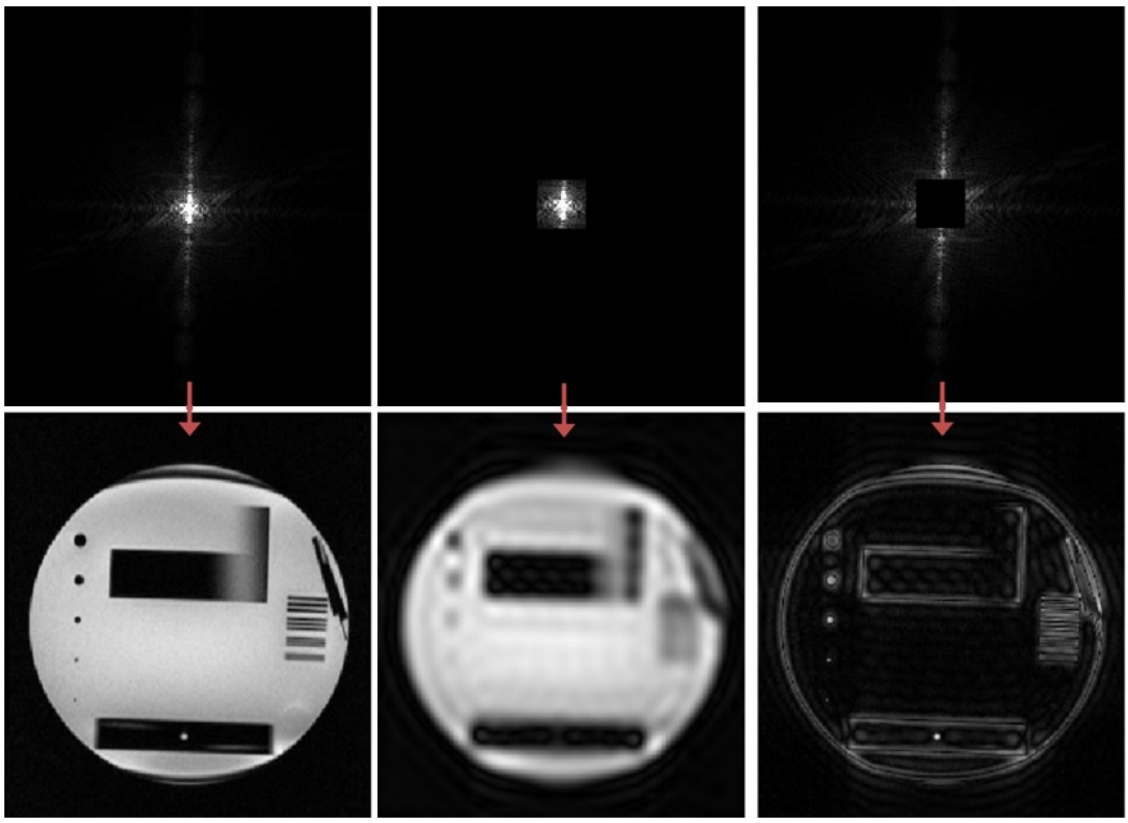

Fig. 2.2.13. A standard image (left) is composed of different regions of k-space. The outer region contains high frequency information at the edges of regions of high contrast (right), while the majority of the image signal is contained in the centre of k-space (centre).

in the phase encoding direction due to a lack of signal refocusing from the modified excitation pulses [Brown, 2003].

In order to further limit the acquisition time, there are sequences that populate only a limited region of k-space and then either interpolate the information in the empty regions or fill them with zeroes [McRobbie, 2007]. The properties of the 2D Fourier transform used to calculate the image from k-space mean that the loss of image quality is limited relative to the significant reduction in the amount of data acquired (Fig. 2.2.10).

Respiratory motion can be eliminated by breath-holding - this requires the entire image sequence to be completed in less than approximately 20 seconds and relies on the use of rapid image sequences discussed above. Breath-holding is not appropriate for many patients due to their age, illnesses that prevent them from holding their breath for an extended period, or anaesthetised patients [Atkinson, 2011].

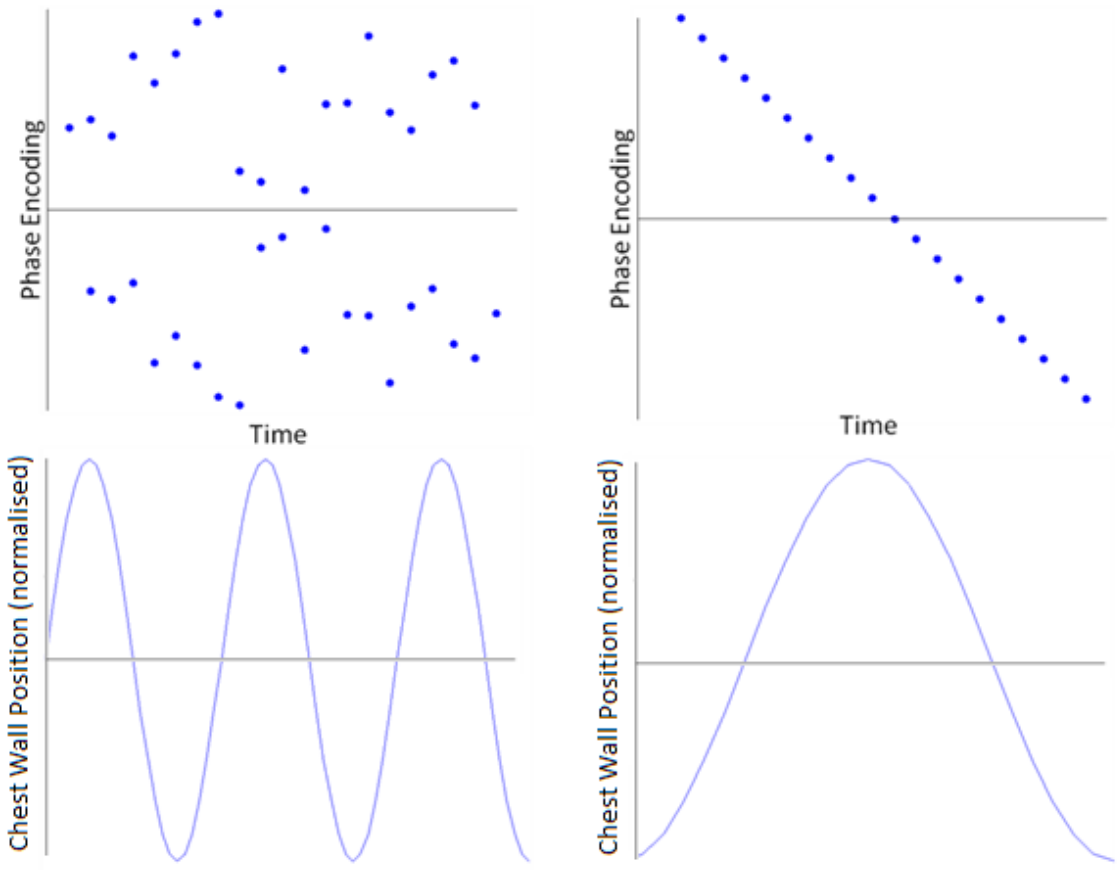

Fig. 2.2.14. ROPE motion compensation strategy. Data is acquired over several breathing cycles, with the order of phase encoding rearranged to match the diaphragm position (left). When the image is reconstructed, the effect is as if the data have been acquired over a single, slower breathing cycle (right). Reproduced from [McRobbie, 2007].

It is possible to limit the effect of periodic motion by limiting the acquisition of data to a set period within the motion cycle, known as gating [Atkinson, 2011]. A signal of the periodic motion is acquired and the MRI scanner set to acquire data only during the period immediately following a certain feature on the periodic motion signal (Fig. 2.2.11). Depending on the sequence used and the size of the gating window, this acquisition could result in a single line of k-space or an entire image slice being acquired at each trigger point. This technique can result in excellent motion compensation as the acquisition extent and window can be limited so that there is effectively no motion during acquisition. However, it does rely on the motion being the same from one cycle to the next and can result in the total image acquisition time being very significantly extended. This in turn increases the risk of gross patient movement and peristalsis as well as having implications for patient safety and clinical practicality.

The signal used for gating can be acquired in a number of ways. In cardiac imaging a single ECG lead is usually used to determine the peak of the R-wave in the cardiac cycle.

This peak is used by the scanner to trigger the imaging sequence. For respiratory motion, a common technique is to use a pneumatic bellows mounted on a belt worn around the patient's chest. The change in pressure in the bellows due to expansion of the chest provides a measure of respiration, and allows the peak of inspiration to be used to trigger the scanner. A chest belt is usually not sufficiently accurate to determine how deep a particular breath is compared with another, so it relies on the patient consistently breathing at the same depth (Fig. 2.2.11).

More detailed information about the respiratory cycle can be acquired using a Navigator sequence. This is a very rapid MRI sequence that acquires signal only from a narrow columnar region placed over the patient's diaphragm. The abrupt change in signal from the air in the lungs to the liver tissue means that the position of the diaphragm can be accurately determined at a high temporal resolution (Fig. 2.2.12). This increased accuracy means that data can be acquired during particularly deep or shallow breaths, which improves the motion compensation of the technique.

The principles of gating and k-space manipulation are combined in a technique known as respiratory ordered phase encoding (ROPE). This takes advantage of the fact that the signal amplitude in the central region of k-space is much larger than the peripheral regions. Fig. 2.2.13 demonstrates that the majority of the signal in the image comes from the central region of k-space only. The periphery of k-space provides information about the tissue boundaries, but there is very little contrast and the total image signal is very low.

This characteristic means that the effect of tissue motion on the final image is less significant if it occurs during acquisition of the peripheral regions of k-space. The ROPE technique uses a respiratory motion signal (Navigator sequence or chest belt, as described above) and orders the phase encoding sequence so that the central regions of k-space are acquired around the peak of inspiration when the speed of respiratory motion is at it's lowest (Fig. 2.2.14). This technique has the advantage of allowing high quality abdominal imaging to be performed without a restriction on the sequence time. However, it is relatively complex to implement, and due to the nature of the phase encode ordering is not compatible with certain imaging sequences, and it is reliant on an accurate respiratory motion signal [McRobbie, 2007].

Zone 1	The object remains within the region of interest and in contact with the patient during the procedure and imaging.
Zone 2	The object is not within the region of interest but remains in contact with the patient and within the imaging volume during the procedure.
Zone 3	The object is within the imaging volume but is removed during imaging or when not in use.
Zone 4	The object can be used within the magnet room during the procedure if it is kept at a distance of more than 1m from the magnet centre or outside the 200 Gauss line.

Table 2.2.2. Spatial and temporal zones of MRI compatibility. Reproduced from [Chinzei, 1999].

The fact that motion artefact is a particular challenge when performing MRI of the abdomen makes the techniques used to overcome it of particular interest to this research notably the system experiments designed in Chapter 8. In addition, the improvement in imaging speed and extraction of information from limited k-space datasets, which was developed for motion compensation, can be utilised to provide real-time guidance and tracking information during the interventional MRI procedure (see Chapter 7 and 8).

2.3 MRI Compatibility

MRI compatibility refers to the effects that materials and systems have on the MR images, and the effect that the MR environment has on them. It is useful to break down the concept of MRI compatibility into two categories – *MR safe* and *MRI compatible*. An object is considered MR safe if it does not present any danger to people or equipment when introduced into the MR environment. An object is MRI compatible if, in addition to being MR safe, it does not affect the diagnostic quality of the image being generated [Elhawary, 2008b]. In addition to the object's composition, both of these terms are highly dependent on the method of testing (for example the image sequence and experimental setup) and the location of the object, so this information should always be quoted in any discussion on compatibility.

The extent to which an object degrades image quality and the level of degradation that can be tolerated will change for different procedures, hence the MRI compatibility or otherwise will also change. Chinzei et al [Chinzei, 1999] describe a system of further classifying devices as MRI compatible within certain location and timing zones, defined in Table 2.2.2. The definition of each zone can be adjusted to adjust the suitability of this system for a given application.

Material	Density (g/cc)	Susceptibility ($x10^{-6}$)
Pyrex Glass		-13.88
Copper	8.92	-9.63
Water (37°C)	0.933	-9.05
Human Tissues	~1.00-1.05	~ (-11.0 to -7.0)
Air (NTP)	0.00129	0.36
Aluminium	2.70	20.7
Titanium	4.54	182
Stainless Steel	8.0	3520-6700
Iron[a]	7.8	$>10^{11}$

[a] In addition to a high value of χ, M_0 of Iron is $\neq 0$

Table 2.3.1. Magnetic susceptibility of various materials. Reproduced from [Schenck, 1996].

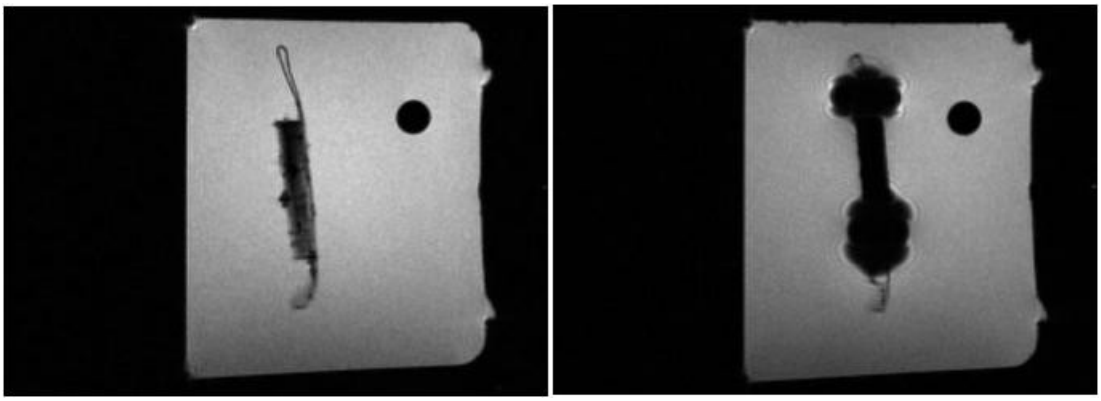

Fig. 2.3.1. MR images of identical cylindrical samples of Macor® (l) and brass (r) suspended by Nylon in a liquid phantom. The susceptibility artefact of the brass cylinder can be clearly seen [Tse, 2011].

Clearly a major source of issues with MR compatibility stems from the presence of the large static magnetic field and pulsed field gradients, which means the magnetic susceptibility (χ) of a material is of prime importance – this is "a dimensionless quantity that is a quantitative measure of a material's tendency to interact with and distort an applied magnetic field" [Schenck, 1996]. This is expressed in the following equation:

$$M = \chi H + M_0$$

(Eq.. 2.2)

Where χ is the magnetic susceptibility of the material, H is the applied magnetic field strength, M_0 is the inherent magnetization of the material and M is the resultant magnetic dipole moment per unit volume. Materials with a non-zero value of M_0 are unsuitable for use in MRI due to the distorting effect of their inherent magnetic field and materials that have low χ are preferred due to their limited interaction with the magnetic field. Values of χ for some materials are shown in Table 2.3.1.

Objects that generate a high M (either due to χ or M_0) will experience large forces in the presence of the scanner main magnetic field, and therefore are generally unsuitable for use in MRI. In very limited cases these materials have been used in Zone 4 (see Table 2.2.2) when appropriate steps have been taken to resist the magnetic forces [Gassert, 2006b].

By definition, any material with a non-zero magnetic susceptibility will interact with a magnetic field surrounding it. This has the effect of perturbing the surrounding magnetic field from the nominal value in regions surrounding the object. The extent of this is determined by the magnetic susceptibility of the material, as well as the shape, position and orientation of the object. Due to complex interactions between these factors the precise level of perturbation cannot be easily predicted [Schenck, 1996], although Tse et al [Tse, 2011] performed work to quantify the differences between materials under controlled conditions.

Due to the manner in which MR images are encoded using magnetic field gradients, this perturbation distorts the appearance of the object in the image (Fig. 2.3.1), and can distort the appearance of features near the object. Collectively these distortions are known as susceptibility artefacts and they can severely affect the diagnostic quality of an image. Objects that produce artefacts can be MRI compatible if placed outside the imaging volume (Zones 2 and 3).

MRI scanners are placed within extensively shielded rooms to remove interference from external sources. However, the rapidly changing gradient magnetic fields and RF pulses can induce eddy currents within any electrically conductive materials inside the scanner room. These eddy currents can be large (RF pulses of 1kW are common [McRobbie, 2007]) and can cause a temperature change in conductive materials due to resistive heating during the imaging sequence. This is primarily a safety concern- the level of energy applied during a sequence must be monitored to ensure it stays within safe levels, and the patient should be insulated from any conductive materials wherever possible.

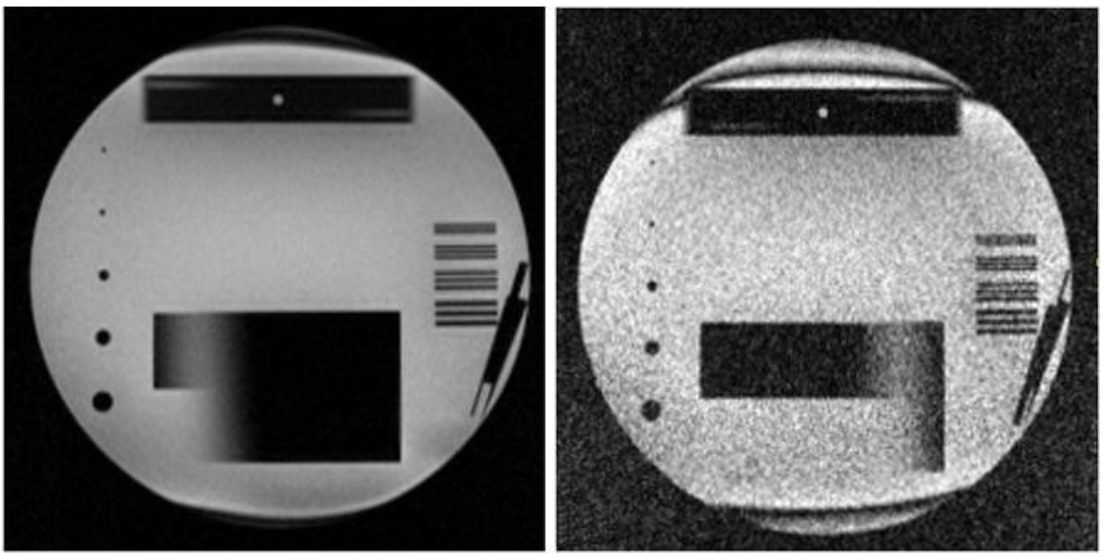

Fig. 2.3.2. Comparison of MR images taken when electronic components inside the MRI scanner room are not powered (l) and powered (r).

In addition, since the NMR signals used to generate an MR image are generally small any electro-magnetic fields generated by eddy currents or actuators and sensors within the scanner room will cause electromagnetic interference (EMI). This has the effect of degrading image quality (Fig. 2.3.2).

The level of electromagnetic interference can be quantified by determining the ratio of signal intensity to background noise (Signal to Noise Ratio, or SNR) for an image, and comparing this ratio with reference images acquired under controlled conditions. Several methods of measuring SNR exist and techniques have been standardised by the American National Electrical Manufacturers Association (NEMA). The magnitude of the SNR calculated depends on the method used, so it is not normally possible to compare SNR values acquired using different methods. Instead values are usually quoted as a percentage change from a reference image acquired using a consistent experimental setup.

SNR can be increased by averaging repeated imaging sequences at the expense of increasing image acquisition time, while noise can be reduced by removing material and systems that generate noise from the scanner room, and correctly shielding any remaining objects [Ott, 1976].

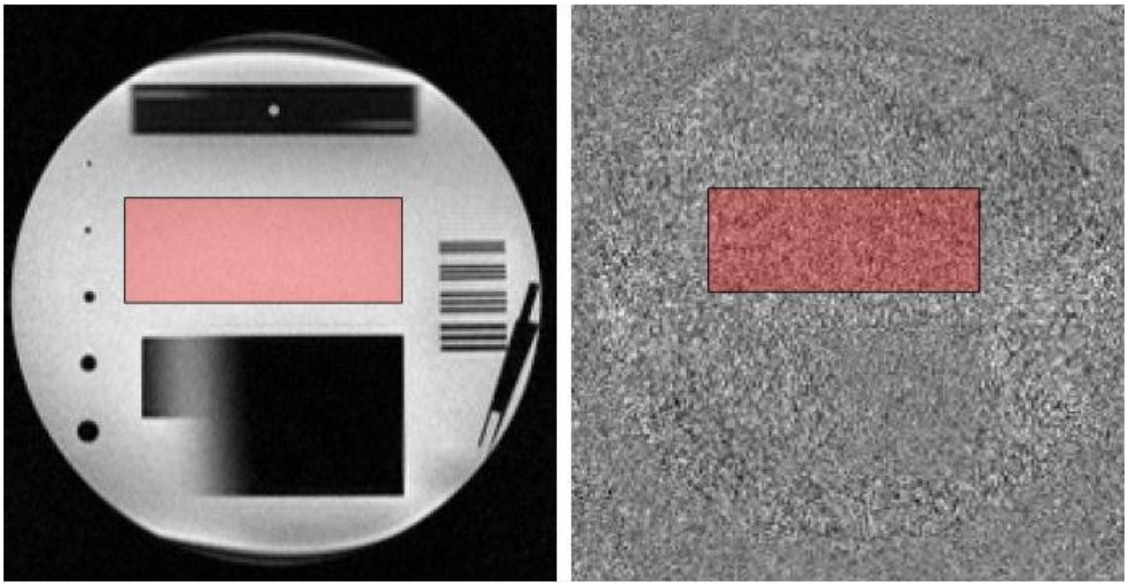

Fig. 2.3.3. Method of SNR calculation using a pair of images. A high signal region of the first image (left) is used to determine the image signal (red). The second image is then subtracted from the first to generate a difference image (right). The same region of the difference image is then used to calculate the image noise (red).

The preferred method of SNR calculation [NEMA, 2008] requires a pair of images to be acquired using identical parameters. The time between image acquisitions should be minimised as far as possible to reduce the effect of time-varying parameters – typically the image pair are acquired in consecutive sequences. The image signal (S) is defined by calculating the mean pixel intensity within a high signal region of interest (ROI) within the first image acquired (Fig. 2.3.3).

The second image is then subtracted from the first to produce a difference image (Fig. 2.3.3). The image noise (N) is then defined as the Standard Deviation (SD) of the pixel intensity within the ROI of the difference image divided by √2.

$$N = \frac{1}{\sqrt{2}} \times \left[\frac{\sum_{i=1}^{n} \sum_{j=1}^{m_i} (S(i,j) - \bar{S})^2}{\sum_{i=1}^{n} (m_i) - 1} \right]^{\frac{1}{2}}$$

(Eq. 2.3)

The additional $1/\sqrt{2}$ term is used due to the difference operation used to generate the image. The SNR is then defined as the image signal divided by the noise.

$$SNR = \frac{S}{N}$$

(Eq. 2.4)

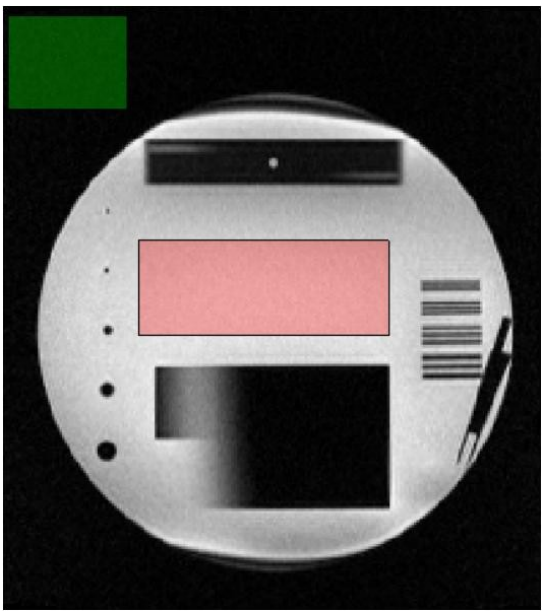

Fig. 2.3.4. Calculation of SNR using a single image, showing a region of high signal (red) and a background region (green).

An alternative method of SNR calculation utilises a single image acquired using a defined sequence. S is defined as the mean signal in a central region of high signal as with the previous method. However, in this method the image noise (N) is simply the SD of pixel intensity of a background ROI from the same image (Fig. 2.3.4). SNR is calculated using (Eq. 2.4). This method has the advantage of requiring only a single image and is therefore not sensitive to any time-varying parameters. However, it requires a clear background region to be defined and can be susceptible to image artefacts within the background region that are not visible.

2.4 Conclusions

The basic principles of operation of MRI scanners have been outlined within this section and some of the implications of these principles explored. A key constraint is the lack of patient access during scanning, which must be overcome by both procedural and technology-based solutions when developing a system for interventional MRI.

High magnetic fields, RF excitation pulses and switching gradient fields impose additional constraints on interventional MRI equipment. The impact of these constraints is explored within a formalised structure in Section 2.3, which introduces concepts which facilitate the development of interventional MRI equipment which is compatible with the MRI environment. A review of literature pertaining to systems which have addressed some of these challenges is presented in Chapter 3, while the approach taken in this

research is detailed in Chapter 5, with the results of MRI compatibility testing presented in Section 6.2.

The basic imaging sequences and motion compensation strategies outlined in Section 2.2 form the basis of research into real-time imaging and tracking sequences which are an essential part of interventional MRI systems. These aspects are reviewed in Section 3.4 and developed further in Chapter 7.

Chapter 3

Interventional MRI Systems

3.1 Introduction

A wide variety of systems designed to enable medical procedures to be performed with the benefit of intra-operative MRI have been presented in published literature. These systems are categorised and summarised in Section 3.2, 3.3 and 3.4. The limited number of previous attempts at MRI compatible endoscopy are summarised in Section 3.5. The relevant lessons learned from recent developments in robotic endoscopy are summarised in Section 3.6.

The majority of interventional MRI systems are focused on needle insertion tasks either for biopsy or oncologic treatment. This includes the only systems that have approached commercial use: The Innomotion system [Melzer, 2008] for abdominal interventions and the Invivo system [Anastasiadis, 2006] for prostate biopsy. Research groups have also designed systems for breast biopsy [Chen, 2004] and neurosurgery [Koseki, 2002] as well as proposing alternative designs for interventions in the prostate [Pondman, 2008] and for abdominal needle insertion [Christoforou, 2006a]. The mechanical design of these systems is clearly tailored to the targeted procedure, but it is useful to categorise them in terms of the actuation, sensing and tool tracking methods used, as outlined below.

3.2 Actuators

The simplest method of actuation within the MR environment is to move objects manually, either directly or by the use of mechanical transmission devices such as rods or pulleys. Provided the mechanism is constructed from the correct materials this method will be completely MRI compatible and it enables the user to receive tactile feedback from the device. Open MRI scanners are particularly suited for this type of system and a number of results have been reported for needle insertion procedures that utilise direct manual actuation to achieve MRI guidance [Haker, 2005; Lu, 1996; Zangos, 2007].

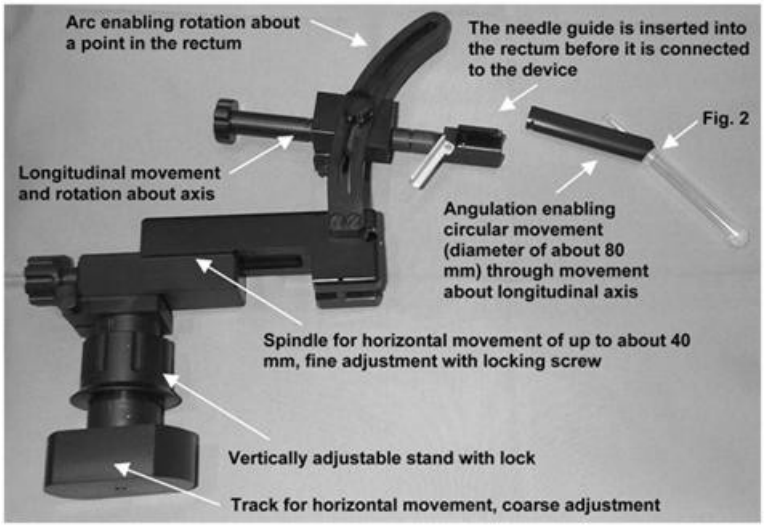

Fig. 3.2.1. Early prototype of the Invivo MRI-guided prostate biopsy positioning arm. Each degree of freedom (DOF) is directly actuated by the operator when the mechanism is outside the scanner [Beyersdorff, 2004].

When high field closed MRI scanners are used, spatial constraints require a directly actuated system to either be removed from the scanner during actuation, or to incorporate mechanical transmission devices that can be accessed from outside the scanner bore. Transmission devices such as flexible shafts or Bowden cables can be used but they have the potential to introduce significant backlash into the system. This is a particularly acute issue since material compatibility issues prevent the use of steel, meaning cables are usually made from high tensile polymers and flexible shafts from phosphor bronze.

Despite the limitations direct actuation has been used by several groups developing MRI compatible devices with some success. The Invivo device for prostate biopsy (Fig. 3.2.1) requires removal of the device and patient from the scanner for repositioning so is unable to utilise real-time MRI to guide the operation. However, it's simplicity means that it has been adopted faster than other devices and relatively large clinical studies have demonstrated it's efficacy [Anastasiadis, 2006]. Other research groups [Fichtinger, 2002; Lambert, 2012; Susil, 2006] have developed devices for the same procedure that utilise flexible shafts to enable all degrees of freedom to be actuated from outside the scanner (Fig. 3.2.2). Another device (Fig. 3.2.3) has been developed for generalised needle insertions within an open MRI scanner which relies on mechanical transmission via timing belts. All three of these mechanisms are designed to be very stiff, which means that acceptable performance can be achieved despite the additional backlash from the transmission devices.

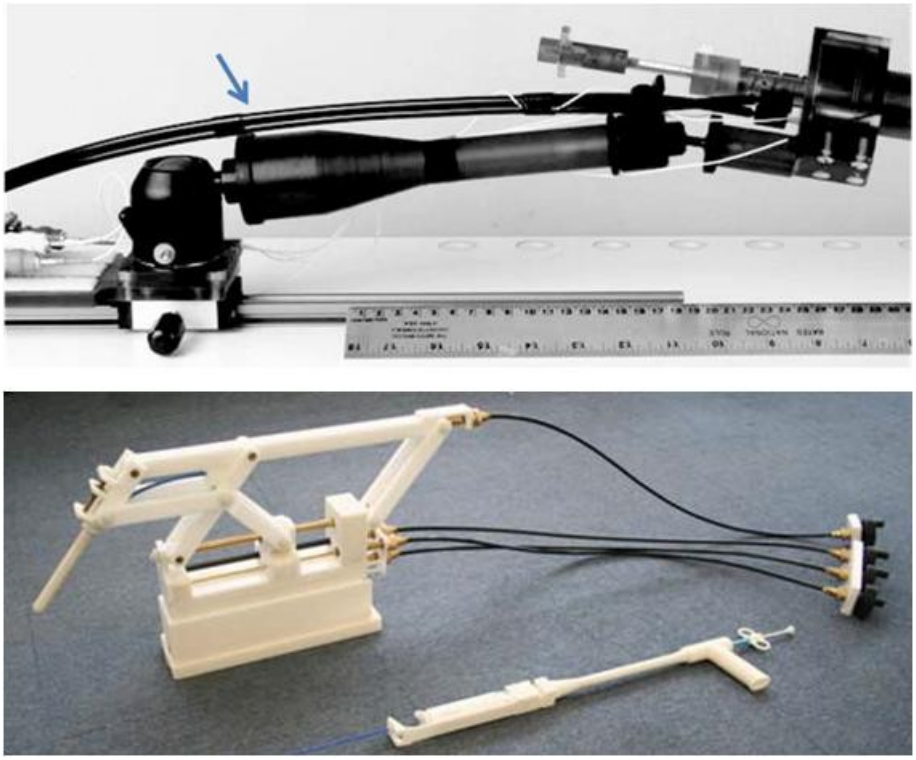

Fig. 3.2.2. Prostate biopsy mechanisms directly actuated by flexible phosphor bronze shafts [Lambert, 2012; Susil, 2006].

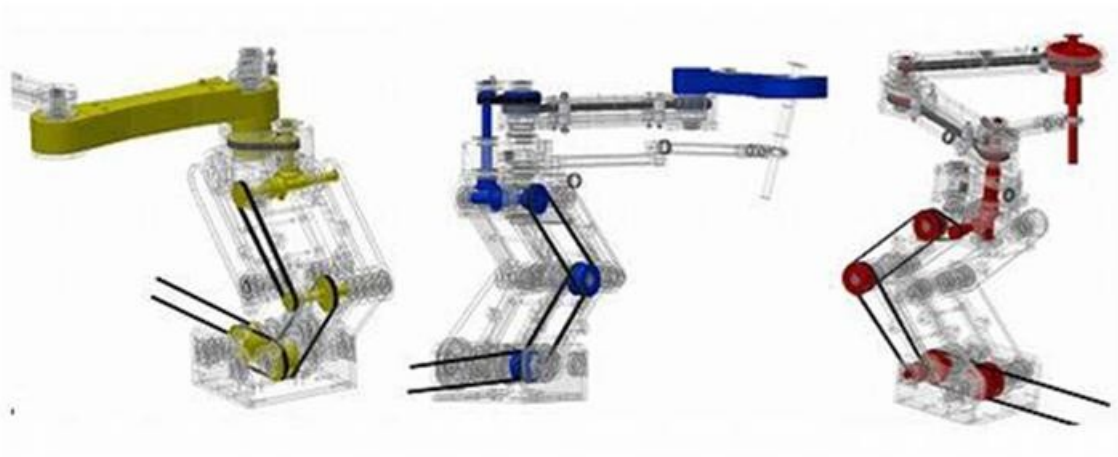

Fig. 3.2.3. MRI-guided needle insertion device actuated by manually controlled timing belts. Due to it's height, this system is designed for use in a vertical open-bore scanner [Oura, 2006].

Electro-magnetic (EM) motors are used for many modern mechatronic devices due to their small size, excellent accuracy, high efficiency and high power. Unfortunately EM motors pose serious issues within the MR environment. Their principle of operation relies on ferromagnetic materials and switched electrical currents to generate magnetic fields within the device. This requires them to be securely anchored and placed a

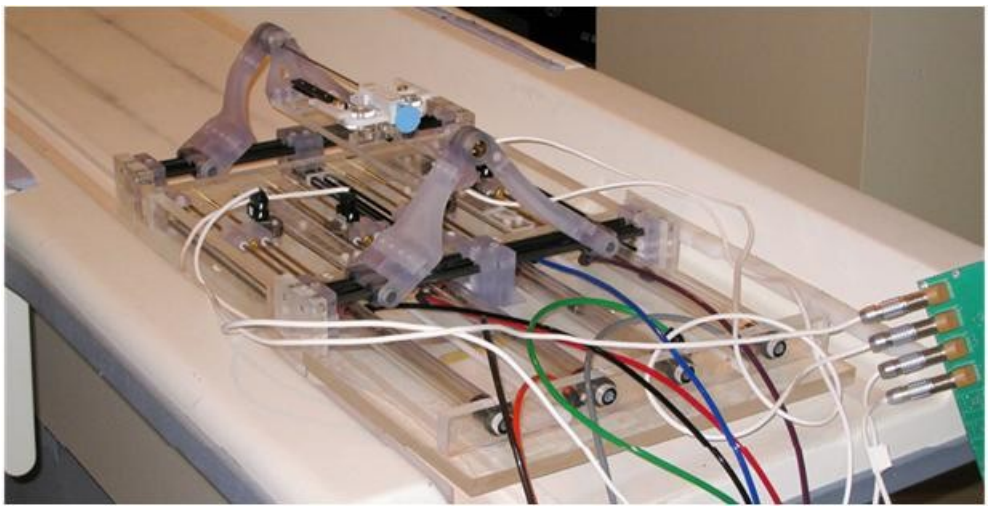

Fig. 3.2.4. Pneumatically operated MRI-guided prostate biopsy mechanism. The coloured tubes supply air to four horizontal cylinders at the base of the mechanism [Song, 2010].

minimum of 2.5m from the scanner bore due to very high magnetically-induced forces [Gassert, 2006b]. Even then extensive shielding is needed to reduce EMI, and long mechanical transmission devices would be required to actuate the mechanism.

EM motors or pumps have been used in hydraulic systems to drive master cylinders placed completely outside the scanner room [Gassert, 2006a]. These are then are connected to slave cylinders via flexible hoses. This method was shown to transmit high forces (up to 30N) with high bandwidth (20Hz). However high fluid pressures are required for this performance, which raises safety concerns as any leakage is generally not acceptable in medical applications. In addition, the performance is limited by joint friction and the viscosity of the fluid, making accurate control challenging.

Pneumatic systems are also an option for motion transmission, and are more attractive in medical applications because leakage is less of an issue and compressed air is readily available. However, issues of joint friction and compressibility are exacerbated with pneumatic actuators, requiring short hoses and high pressures to be used along with complex control regimes to prevent imprecise movements. Fisher et al [Fischer, 2008] used specially designed low-friction glass cylinders (Airpel E9 Anti-Stiction Air Cylinder, www.airpel.com) and piezoelectric valves to reduce hose length along with a parallel piston layout to reduce mechanism size (Fig. 3.2.4). The mechanism achieved an accuracy of 5mm during preliminary evaluations [Song, 2010]. Further iterations of these actuators incorporated a sliding mode control (SMC) algorithm which improved the needle positioning accuracy to less than 1mm in phantom trials [Su, 2012b]. Franco et al [Franco, 2012] investigated the use of an augmented SMC control algorithm with a similar system

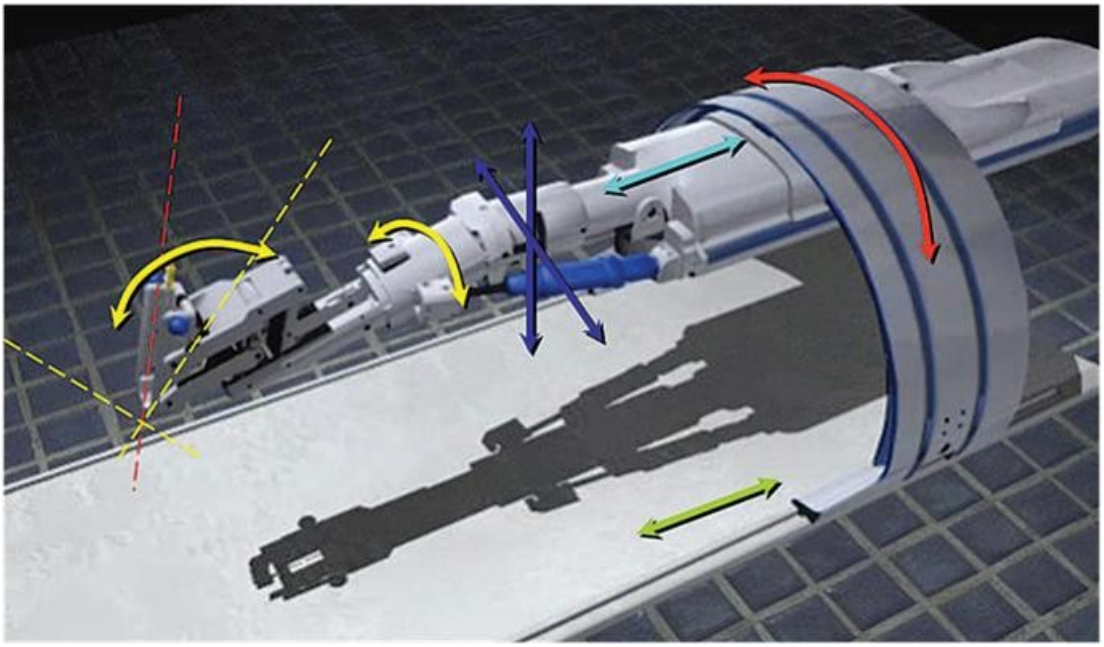

Fig. 3.2.5. Innomotion MRI-guided needle insertion arm with pneumatically actuated DOF shown [Melzer, 2008].

and were able to achieve a steady state error of less than 0.5mm, with a settling time of less than 2.5s.

Pneumatic actuators are preferred in recent versions of the commercially-available Innomotion system (Fig. 3.2.5) because of their MRI compatibility [Melzer, 2008]. The actuators are designed to exhibit a very high dynamic friction, which dominates the static friction and therefore reduces stick-slip control issues. The high dynamic friction also results in a relatively slow and predictable response, while preventing the actuator from moving in the event of an emergency air supply interruption. The system incorporates very high quality fibre optic rotary encoders and tests have demonstrated a 3D system accuracy of 3-4mm in vivo [Moche, 2010].

To overcome issues with linear pneumatic actuators, Stoianovici et al [Stoianovici, 2007a] developed a pneumatic step-motor in which a hoop-gear is rotated using three equal-crank parallelogram mechanisms (Fig. 3.2.6). This motor is capable of rotating at 60 RPM with 350 Nmm torque with a step accuracy of 3.33° when operated with 120 PSI gas pressure and 3m hoses. It is manufactured from entirely MRI compatible materials, rendering the motor itself invisible to MRI, and controlled using piezoelectric valves. The motor performed well in testing [Muntener, 2008; Stoianovici, 2007a], with the only drawbacks being the complex construction and control systems for the motors and valves.

Ultrasonic motors have the capacity to mitigate many of the issues involved with conventional EM motors and have therefore been extensively investigated for use in MR

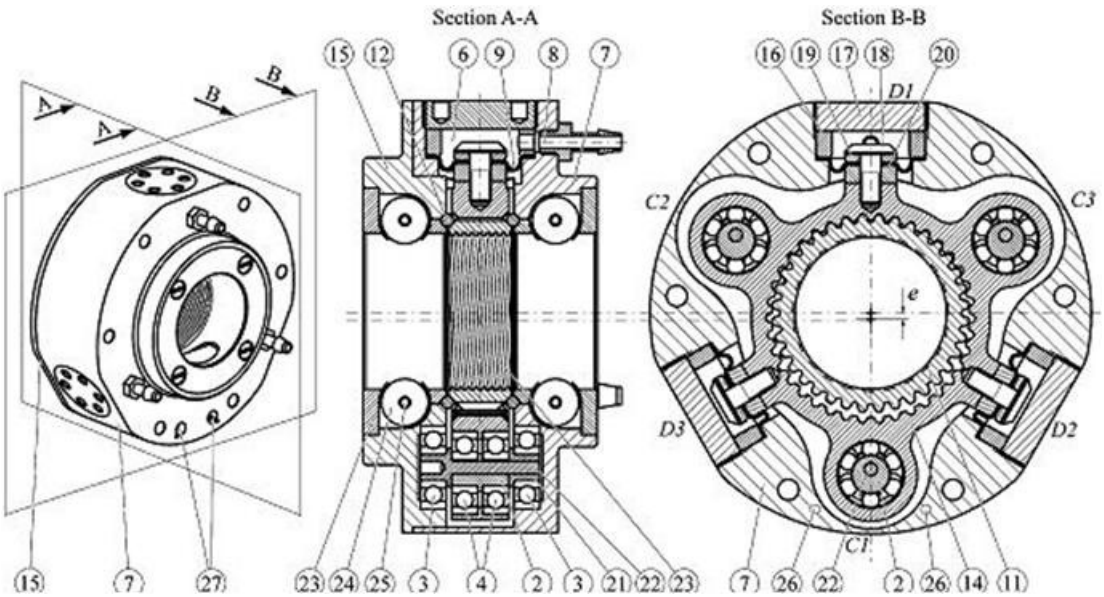

Fig. 3.2.6 Diagram of the Pneustep motor [Stoianovici, 2007a]

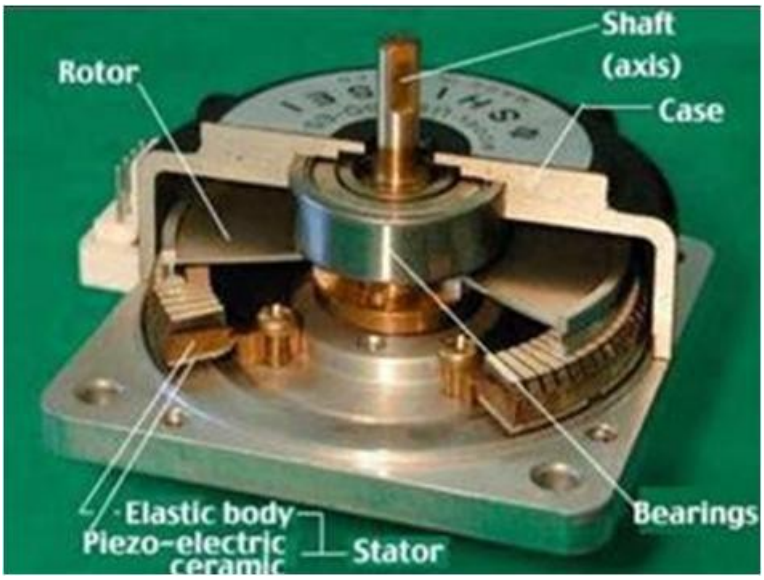

Fig. 3.2.7. Cross-sectional view of an ultrasonic USR-60 non-magnetic motor [Shinsei, 2005].

environments [Elhawary, 2008a]. They utilise ultrasonic frequency modulation of a voltage signal applied to a fixed arrangement of piezoelectric crystals, which alternately hold and move a rotor to generate motion (Fig. 3.2.7). They are accurate and simple to control, requiring a driver unit that can be placed a long distance from the motor with no loss of performance. In addition, they are characterised by good power density and a high holding torque, which means they can be switched off during imaging without losing position.

Ultrasonic motors can be manufactured from non-magnetic materials, and since they do not operate using magnetic forces (unlike EM motors) they are, up to a point, intrinsically MR compatible [Uchino, 1998]. However, they still require careful integration of the power supply and driver unit to ensure that the MRI scanner is protected from EMI. Early versions of the Innomotion system incorporated ultrasonic motors, but these were changed to pneumatic actuators after issues with EMI were encountered [Melzer, 2008]. Despite this, the combination of good power density and accurate motion combined with the potential for limited image degradation has made piezoelectric ultrasonic motors the actuator of choice for many research groups developing systems for interventional MRI [Chinzei, 1999; Christoforou, 2006b; Goldenberg, 2010; Suzuki, 2007].

The MRI compatibility of these motors was tested by Elhawary et al[Elhawary, 2006], who demonstrated an SNR reduction of 14% by an ultrasonic motor (PiezoLegs, PiezoMotor AB Ltd.) located within the scanner field of view and actuated at full speed. Further testing suggested the SNR reduction could be limited to 2% if the motors are separated from the imaging volume by 1m [Elhawary, 2008a]. However, this conflicts with the results of other groups which suggest that there is a decrease in SNR of 40-80% due to the presence of an active motor inside the MRI scanner [Goldenberg, 2010; Koseki, 2002; Krieger, 2010]. The cause of the differences in the reported results are not clear, as there is insufficient detail published regarding the system architecture, precise locations of various components and shielding design. The increase in noise may also be related to the presence of integrated rotary encoders, which do not appear within the published text but are indicated by images and the part numbers quoted. Unshielded rotary encoders can significantly contribute to EMI, as outlined below.

There have been attempts to improve the MRI compatibility of ultrasonic motors using methods that go beyond EMI shielding. The simplest of these is to design a system that interrupts the actuation of the ultrasonic motor during imaging [Suzuki, 2007]. This effectively removes the EMI by ensuring that any periods of noise generation do not coincide with the signal acquisition period of the MRI sequence. However, this method prevents continuous motion and may limit the possibilities for real-time MRI guidance. In addition, it requires a significant level of access to the MRI scanner and imaging sequence, which may not be available in all facilities.

Attempts have also been made to optimise the driver electronics that provide the ultrasonic frequency signals to the motors [Su, 2012b]. Commercially available motor drivers usually generate these waves by performing low-pass filtering of high frequency square waves. This is efficient but has the potential to produce significant higher-frequency noise components that may interfere with the MRI scanner. Su et al [Su, 2012a]

Actuator Type	Advantages	Disadvantages
Manual (Direct)	Simplicity Tactile feedback	Lack of access in closed scanners No option of automated control
Manual (Extended Controls)	Simplicity Tactile feedback Improved access	Increased backlash No option of automated control
EM Motors	High power High power density Precise motion	Compatibility issues Increased backlash
Hydraulic	High Power and bandwidth	Oil safety concerns System complexity
Pneumatic	MRI compatibility	Sophisticated control requirements
Pneumatic Motors	MRI compatibility Good power density Precise motion	Complex design and manufacture Sophisticated control requirements
US Motors	Good power density Precise motion Locking Torque	EMI considerations

Table 3.2.1. Comparison between actuation methods for interventional MRI systems.

designed an FPGA-based waveform synthesizer system to replace the commercially available drivers. When tested with as part of a complete system EMI was reduced to the point that there was no statistically measureable difference in image SNR due to the motor actuation [Su, 2011].

The different options for actuation within the MRI environment all present different strengths and weaknesses and hence the choice of actuator depends on the specific procedure and problem to be solved. Table 3.2.1 shows a list of the key features of each actuation method discussed in this section.

3.3 Sensors

Research into sensing within the MR environment has fallen into two broad categories – position sensing and force sensing. Most interventional MRI systems rely on tracking using intra-operative MR sequences to determine the position of the device end effector. This has the advantage of avoiding any inaccuracies in kinematic calculations or

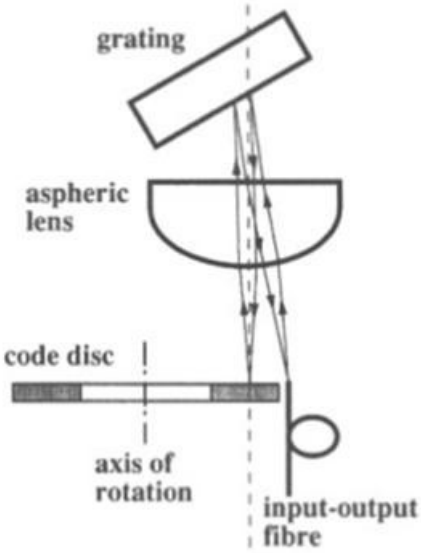

Fig. 3.3.1. Schematic showing the operating principle of a wavelength-encoded fibre optic rotary encoder [Maghoo, 1994].

mechanism backlash. However, position sensing can be valuable to enable closed loop control and to provide information about mechanism joint positions. This is particularly true for systems that rely on pneumatic actuators.

Position sensing in robotics is traditionally performed using optical encoders with either code-wheels or code-strips for rotary or linear motion, respectively. A number of attempts at introducing optical encoders into the MR environment have been explored. Elhawary et al [Elhawary, 2006] investigated the MR compatibility of a standard reflective surface mount optical encoder (Agilent AEDR-8300) for position sensing. The sensor's presence produced an SNR reduction of 2.6%, however if it was coupled with a moving motor then the encoder contributed to an estimated additional 12% reduction in SNR. This effect was ascribed to signal pulses as the sensor passes the lines on the encoder strip. This phenomenon was also reported by Suzuki et al [Suzuki, 2007]and Chinzei et al [Chinzei, 1999], who demonstrated that attaching a rotary encoder to a non-magnetic ultrasonic motor caused a significant reduction in image SNR when the motor was running.

The compatibility of optical encoders can be improved by the use of fibre optic cables to transmit the light source and reflective signal, removing all electronics from the imaging volume. This approach has been used by several groups [Harja, 2007; Hempel, 2003; Krieger, 2006; Stoianovici, 2007b] to good effect, provided the optics are carefully controlled to avoid losses due to bending or misalignment of the optical fibres. The light signals can either be passed through a code wheel or strip for digital encoding or reflected off a parallel surface to gain an analogue intensity measurement. More sophisticated

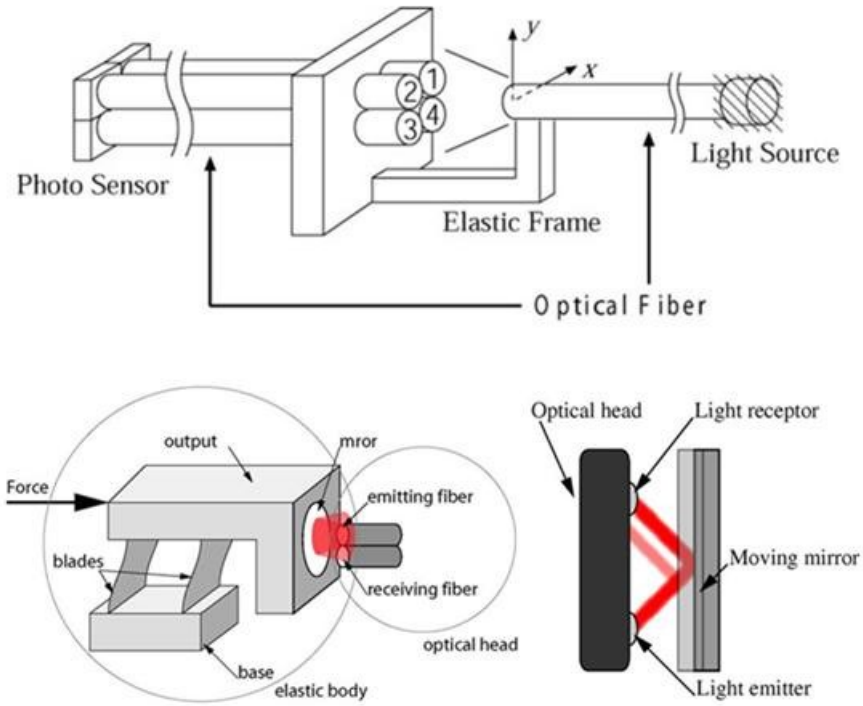

Fig. 3.3.2. Fibre optic force sensor systems, showing (top) direct and (bottom) reflected light transmission [Gassert, 2008].

versions of this design incorporate a grating into the code wheel to enable the light signal to be wavelength encoded (Fig. 3.3.1).

Fibre optic sensors have been used to construct MRI compatible force and torque sensors for use in fMRI brain studies [Gassert, 2008; Tan, 2011]. These rely on the receiver and reflector surface or photosensor being mounted on an elastic frame that is designed to be rigid in all directions other than one (Fig. 3.3.2). Force applied to the frame in this direction will then cause a change in distance between the receiver and reflector, changing the received signal. With careful design and calibration these have shown to perform well, but the requirement for stiffness can make the mounting frame large and challenging to integrate into an active mechanism.

MRI-compatible force sensors can also be constructed by applying force directly to a fibre optic and measuring changes in it's properties due to deformation under load. A Fibre Bragg grating (FBG) is a fibre optic that has been modified so that there is a periodic change in the refractive index of the fibre along it's length. This causes the FBG to reflect a narrow spectrum of light back to the source. The frequency of this spectrum changes as the fibre is deformed, which enables a system to be constructed that measures force analogously to a traditional strain-gauge based force sensor [Hill, 1997]. The advantage of this is that the fibres are MRI compatible and since the signals are wavelength encoded

they can be transmitted outside of the MRI scanner for analysis without intensity loss concerns. However, the sensors are very sensitive to temperature and polarization effects and so require very careful design and calibration [Pevec, 2011]. In addition, the sensors require a high-resolution spectroscope to monitor the signals, which significantly adds to system cost and complexity.

An alternative force sensor based on a Fabry-Perot Interferometer (FPI) strain sensor has been developed for use in MRI [Su, 2011]. FPI sensors consist of two partially reflective surfaces arranged inside the fibre and mounted inside a glass capillary, which is fused to the end of a fibre optic [Pevec, 2011]. When light is passed down the fibre the sensor produces a spectral pattern of light and dark bands, which can be measured as a repeating pattern of spectral intensity peaks. The distance between the peaks is determined by the length of the sensor, so the system can again be made to function like a traditional strain gauge. Due to the presence of the capillary and periodicity of the spectral pattern, the sensors are less temperature sensitive than FBGs and require a lower spectral measurement resolution. As such, the technology is promising for the future development of interventional MRI systems.

Due to the availability of intra-operative MR images for guidance, the potential for increased EMI and the significant increase in system complexity, most interventional MRI devices to not rely on direct sensing. However, this is an active area of research and the potential for providing haptic feedback to the user or closed loop control of devices is attractive.

3.4 Tool tracking in interventional MRI

As noted above, interventional MRI systems traditionally rely on the MR images and the MRI scanner to determine the position of the interventional tool. This can be achieved by a variety of different methods, the commonest of which are outlined in this section.

The simplest method of determining the position of an interventional tool in MRI is to acquire an image of the tool in question. Although tools are usually made from materials that do not produce any NMR signals themselves (such as plastics or metals), the signal void produced by their presence in tissue can show up very well in images and can be tracked [Chen, 2004]. This is particularly true for needle insertion applications (Fig. 3.4.1), where the needle is surrounded by tissue. However, the artefact associated with metallic objects makes precise determination of the true needle position challenging [DiMaio, 2005].

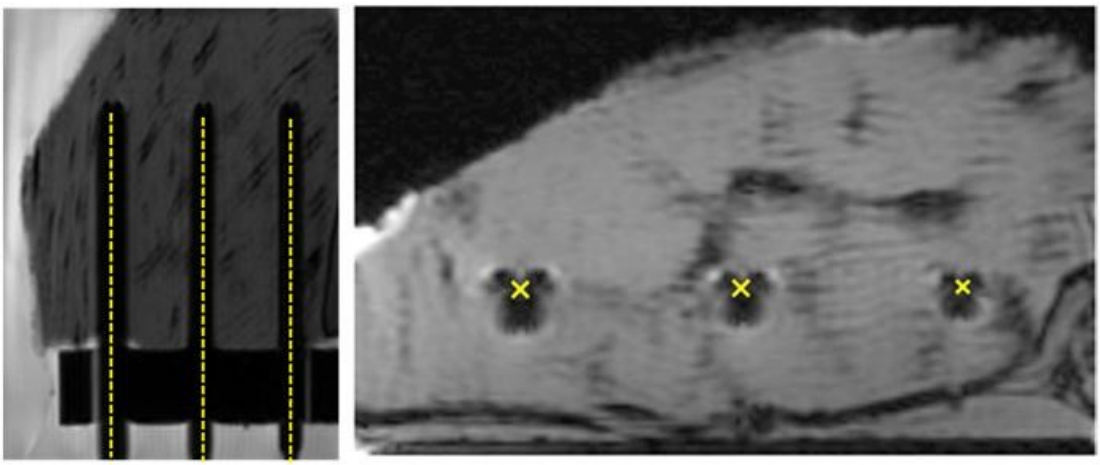

Fig. 3.4.1. Image voids in tissue surrounding inserted needles, with (l) needle in image plane and (r) cross sectional image. The true location of the needle centres and axes are shown in yellow [DiMaio, 2005].

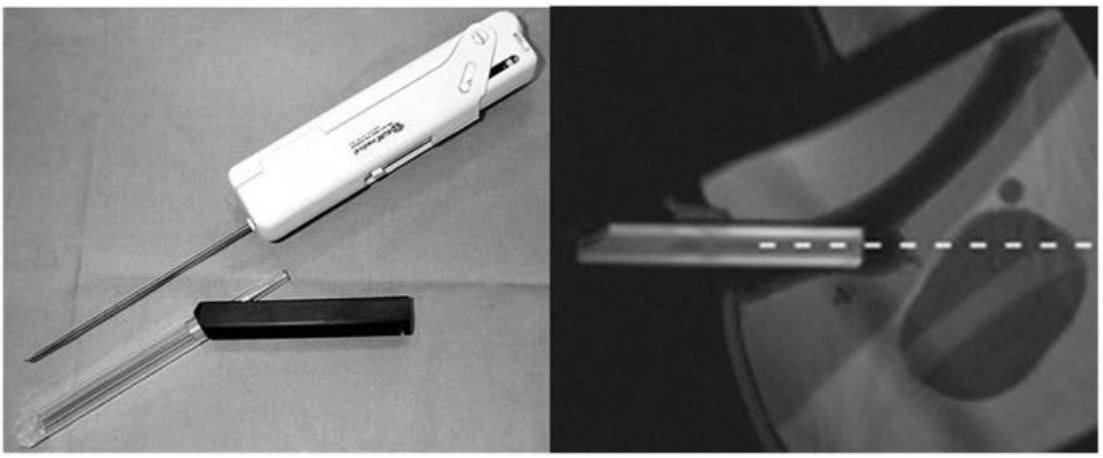

Fig. 3.4.2. (l) MR contrast gel-filled needle guide with biopsy needle gun and (r) planar MR image of needle guide [Beyersdorff, 2004; Oliveira, 2007].

Direct imaging is less suitable if the tool is inside a natural orifice, for example the rectum or upper gastrointestinal tract. In these situations there are likely to be additional signal voids around the tool due to the body cavities, making the position and shape of the tool impossible to accurately determine. To overcome this, the Invivo prostate biopsy system [Beyersdorff, 2004] incorporates an MR visible fiducial marker rigidly mounted on the biopsy needle guide. This marker is a hollow cylindrical tube filled with MR contrast gel that appears as a distinctive region of high signal in diagnostic images (Fig. 3.4.2), enabling the device position to be determined using imaging processing techniques [Oliveira, 2007]. A similar system which relies on a distinctive "Z frame" of MR visible cylinders mounted adjacent to the needle guide is proposed by Fischer et al [Fischer, 2008]. The advantage of this system is that the position and orientation of the frame can be determined from a single image slice.

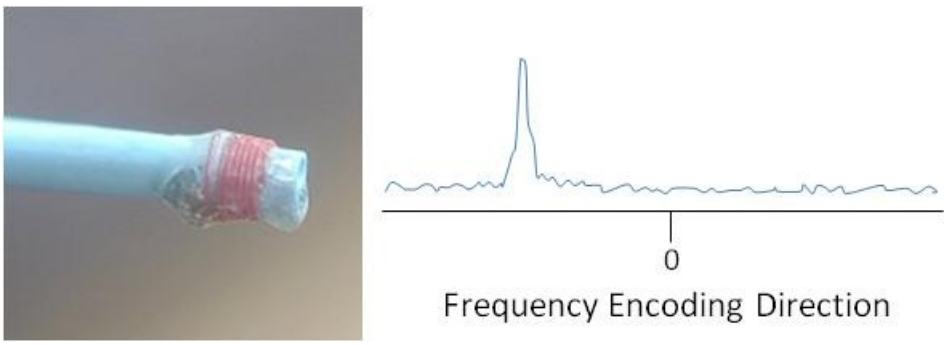

Fig. 3.4.3. Active device tracking using a miniature solenoidal microcoil mounted on a vascular catheter (l). A 1D projection enables the position of the coil to be determined accurately due to the presence of a single, well defined signal peak (r) [Dumoulin, 1997].

The drawback of direct tracking is that it requires at least one high quality MR image to be acquired and processed before any measurement can be made. Frequently an entire image set is required for accurate measurements. This limits the measurement update rate to significantly less than the image update rate. For directly actuated devices such as the Invivo system this may be acceptable, but it limits the opportunities for accurate real-time guidance.

A hybrid tracking system has been developed to overcome the speed limitation of direct tracking [Krieger, 2006]. This system relies on the position of the device being registered to the MRI scanner coordinate system using an initial set of images of MR visible markers. These markers are then removed, and the movement of the device during the procedure is calculated using data from position sensors mounted on the mechanism joints. This removes the need to repeatedly acquire images for device tracing, but it relies on the accuracy of the initial registration and a stiff mechanism to enable precise kinematic calculations to be performed. Any movement of the device base plate or patient during the procedure requires the registration step to be repeated.

The most popular method of device tracking within MRI was initially proposed by Dumoulin et al [Dumoulin, 1993] and has since been widely adopted, particularly in the field of vascular MRI [Dumoulin, 1997; Rasche, 1997; Wendt, 2000]. This method utilises a small MR receiver coil (typically a solenoid) mounted on the device and filled with MR signal producing material. The coil is connected to the MRI scanner and used to acquire a 1 dimensional (1D) frequency encoded signal. The coil receives signal only from a limited area due to it's small size, so the 1D projection exhibits only a single peak (Fig. 3.4.3). This peak is intrinsically located in the MRI coordinate system by the sequence frequency encoding, making it simple to use several such projections to determine the 3 dimensional location of the coil.

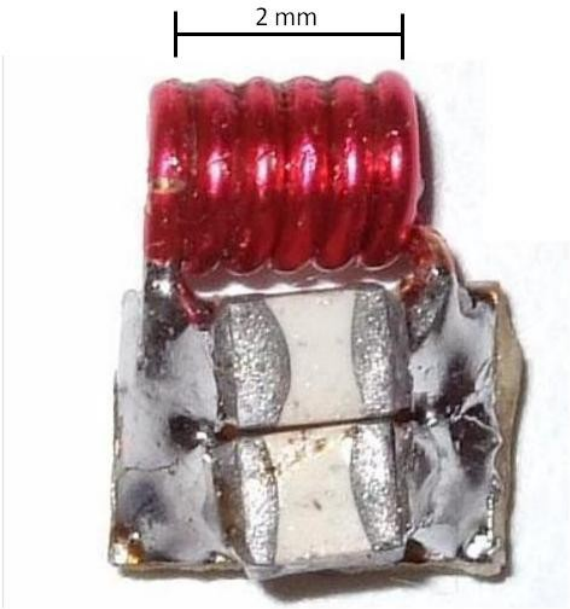

Fig. 3.4.4. Passive resonant microcoil fiducial, showing inductor coil (red) and capacitors (white) soldered to a circuit board [Rea, 2010].

Provided the tracking coil is small and sufficiently well made, active tracking is very fast and accurate. It is well suited to real-time guidance of small interventional tools, provided there is space to mount the coil on the tool and to provide a connection to the MRI scanner [Wendt, 2000]. Active tracking MR sequences are not standard on most clinical scanners, requiring some access to the sequence coding and data transfer operations of the scanner. Additional coils must be mounted on the tool to enable orientation to be measured as well as position.

A method to overcome the need to provide a connection between scanner and tracking coil was proposed by Rea et al [Rea, 2008] and further developed by Brujic et al [Brujic, 2012]. The active tracking coil was replaced by a passive microcoil, which consists of an inductor and capacitor tuned to resonate at the scanner Larmor frequency and requires no connection to the scanner (Fig. 3.4.4). Unlike the active tracking microcoils, which are typically detuned during the excitation phase of the imaging sequence and are used only to receive signal, the microcoil resonates with the RF excitation pulse, enhancing the magnitude of the NMR signal in it's immediate vicinity.

Tracking is performed by generating a 1D projection with a low intensity excitation pulse, leaving the majority of the imaging volume unaffected except for the area in the vicinity of the fiducial. This signal is then received by the scanner imaging coil and the position of the fiducial determined in the same way as for the active tracking coil.

Passive resonant microcoil fiducials are fast and accurate, with the additional advantage that they do not require a scanner connection. However, they suffer from a

Tracking Type	Advantages	Disadvantages
Direct device tracking	Utilises diagnostic images Tool position directly visible	Slow Relies on tissue surrounding tool Susceptible to artefacts
Device markers	Utilises diagnostic images Can be used in natural orifices Orientation measurement	Slow
Hybrid	Speed improvement over passive methods	Registration time and accuracy Requires joint sensors Susceptible to kinematic errors
Active microcoils	Fast Inherently accurate	Connection to scanner Projection sequences Orientation measurement
Passive resonant microcoils	Fast Inherently accurate No scanner connection	Low SNR Interference with local imaging Orientation measurement Projection sequences

Table 3.4.1. Comparison between tracking methods for interventional MRI systems.

lower signal to noise ratio (SNR) than the active method as they rely on the body coil for signal reception. This makes them susceptible to surrounding tissue and EMI issues. In addition they may interfere with imaging in the immediate vicinity, since the microcoil will resonate with the excitation pulse during the imaging sequence.

As with the use of actuators in interventional MRI, the choice of tracking method is dependent on the challenges posed by the specific application. Table 3.4.1 lists the characteristics of each tracking method outlined in this section.

3.5 MRI Compatible Endoscopy

MRI compatibility of an endoscope must be addressed before attempting to combine MRI and endoscopy. Modern endoscopes incorporate a charged coupled device (CCD) into the distal tip for digital video capture, which can cause major MRI artefacts due to magnetic field distortion and significant EMI. This can be improved by using a coherent fibre optic bundle to transmit light along the length of the endoscope and placing the digital imaging device outside of the imaging bore [Coutts, 2003], which results in a poorer optical image

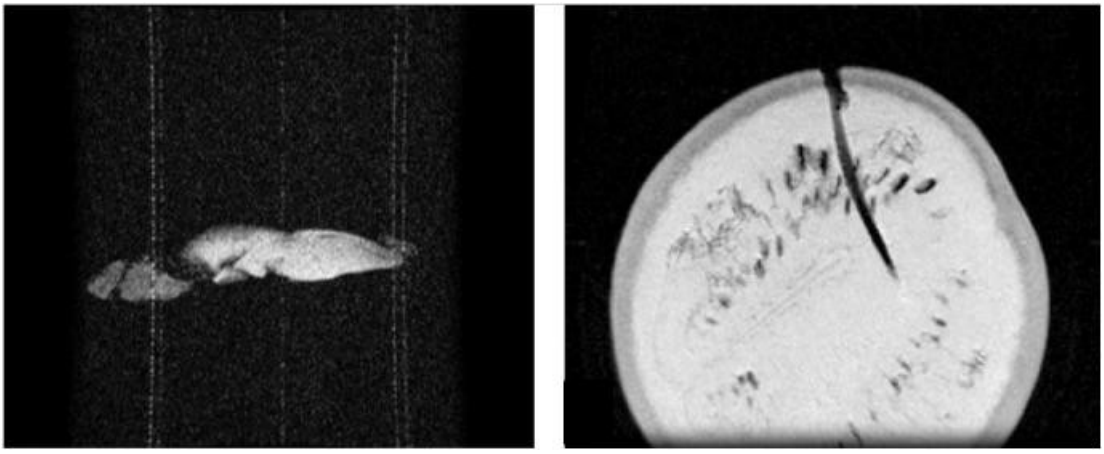

Fig. 3.5.1. MR images of identical phantoms. When a standard endoscope is inserted into the phantom (l) the image is degraded to the point of uselessness. If the endoscope is modified to remove the CCD chip to the proximal end and replace it with fibre optics (r) the image improves significantly [Gross, 2001].

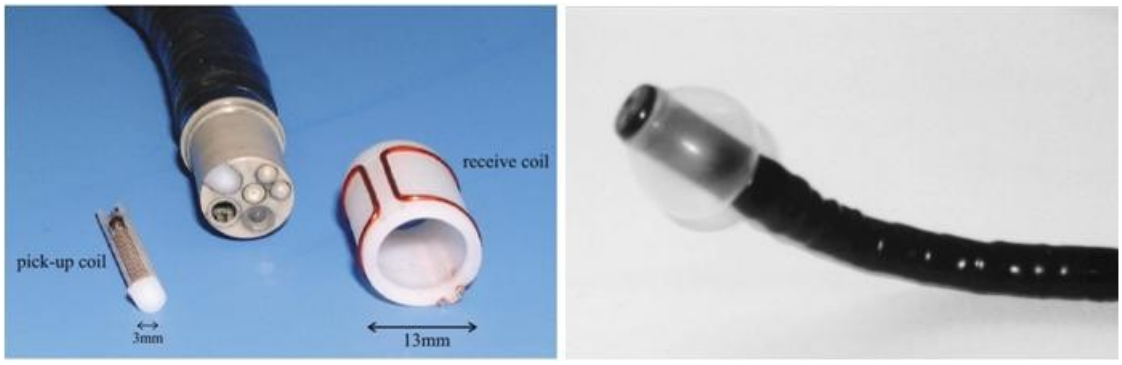

Fig. 3.5.2. MRI compatible endoscopes manufactured by Endsocan Ltd (l, with removable tip receiver coil) and Olympus (r, with inflatable latex balloon for positioning stability) [Gilderdale, 2003; Ichikawa, 2001].

compared with modern endoscopes, but limits the degradation of the MR images (Fig. 3.5.1).

A further complication with conventional endoscopes is the tip steering mechanism, which in standard endoscopes utilises steel Bowden cables. Instead of this, endoscopes can be manufactured with polymer cables or compound cables comprising polymer for the distal end (inside the imaging volume) and an MRI compatible metal (such as Ti or CrMo) for the remaining cable length. A challenge with this approach is to reproduce the accuracy and control afforded by steel cables, particularly with longer instruments designed to reach the lower regions of the gastric system.

Several groups have built and tested MRI compatible endoscopes based on these construction principles (Fig. 3.5.2), ranging from instruments handmade by research groups [Gross, 2001; Heye, 2006], through small scale production models [Ahmad, 2008;

Fig. 3.5.3. Spatial constraints posed by flexible endoscopy inside closed-bore MRI scanners [Naka, 2012].

DeSouza, 1995; Gilderdale, 2003] and including a model produced by Olympus, a major manufacturer in the medical devices industry [Feldman, 1997; Ichikawa, 2001; Inui, 1998; Kulling, 1997]. In all cases, these endoscopes have been used to manually position internal receiver coils in a patient for subsequent imaging and the imaging technology is the primary research focus of these publications.

In the published studies referenced above, adjustment of the position of the endoscope once imaging has started is not discussed. Movement, or at least manual locking, of the endoscope may nevertheless have been performed either in open MRI scanners [Hashizume, 2007] or in high-field close scanners on a limited basis, as demonstrated in Fig. 3.5.2, but there is no mention of intra-operative MRI being generated or used for guidance.

In summary, while the combination of internal, intra-operative MR images with endoscopy has been attempted by research groups in the past, the use of remote actuators to perform complex endoscopic procedures under MRI guidance has not been attempted previously. Each example in the literature discussed here has relied on direct actuation of the endoscope by the operator, with the requirement that the patient is moved out of the closed-bore MRI scanner while the endoscope is operated.

3.6 Robotic Endoscopy

The field of robotic endoscopy is relatively small but has grown in recent years. This is partly due to the success of the Da Vinci robotic laparoscopic surgical system [Maeso,

Fig. 3.6.1. Flexible tools for NOTES interventional procedures [Abbott, 2007; Phee, 2009; Shang, 2011].

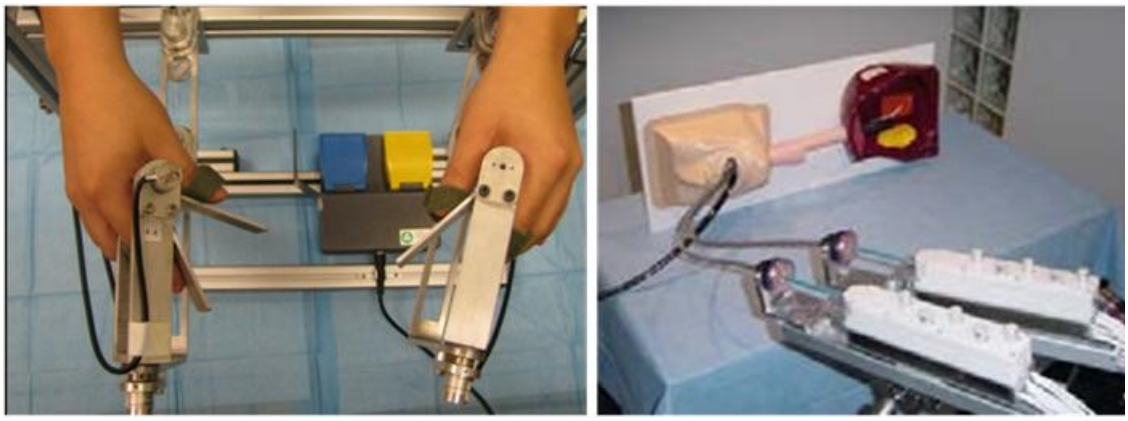

Fig. 3.6.2. NOTES user interfaces, showing (l) master user-controlled device that transmits control signals to (r) slave motor driven device [Abbott, 2007].

2010], which has been used for a wide variety of procedures and despite the learning curve associated with it and the high system cost has proven to be effective in enabling surgery to be performed with extremely precise and controlled movements [Corcione, 2005]. Safety concerns raised by the removal of direct operator control of tools do remain in some circles, but have been allayed by familiarity and rigorous system testing.

While the Da Vinci system has demonstrated the clinical feasibility of surgical robotics in the field of laparoscopy, research into minimally invasive surgical techniques has also gathered pace. Whereas laparoscopy utilises rigid tools that are inserted into the abdomen through multiple incisions, the field of natural orifice trans-luminal endoscopic surgery (NOTES) attempts to combine the traditionally diagnostic techniques of colonoscopy and gastroscopy with flexible surgical tools [Canes, 2009], enabling abdominal operations to be performed without any external incisions.

A variety of endoscopes and flexible tools have been developed for NOTES applications (Fig. 3.6.1). These enable more complex interventional procedures to be performed using access through natural orifices. However, the increase in the number of degrees of freedom (DOF) of the tools means that the endoscopist is required to perform

more dexterous movements and must exhibit excellent spatial awareness to be able to coordinate movements [Swanstrom, 2011].

The tools shown are designed as robotic master and slave remote manipulators (Fig. 3.6.2) to assist with these issues and to take advantage of the precision and control benefits offered. The master control interface drives the slave manipulator via either external motors and long Bowden cables [Abbott, 2007; Phee, 2009], or via miniaturised motors mounted inside the slave manipulator [Canes, 2009; Shang, 2011].

The target of NOTES instrumentation research is to enable these tools to be delivered to the operation site using a standard flexible endoscope [Phee, 2009; Swanstrom, 2011]. The existing tools are currently much too large to pass down the instrumentation channel of standard endoscopes, leading to a variety of customised insertion tubes being used for initial studies. These tubes have been shown to be stiff and have limited DOF, which has limited the sites which can be accessed with the NOTES tools [Shang, 2011].

Studies have shown that control of the flexible endoscope in standard diagnostic endoscopy could also benefit from remote actuation due to the task load demand [Ruiter, 2012; Shergill, 2009]. A situation in which the operator uses a traditional flexible endoscope for access and NOTES tools for surgery would require the operator to control an even larger number of flexible degrees of freedom – typically 5 or 6 for the flexible endoscope and an additional 6 per interventional tool [Abbott, 2007]. This situation would make direct control of the tools very challenging due to the large number of controls that must be simultaneously locked or controlled.

In anticipation of this challenge, researchers have developed robotic systems that are attached to a standard endoscope and enable remote control of the endoscope tip steering [Allemann, 2009; Ruiter, 2012; Zhang, 2002]. These hybrid systems consist of an actuator unit that fits over the duodenoscope tip steering wheels and is driven either directly or by a separate motor unit via Bowden cables (Fig. 3.6.3). The user interface is either a joystick unit or small touchpad (Fig. 3.6.4). An experiment which compared the operator's performance at simulated colonoscopy concluded that the robotic system with joystick interface reduced the task load and insertion time compared with manual operation [Ruiter, 2012].

This result was contradicted by Allemann et al [Allemann, 2009], who performed an endoscope handling dexterity test using a live anaesthetised porcine model. Limited numbers of participants were recruited, but the results suggested that the task was completed more slowly with the robotic system. This was ascribed to the unfamiliarity of

Fig. 3.6.3. Colonoscope remote actuation device, showing (1) optical encoders, (2) Bowden cables and (3) force sensors [Ruiter, 2012].

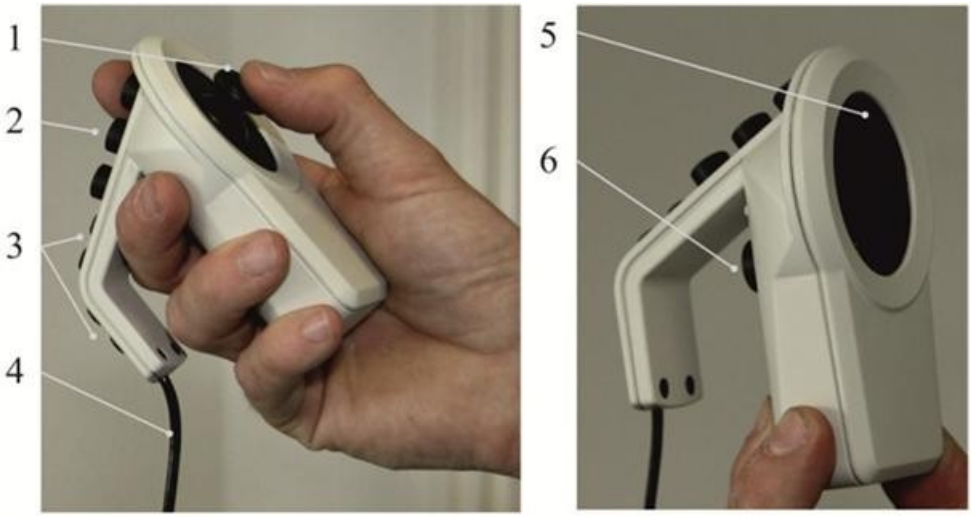

Fig. 3.6.4. Alternative colonoscope remote actuator user interfaces, showing (1) joystick, (2) buttons for auxiliary controls, (3) programmable switches, (4) connection to drive unit, (5) touchpad and (6) safety switch [Ruiter, 2012].

the interface; however in this study the presence of the robotic system also limited rotation of the endoscope insertion tube, which may have further limited performance.

None of the robotic laparoscopic or endoscopic systems discussed here have been developed with MRI compatibility in mind and are consequently unsuitable for the MRI-guided endoscopy application in their current formats. Systems that rely heavily on miniature actuators and precise sensing [Canes, 2009; Corcione, 2005; Shang, 2011] would be very challenging to make MRI compatible due to the limitations posed by the MR environment (see Section 2.3).

Systems similar to those with external motors [Abbott, 2007; Allemann, 2009; Phee, 2009; Ruiter, 2012; Zhang, 2002] may be more suitable for the MR environment

provided that material compatibility considerations are taken into account. These will impose constraints on features such as the degree of miniaturisation and complexity of end effector designs as well as the length of mechanical transmission components.

3.7 Conclusions

The use of intra-operative MRI to guide procedures is a growing area of research, with significant contributions made to the field of materials compatibility and mechanism design. While operating interventional equipment in the MR environment is not trivial, the underlying principles are well understood at this point. These are primarily associated with the magnetic compatibility of materials and electromagnetic interference (EMI) between active devices and the MRI scanner.

A number of bespoke systems for interventional MRI have been developed, each of which is designed to solve the challenges posed by specific procedures. These are primarily systems for needle insertion tasks in different regions of the body, and a wide range of sensors and actuators have been used with some degree of success. Methods of passive and active tracking have been developed to enable precise measurement of the position of the interventional tool in the MRI scanner coordinate system. The optimal configuration of sensors, actuators and tracking systems is dependent on the challenges posed by the targeted interventional procedure.

This thesis is focused on research into a system to enable endoscopy to be performed with intra-operative MRI guidance. No equivalent systems were found within the literature, which suggests that the system presented in this thesis is the first of it's kind.

However, there has been some related research which is reviewed and presented in this chapter. MRI-compatible flexible endoscopes have been designed and used on a limited basis, but real-time guidance of them has been limited by a lack of access to the endoscope controls during MR imaging. Potential solutions to this problem are indicated by the field of robotic endoscopy, although existing solutions in that field are unsuitable to use in the MR environment in their present forms.

Chapter 4

MRI Guided ERCP System

4.1 Introduction

This chapter explores the motivation for and requirements of an MRI-guided Endoscopic Retrograde Cholangio-Pancreatography (ERCP) system. A description of the relevant anatomy as well as existing procedures and their limitations is presented in Section 4.2. Section 4.3 describes the objectives and procedural steps required to perform MRI-guided ERCP before defining the system architecture. A description of two specific technologies that have been developed with the goal of MRI-guided ERCP is presented in Section 4.4: This work was performed by collaborating research groups and not the author, but is included here since a detailed understanding is necessary to provide context for later chapters.

4.2 Techniques for diagnosis of biliary tumours

4.2.1 Background

The upper section of the small intestine that joins the stomach is known as the duodenum. This is the site of the sphincter of Oddi, which drains bile from the hepatopancreatic ampulla (the duct joining the common bile duct and the pancreatic duct) into the duodenum via the major duodenal papilla (Fig. 4.2.1).

A common complaint is that portions of the bile duct have become blocked, either because of gallstones or a constriction of the ducts. Constrictions can be due to infection of, or damage to the duct (such as primary sclerosing cholangitis), or due to cancer of the bile duct (cholangiocarcinoma or CC). Mortality rates from CC have risen steadily over the past 30 years, and now it accounts for more deaths annually than liver cancer in England and Wales [Khan, 2007]. Mortality of patients with CC is extremely high, as tumours are frequently detected too late for surgical resection (the only cure), while chemotherapy and radiotherapy are of limited effectiveness [Wadsworth, 2012]. Diagnosis of

cholangiocarcinoma is challenging due to the difficulty of accessing the biliary system and of correctly identifying the causes of strictures.

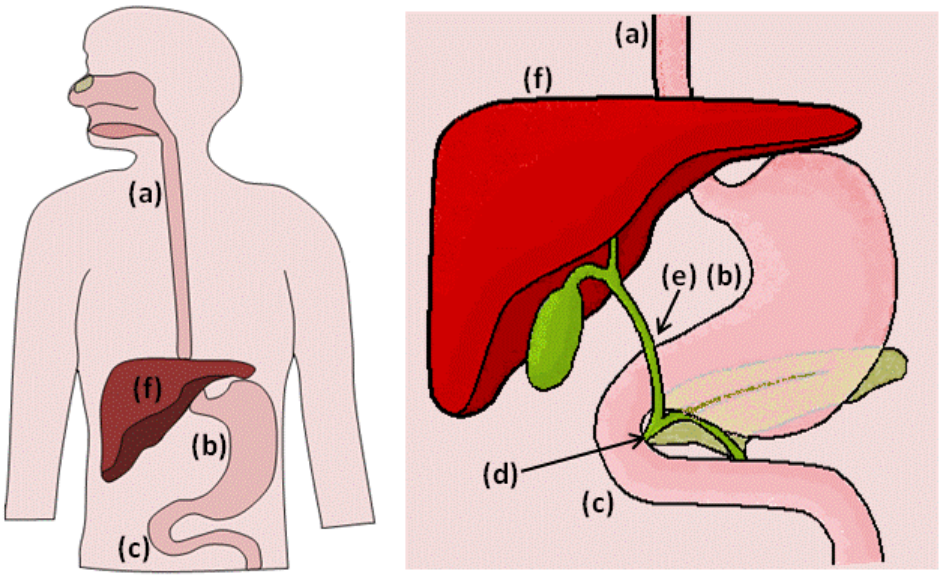

Fig. 4.2.1. Anatomy of the duodenum, pancreas and common bile duct, showing (a) oesophagus, (b) stomach, (c) duodenum, (d) sphincter of Oddi, (e) bile duct and (f) liver.

4.2.2 Endoscopic Investigation of the Bile Duct

Minimally invasive access to the bile duct for diagnosis and treatment is commonly achieved by performing Endoscopic Retrograde Cholangio-Pancreatography (ERCP). In this procedure a side-viewing duodenoscope (Fig. 4.2.2) is inserted into the duodenum and used to advance a catheter through the sphincter of Oddi and in to the bile duct. This is performed using a combination of the optical channel of the endoscope and fluoroscopic imaging for guidance (Fig. 4.2.3).

The process of introducing a catheter into the bile duct is known as cannulation, and is the most technically challenging phase of the procedure. The side-viewing duodenoscope has a bridge lever, which enables the catheter to be deflected by a variable angle as it protrudes from the duodenoscope tip. By controlling this angle and manoeuvring the duodenoscope tip, the operator must guide the tip of the catheter through the opening in the sphincter of Oddi. Care must be taken to position the catheter in the biliary duct and not the pancreatic duct, which also drains through the ampulla.

Initial cannulation is frequently performed using a thin, soft-tipped guidewire instead of a catheter [Petersen, 2007]. The more flexible wire is thought to be more compliant and therefore associated with a lower risk of causing a tissue perforation. Once wire access has been gained a catheter can be advanced over the guidewire and the

procedure continued as normal. Whichever method of cannulation is used, considerable dexterity is required to obtain access to the correct duct.

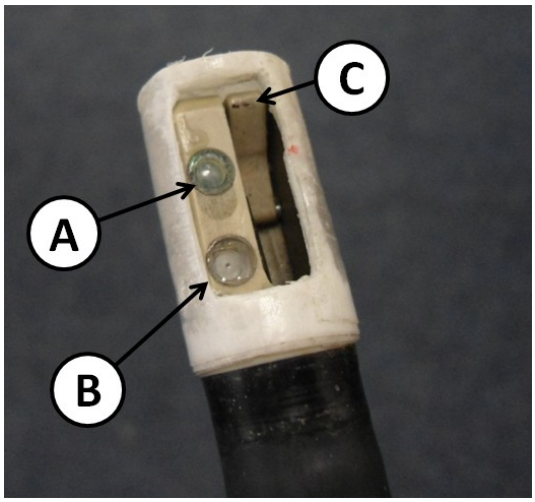

Fig. 4.2.2. Side viewing duodenoscope tip, showing (A) camera lens, (B) light source and (C) catheter deflection bridge.

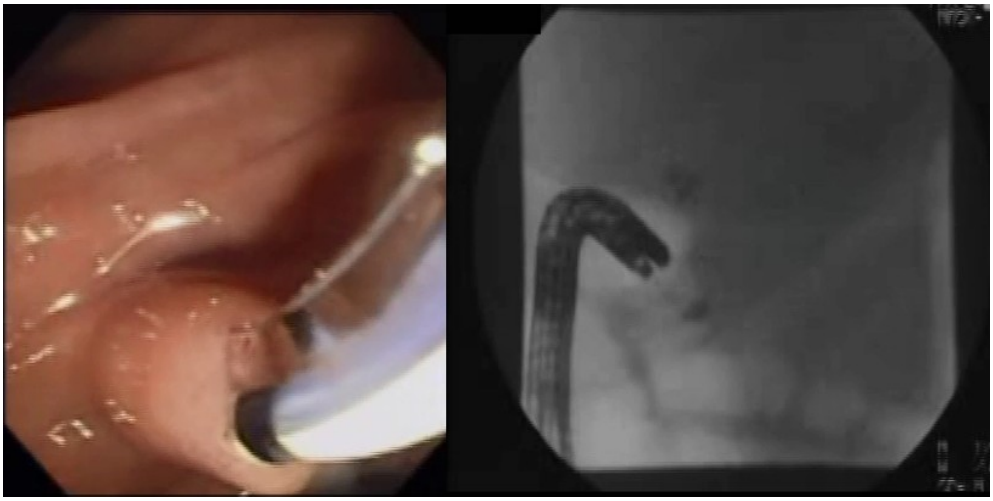

Fig. 4.2.3. ERCP procedure, showing duodenoscope optical image of sphincter and catheter (left) and fluoroscopic image of duodenoscope and bile duct structure (right) [Padda, 2010].

Once catheter access to the bile duct is gained, fluoroscopic contrast medium is injected into the biliary system to enable the ducts to be visualised and strictures or blockages to be identified. At this step in the procedure a wide range of endoscopic tools are available to the operator to diagnose and treat disorders of the bile duct. Baskets and balloons are used to drag stones from the duct, frequently after the sphincter has been cut with a sphincterotome to widen the orifice. Strictures can be dilated with a variety of stents, while tissue samples for histological diagnosis of cholangiocarcinoma can be obtained using forceps or brush cytology [Foutch, 1990].

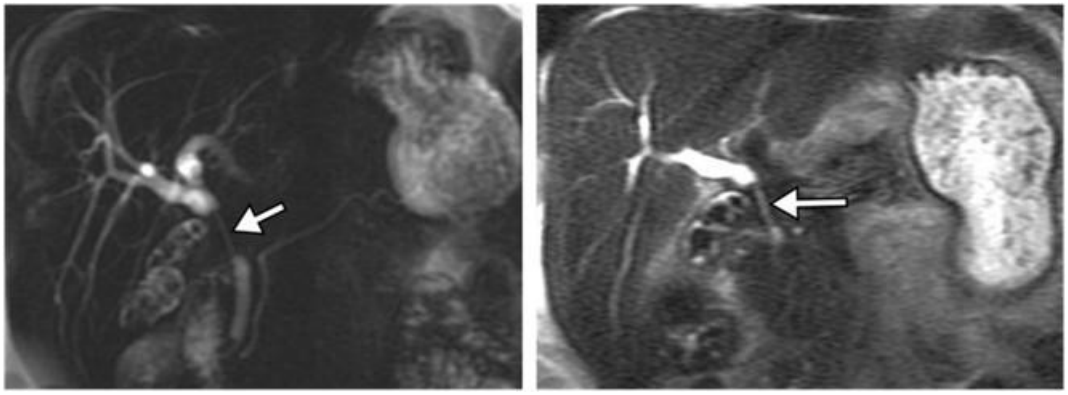

Fig. 4.2.4. Malignant stricture identified from MRCP images [Yeh, 2009].

4.2.3 Diagnostic Imaging of the Bile Duct

MRI is also used to obtain diagnostic information about the biliary system, using a technique known as magnetic resonance cholangio-pancreatography (MRCP) [Magnuson, 1999]. Since it is non-invasive and less subject to operator dependence, MRI is seen as potentially superior to ERCP for the diagnosis of biliary system disorders [Bilgin, 2009]. Typically T2-weighted Spin Echo sequences are used to provide contrast between bile and tissues, with serial contrast enhancement used in some cases [Yeh, 2009]. Images are acquired either as a thick slab or a multi-slice set, depending on the structures visualised and the reconstruction method.

Organ motion due to respiration and peristalsis means that MRCP sequences are generally designed to have an acquisition time of less than 20 seconds so that they can be acquired in a single breath hold. If patients are unable to hold their breath, or for longer sequences, then respiratory motion compensation must be employed (see Section 2.2.3). Images are acquired using a phased array of chest and spine surface coils.

MRCP images are reviewed by radiologists, who are able to identify constrictions, filling defects and dilated ducts (Fig. 4.2.4). The appearance of structures changes with the imaging sequence and the presence of pathology. Comparing the relative intensity of different features on different images enables the radiologist to diagnose the cause of some strictures or blockages (Fig. 4.2.5).

The additional information available from cross-sectional imaging with variable contrast combined with histological analysis of biopsy samples and fluoroscopic images from ERCP provides the most effective method of diagnosing CC currently available [Khan, 2007].

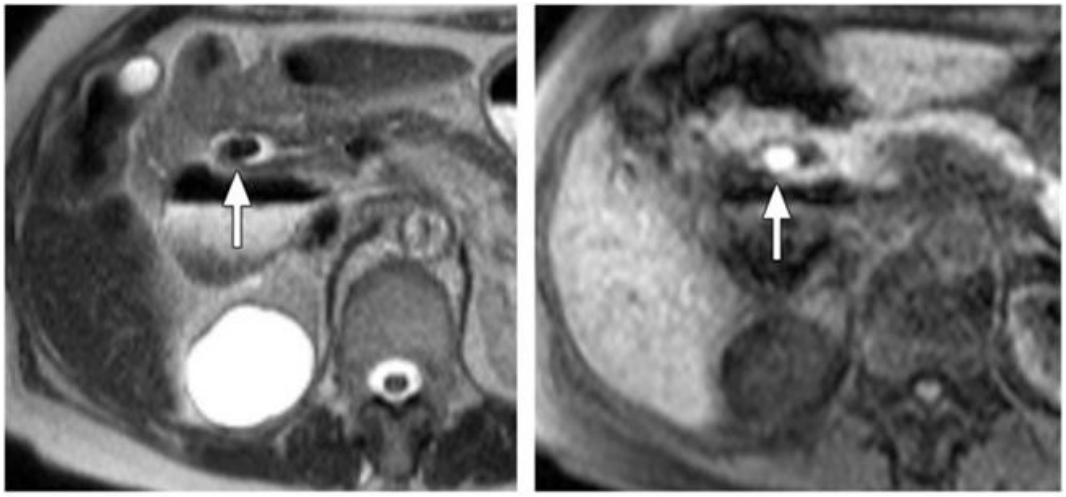

Fig. 4.2.5. Bile duct stone identified by MRCP images. The stone appears as hypo-intense on a T_2-weighted MR image (l), but is hyper-intense on a T_1-weighted image [Yeh, 2009].

4.2.4 Limitations of Existing Techniques

ERCP, despite being classed as a minimally invasive procedure due to the use of natural orifices, carries the highest risk to the patient of any endoscopic procedure [Andriulli, 2007]. Risks include perforation of the bile duct or haemorrhage due to endoscopic tools, complications associated with sedation and infection of either the gallbladder or bile duct. Each of these complications has an incidence of less than 1.5% [Anderson, 2012].

However, by far the most common complication of ERCP is pancreatitis, or infection of the pancreas and pancreatic duct. Meta-analysis of 21 studies has put the incidence at 3.5% [Andriulli, 2007], although this varies from 1.6%-15.7% depending on patient selection. A major cause of pancreatitis is inadvertent cannulation of the pancreatic duct and injection of contrast medium into the pancreas, which means complication rates are dependent on operator experience and technique [Anderson, 2012]. Cannulation with a guidewire prior to introducing a catheter can reduce this risk [Petersen, 2007] but it remains significant and operator dependent.

Pancreatitis rates are compounded by the difficulty of inserting the catheter into the correct duct during fluoroscopic-guided ERCP. Experienced doctors can achieve cannulation rates of over 95%, however it has been shown that generally over 200 ERCPs are required before the doctor can achieve a rate of 80% for simple cases [Lehman, 2002]. A study of ERCP units suggested that even senior trainees recorded a cannulation rate of only 66%, and overall the intended treatment was performed in only 70.4% of cases [Williams, 2007].

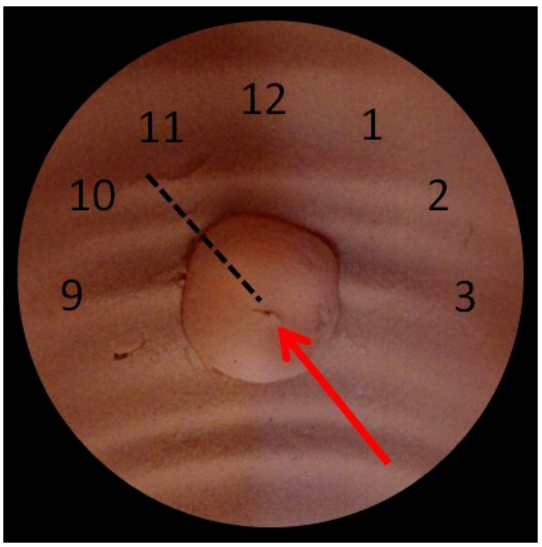

Fig. 4.2.6. During ERCP training operators are taught to approach the papilla (raised central feature on duodenum wall) in the direction of 10 or 11 on a clock face (red arrow).

A major cause of cannulation failure is a lack of information about the biliary structure. Before contrast medium is injected, fluoroscopic guidance gives poor contrast of the bile duct structure and is limited to 2D images, so the operator is frequently unable to determine the optimum direction of approach to the papilla. Operators are taught to push the catheter in a direction corresponding to 10 o'clock when positioned opposite the papilla (Fig. 4.2.6), which in most patients avoids the pancreatic duct. However there is a significant population for which this is not the optimum approach, particularly those who have had prior gastric surgery [Chutkan, 2006]. Repeated failed attempts will cause inflammation, which further inhibits cannulation and heightens the risk of infection. This issue is explored in more detail in Chapter 8.

A further issue, particularly for junior trainees, is control of the duodenoscope itself. When passed through the stomach and upper part of the duodenum the flexible section is significantly curved and in some cases forms a complete loop. This means that when positioned opposite the papilla, control inputs can result in paradoxical motion. For example pushing on the duodenoscope flexible section can induce a motion that appears to correlate with pulling and vice versa. Even experienced operators describe this motion as non-intuitive and it can be very confusing for novices.

Brush cytology can be an effective method of diagnosing cholangiocarcinoma. However it can have a low success rate due to the difficulty of accurately guiding the brush to the correct site using fluoroscopic guidance. In addition, brush cytology risks seeding cancers by spreading cancerous cells to different areas of the bile duct [Foutch, 1990].

MRCP suffers from a different range of issues. The resolution and contrast of images generated during MRCP limits the size of features that can be identified. The trade-off that MRI presents between imaging speed, signal-to-noise ratio (SNR) and resolution (see Section 2.2.1) is significant in MRCP, since the structures of interest are very small (under 5mm diameter), are very mobile and can be a significant distance from the MR receiver coils.

Motion is tackled by either limiting the duration of the scan sequence to enable acquisition within a single breath-hold, or by the use of a motion compensation system such as the Navigator sequence (see Section 2.2.3). Combined with a desire to average multiple acquisitions to improve SNR this leads to a practical limit on the image quality, which can limit the diagnostic utility of MRCP [Wadsworth 2012].

4.3 MRI-guided ERCP Procedure

4.3.1 Objectives

This procedure for MRI-guided ERCP is designed to improve on the standard MRCP and fluoroscopic-guided ERCP techniques outlined above. The aims are for the procedure to improve on the following characteristics:

- *Increase in cannulation rate.* The use of intra-operative MRI during the cannulation phase will provide contextualised information to the operator that has the potential to improve cannulation rate and decrease the incidence of post-procedural pancreatitis.

- *Reduction in training requirement.* Due in part to a lack of information during the cannulation phase of the procedure, the training period required for ERCP operators is extensive. By providing more information in an intuitive context, the procedure should be easier for less experienced operators to complete.

- *Improve MRCP by using intraluminal receiver coils.* The procedure will enable a significant increase in the quality of MRCP images available for diagnosis, by using the endoscope to introduce intraluminal MRI receiver coils in close proximity to the region of interest.

- *Integrated diagnosis and treatment.* By performing high-quality MRCP and ERCP simultaneously, the opportunity exists for all CC diagnostic techniques (such as staging

with MRCP and biopsy) and therapeutic treatments (such as stenting and stone removal) to be performed during the same procedure.

- *Facility Independence.* It is intended that the procedure can be performed at a wide range of facilities, so the system should not rely on features that are not available as standard in clinical MRI scanners. This precludes the use of open bore scanners, software features particular to certain scanner systems or reliance on a specific scanner room layout or features.

- *Clinical Viability.* The development of the procedure and associated system is focused on producing a solution that is clinically acceptable, in terms of workflow and time taken to complete the procedure.

4.3.2 Procedure Outline

The procedure is split into 5 phases, each of which places different demands on the endoscope, actuation and imaging:

1. Manual insertion of endoscope and positioning adjacent to bile duct. This will be performed with the same approach as currently used for standard ERCP. This part of the procedure will be performed inside the MRI scanner room with the patient on the bed outside of the scanner bore. The endoscope will be inserted into the patient and positioned in the region of the hepatopancreatic ampulla. A catheter will be manually loaded into the biopsy channel of the endoscope, positioned so that the tip of the catheter is close to the end of the biopsy channel and the steering bridge.

2. MRCP imaging to obtain 3D images of bile duct structure and locate endoscope. Patient will be loaded into MRI scanner bore with the endoscope in situ. The imaging sequence will also allow a thick (~1cm) slice to be defined that shows a large section of the bile duct structure in a single image. This will be used in future steps to facilitate catheter location.

3. Guide catheter into bile duct. To assist in determining the correct angle to approach the hepatopancreatic ampulla a combination of an MRI tracking sequence, the high quality images from Phase 2, the duodenoscope video channel and intra-procedural MRI will

be displayed to the doctor. Successful access to the bile duct will be verified by locating the catheter using MR images.

4. A combination of receiver coils mounted on the catheter and endoscope tip will be used to generate images of the bile duct and surrounding tissue. The catheter can be moved along the bile duct using remote actuation, with MRI images taken in the plane of the bile duct (see Phase 2) to assist in imaging areas of interest using the microcoil. It is anticipated that several series of images will be generated and combined to give a complete picture of the bile duct and surrounding tissues.

5. Further interventions as required. Once detailed images of the bile duct and surrounding tissues have been generated, the doctor will be able to assess the situation and further interventions may be performed. Potential procedures include stone removal using a balloon catheter, stent placement and cytology using a brush catheter.

4.3.3 System Requirements

The principal objectives outlined above will be achieved by successful integration of the MRI and endoscopic procedures. An increase in cannulation rate and reduction in training requirement can be realised by utilising intra-operative MRI instead of fluoroscopic imaging to provide more detailed information during the cannulation phase. The use of intraluminal MR receiver coils will enable improvements in diagnostic MRCP due to their inherent benefits to imaging (Section 4.4.2), and mounting the intraluminal coils on a fully operative duodenoscope enables both therapeutic and diagnostic treatments to be performed during a single procedure.

To successfully integrate the two procedures and ensure the objectives of facility independence and clinical viability are achieved, key system requirements can be derived from the list of objectives and the procedure description. These are explored in further detail in the following sections and were used to guide the system design and testing outlined later in this thesis.

4.3.3.1 Workspace

The system should be designed to work within standard closed-bore MRI scanners to take advantage of the superior imaging capacity and wider availability that they offer. However, closed bore scanners present a significant challenge in terms of access to the patient and endoscope controls (Fig. 4.3.1). This is reflected in the fact that previous work

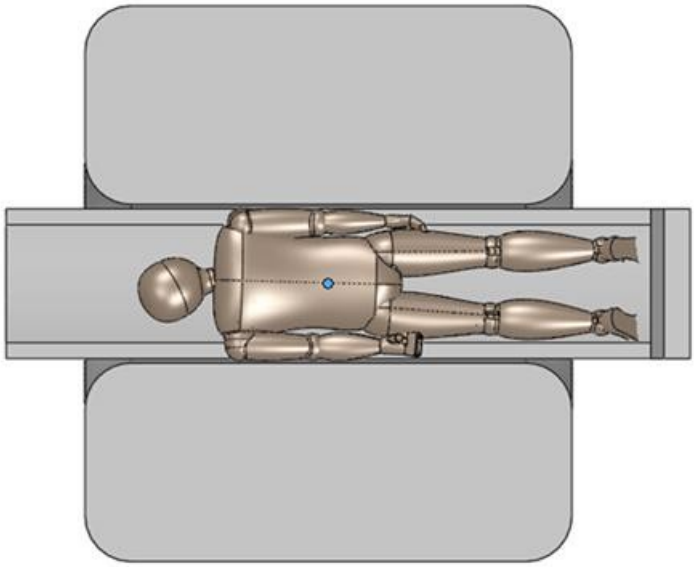

Fig. 4.3.1. Working in closed-bore MRI scanners limits access to endoscopy patients. Sketch shows an average-sized patient with their abdomen at the scanner isocenter.

in this area has not demonstrated true real-time MRI guidance but has involved repeated moving the patient into and out of the scanner for MR imaging and manual endoscope actuation respectively (see Section 3.5).

Fig. 4.3.1 demonstrates that the patient's mouth will be inside the scanner bore during abdominal imaging, meaning that control of the flexible section is particularly challenging and would require reaching into the bore. In addition, the length of the existing MRI compatible duodenoscope (see Section 4.4.1) means that the handle-mounted controls are extremely close to the end of the scanner bore. The two limitations combine to make precise control of the duodenoscope while the patient is inside a closed-bore scanner extremely challenging and not practical in a clinical situation (Fig. 4.3.1), particularly when attempting to co-ordinate MR imaging and endoscope control.

Increasing the length of the duodenoscope flexible section would improve the situation for the clinician's left hand but not their right. In addition, due to the need for MRI compatible coherent fibre optic for video transmission and polymer steering cables (Section 4.4.1), a lengthened flexible section would result in significantly degraded instrument performance and was not considered a clinically viable solution for this issue.

The solution presented here is to construct a remotely controlled MRI compatible endoscope actuation system that can be docked onto the MRI compatible duodenoscope at the start of phase 3 of the procedure (see above). This will enable precise control of the duodenoscope while the patient is lying within a closed-bore scanner during the critical

bile duct cannulation phase and subsequent phases, whilst enabling the operator to direct and utilise the intra-operative MRI.

The use of a remote actuation system has additional requirements associated with it, which are summarised here:

- *MRI Compatibility*. Clearly the remote actuation system must be safe to operate within the MR environment whilst also being MRI compatible to enable the high-quality diagnostic imaging to be performed (see Section 2.3).

- *User Control.* Due to the complex and potentially harmful nature of the procedure, safe control of the duodenoscope throughout the procedure is essential. For this reason, the remote actuation system should have no elements that rely on automated movements and instead be fully under the control of the user at all times.

- *Manual Actuation Facility.* As this procedure is an experimental one being carried out in an unusual environment for endoscopy, a further safety concern is that it must be possible to disengage the duodenoscope from the remote actuation system and revert the procedure from remote to manual control rapidly in an emergency.

4.3.3.2 Imaging

The capacity of the system to generate high quality MR images is paramount, and is assisted by the intraluminal MR receiver coil developmental work performed by collaborating research groups (see Section 4.4). In order that the imaging benefit from the intraluminal imaging coils is not compromised, MRI compatibility of all system components must be maintained, as outlined above.

Patients are sedated prior to intubation with a duodenoscope for comfort and safety reasons. This means that breath-hold MRCP sequences will not be possible during the MRI-guided ERCP procedure, so there is a requirement for the system to incorporate motion compensation to remove motion-related image artefacts.

Standard techniques such as the Navigator sequence compensate for respiratory motion, but additional information is desirable to account for movement of the biliary tract relative to the diaphragm and to enable higher quality images of the region of interest to be obtained.

Measurement of the duodenoscope position is also required to enable the MR guidance images to be contextualised during the cannulation phase. The anatomical

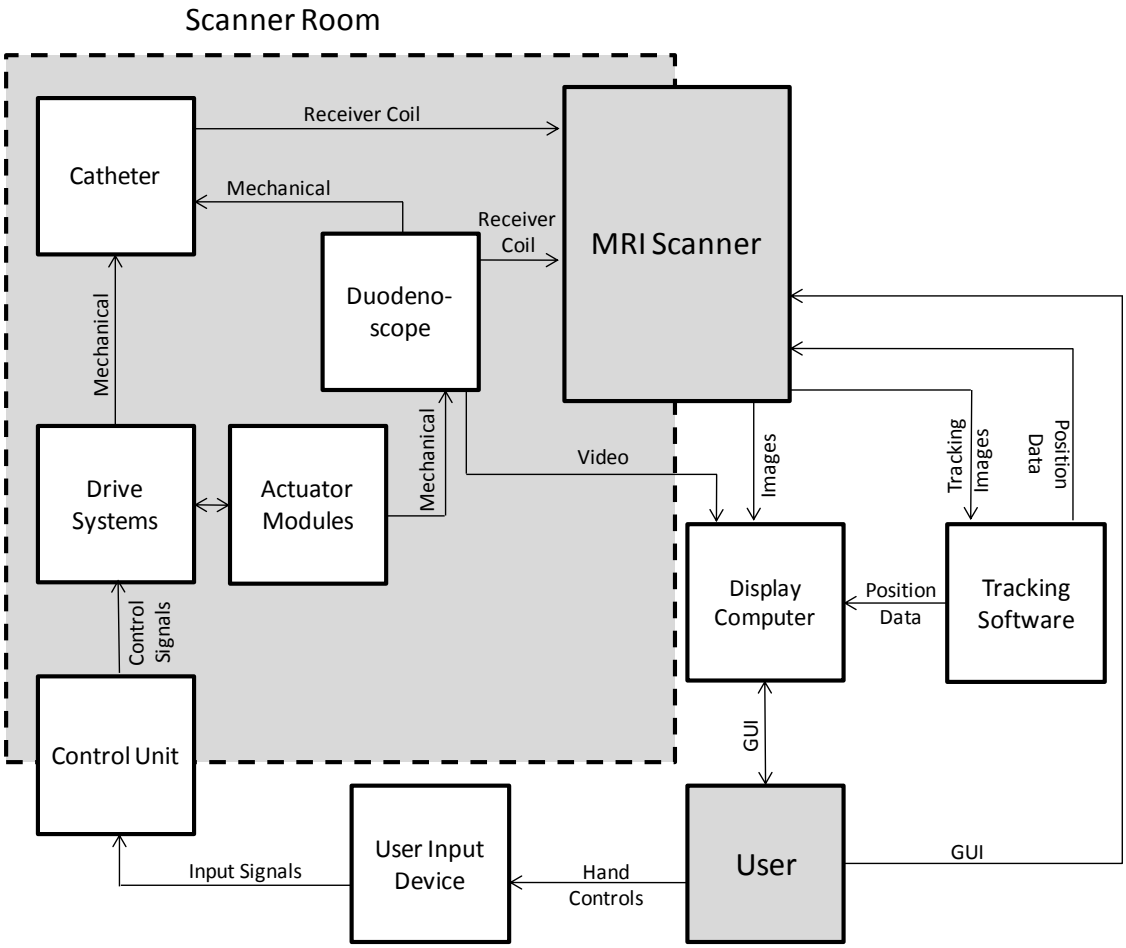

Fig. 4.3.2. Schematic of the MRI-guided ERCP system. The 'MRI scanner' in this diagram includes the scanner itself as well as the image processing computers and graphical user interface. The nature of the connections between subsystems is labelled.

images must be combined with a frame of reference to allow the user to translate information into control inputs. This can be learnt through experience, but precise location information will enable the potential improvement of intra-operative MRI over traditional fluoroscopic imaging to be fully utilised.

4.3.4 System Overview

Fig. 4.3.2 is a schematic diagram of the MRI-guided ERCP system designed to achieve the objectives outlined above. The various sub-systems and the connections between them are displayed as arrows with a description of the nature of the connection.

The user is provided with intra-operative MRI and localisation information from the scanner, as well as video from the duodenoscope. Based on this information the user manoeuvres the duodenoscope via the remote actuator system user input device and

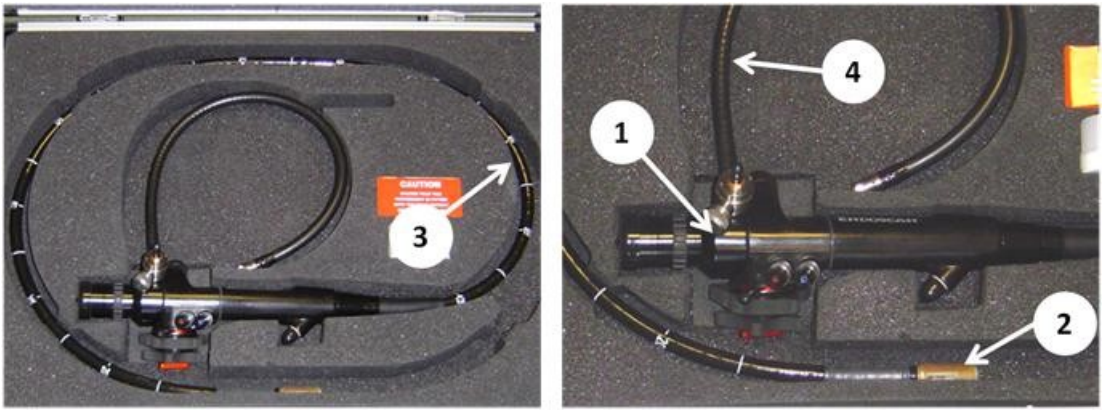

Fig. 4.3.3. MRI compatible duodenoscope manufactured by Endoscan Ltd., showing (1) control handle, (2) distal tip, (3) flexible section and (4) light guide attachment.

actuator modules, which are mechanically interfaced with the duodenoscope and catheter. The user is also able to control the MRI scanner to alter the imaging parameters as desired, and remains fully in control of the duodenoscope and MRI scanner throughout the procedure.

Intra-luminal MR receiver coils mounted on both the duodenoscope and catheter transmit signals to the MRI scanner for imaging and tracking purposes. Tracking is performed by a dedicated software module, which processes the tracking images to determine the location of the duodenoscope and catheter. This information is then sent in real-time to the MRI scanner to dynamically update the imaging parameters and to the user for contextual visualisation.

4.4 Enabling Technologies

The MRI-guided ERCP system relies on an MRI compatible duodenoscope and intra-luminal MR receiver coils that have been developed over a number of years by collaborating research groups. As key components of the system, a description of their operation is included here for completeness. Characterisation of the component performance was carried out to assist with the design of the duodenoscope remote actuation system (see Chapter 5).

4.4.1 MRI Compatible Duodenoscope

The endoscope used for this project is an MRI-compatible duodenoscope, produced by Endoscan Ltd. (Fig. 4.3.3). The endoscope was designed to be used in a clinical setting and is completely sealed to allow sterilisation. The basis of the design is described in [Coutts,

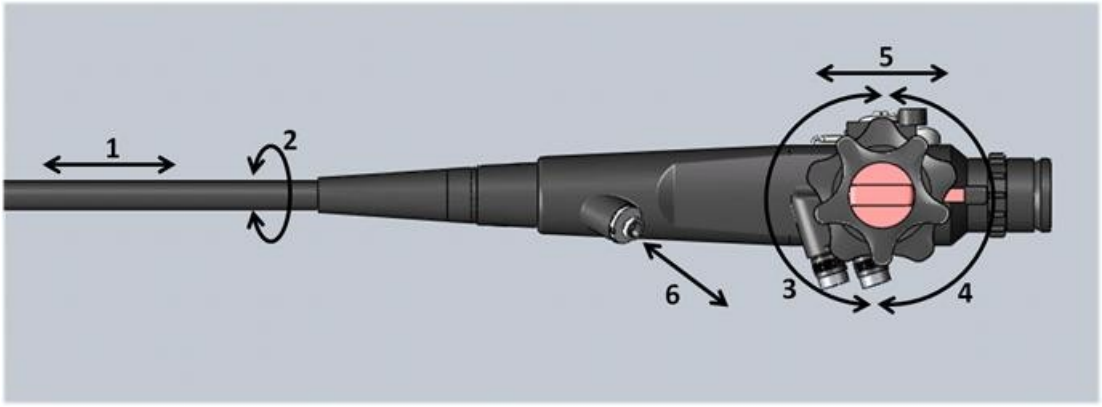

Fig. 4.4.1. Duodenoscope degrees of freedom (DOF): (1) flexible section insertion and retraction, (2) flexible section rotation, (3) distal tip steering up and down (U-D), (4) distal tip steering left and right (L-R), (5) catheter deflection bridge and (6) catheter insertion and retraction.

2003] and earlier versions have been used previously in limited research studies [Ahmad, 2008; DeSouza, 1995].

The duodenoscope consists of a control handle connected to a 1.5m long flexible section. The distal tip of the flexible section is articulated and includes side-viewing lenses for video capture as well as a light source and nozzles for air, suction and water injection. A 3.2mm diameter tooling channel runs the length of the duodenoscope from a port on the side of the handle to an opening on the distal tip – tools such as catheters can be passed along this channel, and are steered at the distal tip by use of a catheter deflection bridge. The distal tip also incporates a cavity for the pickup electronics of an inductively coupled MR receiver coil, as described below (Fig. 4.4.8).

The duodenoscope handle incorporates two control wheels; one of these steers the distal tip up and down, while the other causes it to bend left and right. In addition there is a lever to articulate the catheter deflection bridge. Combined with translation and rotation of the flexible section, and transltation of the tool relative to the handle, the duodenoscope has six user controlled degrees of freedom (DOF) that are used by the operator to position the distal tip and tool during a procedure (Fig. 4.4.1). The handle also incorporates buttons to activate the air, water and suction channels at the distal tip. On the handle there is a connection for the umbilical cable that connects the instrument to supplies of air, water and suction. The handle controls are designed to be operated with the clincian's left hand, with the right hand free to position the flexible section while the catheter is advanced either by the user's right hand or by an attending nurse.(Fig. 4.4.2).

Conventional endoscopes incorporate a Charged Coupled Device (CCD) chip at the endoscope tip to allow high quality video capture. Due to the high magnetic field, CCD chips are unreliable inside the MRI scanner bore and have the potnetial to introduce

Fig. 4.4.2. The duodenoscope handle is designed to be held and operated by the user's left hand, while the right hand controls the flexible section.

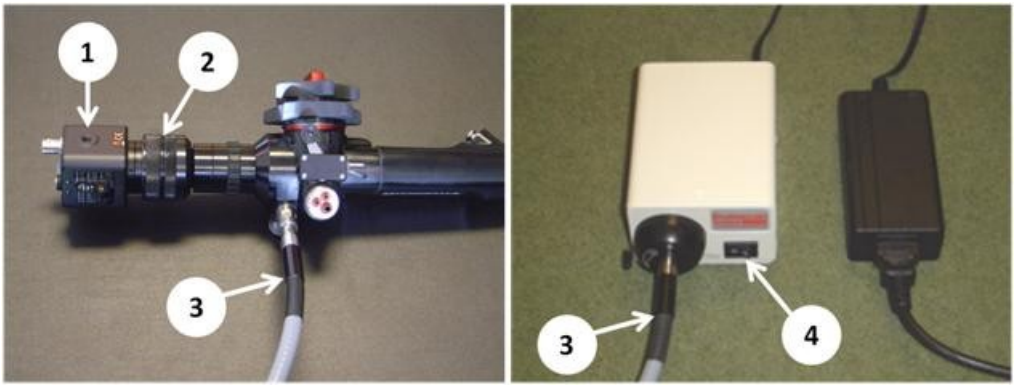

Fig. 4.4.3. Duodenoscope optics, showing (1) external camera, (2) lens attachment, (3) liquid light guide and (4) light source.

significant noise into the MR envionment. For this reason, the Endoscan MRI compatible duodenoscope utilises an external camera that is mounted on the control handle (Fig. 4.4.3) and connected to the tip via a choherent fibre optic bundle and lens attachment. An adjustable external light source is placed well away from the MRI scanner, and connected to the duodenoscope via a 6m long liquid light guide.

The flexible section and articulated tip are designed to minimise the presence of materials that produce significant susceptibility artefacts on MR images. The tip itself is

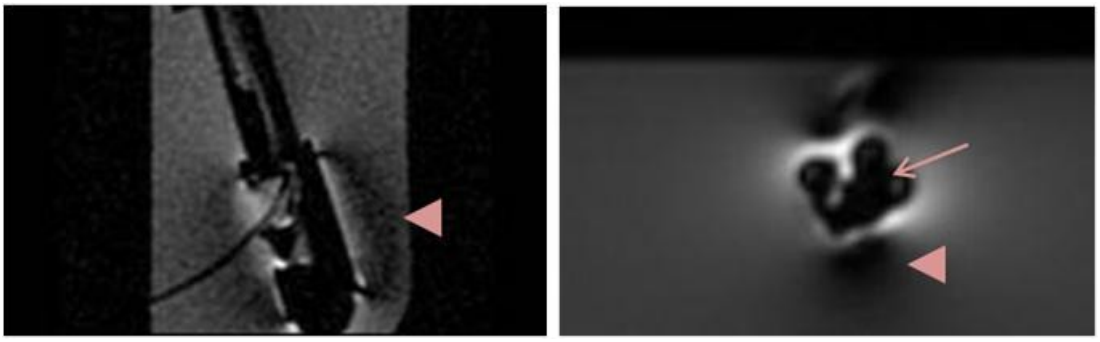

Fig. 4.4.4. Sagital (l) and Axial (r) MRI of duodenoscope tip immersed in water. Limited susceptibility artefacts are visible (arrow); the dark areas behind the tip are due to the tip coil (arrowheads).

made from a polymer, with two Titanium pins for the catheter deflection bridge being the only parts that cause an image artefact (Fig. 4.4.4). The tip is articulated using Bowden cables, with the inner cables made from a high tensile ploymer thread and the outers made from wound nonmagnetic CrMo wire. The outer cables terminate at the proximal end of the articulated section, preventing them from interferring with MR Imaging of the tip.

4.4.1.1 Force and Torque Requirements

In order to specify the requirements for the remote actuation system, the force required to actuate all degrees of freedom of the Endoscan MRI compatible duodenoscope was assessed. Studies have investigated forces required for intubation during colonoscopy and looked at the muscle activity level required for colonoscope tip steering [Shergill, 2009], but no equivalent study has been performed for ERCP. This experiment was performed ex vivo, with an ERCP-trained doctor in assistance. All measurements were designed to provide guideline figures for which prototypes will be designed, with allowances for sizeable margins of error.

The patient's tissue is expected to provide very little additional resistance to the duodenoscope tip steering controls (DOF 3 and 4). Therefore, the required forces and torques were simply measured using spring balances (Fig. 4.4.5).

In contrast, the feed and twist of the duodenoscope flexible section (DOF 1, 2) are very dependent on patient tissue. In vivo testing is challenging to perform on a statistically representative number of patients due to high costs and time constraints. In order to estimate figures of the correct order of magnitude, a rig was designed that would provide resistance to the doctor pushing and rotating the flexible section of duodenoscope (Fig. 4.4.5). The doctor was then asked to manipulate the duodenoscope

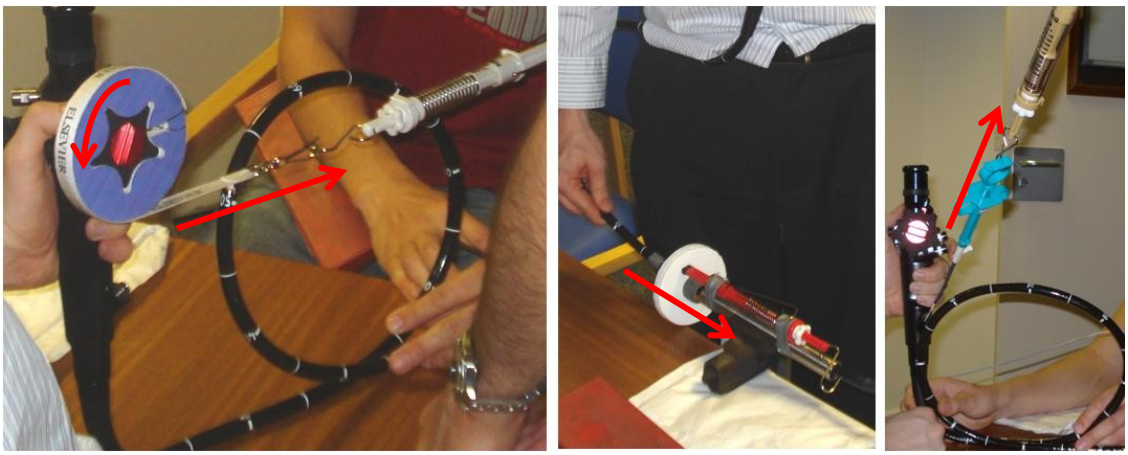

Fig. 4.4.5 Duodenoscope force and torque measurements. Tip steering (left), flexible section feed and twist (centre) and catheter feed (right). Red arrows indicate the DOF measured in each case.

	Degree of Freedom	Force / Torque	Range	Speed	Power (W)
1	Duodenoscope Feed	8 N	200 mm	100 mm/s	1.6
2	Duodenoscope Twist	150 Nmm	±180°	90 °/s	0.24
3	U-D Steering Wheel	750 Nmm	270°	72 °/s	0.94
4	L-R Steering Wheel	750 Nmm	270°	72 °/s	0.94
5	Bridge Lever	20 N	25 mm	5 mm/s	0.10
6	Catheter Feed	10 N	150 mm	30 mm/s	0.30

Table 4.4.1. Results of duodenoscope force and torque measurements

until he felt a representative resistance, and these values were recorded. Repeat tests showed the results were consistent, although clearly very dependent on the doctor's subjective response – for reference the recorded forces were similar to those recorded for intubation during colonoscopy [Shergill, 2009]. As noted above, these results should be used with recognition of their potentially large errors.

Forces required to feed the catheter (DOF 6), and to steer the tip of the catheter with the bridge (DOF 5) are very dependent on the catheter used. In addition, during the procedure the catheter is frequently lubricated with water, which makes it easier to actuate. In order that this test provides a worst-case scenario, these DOF were measured with a dry, stiff catheter (Boston Scientific 3mm Trapezoid RX) as shown in Fig. 4.4.5.

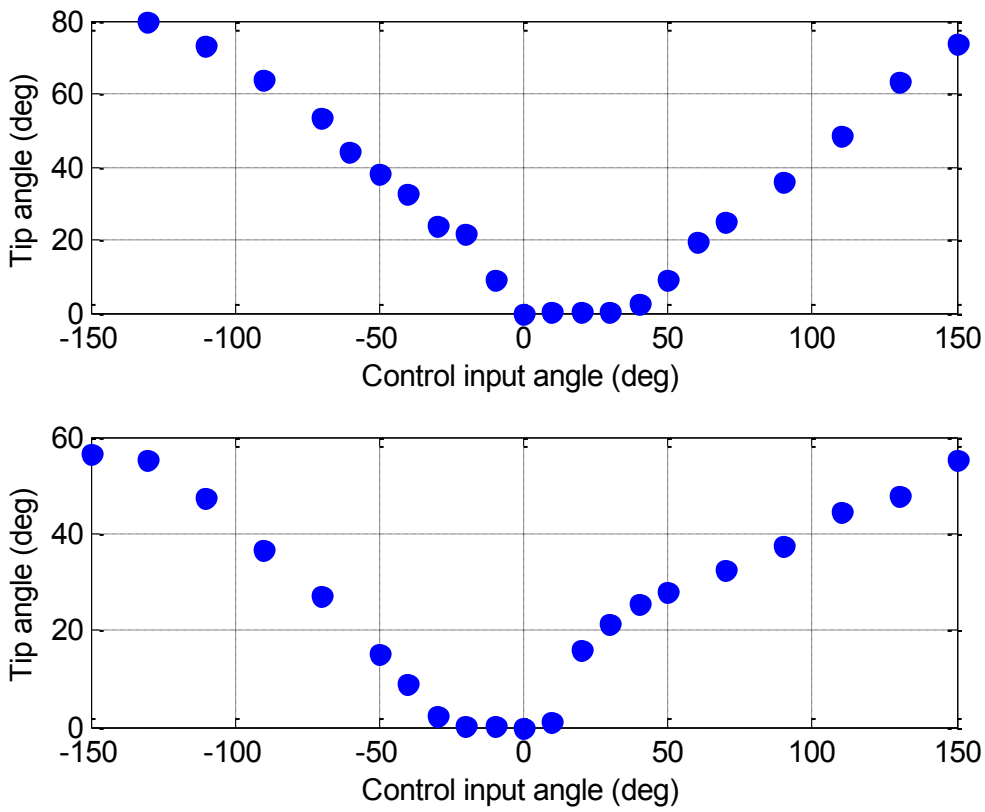

Fig. 4.4.6. Results from Duodenoscope tip steering up-down (U-D) backlash test (top) and tip steering left-right (L-R) backlash test (bottom).

Additional friction was applied by adding a loop to the path of the flexible section of duodenoscope.

Further discussion with the doctor yielded expected ranges of motion and approximate speed for each of the duodenoscope DOF during phase 2 of the procedure (see Section 4.3.2). All results for this testing are presented in Table 4.4.1. The characterisation of the forces and torques required during an ERCP procedure presented here provides a starting point for the actuation system design presented in Chapter 5.

4.4.1.2 Duodenoscope Stiffness and Backlash

The materials used in the construction of the duodenoscope were selected for their MRI compatibility and are therefore do not exhibit optimal mechanical characteristics. The principal impact of this is in the introduction of backlash into the duodenoscope tip controls, as the standard high tensile steel Bowden cables have been replaced by a ploymer that is more susceptible to stretching under load. In addition a standard duodenoscope flexible section is constructed with a steel mesh wrap to increase it's torsional stiffness, which has again been replaced with a polymer for the MRI compatible model.

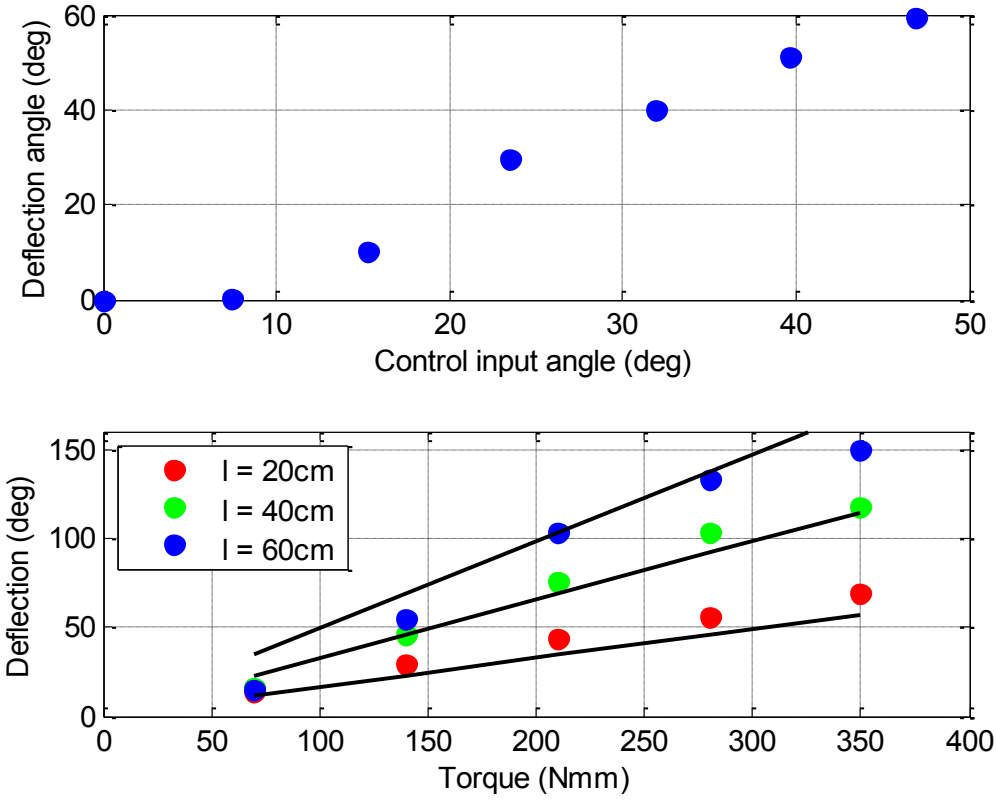

Fig. 4.4.7. Duodenoscope catheter deflection lever backlash (top) and flexible section torsional stiffness (bottom), where l indicates length of flexible section over which deflection was measured

The materials and construction changes make backlash and joint stiffness an issue when operating the MRI compatible duodenoscope. This was measured for the three tip controls (catheter deflection bridge, tip steering up-down and tip steering left-right) and for the flexible section roation DOF. The two remaining DOF (flexible section feed and catheter feed) are not susceptible to backlash, but rather to the flexible parts buckling when pushed against a load. The degree of this buckling is dependent on the structures surrounding the part (such as the oesophagus) as much as the part construction itself.

Backlash of the tip controls was measured by mounting a small electromagnetic tracking sensor (Aurora, Northern Digital Inc., Ontario, Canada) on the tip of the duodenoscope. The controls were moved from the neutral position to their limit in either direction and the angular movement of the tip recorded. Tests were performed with the duodenoscope flexible section straight and with no external load placed on the duodenoscope tip. The flexible section stiffness was measured by applying a torque to the flexible section at a distance from the duodenoscope handle. The handle was fixed, and the rotation of the fleible section at the point of torque application was measured using

the tracking sensor. This was repeated for a range of torques and at different distances from the duodenooscope handle.

The results of the backlash and stiffness tests are summarised in Fig. 4.4.6 and Fig. 4.4.7. The tip steering DOF experience significant levels of backlash, with no tip movement recorded for movements of up to 25° for the L-R sterring wheel and 40° for the U-D steering wheel. This is not centred on the neutral position but offset, suggesting that greater backlash is present in one of the pair of opposing Bowden cables. The catheter deflection bridge lever experiences a similar lack of output for the first 10° of travel, which equates to a linear movement of 6mm.

The theoretical relationship between torque, angular deflection and section length is given by:

$$T = \frac{J_T}{l} G\theta$$

(Eq. 4.1)

Where T is the applied torque, l is the length of the section, θ the angular deflection, J_T is the second moment of area of the section and G is the shear modulus. The duodenoscope flexible section angular deflection due to torque is shown in Fig. 4.4.7, with trend lines corresponding to a J_TG constant of 0.07 shown. These results are significant when compared with the torque that is expected to be applied during the procedure (Table 4.4.1). At a torque of 150 Nmm these results suggest an angular deflection of 13° per 0.1m of flexible section length.

The results presented in this section show that the stiffness of the MRI compatible duodenoscope are less than optimal, and must be taken account of when designing a system to operate the duodenoscope. The level of backlash is significant, and it demonstrates the challenge of designing MRI compatible mechanical force transmission devices, which was discussed in Section 3.2.

4.4.2 Intra-Luminal MR Receiver Coils

The MRI-guided ERCP system utilises two receiver coils, which are mounted on the duodenoscope distal tip and on a standard 9Fr catheter. Both receiver coils are manufactured by etching the conductors from a copper film printed on a sheet of epoxy substrate [Ahmad, 2009]. The thin film receiver coils are then mounted on a former to provide the necessary mechanical support. For this application both coils are tuned to operate in a 1.5T scanner.

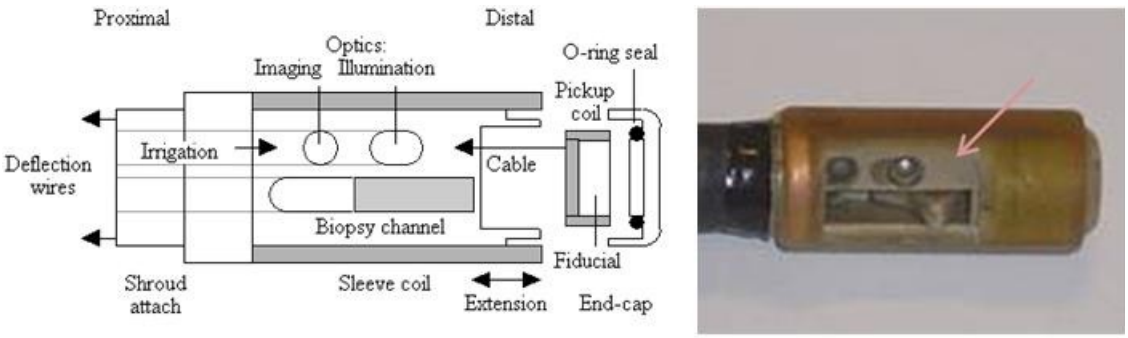

Fig. 4.4.8. Duodenoscope tip receiver coil (l) layout sketch and (r) completed instrument with window for catheter and optics (arrow).

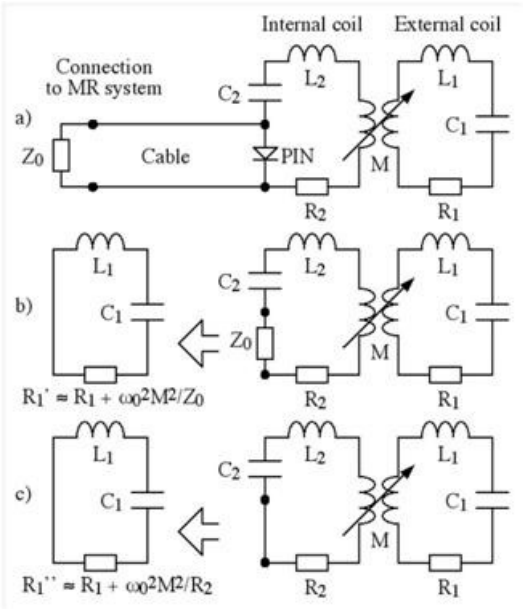

Fig. 4.4.9. Schematics of duodenoscope tip coil system showing (a) overall equivalent circuit, (b) equivalent circuit when PIN diode is open and (c) equivalent circuit when PIN diode is closed.

4.4.2.1 Duodenoscope Tip Coil

The duodenoscope tip coil is embedded in an epoxy sleeve that fits over the distal tip of the duodenoscope. The sleeve can be removed from the duodenoscope for cleaning or maintenance purposes and features a catch that prevents it from being inadvertently moved. The receiver coil itself is a saddle coil with integrated capacitors which has a window cut out of the centre of one saddle loop to enable the duodenoscope distal tip optics and catheter deflection bridge to pass through it (Fig. 4.4.8).

The tip coil integrated into the sleeve inductively couples with an internal pickup coil that is located inside the blind cavity in the duodenoscope distal tip (Fig. 4.4.8). The pickup coil is two-turn thin film saddle coil, with capacitors and a PIN diode soldered onto

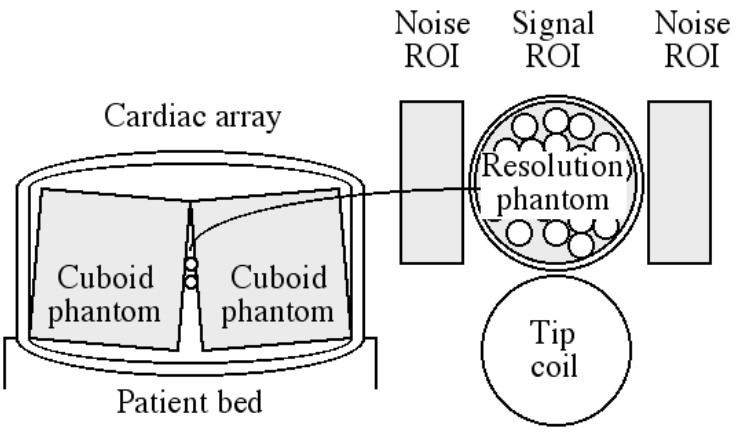

Fig. 4.4.10. Arrangement for comparison of cardiac array surface coil and duodenoscope tip coil [Syms, In Press].

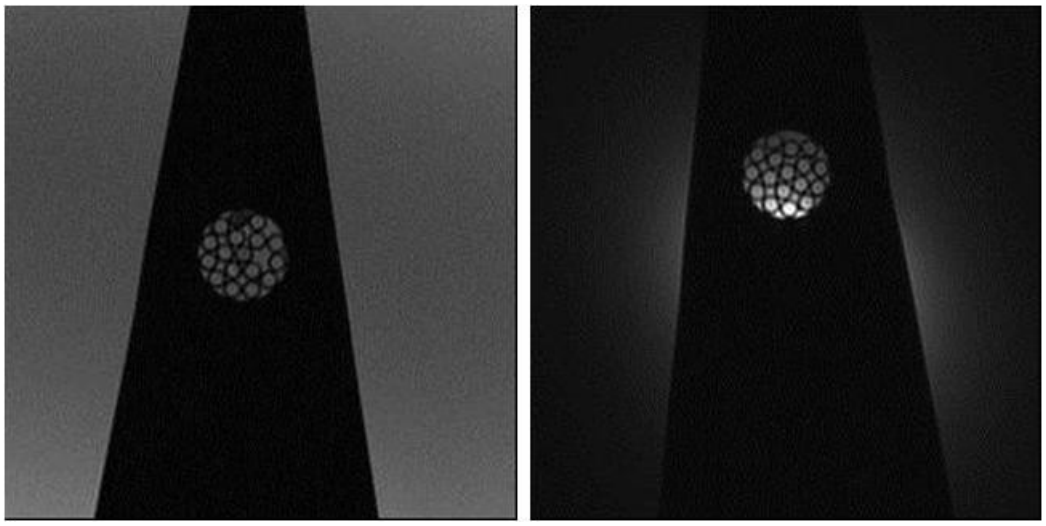

Fig. 4.4.11. Comparison of (l) surface array coil and (r) duodenoscope tip coil images (160mm field of view (FOV), number of excitations (NEX) 4).

mounting pads. It is connected to the scanner via a miniature coaxial cable that runs the length of the duodenoscope flexible section and terminates in a standard RF socket at the duodenoscope handle.

The two coils form a mutually inductive circuit, which when the PIN diode is open (Fig. 4.4.9) matches the scanner system impedance Z_0 (50 Ω) when resonating with at the Larmor frequency of 63.8 MHz. This results in low reflection (<-30 dB) and good transmission of MR signals to the scanner. When the PIN diode is closed (Fig. 4.4.9) the impedance of the coils increases, which significantly increases the resistance and prevents large currents being induced in the coil during the excitation phase of the MRI sequence (signal attenuation of 37 dB compared with PIN diode open) [Syms, In Press].

Coil	NEX	Time	Avg. Signal	Avg. Noise	Avg. SNR	SNR Gain
Array	1	44s	396	16.6	28.3	
Scope	1	44s	5803	87.8	66.1	2.8x
Array	4	2m 49s	366	8.26	44.3	
Scope	4	2m 49s	5512	39.2	140.6	3.2x

Table 4.4.2. Acquisition time, signal and noise results for images acquired with the surface array coil and duodenoscope tip coil.

The duodenoscope tip coil was tested in a 1.5T clinical scanner facility (GE Sigma Excite) to compare it's performance with an 8-element GE HD cardiac array coil (Fig. 4.4.10). SNR measurements suggest that the tip coil offers a significant improvement compared with the standard array coil up to a distance of 3cm from the coil. In the region of interest, the improvement is approximately a factor of 3 (Table 4.4.2, Fig. 4.4.11). This improvement enables high quality imaging of the duodenum and proximal biliary system to be performed faster and more reliably under the challenging conditions of the abdomen.

4.4.2.2 Catheter-Mounted Coil

Early versions of the catheter-mounted coil are demonstrated in [Ahmad, 2009; Ahmad, 2008]. This section describes more recent developments and results relating to the technology. The catheter coil is a thin-film RF detector wrapped around a length of PTFE tubing and encased in heat-shrink tubing. The coil is flexible enough to be bent through 90° without kinking, and includes a softened tip to prevent tissue perforation during ERCP. At the proximal end, the catheter is connected to the scanner via a removable inductive tap (Fig. 4.4.12).

The circuit consists of a linear array of L-C resonant circuits with overlapping figure of eight shaped inductors, with the inductor at the catheter tip acting as the MR receiver coil and the remainder of the array forming a magneto-inductive output cable (Fig. 4.4.13). Coaxial shielding is not possible due to space so the arrangement of the resonant circuits on the output cable is required to shield the MR signals. The shape of the inductors protects against external magnetic fields while the overlapping of the circuits acts as a transformer and protects against external electrical fields. This configuration means that the catheter coil is not susceptible to RF induced heating during the MR sequence and results in a transmission loss of around 7 dB.

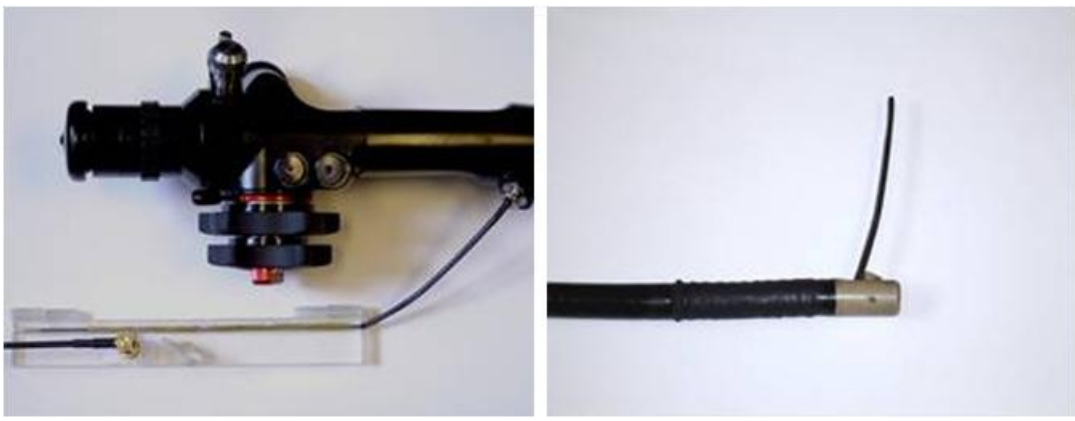

Fig. 4.4.12. Catheter coil (l) distal tip deflected through 90° by the duodenoscope, and (r) inductive tap connector at proximal end.

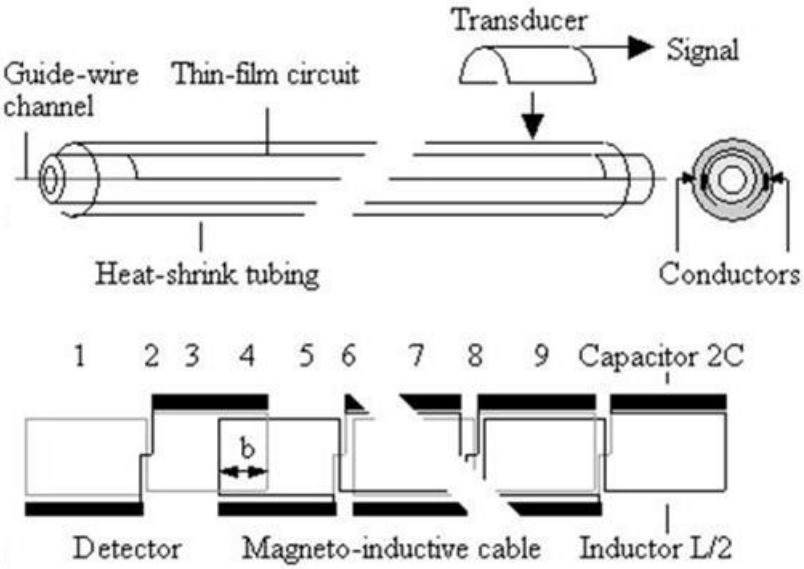

Fig. 4.4.13. Construction of the catheter-mounted receiver coil (top) and circuit board layout of figure of eight inductive loops with printed film capacitors (bottom).

The magneto-inductive output cable of the catheter has some sensitivity to MR signals, particularly in the regions adjacent to the inductive loops. This can be seen from images obtained with the catheter on top of a cuboid phantom (Fig. 4.4.14), with the alternating light and dark areas corresponding to the inductive loops and the overlapped areas respectively.

Comparative measurements between the catheter coil and a surface array coil were obtained using the same configuration as in (Fig. 4.4.10) above. The catheter coil provides a significant improvement in SNR in the surrounding region, as with the duodenoscope tip coil (Fig. 4.4.15). However, due to the smaller size and more complex

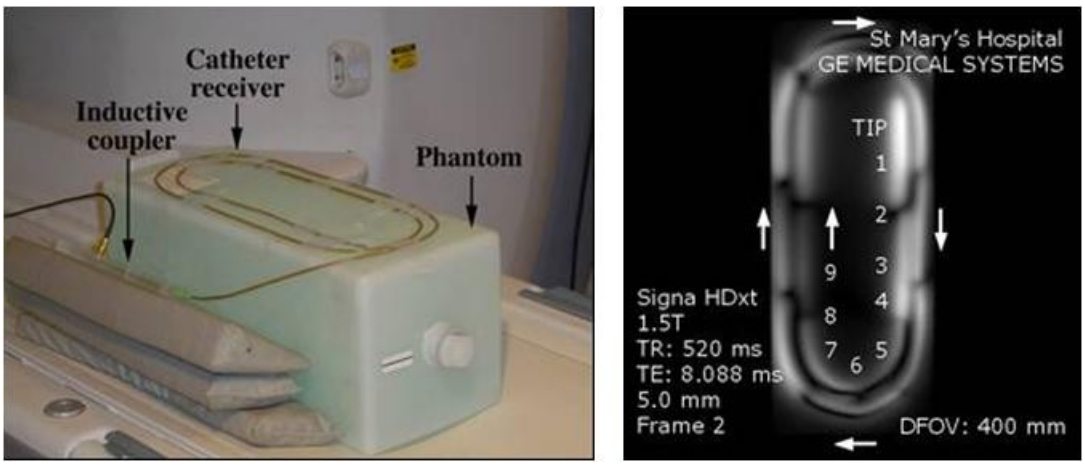

Fig. 4.4.14. Catheter coil imaging, with (l) experimental arrangement and (r) coronal MR image. The MR image labels correspond to the labels in Fig. 4.4.10 (b) above.

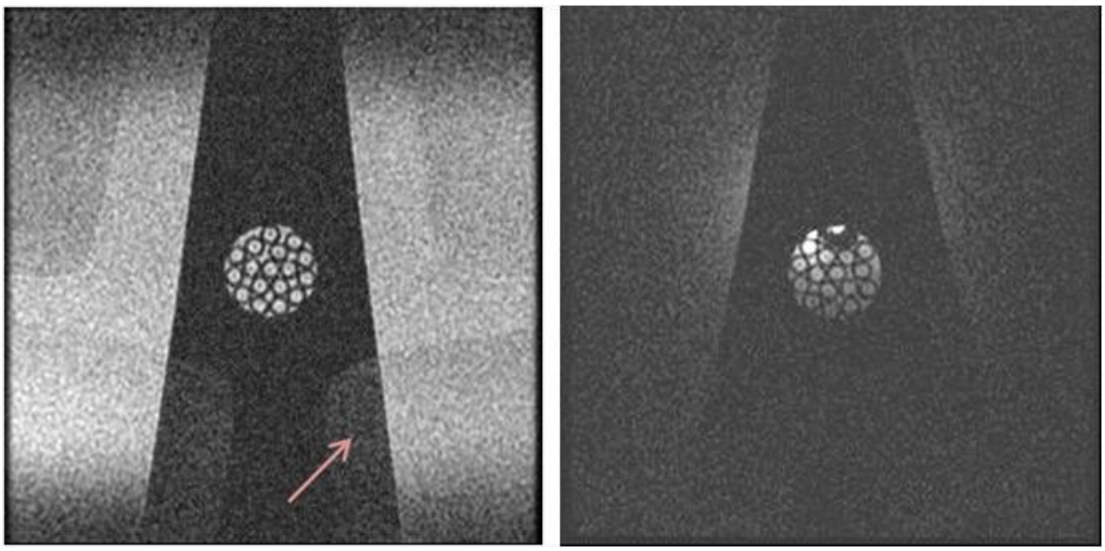

Fig. 4.4.15. Comparison of (l) surface array coil and (r) catheter coil images (80mm FOV, 4 NEX). Phase wrap is visible as ghosting in the surface coil image (arrow).

transmission arrangement this effect is less pronounced, with an SNR increase of between 25% and 50% (Table 4.4.3).

A further benefit of using internal microcoils is exhibited by the presence of phase wrap artefacts in Fig. 4.4.15. These occur when signal is produced from areas outside the field of view and therefore complicate high resolution imaging of small regions inside the body using surface coils. They are removed by a technique known as phase oversampling, which increases scan time. Due to their size, the internal microcoils detect signal only in regions immediately adjacent to them, and therefore are relatively immune to phase wrap artefacts.

Coil	FOV	NEX	Time	Av Sig	Av Noise	SNR	Ratio
Array	80	1	44 s	723.0	65.3	11.1	
Catheter	80	1	44 s	691.5	49.5	13.9	1.25
Array	80	4	2 m 49 s	610.8	32.9	18.6	
Catheter	80	4	2 m 49 s	670.5	25.6	26.2	1.40
Array	160	4	2 m 49 s	581.1	8.42	69.0	
Catheter	160	4	2 m 49 s	675.4	6.44	104.9	1.52

Table 4.4.3. Acquisition time, signal and noise results for images acquired with the surface array coil and catheter coil.

4.5 Conclusions

Existing techniques for investigation of the biliary system were introduced in this chapter, and the clinical challenges facing those techniques described. A proposed MRI-guided ERCP procedure was outlined and the benefits which it is capable of offering over existing techniques were explored. By combining the use of the MRI compatible duodenoscope and intraluminal MR receiver coils with a clinically viable and flexible system, benefits in procedural success rate and diagnostic capability are envisaged.

The MRI-guided ERCP procedure in Section 4.3 presents a novel hybrid approach to MRI-guided endoscopy which combines both manual and remotely actuated elements and takes advantage of the benefits offered by both. Previous attempts at MRI-guided endoscopy (see Section 3.5) have been purely manual operations, which resulted in a cumbersome clinical workflow.

The MRI compatible duodenoscope and intra-luminal MRI receiver coils, which are critical components of the MRI-guided ERCP procedure, have been developed under previous research projects. This chapter contains descriptions of these components and the results of experiments designed to characterise their performance.

Development and validation of an endoscope actuation system to enable MRI guided ERCP is explored in Chapter 5 and Chapter 6 of this thesis respectively, while the use of the intraluminal MR receiver coils for tracking purposes is demonstrated in Chapter 7. Demonstration of the ability of the system to enable the operator to reliably align the catheter with the correct anatomy is shown in Chapter 8.

Chapter 5

Endoscope Remote Actuation System Design

5.1 Introduction

The design of a system that enables the use of the MRI compatible duodenoscope whilst intra-operative MR images are simultaneously acquired is presented in this chapter. Without such a system the use of intra-operative MRI to cannulate and perform further investigations on the biliary tract would not be feasible, as outlined in Section 4.3.

An overview of the system is described in Section 5.2, with designs for the individual actuation modules explained in Section 5.3. Section 5.4 presents the design of a miniature pneumatic clutch that reduces the cost of the actuation modules with little significant loss of functionality. Sections 5.5, 5.6, and 5.7 describe the actuation system user interface, the control unit and the steps taken to ensure that the actuation system is compatible with the MR environment respectively.

5.2 Design Overview

The core requirement of the endoscope remote actuation system is that it enables the clinical procedure to be performed, an aspect which is explored further in Chapter 6. Section 4.4.1 described an experiment intended to characterise the expected performance required to actuate the duodenoscope during ERCP. As noted previously these results were obtained *ex vivo* and as such are not anticipated to give more than an approximate indication of the expected force and speed requirements in a clinical situation. However, these results were sufficient to guide the initial design of the actuation system.

Fig. 5.2.1 shows a schematic of the complete endoscope actuation system and how it is arranged within the MRI scanner facility. The endoscope, camera and actuation modules are placed on the scanner bed with the patient. The position of the user interface is variable, as in some circumstances the operator may want to be inside the scanner

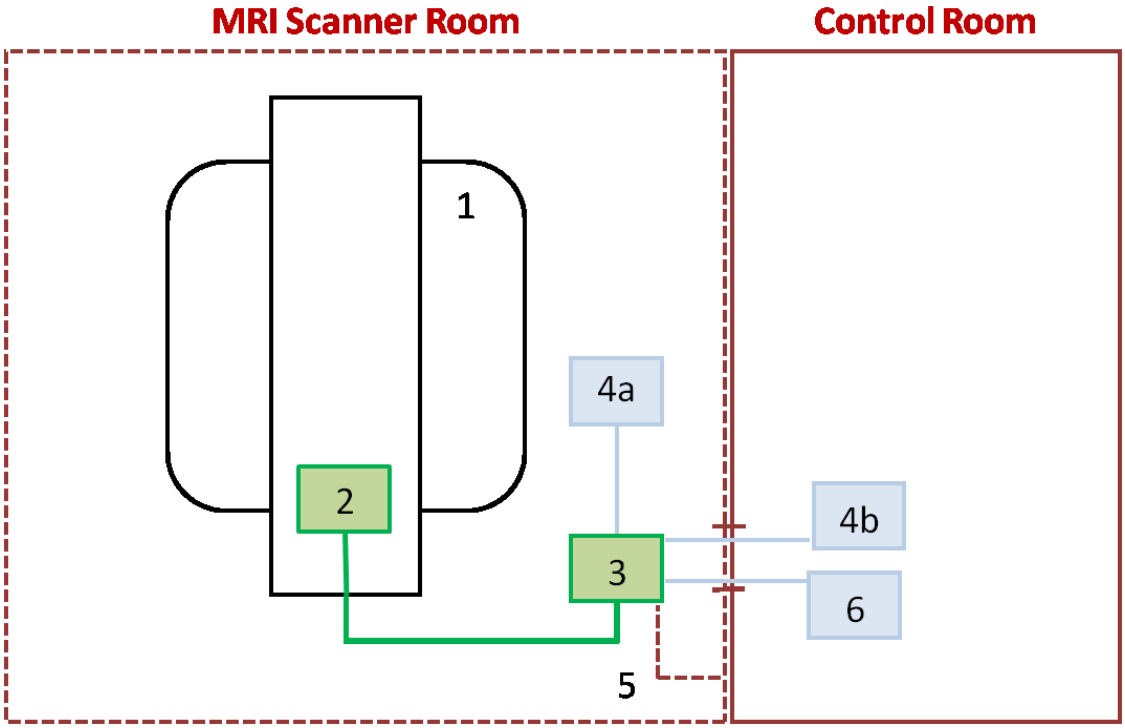

Fig. 5.2.1. Schematic of MRI compatible endoscope remote actuation system showing (1) MRI scanner, (2) Remote actuator modules, (3) Control box, (4) User input handle in either (a) the scanner room or (b) the control room, (5) Ground connection between control box and MRI scanner room shield and (6) Endoscope video visualisation device.

room and closer to the patient, whilst at other times it may be more beneficial to be in the control room to assist with visualisation and interpretation of the MR images.

The video output from the duodenoscope camera is accessed inside the control room via a filtered socket, from where it can be visualised either on screens in the control room or screens integrated into the MRI scanner room, if present. Despite presenting a potential source of EMI, the motor drivers and associated control electronics are shielded and located inside the MRI scanner room as a consequence of issues with signal filtering a

The actuation system is designed to reproduce the way in which the duodenoscope is manually operated (see Section 4.4.1) by using a modular approach, replacing the clinician's left and right hands with separate modules and providing a third module for catheter actuation. This is a flexible configuration that takes into account the challenges posed by patients of varying size and alternative MRI scanner configurations.

A prototype left hand module (see section 5.3.2) that utilised 1.5m long NiCr Bowden cables to actuate the duodenoscope tip steeping wheels was designed initially to investigate the potential of a direct actuation system. However the increase in mechanism stiffness and backlash resulting from the cables combined with the steering cables in the duodenoscope itself made the prototype unusable.

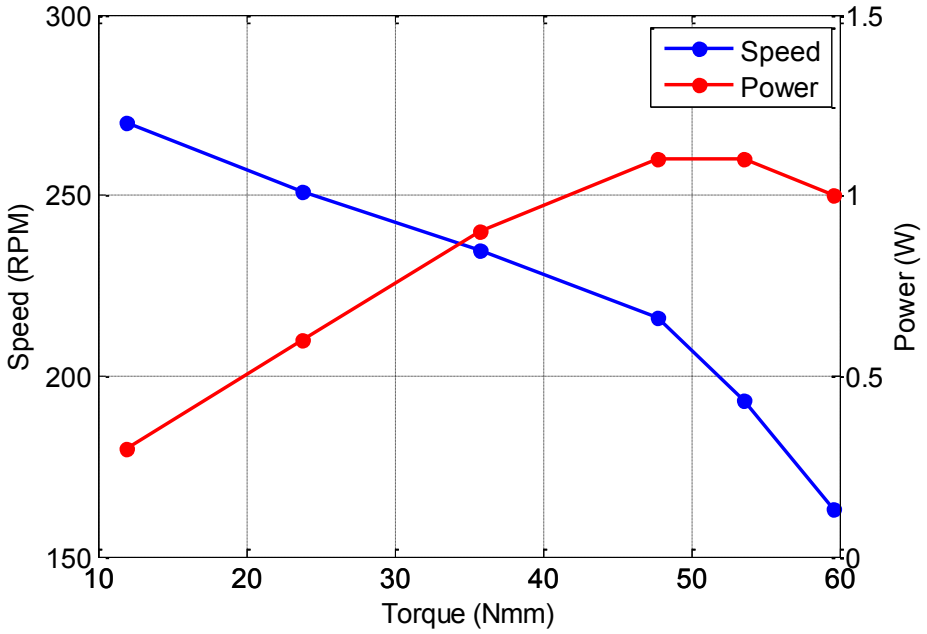

Fig. 5.2.2. Experimentally measured torque and output power curve for USR-30-NM motor at maximum input power.

Module	DOF	F/T @PP	Max F/T	Speed @ PP	Max Speed
Right Hand Module	Duodenoscope Feed	26.5 N	31.8 N	7.0 mm/s	8.9 mm/s
	Duodenoscope Twist	1400 Nmm	1680 Nmm	45.2 °/s	58.1°/s
Left Hand Module	L-R Steering Wheel	2000 Nmm	2400 Nmm	31.6 °/s	40.7°/s
	U-D Steering Wheel	2000 Nmm	2400 Nmm	31.6°/s	40.7°/s
	Bridge Lever	68.2 N	81.8 N	16.1 mm/s	20.8 mm/s
Catheter Feed Module	Catheter Feed	13.5 N	16.2 N	81.4 mm/s	105 mm/s

Table 5.2.1. Predicted output speed and force or torque (F/T) for each endoscope actuation system DOF based on gear ratios and motor performance. Maximum and peak power (PP) values shown.

For this reason, ultrasonic motors are the preferred actuation mechanism. Their high power density (Fig. 5.2.2) when compared with other methods of actuation as well as their capacity to provide accurate motion with a minimum of complexity make them superior for this application (see Section 3.2). The same motors are used for all DOF to simplify the design process (USR-30-NM, Fukoku Co. Ltd., Saitama, Japan). The small package size of these motors enables each module to be light and portable to facilitate docking.

Some of the requirements in Table 4.4.1 are not be possible to meet with the USR-30-NM motor due to a peak power (PP) limitation. Therefore, the torque transfer gearing has been selected to prioritise high force / low speed modes, taking account of the uncertainty regarding the upper limits of force required to actuate the duodenoscope in vivo (see Section 4.4.1.1) and the need for fine positioning control during the cannulation phase of the procedure.

Using the motor performance curve shown in Fig. 5.2.2, the expected maximum performance of each actuator module is shown in Table 5.2.1. This analysis does not take into account the mechanical efficiency of each mechanism – the capability of the actuation system to perform endoscopy in a realistic environment is assessed more fully in Section 6.4.

The MRI-guided ERCP procedure is by definition image-guided, hence the actuator designs presented here are designed to be open-loop controlled by an operator in full control of all DOF at all times. Feedback is supplied to the user by the duodenoscope video and intra-operative MRI. In addition, the procedure involves actuating the flexible duodenoscope and therefore precise forward-kinematic calculations are impossible without onerously extensive position sensor arrangements. For these reasons the designs presented here do not include provision for sensing the actuator position because this is derived by the operator using their experience and image guidance. This has the advantage of avoiding the introduction of rotary encoders into the MR environment, which is known to cause issues with image degradation (see Section 3.3).

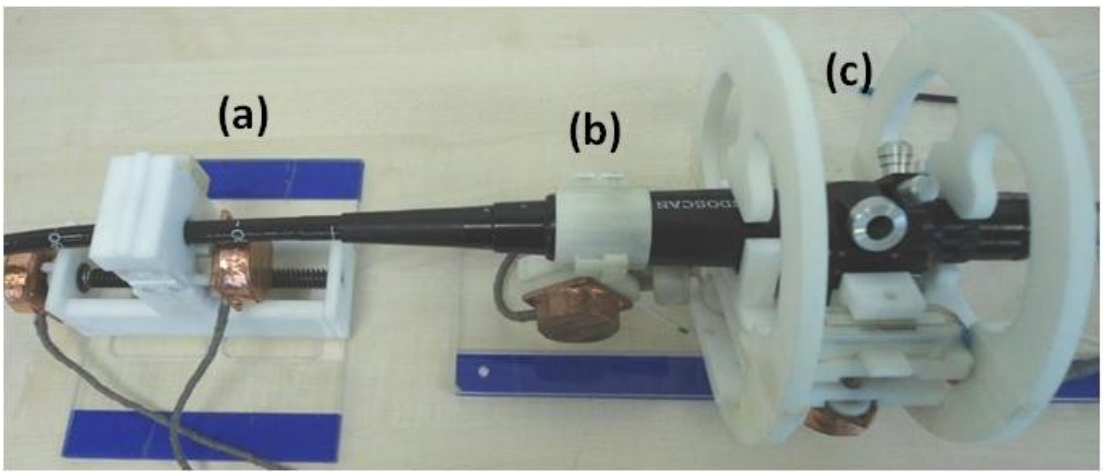

Fig. 5.3.1. Complete endoscope remote actuation modules with duodenoscope handle docked, with (a) right hand module, (B) catheter feed module and (C) left hand module shown [North, 2012].

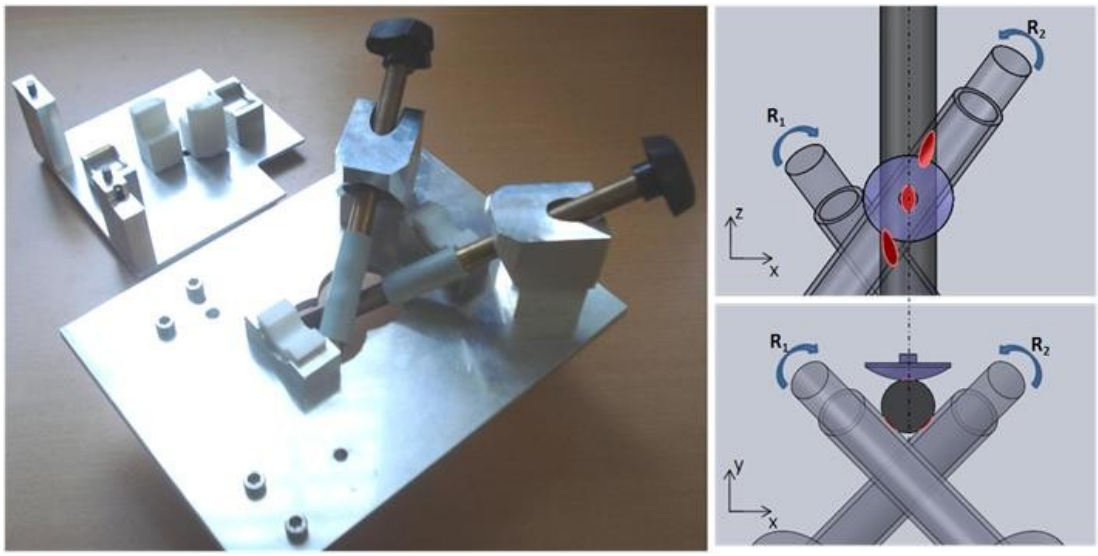

Fig. 5.3.2. Prototype right hand module based on angled friction rollers, showing (l) actuator prototype and (r) contact patches between rollers and duodenoscope.

5.3 Actuator Module Designs

5.3.1 Right Hand Module

The right hand module translates the duodenoscope flexible section into and out of the patient's mouth and rotates the flexible section. In addition, this is the only one of the three actuation modules that is to be placed in a fixed position relative to the patient and therefore all movements of the right hand module will result in movement of both the duodenoscope flexible section, the duodenoscope control handle and the attached actuator modules.

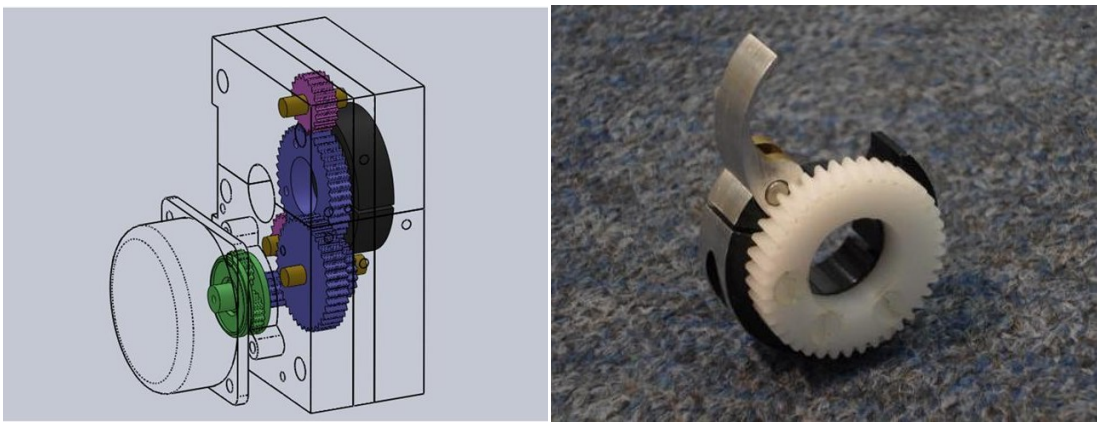

Fig. 5.3.3. Duodenoscope flexible section actuation is achieved via a quick-release collar (left) with gear attached. A dedicated motor is used to rotate the flexible section via the quick-release collar and a 3 stage gear train (right).

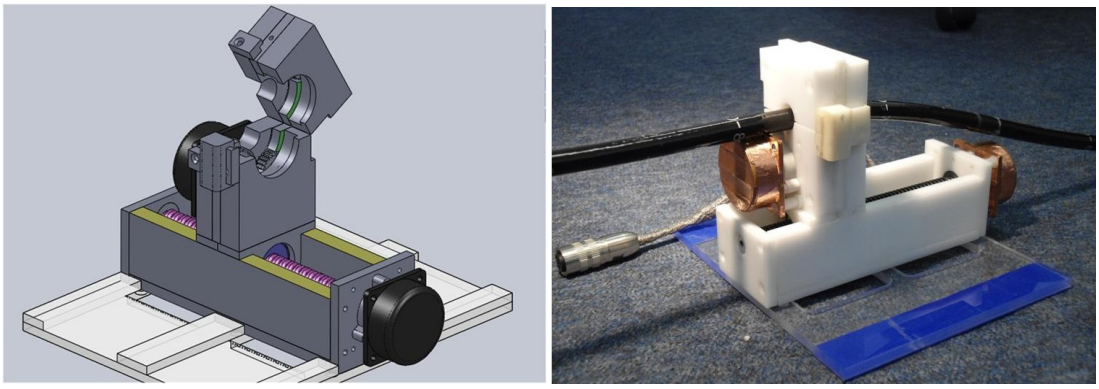

Fig. 5.3.4. A dedicated motor is used to translate the endoscope flexible section via a leadscrew (left). Prototype actuator module is shown (right).

The right hand module is placed close to the patient's mouth to minimise the unsupported length of flexible section between the actuator and the patient. This means that the point at which the module docks to the duodenoscope will vary with patient size and anatomy. In order to achieve this, an initial prototype based on differential drive from two angled rollers was constructed (Fig. 5.3.2). By driving the rollers at different speeds and directions relative to each other this design is capable of both feeding and twisting the duodenoscope flexible section. It can be docked at any point on the duodenoscope flexible section in a single movement as it does not require a locating feature.

However, the friction drive principle proved to be unsuitable for this application. The surface of the duodenoscope flexible section is designed to be very low friction, to facilitate intubation. This makes the differential friction drive very inefficient, since it requires a high clamping force to operate. In addition, load transfer was inconsistent due to small variations in surface finish and duodenoscope thickness. For these reasons, friction drive of the duodenoscope flexible section was not pursued.

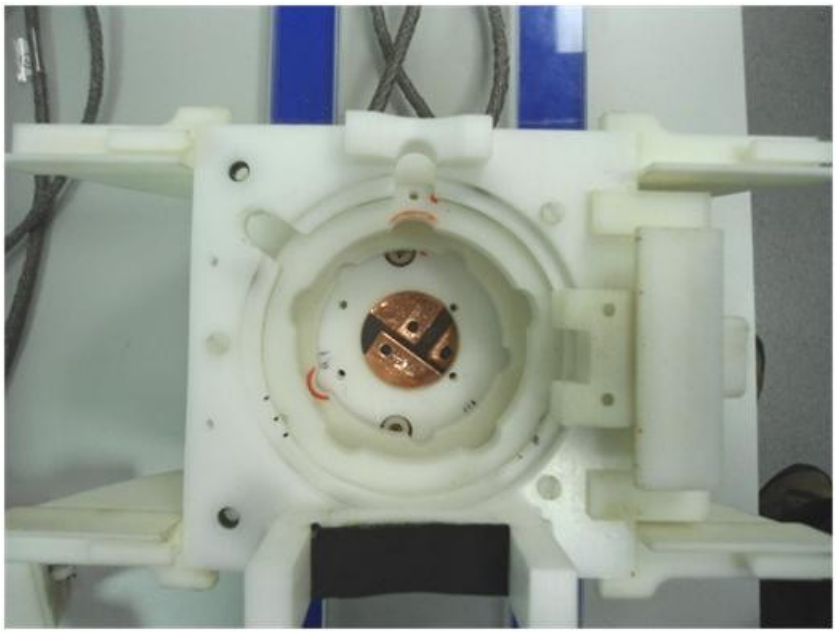

Fig.5.3.5. Top view of left hand module prototype, showing large helical gear with central cutouts for endoscope tip steering wheels

The working prototype right hand module is shown in Fig. 5.3.3 and 5.3.4. A moveable docking point is achieved by using a quick release collar that can be clamped and repositioned anywhere along the length of the flexible section. Once clamped in place, this part acts as a fixed point through which torque and translational forces can be applied to the duodenoscope.

The rotation stage consists of an ultrasonic motor-driven two-stage spur gear train with a reduction ratio of 8:1. The final stage of this is a gear attached to the quick release collar, which is mounted in the actuator module frame by an idler gear and drive gear at the bottom, with a second idler gear mounted on the hinged upper section of the frame.

The spur gear ratio was derived from measurements of the required torque on the flexible section (see Section 4.4.1.1). It became clear during initial testing that the parasitic torque caused by lifting the duodenoscope handle and left hand module (see below) meant that this reduction ratio was insufficient. To rectify this, an epicyclic gear stage with fixed annulus (reduction ratio 7:2) was added to the outside of the mechanism, giving an overall reduction ratio of 28:1.

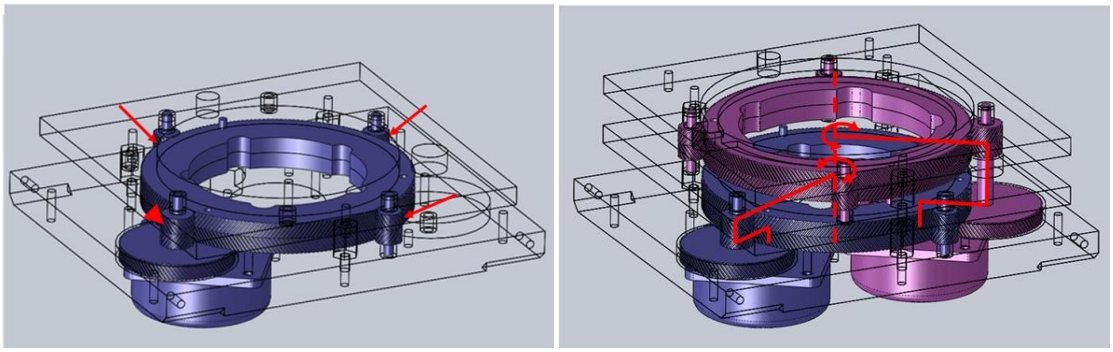

Fig. 5.3.6. Endoscope tip steering wheel drivetrains. Three idler gears (arrows, left) and a drive gear (arrowhead, left) are used to mount the large central gears concentrically. Each tip steering wheel is actuated by a dedicated motor via a two stage drivetrain (right).

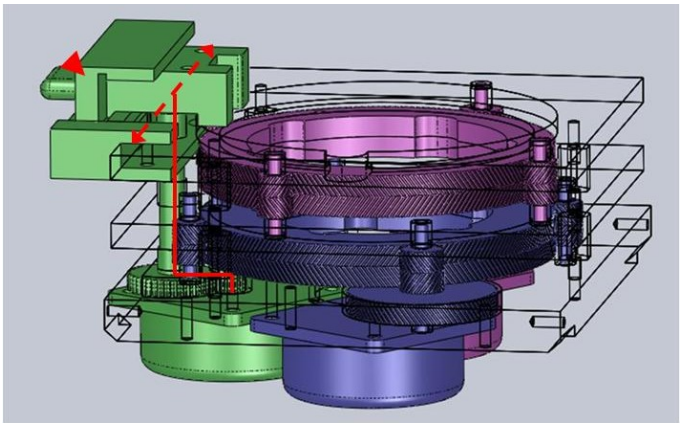

Fig.5.3.7. Left hand module design, highlighting catheter bridge deflection lever actuator drivetrain (green parts) and retractable yoke (arrowhead).

Compact and accurate translation of the flexible section is achieved by a leadscrew (3° lead angle, 12mm PCD) driven by a separate ultrasonic motor. The frame that supports the motor and leadscrew acts as a linear slide for the rotation stage (yellow areas in Fig. 5.3.4 left). Translational force is applied to the quick release collar by the rotation stage frame inner surfaces (green areas in Fig. 5.3.3 left). The right hand module is mounted on a wide base plate with slots to allow it to be strapped to the MRI scanner bed (Fig. 5.3.4 right).

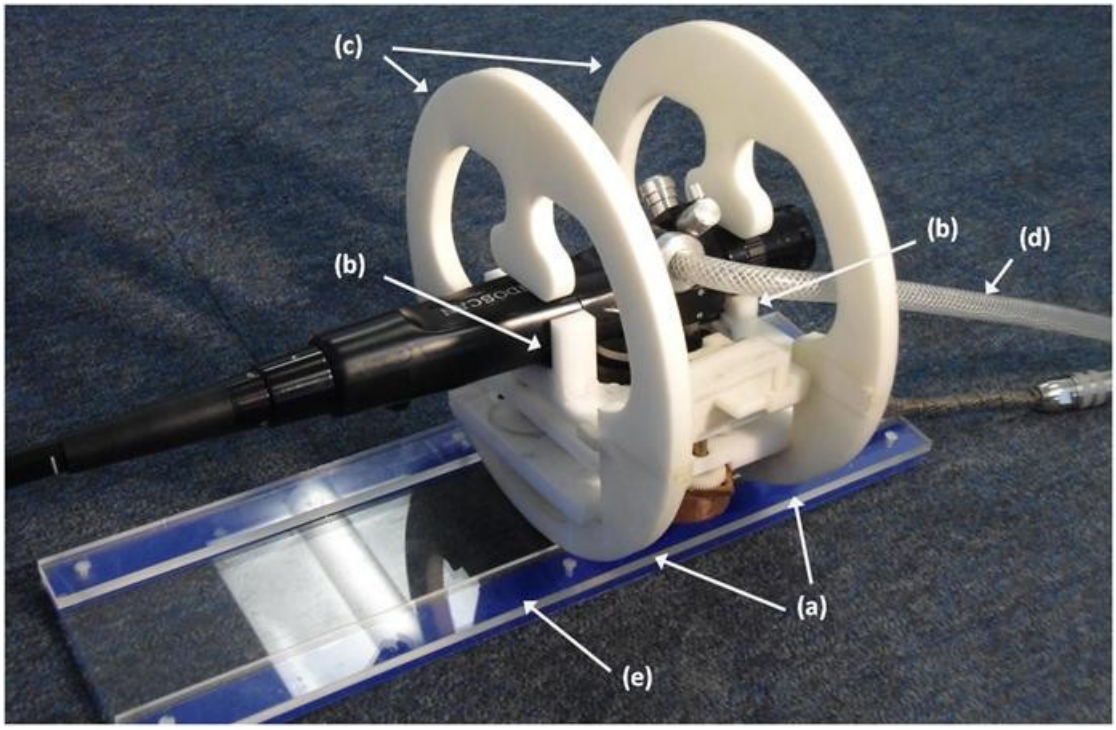

Fig. 5.3.8. Left hand module prototype showing (a) lower circular housing, (b) contact points between duodenoscope handle and actuator module, (c) upper, removable circular housing parts and (d) duodenoscope umbilical.

5.3.2 Left-Hand Module

The left hand module actuates the controls that are present on the duodenoscope handle – the two steering wheels to control the tip steering and the lever to control the catheter deflection bridge. Each degree of freedom is independently actuated by an ultrasonic motor. The handle and left hand module are moved passively by translation and rotation of the duodenoscope flexible section by the right hand module and therefore must be able to slide and rotate without actuating any of the duodenoscope handle controls. To avoid excessive parasitic load on the right hand module, the left hand module has to be as compact and light as possible.

Each tip steering wheel is rotated by a large double helical gear with a central cutout. The steering wheel fits inside the cutout and is driven by a two-stage gear train (total reduction ratio of 40:1) on the outside of the large helical gear (Fig.5.3.5). The large helical gears are supported by three small idler gears, which along with the driving gear eliminate the need to mount the large central gears on shafts and results in a significant size reduction (Fig. 5.3.6). The double helical tooth shape means that the large gears float within the module frame, which reduces the drivetrain friction. There is a pin on each

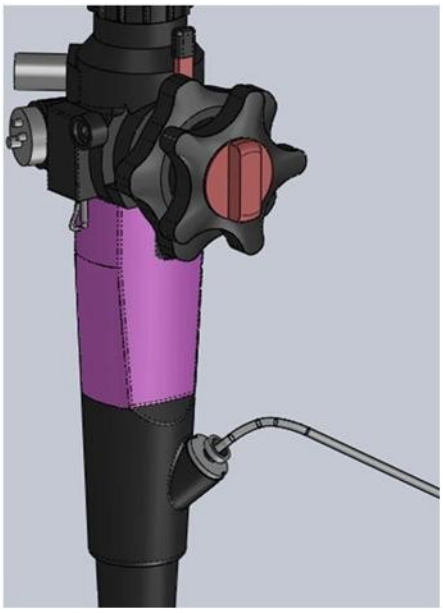

Fig. 5.3.9. Duodenoscope handle prior to docking, with region covered by operator's left hand shown in magenta.

large central gear that prevents the gear from being rotated past the duodenoscope's limit of travel and damaging the duodenoscope tip steering mechanism.

The catheter deflection lever is rotated by a sliding yoke mounted on the side of the module (Fig.5.3.7). The yoke forms a prismatic joint with the end of the lever and is driven by a rack and pinion spur gear train (reduction ratio 3:1). To facilitate docking, the yoke can be retracted from the duodenoscope handle, which simultaneously moves the yoke clear of the lever and disengages the rack and pinion so that the yoke can slide to a new position.

During the docking phase of the procedure the duodenoscope handle could be at a range of angles to the patient bed, depending on the patient's position and anatomy. For this reason the left handle module has a circular housing that enables it to be placed on the patient's bed in any orientation. The duodenoscope handle is held in place both by fixed contact points mounted on the module frame and removable parts that complete the circular housing (Fig. 5.3.8). The removable parts contain cutouts to allow the duodenoscope umbilical and light guide to be routed through the circular housing. Once docked, the module is placed on a baseplate on the patient's bed that allows it to slide and rotate passively when moved by the right hand module.

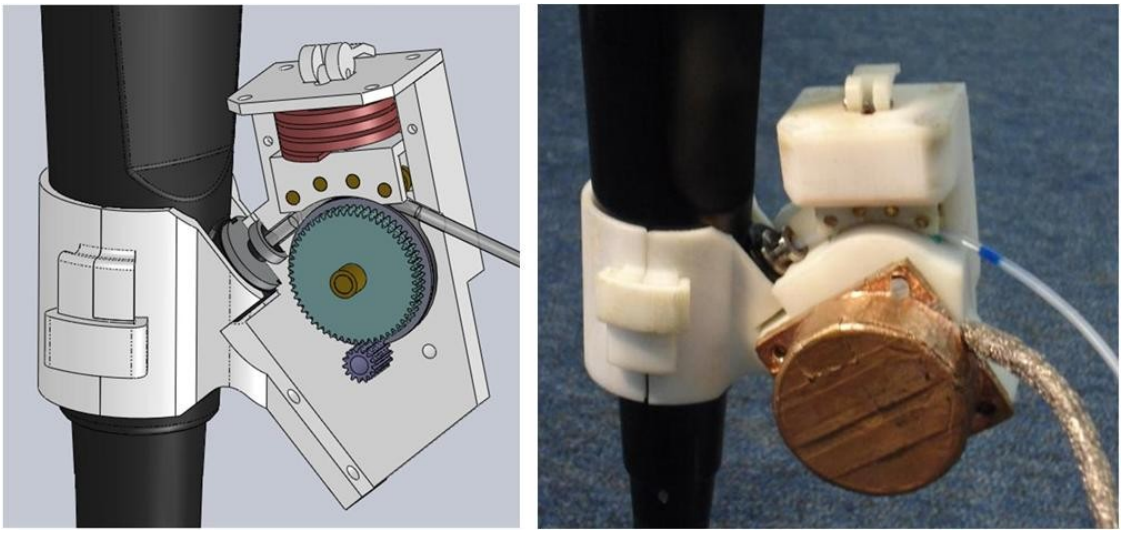

Fig. 5.3.10. Catheter feed module showing internal load transfer parts and geartrain (left) and prototype mounted on duodenoscope handle (right).

5.3.3 Catheter Feed Module

The catheter feed module drives the catheter into and out of the duodenoscope control handle. It has two docking points – one to the duodenoscope and one to the catheter. The module is designed to be docked to the duodenoscope handle relatively early in the procedure, enabling the left hand module to be docked afterwards. This means that the module has to be clear of the operator's left hand (pink area in Fig 5.3.9) when docked to the handle. The module is attached to the handle using a hinged clamp (Fig. 5.3.10) which locates on the moulded part of the duodenoscope handle and the end of the biopsy port.

A wide variety of catheters and tools may be used with the catheter feed module, all of which must be driven from a single point for relatively long distances and must be unaltered by the driving process. Therefore the most suitable method of actuation is friction drive. Due to spatial constraints the mechanism has a single drive pulley and a sprung passive follower to provide the normal load on the catheter. The follower can be retracted, and the catheter released, by lifting the cam on top of the mechanism. The pulley is driven by an ultrasonic motor via a spur gear train with a reduction ratio of 4:1.

Friction drive of the catheter is a challenge due to two factors: the relatively low crush strength of the hollow tube structure and the material used to manufacture the catheter. A simple crush strength test on a commercially available 8 Fr (2.7mm diameter) catheter (Boston Scientific, Boston, MA, USA) suggested that the catheter could withstand a 10.8kg load applied over a 5mm length before being damaged.

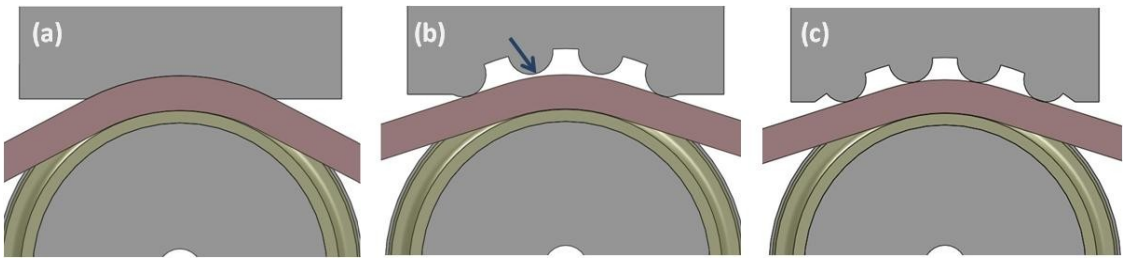

Fig. 5.3.11. Catheter follower designs (a) solid, (b) with cutouts to reduce parasitic friction but without taking into account the force required to deflect the catheter, and (c) final configuration.

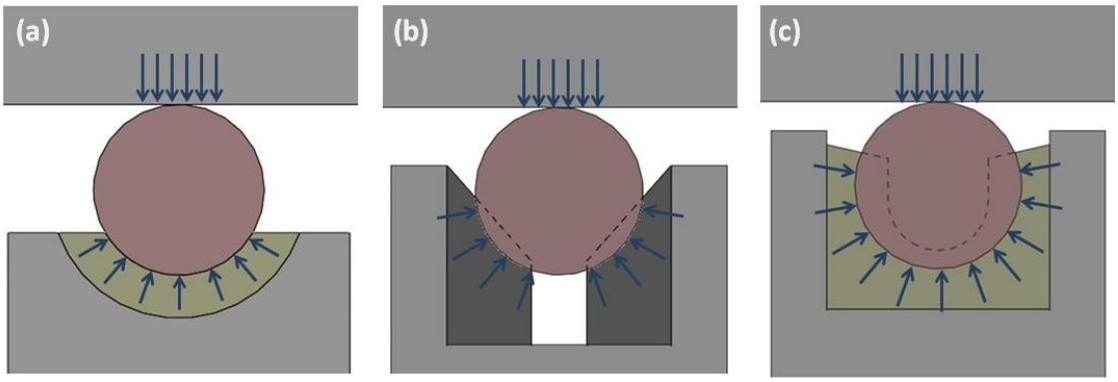

Fig. 5.3.12. Catheter feed pulley friction coating, with arrows indicating direction of force applied to catheter.

This limitation is compounded by the fact that catheters have to be made from a material suitable for use inside the body and they are designed to be easy to push along the length of the endoscope. A material commonly used for catheters is PTFE, which has a very low friction coefficient and is biocompatible. The coefficient of friction limitation means that the friction drive must be designed to spread the normal load on the catheter as much as possible to avoid crushing the catheter.

The follower contact surface is curved to spread the load over $^1/_6$ of the pulley's circumference (approx 16mm). The initial design (Fig. 5.3.11 a) incorporated a solid follower but this greatly increased the parasitic friction between the follower and catheter. It was replaced with a follower with just four contact points. The force required to bend the catheter to the pulley radius has to be taken into account by putting the contact points at either end on a larger pitch circle, otherwise the catheter tends to push the follower upwards and lift itself away from the pulley (Fig. 5.3.11 b).

The profile of the pulley and friction coating was developed to maximise the transmission of torque to the catheter via friction, but also provide enough lateral stability to keep the catheter within the mechanism (Fig. 5.3.12). The catheter experiences

Coating Material	Hardness	Pulley shape (Fig. 5.3.12)	Maximum Dynamic Friction Drive Force (N)
Synthetic Rubber (Plasti-Dip)	Shore A 70	(a)	0.75
Neoprene Rubber	IHRD 60°	(b)	2.0
Silicone Rubber (SuperSil 25)	Shore A 25	(c)	11.2
Silicone Rubber (Platsil 7315)	Shore A 15	(c)	9.6

Table 5.3.1. Maximum driving force of catheter feed module with different pulley friction coatings. Synthetic rubber was supplied by Plasti-Dip Ltd, UK while the silicone rubbers were from Mouldlife UK Ltd.

additional normal force due to the deformation of the friction material on either side, increasing the driving friction contact.

The friction coating was chosen to be soft enough to adequately spread the normal load along a length of catheter, whilst also being hard enough to exert sufficient normal force on the catheter when compressed. Table 5.3.1 shows the friction drive force generated by different coating materials, when tested with a standard catheter and follower as described above and a spring force of 25N. Due to manufacturing limitations not all combinations of pulley shape and material were tested. The softer silicone rubbers perform better due to improved load spreading- since they are also mouldable it is possible to create the more complex shapes that offer the benefits described above. The softer silicone rubber appears to be too soft and therefore unable to provide as much additional normal force from compression.

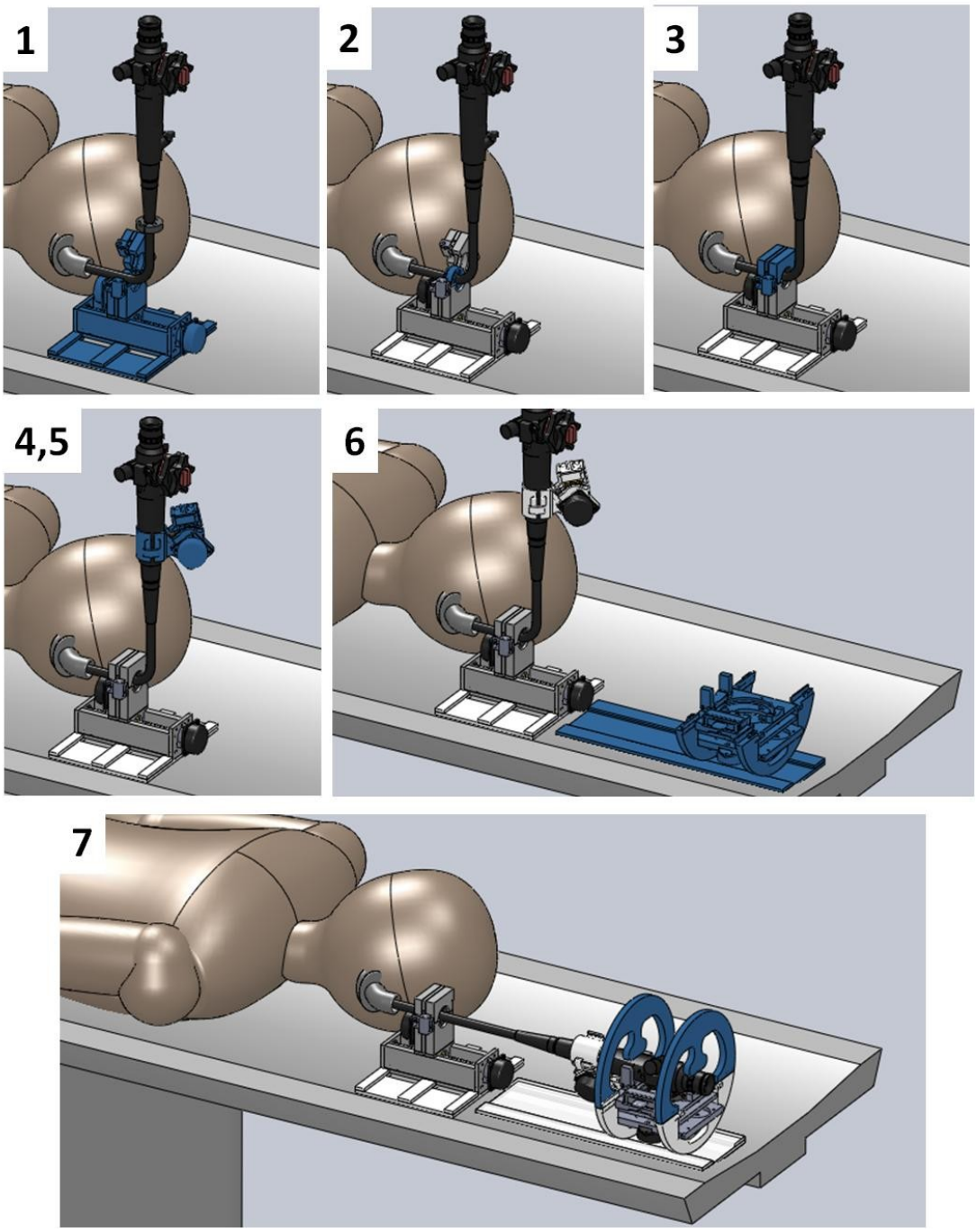

Fig. 5.3.13. Endoscope remote actuation system docking procedure. The action performed in each step is highlighted blue.

5.3.4 Docking Procedure

Docking of the duodenoscope to the actuator modules is performed in the following sequence (Fig. 5.3.13). The operator's left hand will remain holding the duodenoscope handle to maintain control over all movement until the duodenoscope is fully docked.

1. Position right hand module and strap to scanner bed

2. Position quick release clamp on endoscope flexible section
3. Place clamp into right hand module and clip together
4. Dock catheter feed module (with follower up) onto endoscope handle
5. Position catheter on pulley and release catheter feed follower
6. Position left hand module and base plate on scanner bed
7. Dock handle into left hand module and attach circular clamps

The docking procedure requires positioning all three modules; however the undocking procedure, which may need to be performed rapidly in the event of an emergency, is considerably shorter. To undock, the operator must reverse only steps 7, 5 and 3 in that order. This will leave the left hand and right hand modules on the patient's bed and the catheter feed module attached to the duodenoscope, but will allow the operator to manually actuate all degrees of freedom.

5.4 Miniature Pneumatic Clutch

The endoscope remote actuation system modules presented in Section 5.3 utilises a total of 6 ultrasonic motors; one to actuate each DOF. MRI compatible actuators are generally much more expensive than their standard equivalents – typically the USR-30-NM costs up to US$2500 per unit, including motor driver and cabling.

The requirement for precise movements encourages users to use only a limited subset of the duodenoscope controls at a time. Testing using a synthetic biliary cannulation simulator (see Section 6.4) confirmed this hypothesis – analysis of six simulated cannulations using the endoscope remote actuation system suggested that at no time was more than one DOF from each module activated (Fig. 5.4.1).

A low cost MRI compatible clutch device, which allows multiple DOF to be actuated by a single motor, was developed to take advantage of this result. This allows significant cost savings to be achieved without compromising functionality. The clutch operates with long pneumatic hoses, allowing the control valves to be placed away from the scanner bore in the shielded control box (Section 5.6), and is manufactured entirely from materials suitable for use in the MR environment.

5.4.1 Design Requirements

The following requirements were used to guide the design process:

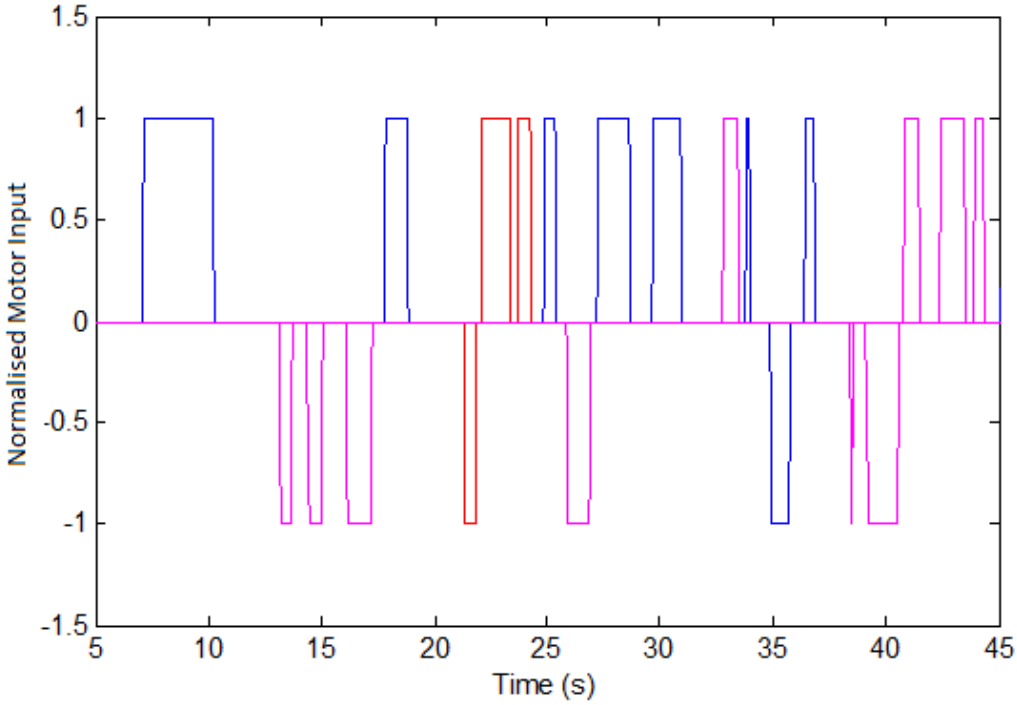

Fig. 5.4.1. Excerpt from time series of control inputs during simulated biliary cannulation (see Section 6.4). Positive and negative motor inputs correspond to clockwise and counter-clockwise motion respectively. Each coloured line represents one motor input.

- *Load Transfer.* The clutch is designed to transmit torque from the USR-30-NM motor, which is capable of transmitting up to approximately 50 Nmm of torque (Fig. 5.2.3). The clutch must be able to transfer at least this amount of torque to make use of the full capacity of the motor.

- *Response Time.* The time taken to engage and disengage the clutch should not force the operator to wait before they complete a desired movement. Therefore the clutch response time target is equal to the time taken for the motor to activate, which for the USR-30-NM motor is 50ms [Shinsei, 2005].

- *Package Size.* Devices for use within the MRI scanner must take into account the extremely limited workspace. The pneumatic clutch will replace at dedicated motor for each degree of freedom, and given that there are likely to be additional drive-train components required to incorporate the clutch, it is desirable for the clutch to be smaller than the equivalent motor. The USR30-NM motor is 43 mm x 43 mm x 18 mm (plus a 10 mm long driveshaft), while for comparison a typical electromagnetic clutch (SL08, Huco, Hertford, UK) is 23 mm x 23 mm x 38 mm.

- *Low Pressure Operation.* Most MRI facilities have a supply of pressurised air which could be used for actuation of the clutch. Due to safety concerns this is usually regulated to a low pressure (which varies with facility), so the operation pressure of the pneumatic clutch must be low enough to cope with this. In addition, operation at low pressure is desirable because actuation pressure contributes to the parasitic torque generated by the clutch (see below).

- *MRI Compatibility.* As with all devices introduced into the MR environment, the pneumatic clutch must be MR safe – this mean that the clutch must not experience any dangerous forces due to the magnetic field or any excessive heating due to gradient switching or RF excitation. In addition, the clutch must be MRI compatible and therefore not degrade the images by introducing electromagnetic interference.

5.4.2 Clutch Theory

For a pneumatic friction clutch there is a direct relationship between the maximum torque that can be transferred and the size of the clutch. The torque transfer for a single friction plate can be calculated using the following equation [Rahnejat, 2010]:

$$T = \frac{\mu \times F_N \times \left[D_o^3 - D_i^3\right]}{3 \times \left[D_o^2 - D_i^2\right]}$$

(Eq. 5.1)

Where F_N is the net normal force acting on the plate, □ is the coefficient of friction between the plates, D_o is the outer diameter of the friction plate and D_i is the inner diameter of the friction plate. F_N is supplied by the pressurised pneumatic actuator, minus the force required to overcome the actuator return spring (if present) and the force required to overcome internal stresses in the actuator:

$$F_N = F_P - F_{RS} - F_{act}$$
$$F_N = [p \times A] - \left[k \times \left(l_f - l_e\right)\right] - F_{act}$$

(Eq. 5.2)

Where p is the applied pressure, A is the area of the actuator in contact with the friction plate, k is the constant of the return spring, l_f is the free length of the return spring and l_e

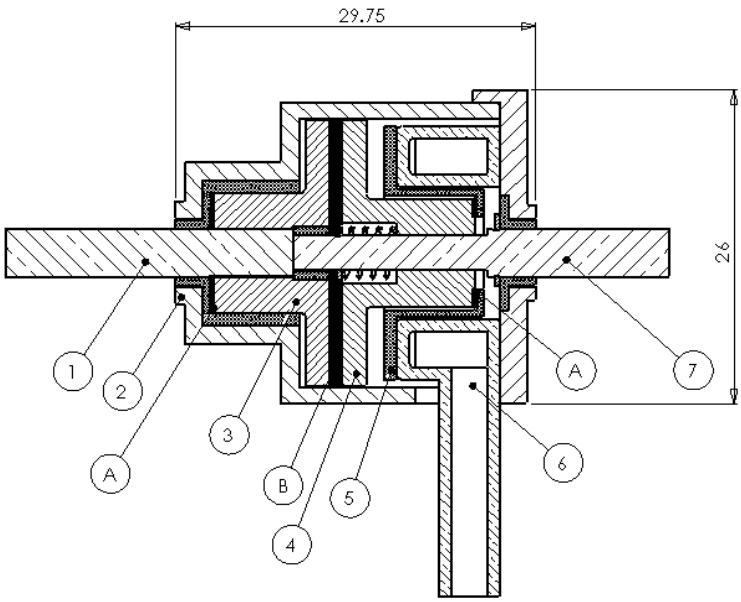

Fig. 5.4.2. Cross-sectional drawing of miniature pneumatic clutch showing 1) Input shaft; 2) Casing; 3) Input Friction Plate; 4) Output Friction Plate; 5) Load Transfer Plate; 6) Pneumatic Actuator; 7) Output Shaft. The parasitic friction contacts (A) and contact between the friction plates (B) are shown. Dimensions are in mm.

is the length of the spring when the plates are engaged. F_{act} will vary depending on the type of actuator used and could encompass elastic deformation, as well as an effective reduction in cross-sectional area due to poor contact between the actuator and load transfer plate. (Eq. 5.1) can also be used to calculate parasitic torque caused by contact between rotating and static plates, using the relevant diameter and coefficient of friction for the contact points.

The efficiency of the clutch can be defined as:

$$\eta = \frac{T_{out}}{T_{motor}} = \frac{T_{out}}{T_{out} + T_{parasitic}}$$

(Eq. 5.3)

Where T_{out} is the output torque of the clutch, T_{motor} is the torque supplied by the motor and $T_{parasitic}$ is the parasitic torque in the clutch. From (Eq. 5.1) and (Eq. 5.2) it can be seen that $T_{parasitic}$ rises with pneumatic pressure, so in order to maximise efficiency the actuation pressure must be minimised whilst still providing enough force on the friction plates to transmit the necessary T_{out}. For simplicity the actuation pressure will normally be set prior to operation and the valve operated simply in on/off mode, although active pressure control could be achieved with output motion sensors and proportional pneumatic control valves.

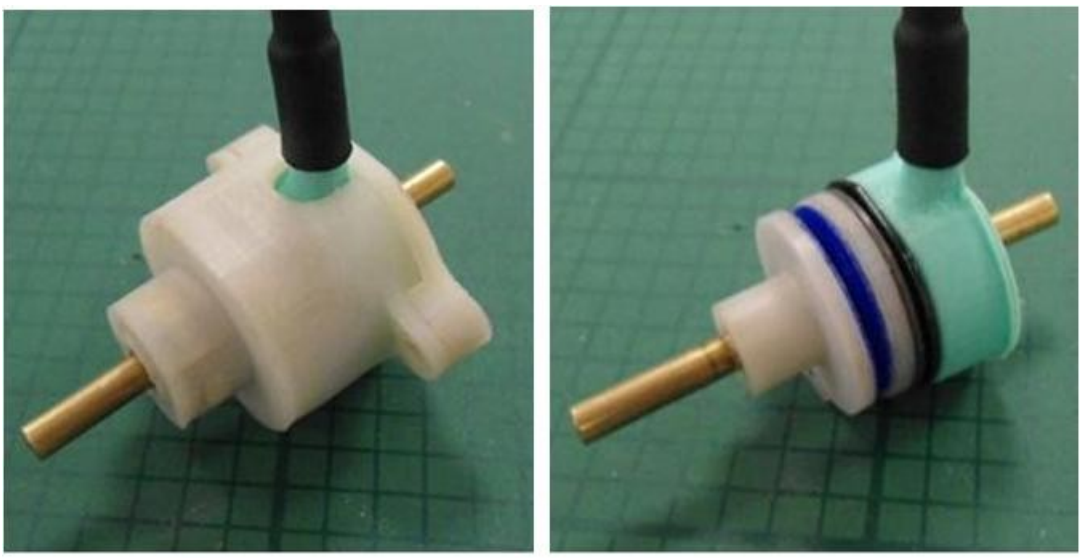

Fig. 5.4.3. Prototype clutch, with (l) and without (r) outer casing.

5.4.3 Prototype Design

For a given clutch package size a key challenge with the design is to maximise the area of the pneumatic actuator and the diameter of the friction plate. The coefficient of friction of the plates must also be maximised. Management of the contact points between rotating and static parts is also important, as these contacts contribute to parasitic friction when the clutch is engaged.

The prototype pneumatic clutch is shown in Fig. 5.4.2 and Fig. 5.4.3. The concentric design of pneumatic actuator and friction plate makes for a compact overall package size whilst maximising the available actuator area. In addition, the design provides for internal bearing surfaces to minimise parasitic torque and allow in-line mounting without external bearings.

Alternative designs based on plates with extruded engagement features were considered (Fig. 5.4.4), but despite presenting a benefit in terms of torque transferred per unit pressure, the additional travel required to engage these plates put an unacceptable strain on the pneumatic actuator (see below) and significantly increased the clutch response time. As a result, the single, flat friction plate design was preferred.

In order to maximise the coefficient of friction between the two plates, both have a non-slip polymer coating bonded to the mating surface (Dycem Ltd, Bristol, UK). This material has a coefficient of friction of up to 2.5 depending on conditions. Two material variants were investigated – material A has a degree of compressibility which improves

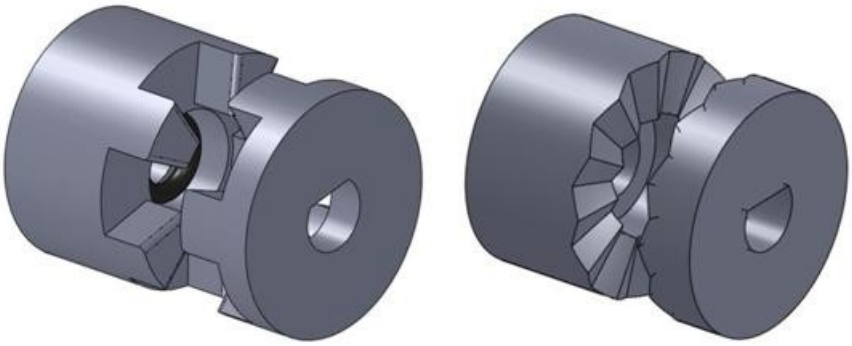

Fig. 5.4.4. Alternatives to flat friction plate design, with crenellations at 90° (l) and 35° (r).

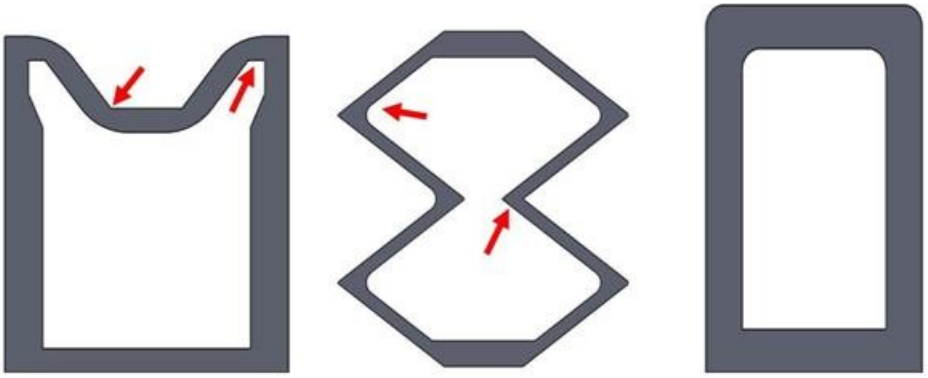

Fig. 5.4.5. Alternative pneumatic actuator designs. Two designs (left and middle) are intended to preferentially expand in one direction when inflated, which causes particular stress on the areas arrowed. The third (right) is moulded oversized and is compressed on assembly. Wall thicknesses in these sketches are indicative – multiple variants of all designs were tested.

load spreading across the plate in the presence of unevenness, while material B is solid and therefore tougher.

During the initial design phase of the pneumatic actuator several designs and manufacturing methods were investigated. Initially convoluted shapes, which are intended to preferentially expand in one direction when inflated, were used (Fig. 5.4.5). These were manufactured from cast latex and silicone rubbers using a two stage moulding process, as well as being printed from a rubber-like material using a rapid prototyping machine (Connex Objet 500, Stratasys, MN, USA).

For all manufacturing methods the convoluted pneumatic actuators proved not to be durable enough for further testing. The rubber casting method proved to be unable to produce actuators with consistent wall thicknesses, and consequently the actuators rapidly failed around the areas of highest elongation (arrowed in Fig. 5.4.5). Due to the laminar printing process, the rapid prototyped actuators also proved unable to withstand repeated inflations and failed in the same areas.

These results lead to the use of the unconvoluted balloon shape shown. The balloon is sized so that when deflated and inserted into the assembly it is compressed in the axial direction by the output plate return spring. Inflation causes it to return to it's original shape and engage the friction plates without significant elastic deformation of any part of the balloon. This limits the maximum travel of the actuator, but reduces strain on the balloon and improves it's durability. The balloon is constrained by the casing and load transfer plate so that it expands only in the axial direction against the return spring. A cast silicone rubber (Transil Gel 20, Mouldlife Ltd, Suffolk, UK), was used for the balloon, with a PVC tube bonded for inflation (Fig. 5.4.3).

There are two contact areas that contribute to the parasitic torque of the mechanism (labelled 'A' in Fig. 5.4.2). The load transfer plate is prevented from rotating by the casing and is in contact with the output friction plate in a small area near the output shaft. This contact acts as a load against the driving motor as well as the friction plates, meaning it reduces both the efficiency and the slip torque of the mechanism. When the clutch is actuated the input plate is pushed into contact with the casing - parasitic friction from this contact is managed by a thrust bearing. This contact acts as a load on the driving motor but does not limit the mechanism slip torque.

5.4.4 Performance Testing

The pneumatic actuator was characterised by mounting it against a force sensor and inflating it with a gas pressure varying from 0.4 to 0.8 bar. The pneumatic actuator was constrained by the clutch casing and load transfer plate and was positioned so that it deflected 1 mm before contacting the force sensor to reproduce the actuator position within the clutch.

Clutch performance was assessed using the test rig shown in Fig. 5.4.6. The rig is driven by an ultrasonic motor (USR-60-E, Fukoku Co. Ltd., Saitama, Japan) and includes an optical encoder to determine output speed and a pair of force sensors connected to a 45 mm diameter pulley via a friction belt to apply and measure dynamic torque. The clutch was controlled by a solenoid valve with a maximum flow rate of 393 Nl/min. Motor control, valve activation and data collection were performed by a programmable microcontroller (Arduino Mega 2560) and custom interface (LabView, National Instruments, TX, USA).

The parasitic torque of the clutch mechanism was assessed by disconnecting the motor and determining the pneumatic actuation pressure at which a known weight applied to the pulley could be balanced by the clutch alone.

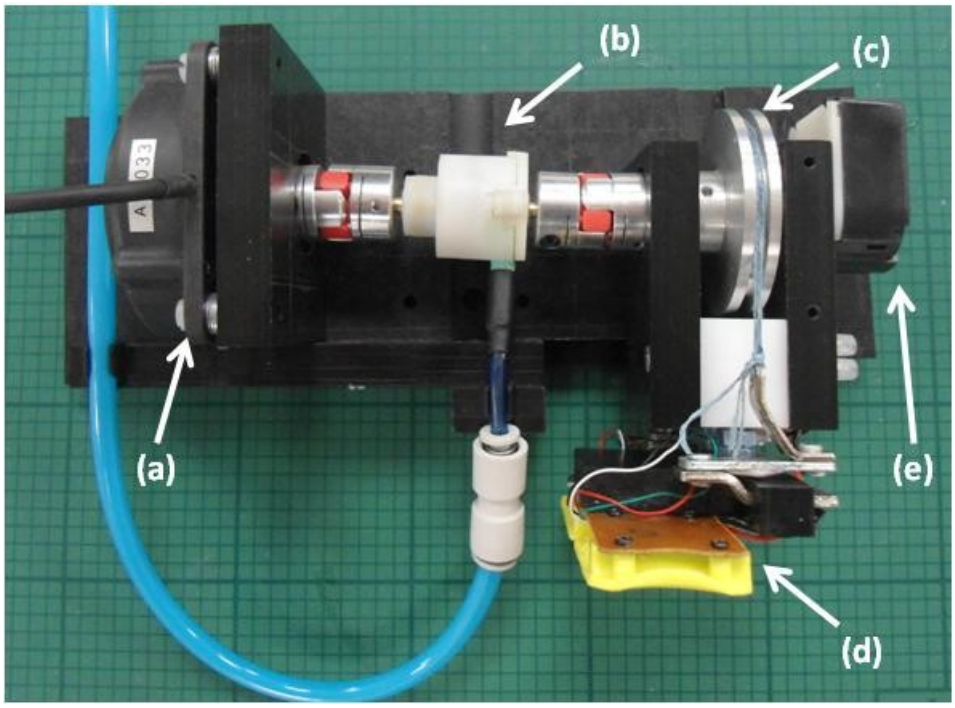

Fig. 5.4.6. Clutch performance testing rig, showing (a) motor; (b) clutch, (c) pulley with friction belt; (d) force sensors and (e) optical encoder.

The time taken for the clutch to engage and disengage was measured by running a microprocessor sequence which first activated the motor and then activated the pneumatic valve. The time between the valve activation command and the first movement of the optical encoder was taken to be the activation time of the clutch. The sequence was repeated in reverse, with the valve deactivated and the time taken for the encoder to stop moving recorded as the clutch deactivation time. This test was repeated with gas pressures varying from 40 to 80 kPa and with hose lengths (between the valve and clutch) varying from 0.4 to 6 m. In all cases the hose ID was 4 mm.

The clutch torque transfer limit was assessed by activating the pneumatic valve and then the motor before incrementally increasing the tension on the friction belt until the clutch was unable to transfer the torque and the output plate slipped relative to the input plate. At the point of slipping, the two force sensor readings were recorded and the difference between them multiplied by the pulley radius to calculate the slip torque. This test was repeated with gas pressures varying from 40 to 80 kPa.

Durability testing of the pneumatic clutch was performed by first applying a level of preload on the friction belt corresponding to 50 Nmm of torque and setting the activation pressure to 70 kPa. The valve and motor were then activated simultaneously and allowed to run for 1s, before being deactivated simultaneously. This cycle was

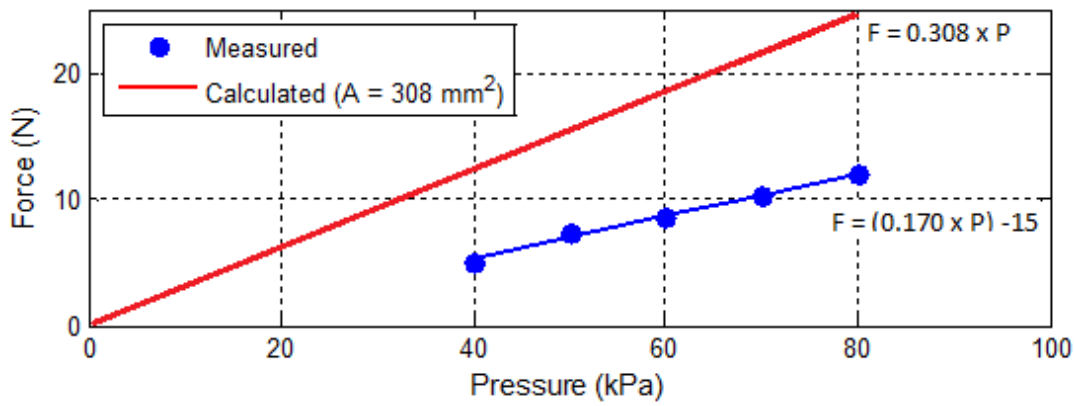

Fig. 5.4.7. Chart showing calculated pneumatic force using A = 308mm² (the cross-sectional area available for the balloon), compared with measured pneumatic actuator output force.

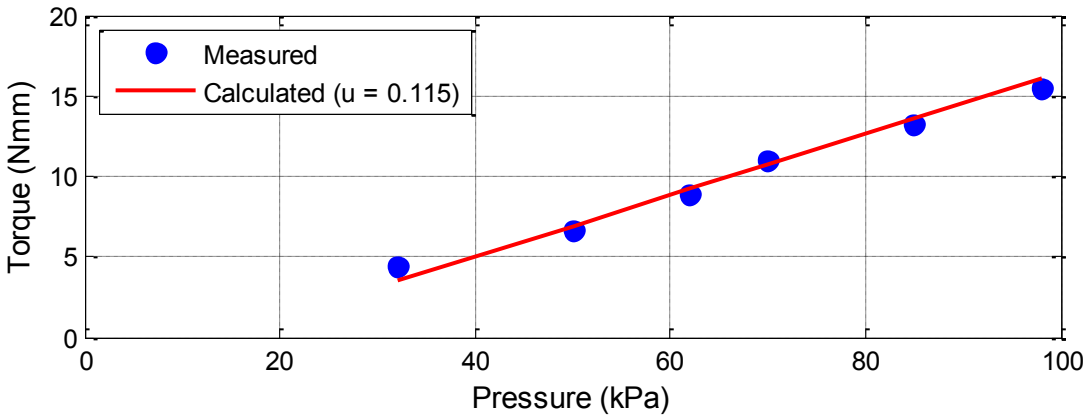

Fig. 5.4.8. Chart showing parasitic torque calculated using = 0.115 compared with experimentally measured parasitic torque.

repeated, and approximately every 500-1000 cycles the pressure was reduced to determine the point at which the clutch was unable to transfer 50 Nmm of torque.

5.4.5 Results

Fig. 5.4.7 shows the relationship between actuation pressure, calculated pneumatic force (based on the available cross-sectional area for the balloon) and measured actuator output force. Losses in the pneumatic actuator (F_{act} in Eq. 2) amount to a constant output force reduction of approximately 1.5 N due to the force required to elastically deform the balloon and limited utilisation of the effective contact area (170 mm² of a possible 308 mm²).

The measured total parasitic torque of the clutch is shown as a function of input pressure in Fig. 5.4.8. This is displayed alongside the expected parasitic torque calculated

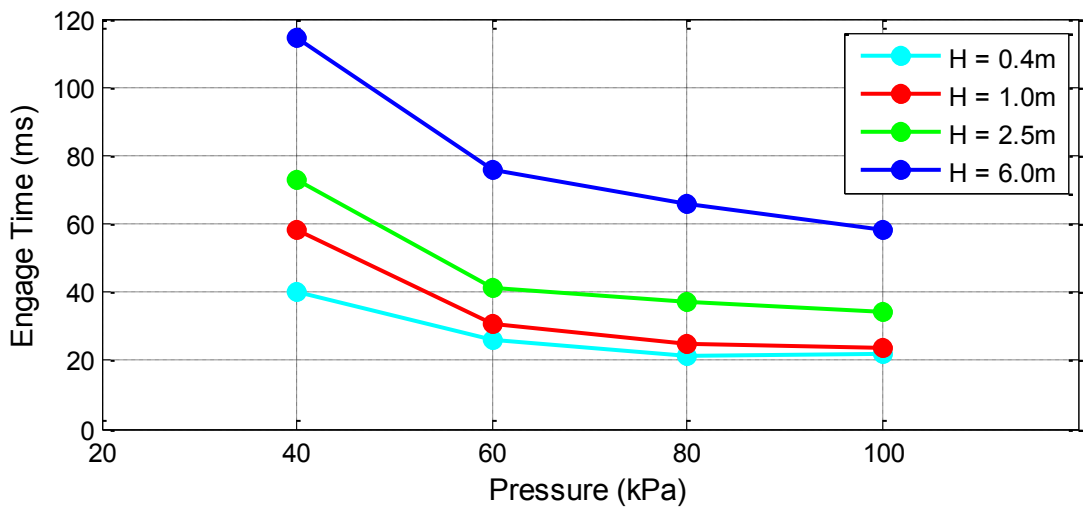

Fig. 5.4.9. Time taken for clutch to engage, as a function of pneumatic pressure and hose length (H).

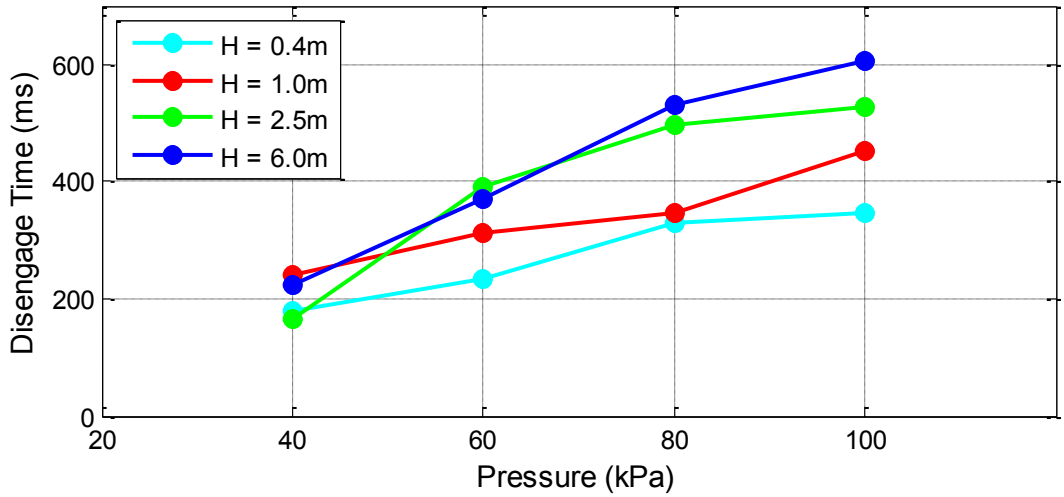

Fig. 5.4.10. Time taken for clutch to disengage, as a function of pneumatic pressure and hose length.

using (Eq. 5.1), the pneumatic actuator characteristics displayed in Fig. 5.4.7, and a coefficient of friction of $\mu = 0.155$.

The time taken for the clutch to engage and to disengage is shown in Fig. 5.4.9 and Fig. 5.4.10, respectively. Clutch engage time increases with increasing hose length while the inverse is true for disengage time. Engage and disengage time increase with decreasing actuation pressure.

Fig. 5.4.11 shows the evolution of the torque transfer characteristics of the clutch with repeated durability cycling. When fewer than 2,500 and 4,000 cycles had been completed for material A and B respectively, the clutch was unable to slip at 50 Nmm

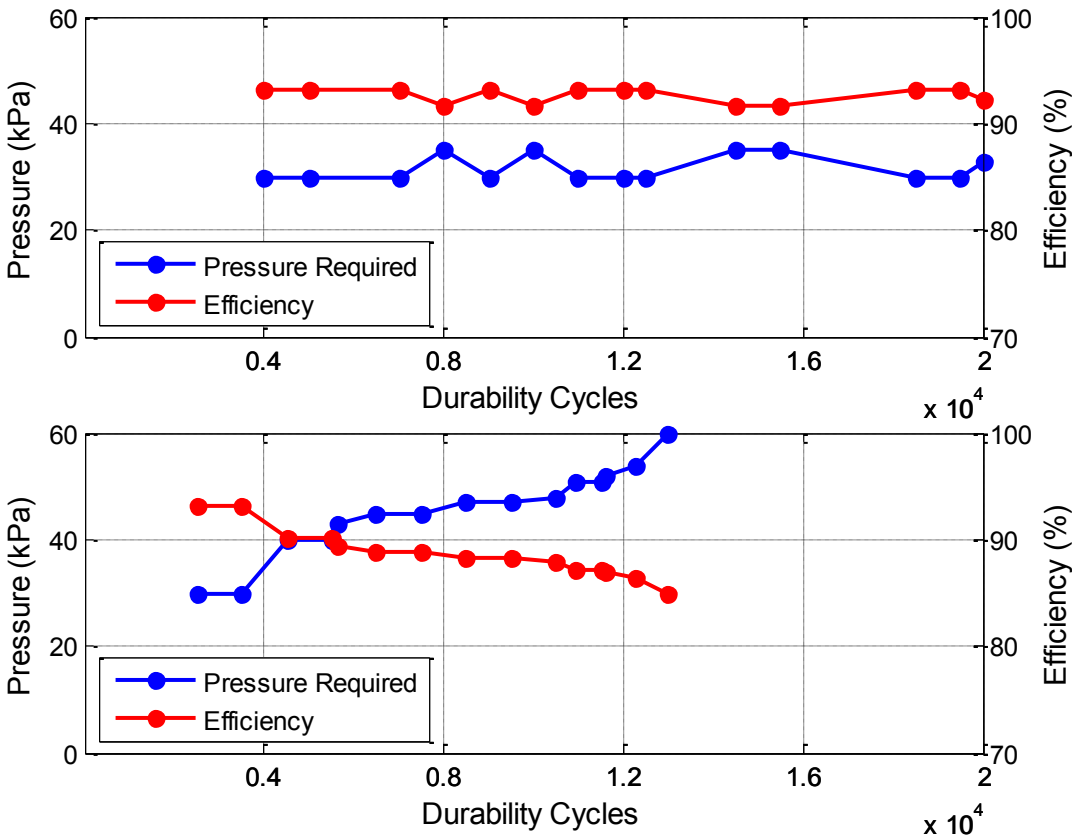

Fig. 5.4.11. Effect of repeated activation cycling on clutch output torque and clutch efficiency for material A (top) and material B (bottom).

output torque – as soon as the pneumatic actuator was engaged at 30 kPa the mechanism was capable of transmitting the required torque. Repeated cycling of material A beyond this point caused a gradual deterioration of the friction plate coating and a gradual increase in the pressure required to transmit 50 Nmm of torque. The increase in pressure caused the parasitic torque to rise (see Fig. 5.4.8) which, with the output torque constant at 50 Nmm, caused a fall in efficiency from 90% to 85% after 13,000 cycles. At this point the test was terminated. Material B experienced little discernable degradation, and the efficiency stayed approximately constant (at 92%) up to 20,000 cycles. The same pneumatic actuator was used throughout all testing and experienced in excess of 38,000 inflation cycles without exhibiting any signs of degradation.

The measured maximum output torque of the clutch when first assembled and after durability cycling is shown as a function of input pressure in Fig. 5.4.12. Also displayed is the expected output torque calculated using (Eq. 5.1) and the pneumatic actuator characteristics (Fig. 5.4.7). This shows that for material A the calculated coefficient of friction of the friction plates falls from approximately $\mu = 2.2$ when assembled to approximately $\mu = 1.35$ after 12,500 durability cycles. The coefficient of

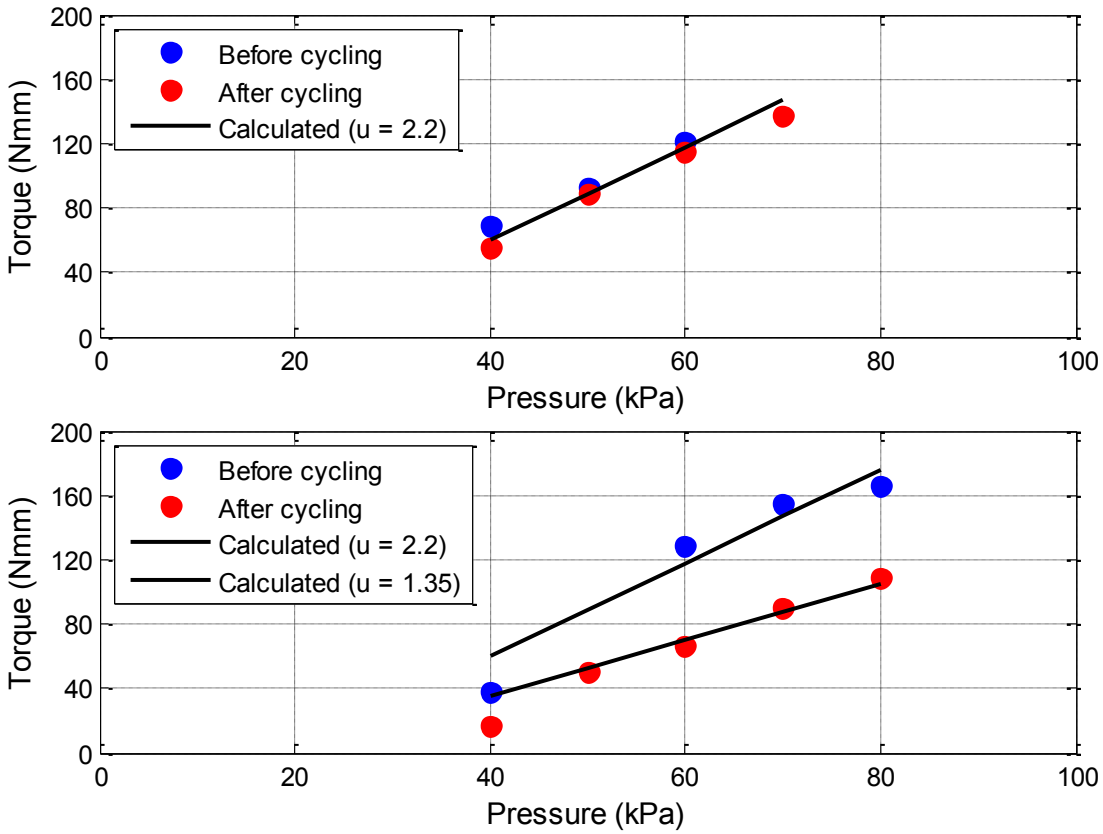

Fig. 5.4.12. Maximum torque that can be applied to clutch before slipping, as a function of pneumatic pressure for material A (top) and material B (bottom). Data displayed from the clutch before and after durability cycling, and compared with calculated values.

friction of material B is $\mu = 2.2$ on assembly and stays approximately constant after 20,000 cycles.

5.4.6 Discussion

The harder material B appears to be the more suitable of the two friction coating materials tested for this application. The degradation of the softer material due to repeated engagement cycling is much faster, resulting in a significant loss of performance. This degradation is shown in Fig. 5.4.13, and suggests that the looser structure of the soft material leads to it increasingly wearing away over time. The expected improvement in initial performance due to the softer material coping with uneven friction plates is not seen, as the initial effective friction coefficient of both materials is comparable.

In most facilities, a pneumatic hose of 4 to 5 m allows the control valves and other associated electronics to be placed near the edge of the MRI scanner room. This means that with an inflation pressure of 40 kPa (giving an efficiency of 90% for up to 20,000 cycles from Fig. 5.4.11), the engage and disengage time will be in the order of 95 ms and 200 ms respectively. Since the USR-30-NM motor takes 50 to 60 ms to start or change

Fig. 5.4.13. Friction coating material A is severely worn after 12,500 clutch activation cycles.

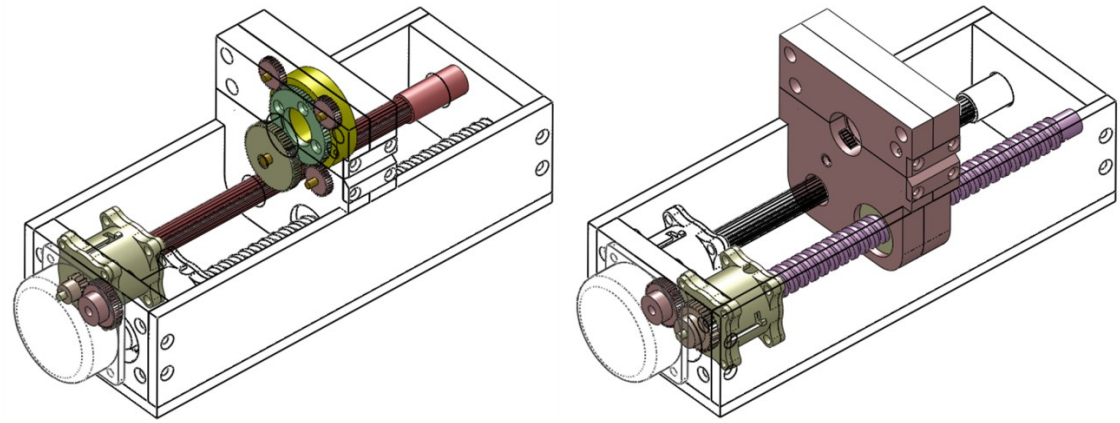

Fig. 5.4.14. 2-DOF modified right hand module. A single motor drives the rotation DOF (l) via a clutch (yellow) and splined shaft (red). Activation of the second clutch (r) drives the translation DOF via a leadscrew (purple).

direction [Shinsei, 2005], the results are slightly slower than ideal. The engage time is not anticipated to be an issue, however it is possible that the longer disengage time would limit rapid switching between clutches. The time taken to disengage the clutch can be reduced by the use of a control valve with a higher maximum flow rate or by incorporating a quick exhaust valve closer to the clutch.

In Fig. 5.4.1 there are 81 control inputs for a simulated biliary cannulation procedure that lasted 183 seconds. In addition, during user testing of the endoscope remote actuation system the longest time taken to complete biliary cannulation was 12 minutes (see Section 6.4). Combining these values, the indicated minimum lifetime of the clutch (20,000 control inputs) would translate to over 125 procedures, assuming no single DOF accounted for more than half of all control inputs.

The MRI-compatible endoscope remote actuation modules presented in Section 5.3 have 6 MRI compatible ultrasonic motors mounted on 3 different modules. These motors drive 6 separate degrees of freedom, but since the system is used for fine positioning and control of the endoscope, it is very rare that more than one degree of freedom is required at some time. With the miniature pneumatic clutch each module can be reconfigured to require only a single motor (example shown in Fig. 5.4.14), saving the cost of highly expensive components with negligible loss of performance.

5.5 User Interface Handle Design

The user interface for the remote actuation system is designed to require a minimum level of retraining for users already familiar with the use of a duodenoscope. Operation of the system will generally be performed by a clinician experienced in ERCP and reducing the requirement to learn the user interface will increase acceptance and technology uptake.

The user interface handle is shown in Fig. 5.5.1. The shape replicates the standard duodenoscope, with the controls for tip steering, catheter feed and catheter deflection all located in the same places as on the standard handle. Duodenoscope flexible section feed and twist are controlled from the rod incorporated into the user interface handle base, in a position that allows the controls to be operated with the operator's right hand.

The handle is manufactured predominantly from ABS plastic using a Fused Deposition Modelling (FDM) rapid prototyping process. This makes it very light and consequently easy to handle – in marked contrast to the heavy standard duodenoscope handle, which studies have shown can cause repetitive strain injuries to operators due to it's weight [Shergill, 2009].

Each control depresses micro-switches embedded into the handle body (Fig. 5.5.2). The controls are mounted in such a way that they move in the same way as on the standard duodenoscope handle (rotation for tip steering wheels, prismatic for catheter feed, and so on) for a small distance before depressing the switch. The motor speed (see below) is adjusted using trimming resistors mounted on the handle.

The operation of the actuation system with image-guided feedback means that it is ideally suited to be operated by speed control. The user selects the speed and direction of the motor using the user interface handle and then maintains that input until the desired position is observed on the guidance images. Due to the locking torque of the ultrasonic motors, this position is then maintained until a further control input is received. This setup is in contrast with the standard controls, which operate on position control with Bowden cables.

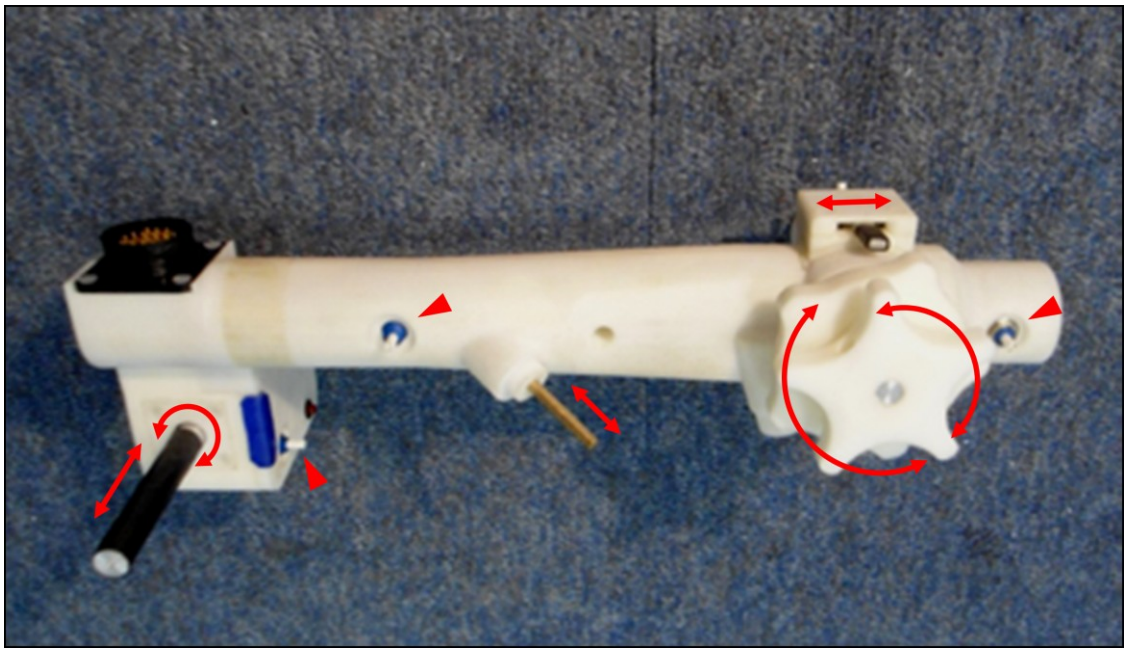

Fig. 5.5.1. User interface handle, showing locations of controls for all 6 DOF (arrows) and trimmer resistors for speed control (arrowheads). Controls are in ergonomically similar locations to the standard duodenoscope controls (see Fig. 4.4.1).

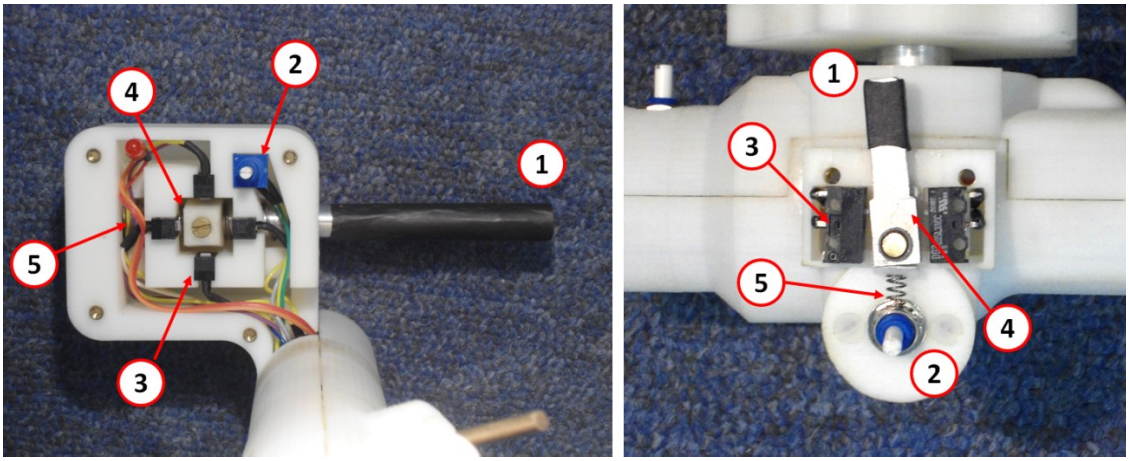

Fig. 5.5.2. User input controls for right hand module (left) and catheter deflection bridge (right) with covers exposed. Showing (1) control input rod/lever, (2) speed control resistor, (3) microswitches for direction control, (4) control input rod/lever feature that depresses microswitch and (5) return spring.

5.6 Control Unit

The majority of the active electronic parts of the endoscope remote actuation system are housed within the control unit. This is a closed aluminium box (see Section 5.7.2) that

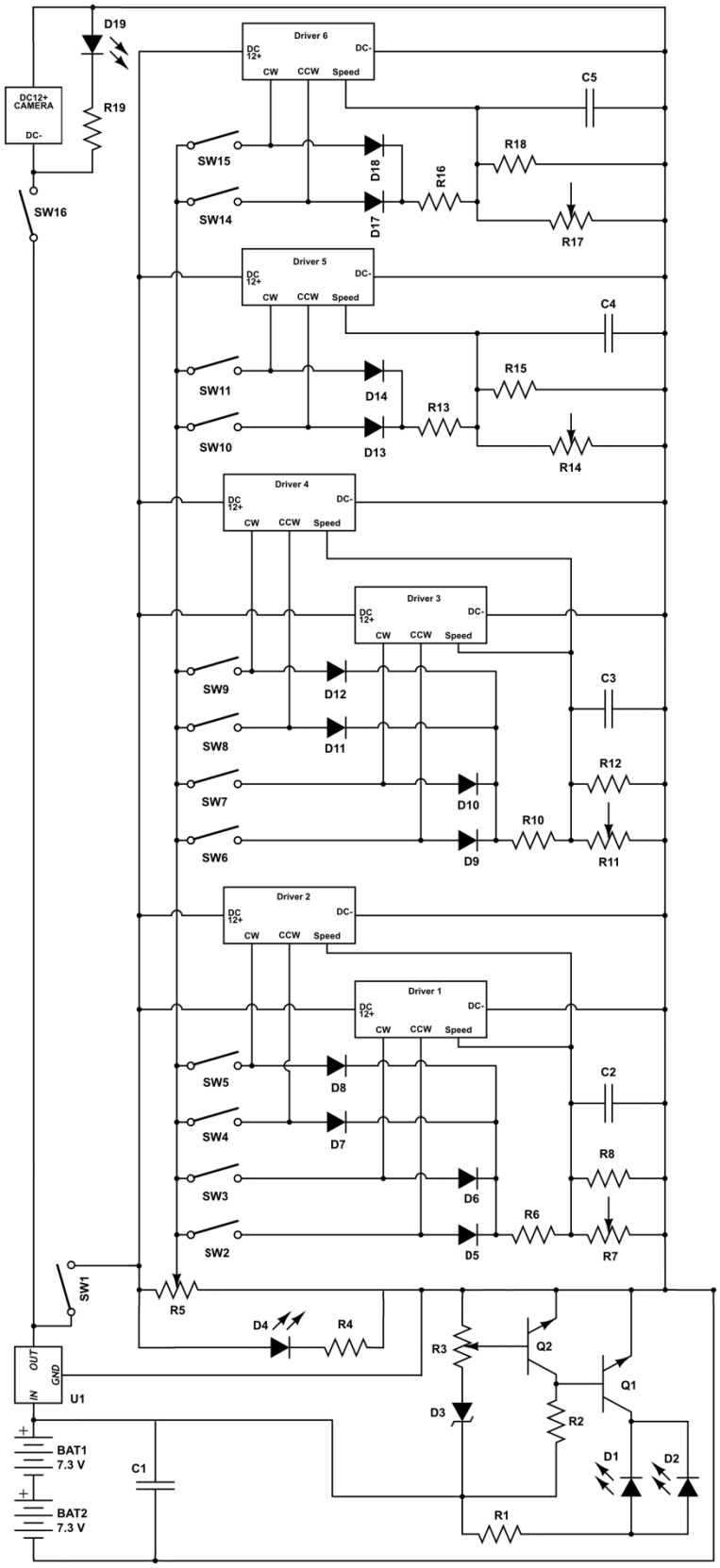

Fig. 5.6.1. Schematic of control box wiring for original actuator module designs presented in Section 5.3.

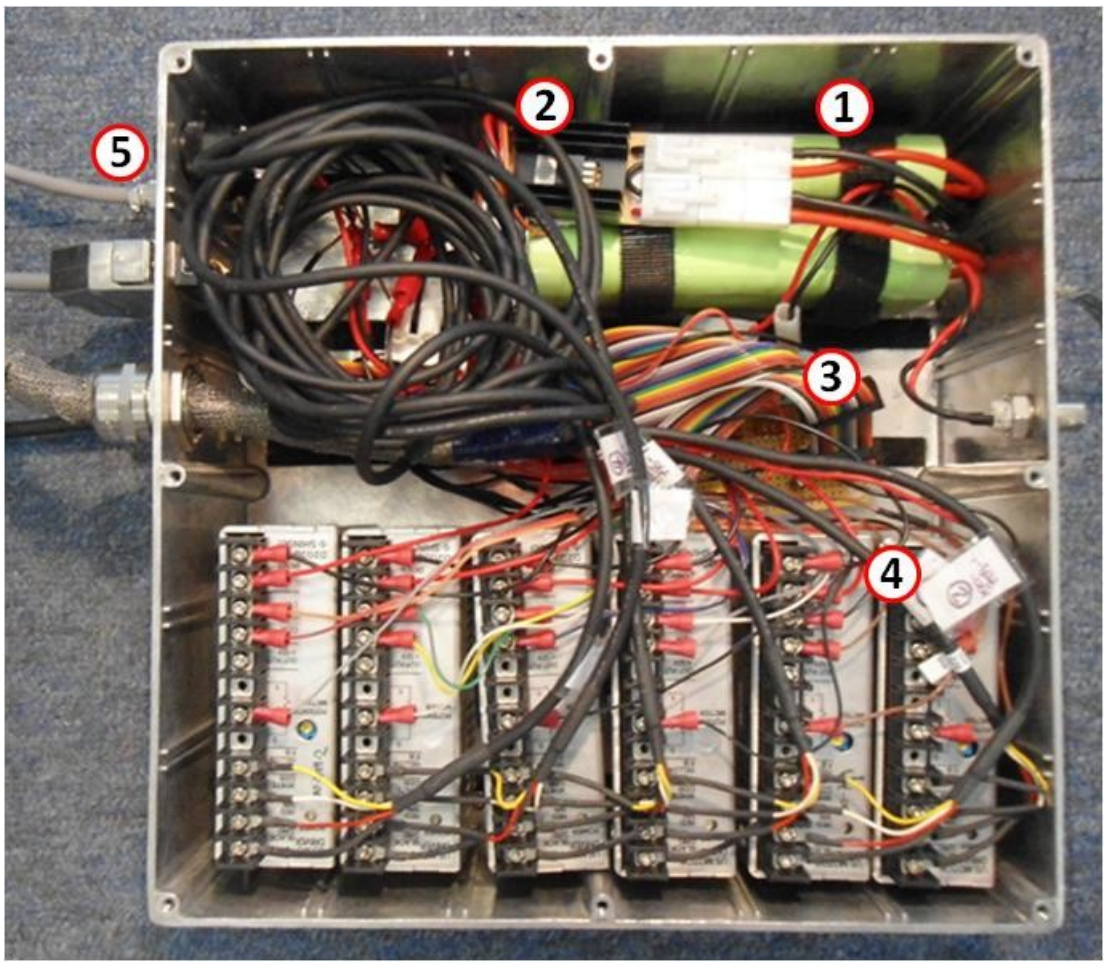

Fig. 5.6.2. Control box, opened to show batteries (1), voltage regulator (2), motor control electronics (3), motor driver units (4) and external connections to the motors, user interface and camera (5).

contains driver units for each motor, pneumatic valves, batteries and circuitry (Fig. 5.6.2). A schematic of the control unit wiring is shown in Fig. 5.6.1.

The motor direction and speed control circuits have been designed to reduce the number of connections between the user interface handle and control box. Switches SW2-15 and variable resistors R7, R11, R14 and R17 are mounted on the handle, which along with a +5V DC supply (from the trimmer R5), limits the number of wires external to the control box to 21. In this configuration the motor speed is controlled by a voltage that varies between 0 and 1.6V. The motor driver requires this to be raised from 0 as the direction control is activated, necessitating the RC filter circuits formed by R8/C2, R12/C3, R15/C4 and R18/C5.

The actuated endoscope system is battery powered, to reduce the potential sources of EMI (from mains connections or power supply units) and to reduce the number of external connections, making the system easier to use in a wide range of

Sub-Circuit	Activating Switch	Voltage (V)	Current (mA)
Low voltage indicator	-	14.5-12.6	0.7
Low voltage indicator	-	<=12.5	30
LDO Regulator	-	14.5-11.5	0.006
LDO Regulator	SW1 / SW16	12	10
Indicator LEDs (D4, D19)	SW1 / SW16	12	15[a]
Motor Drivers 1-6	SW1	12	180
Camera	SW16	12	150
Motor	SW2 - 15	12	600-850[b]
5V Signal Circuit	SW1	12	0.12
Motor control	SW2 - 15	5	0.5-0.8[b]

[a] Per indicator LED
[b] Per motor. Variaes with motor speed

Table 5.6.1. Control and power consumption for endoscope remote actuator system

facilities. Two 6-cell NiMH battery packs are used in series (Enix Energies, Saint Egrève, France), to provide between 14.6 and 11.3V DC depending on charge level. Although NiMH cells have a relatively stable voltage output over a range of charge levels, any variation will impact the motor speed control, so the system includes a 12V DC low dropout regulator and a low voltage indicator circuit that lights two warning LEDs when the supply drops below 12.5V.

Table 5.6.1 summarises the power requirements for each sub-circuit. From this it can be seen that the system will draw around 370mA when in 'standby' mode (with camera on and motor drivers active), around 1220mA with one motor running at full power and 2070mA with two motors running at full power. The batteries have a nominal capacity of 3800mAh, so these three states correspond to a nominal battery life of 9.5, 3 and 1.8 hours respectively, each of which is sufficient given the expected procedure time and duty cycle (see Section 5.4.6).

5.7 MRI Compatibility

5.7.1 Materials and construction

MR safety of the endoscope remote actuation system is achieved by careful selection of materials (see Section 2.3). The remote actuator modules and clutch presented in Section 5.3 and 5.4 are composed solely of the materials listed in Table 5.7.1– care has been taken to remove small components such as grub screws and springs from standard parts to improve their compatibility. The low magnetic susceptibility of the majority of these

Material	Components
Delrin (Polyoxymethylene)	Housing, casings, gears
ABS plastic	Housings, casings
Perspex	Base plates
Brass	Shafts, bushes
Proprietary polymers (Igus, Northampton, UK)	Bearings, leadscrew nut
Nylon	Screws, gears
Copper	Wiring, shielding
Aluminium	Leadscrew, motor casing
Stainless Steel (302)	Springs
Monel (Nickel/Copper alloy)	Shielding

Table 5.7.1. Materials used to manufacture endoscope remote actuator system

materials [Schenck, 1996] means that the actuation system experiences no significant magnetically induced forces.

During the MRI-guided ERCP procedure, the MR imaging volume will be centred on a region of interest surrounding the duodenoscope tip inside the patient's digestive tract. For this reason susceptibility artefacts caused by the endoscope remote actuation modules are not an issue as they are mounted away from the duodenoscope tip.

5.7.2 Shielding

Due to their mode of operation, the active electronic components have the potential to introduce noise into the MR environment which can degrade the image quality (see Section 2.3). In addition the wires connecting the control box to the motors, camera and user interface can act as antennae, modifying the radio-frequency NMR signals and affecting the MR images.

To prevent this, all wires and active electronic components of the system are shielded [Barnes, 1987; Ott, 1976]. The aluminium control box is closed and connected to ground, while all wires have sheath of conductive material that is connected to the box (and therefore ground) via glanded connections.

The motors, motor driver wires and camera all have conductive external cases that are electrically connected to the negative DC terminal of the power supply. However, MRI compatibility testing (see Section 6.3) suggested that isolation of the actuation system power supply from the MRI scanner room shield is essential to ensure that the MR images are not degraded. For this reason, the motor driver wires are bundled together

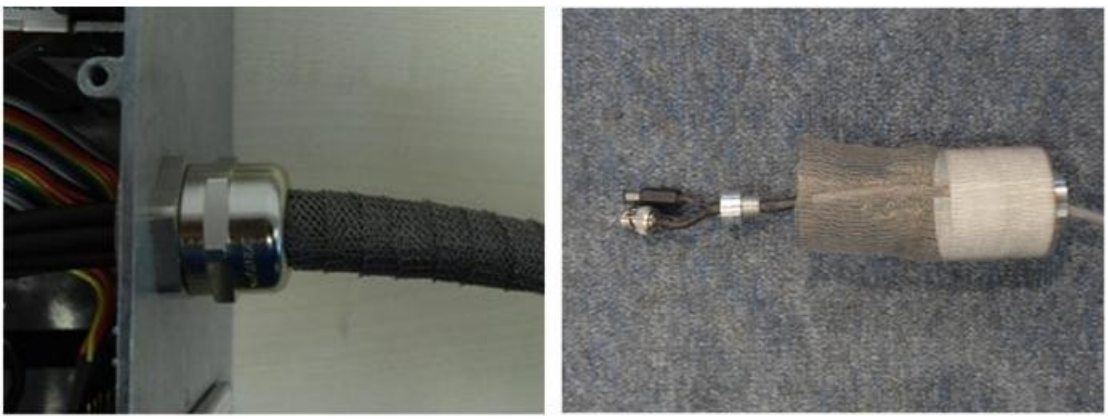

Fig. 5.7.1. Monel mesh shield for motor connection to control box (l) and removable external camera shield (r).

Fig. 5.7.2. Motor shielding, showing the motor encased in insulation (left) prior to shielding with a continuous layer of copper tape (right).

and shielded with a wrap of Monel mesh (Fig. 5.7.1), while glanded connectors are used ensure the shield integrity over connections.

A removable external mesh shield that encloses the camera once it has been mounted on the duodenoscope is connected to the camera power cable coaxial shield by means of a threaded attachment (Fig. 5.7.1). The motors are each individually shielded by layers of copper tape that are electrically connected to the Monel mesh wrap around the motor driver wire. The conductive motor casing is covered in electrical tape prior to the shield being added to ensure electrical isolation between the shield and casing (Fig. 5.7.2).

5.7.3 Filtering

The endoscope actuation system includes two connections between the inside and outside of the MRI scanner room shield. Wiring that passes from outside to inside the MRI scanner room shield should be connected via a filter in order to prevent conduction of EMI from the relatively noisy external environment [Barnes, 1987]. In most cases this is

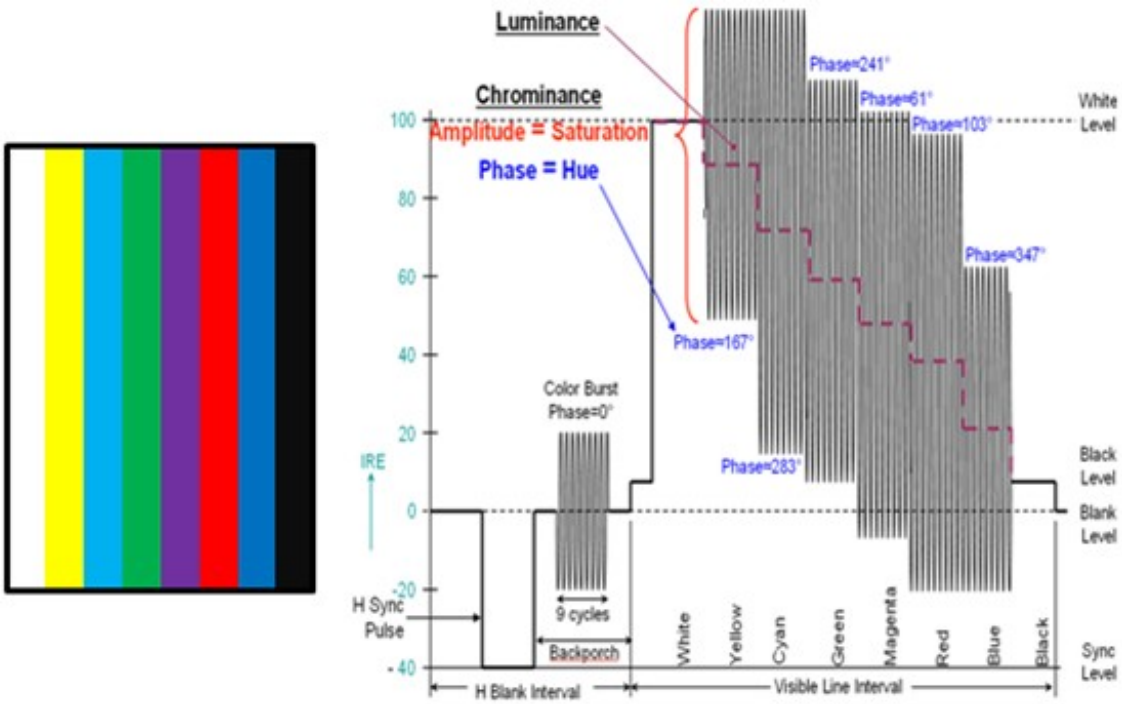

Fig. 5.7.3. Example of composite video encoding, with the chart (r) showing the waveform for a single scan line of the test image (l). Pixel luminance is defined by the magnitude of the waveform mean at the corresponding horizontal position. Pixel colour saturation is defined by the amplitude of the 3-5 MHz oscillation, while hue is defined by the phase difference between the waveform and the colour burst in the backpatch to the left of the screen.

achieved by having filtered connections permanently mounted on a panel set into the scanner room shield. Since EMI becomes an issue for MRI scanners at around the Larmor frequency (see Section 2.2), in most cases low-pass filters with a cutoff frequency significantly below the Larmor frequency are sufficient. The endoscope remote actuation system user interface uses a D-sub socket with integrated filter capacitors for this.

However, low pass filtering of some signals causes attenuation to a level that impairs performance. This is the case for the ultrasonic motors, which are driven by a sine wave of around 40 kHz [Shinsei, 2005]. The motor driver generates this wave by using class-D style amplification of low pass filtered square waves and further low-pass filtering of this signal is sufficient to prevent motor operation. For this reason, the motor driver units are placed inside the MRI scanner room and are not filtered.

The duodenoscope camera outputs a composite video signal, which must be connected through the filter panel into the MRI control room. Composite video is encoded to provide both luminance and chrominance information on a single pair of wires – an example signal waveform for a single image scan line is shown in Fig. 5.7.3. Since chrominance information is encoded using a 4 MHz sinusoidal oscillation, low pass

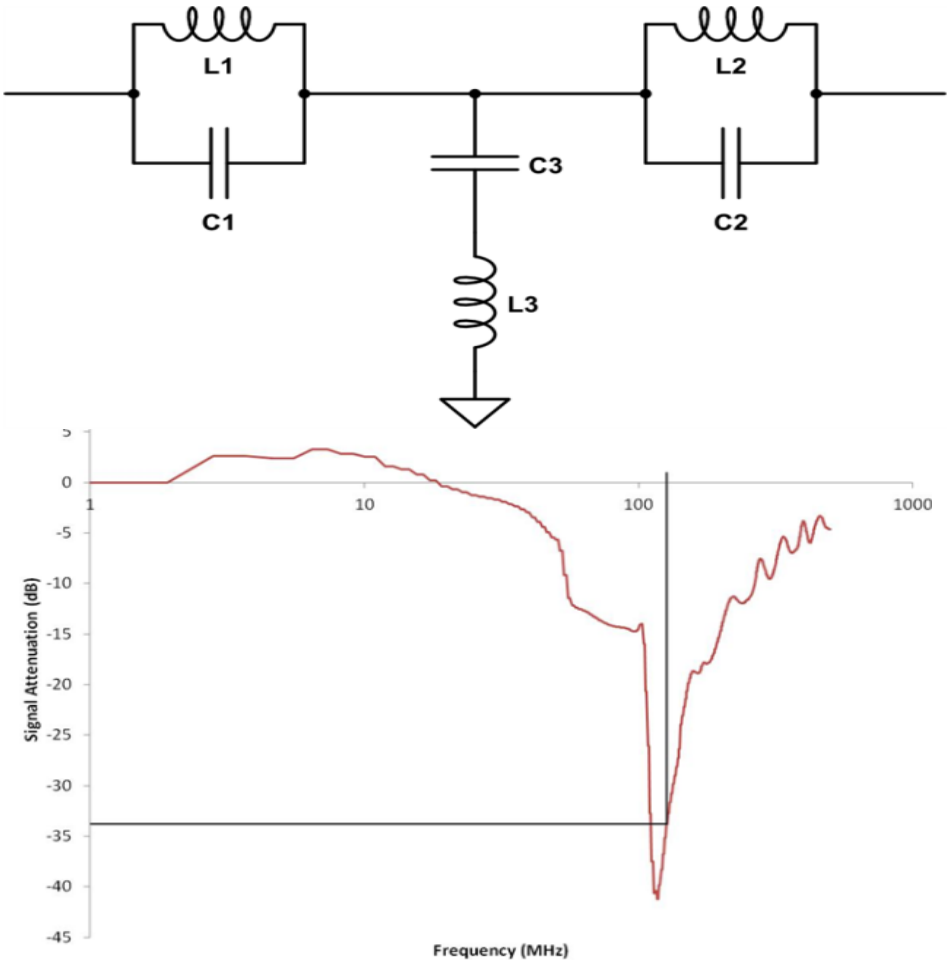

Fig. 5.7.4. Band stop filter constructed for video feed filtering at 3.0T, showing schematic of circuit (top) and signal attenuation (in dB) as a function of frequency (bottom) measured using a network analyser.

filtering below this frequency removes all colour from the image. In addition, low pass filtering at any frequency causes blurring of abrupt changes in the luminance signal. To overcome this, a second-order band-stop filter was constructed (Fig. 5.7.4) to attenuate the composite video signal only at the Larmor frequency and leave it unchanged at other frequencies – this results in the image being qualitatively unchanged after filtering.

5.8 Conclusions

This chapter presents the design and development of a novel endoscope remote actuation system that solves the problem of access during MRI-guided ERCP as outlined in Section 4.3.3. The system actuates all six DOF of the MRI compatible duodenoscope (see Section 4.4.1) using nonmagnetic ultrasonic motors, while the system architecture is designed to facilitate a simple procedural workflow with a minimum of operator retraining.

Initial testing described in this chapter demonstrates that the actuators have the capacity to successfully enable complex endoscopic tasks to be performed simultaneously with intra-operative MRI – both in terms of compatibility with the MRI system and mechanical capability. Further investigation of this is presented in Chapter 6.

The miniature pneumatic clutch presented here offers a significant benefit in the field of interventional MRI and specifically for the endoscope remote actuation system. The clutch is capable of transmitting the torque produced by a USR-30-NM ultrasonic motor using a relatively low, constant inflation pressure of 40 kPa with an efficiency of greater than 90% after 20,000 activation cycles. The clutch is MRI compatible and small enough to be integrated this and other compact remote actuation devices for interventional MRI procedures.

The design of the miniature pneumatic clutch presented here has significant scope for development, both to improve the performance and to add extra functionality to the mechanism. Additional friction plates could be introduced to greatly improve the torque transfer characteristics, at the cost of increasing the length of travel required by the pneumatic actuator. Depending on the system requirements the mechanism could be changed to achieve a normally closed clutch (disengaged when pneumatic valve activated) or a clutch that provides a locking torque when disengaged to prevent back-driving of the mechanism.

Chapter 6

Remote Actuation System Validation

6.1 Introduction

The endoscope remote actuation system presented in Chapter 5 facilitates the MRI-guided ERCP procedure outlined in Section 4.3 by enabling the duodenoscope to be operated during intra-operative MR imaging.

Section 6.2 outlines the two categories of performance criteria used to validate the remote actuation system. Section 6.3 presents the testing performed during the course of the design and development of the endoscope remote actuation system to fulfil the MRI compatibility performance criteria. Due to the need to locate the remote actuation system inside the MRI scanner bore, particular attention has been paid to sources of electromagnetic interference and image noise, and their effect on MRI signal to noise ratio (SNR).

The extent to which the remote actuation system meets the functional performance criteria is explored in Section 6.4 through the use of a biliary cannulation simulator with kinematic analysis, along with a discussion on factors affecting the functional performance of the system.

6.2 Performance Criteria

The capability of the endoscope remote actuation system must be quantified before the system can proceed to clinical trials. Key features of a successful system design are (i) that the remote actuation system must not negate the benefit of the intra-operative MRI by degrading the quality of the MR images and (ii) the system must be functionally capable of performing the intricate endoscopic manoeuvres required for biliary cannulation without the need for extensive operator retraining.

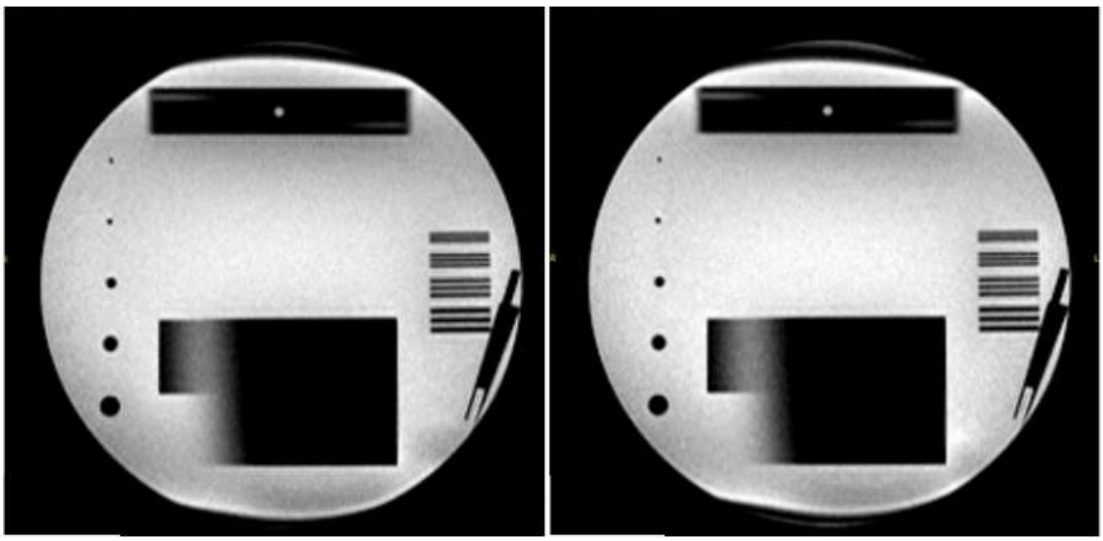

Fig. 6.2.1. MRI of a quality assurance phantom with a reference SNR (l) and a SNR 5% below reference (r).

6.2.1 MRI Compatibility Criteria

In order to determine an acceptable level of MRI quality variation, 30 reference images were acquired with each of the three imaging sequences used for compatibility testing (see Table 6.3.1). Images were acquired in a continuous set to reduce any effect of temporal variation from one image to the next.

Table 6.2.1 and Fig. 6.2.2 demonstrate that SNR measurements in MRI are subject to a degree of variation, even with identical sequences acquired consecutively and with no active devices in the scanner room. This variation is approximately normally distributed around the mean, with a maximum change of around 1.5% for the FSE and GRE sequences and 2.5% for the TrueFISP sequence, suggesting that any variation greater than this is likely to be due to additional devices within the scanner room, if present.

Acceptable image quality is a subjective measure and is dependent on the radiologist interpreting the data, the clinical situation and the availability of other sources of data, among other factors. With this in mind, a greater level of SNR reduction than the values quoted above may be acceptable from the perspective of diagnostic utility. To visualise this, Fig. 6.2.1 shows the effect of a 5% decrease in SNR on images of a quality assurance phantom, demonstrating that the loss in detail due to this change is negligible. Since an SNR reduction of this order of magnitude is unlikely to present diagnostic challenges, a device introduced into the MRI scanner that displays this level of SNR reduction can be considered acceptable.

Scanner Field Strength (T)	Sequence Name	Mean SNR	Standard Deviation SNR	Maximum, Minimum SNR
1.5	FSE	14.9	0.115	15.1 , 14.6
1.5	GRE	16.6	0.155	16.9 , 16.2
3	TrueFISP	57.6	1.33	59.5 , 55.9

Table 6.2.1. Variation in reference image SNR.

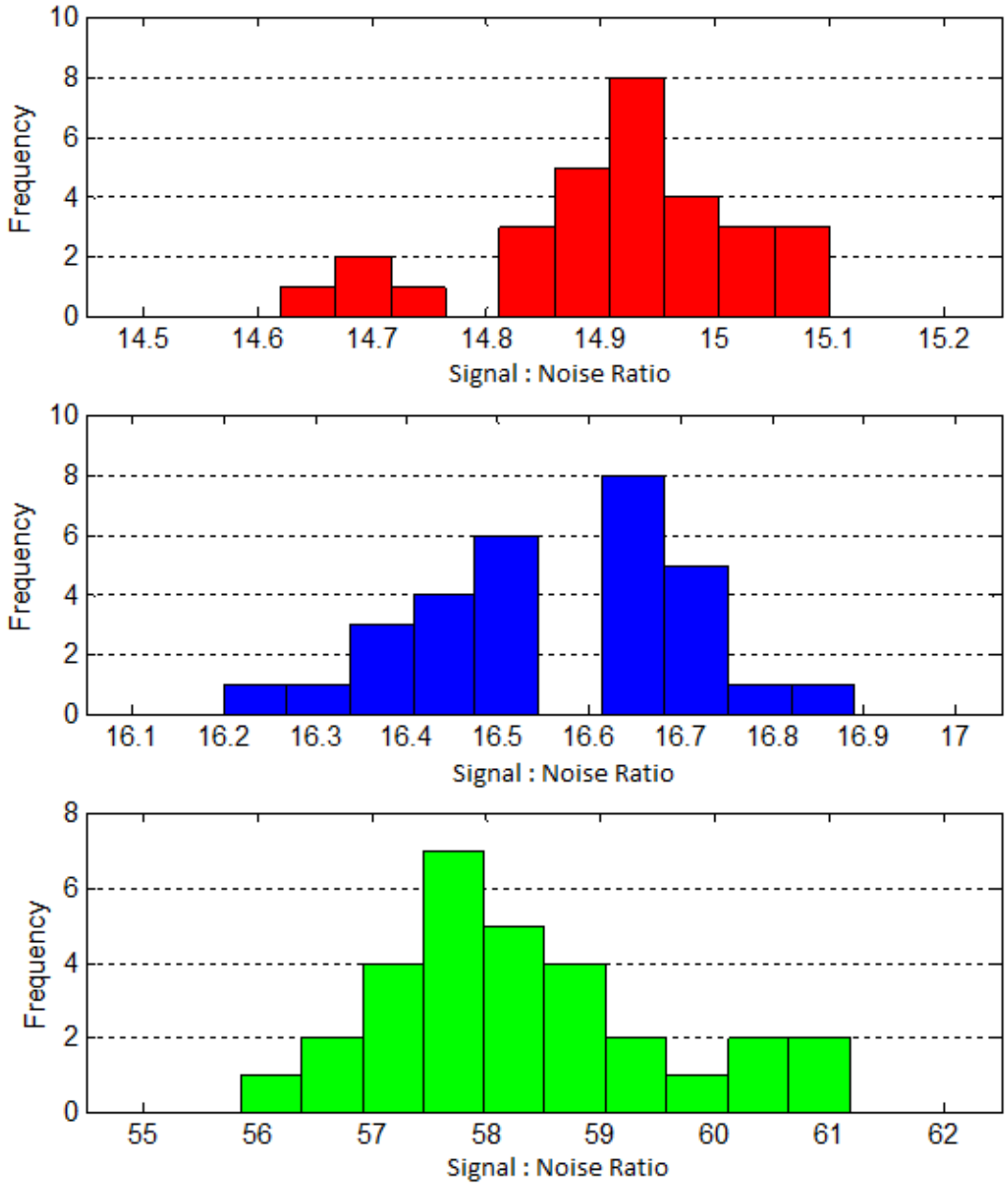

Fig. 6.2.2. Histograms showing variation in reference image SNR for GE sequence (top), FSE sequence (middle) and TrueFISP sequence (bottom).

6.2.2 Functional Criteria

Ideally the remote actuation system will allow clinical biliary cannulation to be achieved with no loss of operator technical performance and no retraining. Assessing compliance with this requirement is challenging to fully assess due to a need to gather data from a large number of clinical procedures. This approach would raise ethical issues due to the potential for significant patient harm of using an un-qualified system. In addition, operator technical performance is a concept which is frequently subjective and challenging to measure, particularly in a clinical environment with little control over experimental variables.

A novel mechanical biliary cannulation simulator and objective assessment tool was used to overcome these issues. This enabled a performance score to be generated for simulated procedures, allowing direct comparison between a traditional manual procedure and a remotely actuated procedure.

Section 6.4.6 details experiments performed to validate the assessment tool using skill levels of novice and experienced endoscopists as a baseline. Based on these experiments, the endoscope remote actuation system can be considered to be functionally successful if the operator performance scores achieved using the system are equivalent to those achieved manually.

6.3 MRI Compatibility Testing

6.3.1 Introduction

Material compatibility issues are well understood and addressed in the literature [Schenck, 1996; Tse, 2011], so achieving an MR safe solution is simply a matter of careful design (see Section 5.7.1). However, there are examples in the literature of varying MRI compatibility of ultrasonic motors due to electromagnetic interference (see Section 3.2). The extent of this interference appears to be sensitive to fine details of component position and wiring as well as shielding strategies. For this reason extensive testing was performed with the individual components as well as the complete prototype system, in configurations relevant to this project.

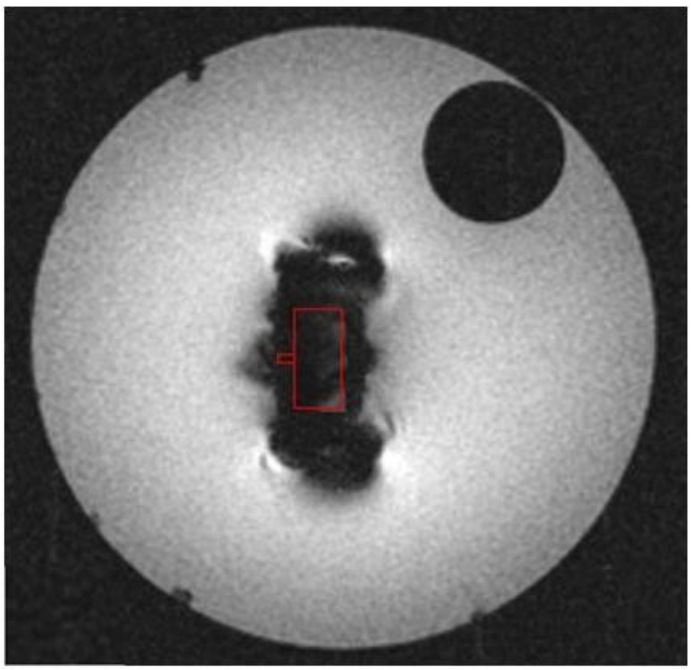

Fig. 6.3.1 Susceptibility artefact of a single USR-30-NM motor immersed in water and imaged at 1.5T using a FSE sequence. The approximate motor position is outlined in red.

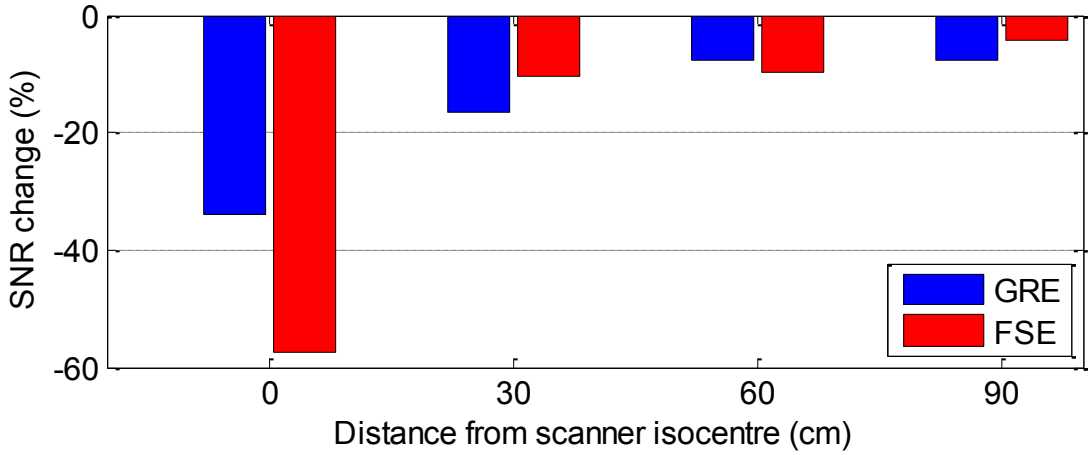

Fig. 6.3.2: Mean change in image SNR due to presence of an unshielded motor placed at varying distances from the scanner isocentre.

6.3.2 Initial Component Evaluation

USR-30-NM motors are manufactured primarily from Aluminium, Brass and ceramics and, as Fig. 6.3.1 shows, the susceptibility artefact cause by the motor on MRI images is limited to a volume up to approximately 2x the size of the motor. The distance of the motor from the imaging volume has a significant effect on the electromagnetic interference (EMI). Fig. 6.3.2 shows this effect very clearly, with the loss in SNR dropping to around 5% as the motor is moved out of the scanner bore. These tests were performed using a 1.5T clinical

Sequence	Field Strength (T)	Flip angle (°)	TR (ms)	TE (ms)	FOV (mm)	Matrix Size	Slice Thickness (mm)	NEX
FSE	1.5	90	600	8.9	240 x 240	256 x 256	5	1
GRE	1.5	50	68	3.4	240 x 240	256 x 256	5	1
TrueFISP	3.0	44	957	1.57	256 x 256	256 x 230	8	1

Table 6.3.1 Parameters of imaging sequences used for MRI compatibility testing, including repetition time (TR), echo time (TE), field of view (FOV) and number of excitations (NEX). Matrix size referes to the number of pixels in the image

closed bore MRI scanner (GE Sigma Excite) and two different scanning sequences (Table 6.3.1).

During the ERCP system's operation the motors will be mounted at least 45cm from the imaging volume and hence the susceptibility artefact is not an issue. In addition, these preliminary results show a 'worst-case' scenario for EMI, as in this example the motor and cabling were unshielded and the driver cable passed through the waveguide panel from the scanner control room. Hence electromagnetic noise from the control room could be conducted into the scanner bore by the motor driver cable.

A further potential source of electromagnetic interference in the system is the endoscope camera. As with the motors, this is positioned on the duodenoscope handle and well away from the imaging volume so susceptibility artefacts are not an issue. Nevertheless, the camera must be powered and transmitting video during imaging sequences so any electromagnetic noise must be managed.

6.3.3 System Evaluation

A series of compatibility tests were performed using a 1.5T MRI scanner (GE Sigma Excite) to assess alternative approaches to management of EMI produced by the motors and driver unit. All tests were performed with both Gradient Recalled Echo (GRE) and Fast Spin Echo (FSE) sequences as specified by the relevant ASTM standard [ASTM, 2007]. In addition, the complete actuation system and camera were tested in a 3.0T scanner (Siemens Verio) using a True Fast Imaging with Steady state Precession (TrueFISP) sequence – the higher field strength and known sensitivity to frequency offsets of this sequence [Deshpande, 2003] can make this a harsher test of EMI. Sequence parameters are shown in Table 6.3.1.

Test Number	Motor / System	Motor /Cable Shielding	Control Box Shielding	Power Source	-DC Grounded	Motor Control Location
1	M	N	N	PSU	N	Control Box
2	M	N	Y	PSU	N	Control Box
3	M	Y	Y	PSU	N	Control Box
4	M	Y	Y	PSU	N	Control Box
5	M	Y	Y	PSU	N	Control Room
6	M	Y	Y	PSU	N	Scanner Room
7	M	Y	Y	Batteries	N	Scanner Room
8	S	Y	Y	Batteries	Y	Scanner Room
9	S	Y	Y	Batteries	N	Scanner Room
10	S	Y	Y	Batteries	N	Control Room

Table 6.3.2 Motor and actuation system MRI compatibility test variables.

Signal to Noise ratio (SNR) for each image was measured by using the first method described in Section 2.3. Each image was acquired multiple times over a short period of time, with the image signal being defined as the mean pixel intensity in a region of high signal. The image noise was defined by subtracting two consecutive images from each other and measuring the standard deviation of the pixel intensities in the same region on the resultant image. The test images were compared to reference images of the phantom acquired without any equipment present in the scanner room.

Multiple images were acquired for each test case and the results averaged. The scanner body coil was used for all tests. To correct for variations in scanner setup and ambient conditions, all results are expressed in terms of a percentage change in SNR compared with the mean SNR of a reference image taken during the same scanning session.

In all cases the motor driver was placed in the corner of the scanner room, well away from the scanner bore, while a phantom was placed in the scanner isocenter. The motor, actuation system and/or camera were all placed on the scanner bed in the position

Test Number	Endoscope	-DC Grounded	External Shielding	Monitor	Monitor Location
11	N	N	N	N	-
12	Y	N	N	N	-
13	Y	Y	N	N	-
14	Y	Y	Y	N	-
15	Y	N	Y	N	-
16	Y	N	Y	Y	Scanner Room
17	Y	N	Y	Y	Control Room

Table 6.3.3 Camera MRI compatibility test variables.

they would occupy during the clinical procedure, and all were operating at full power during the imaging sequence.

6.3.3.1 Motor Shielding

The effect of shielding on a single motor and driver unit was assessed by a series of images using the setup described in Table 6.3.2 lines 1-3. Where indicated, the driver unit and motor controls were shielded by placing them inside an aluminium enclosure that was connected to ground, while the motor and cable were shielded as described in Section 5.7.2.

6.3.3.2 Motor Control Position and Motor Power Supply

Lines 4-7 of Table 6.3.2 describe the setup used to acquire a series of images that were used to assess the effect of moving the motor controls and of powering the motor from batteries instead of a power supply unit (PSU). When present, the external power supply was connected to the motor driver unit via a filter panel, while the batteries were placed inside the motor driver shielded enclosure. The motor controls (switches for direction control and a variable resistor for speed control) were placed either inside the motor driver shielded enclosure, inside the scanner room or inside the control room. In all cases the controls were connected via a shielded cable.

6.3.3.3 Actuation System Shielding and Control Position

The entire actuation system (as described in Section 5.3) consisting of six motors and associated mechanisms was tested using the setups described in lines 8-10 of Table 6.3.2.

The effect of motor control position was assessed, as well as the effect of connecting the negative battery terminal to ground. When the motor controls were inside the control room they were connected to the driver box using a shielded cable via a wall-mounted filter panel.

6.3.3.4 Camera Shielding and Monitor Position

The endoscope camera was assessed separately from the actuation system using the setups described in Table 6.3.3. The camera was connected via a shielded cable to batteries placed in the corner of the scanner room well away from the scanner bore. The camera was imaged both on it's own and mounted on the endoscope. As with the actuation system the negative battery terminal was either isolated or connected to ground, and a removable external shield made from Monel mesh (see Section 5.7.2) was available to be placed over the camera. The monitor used was a small battery operated screen (CCTV Test Monitor, XVision Group, Surrey, UK), which was connected to the camera via a shielded cable and placed either inside the scanner room or in the control room.

6.3.3.5 Clutch Pneumatic Valve Position

To determine if the clutch pneumatic actuation valve contributes any EMI to the MR image, a clutch was placed next to a phantom at the scanner isocenter and image slices of the phantom obtained in the axial direction. A pneumatic solenoid valve (SMC VQ21A1) was placed within the shielded control box with a battery pack and a switch to activate the valve. Plastic hoses connected the shielded enclosure both to the clutch and to the supply of pressurised air available in the scanner room. The length of the plastic hoses was varied from 1m to 6m and all tests were performed with the valve activated.

6.3.3.6 Complete System

The complete endoscope actuation system was tested by combining the configurations described in line 17 of Table 6.3.3 and line 9 of Table 6.3.2.

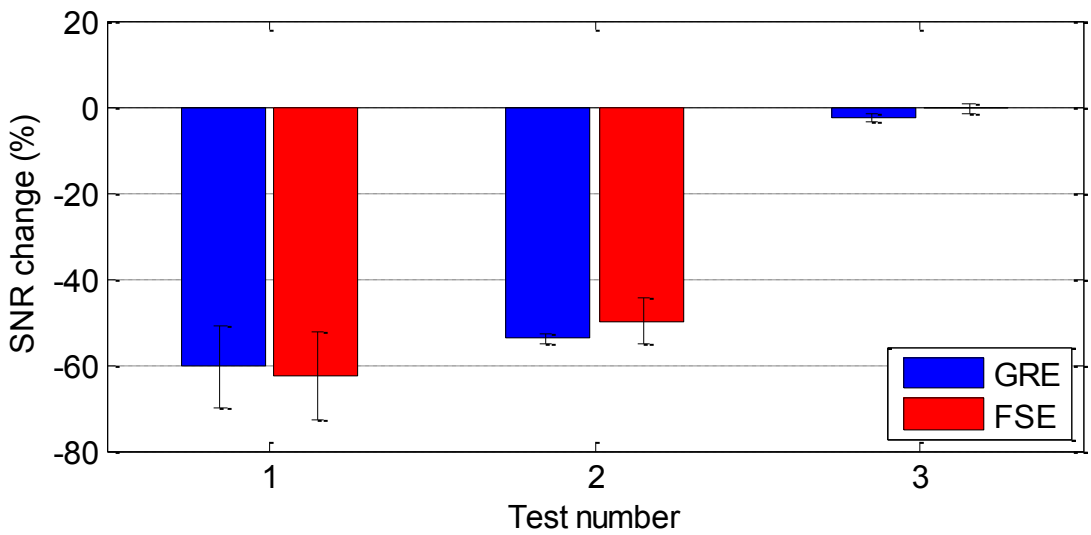

Fig.6.3.3. Effect on image SNR of shielding motor driver, cable and motor when a single motor is placed in the scanner isocenter (see Table 6.3.2). Mean SNR plotted, with error bars representing maximum and minimum results.

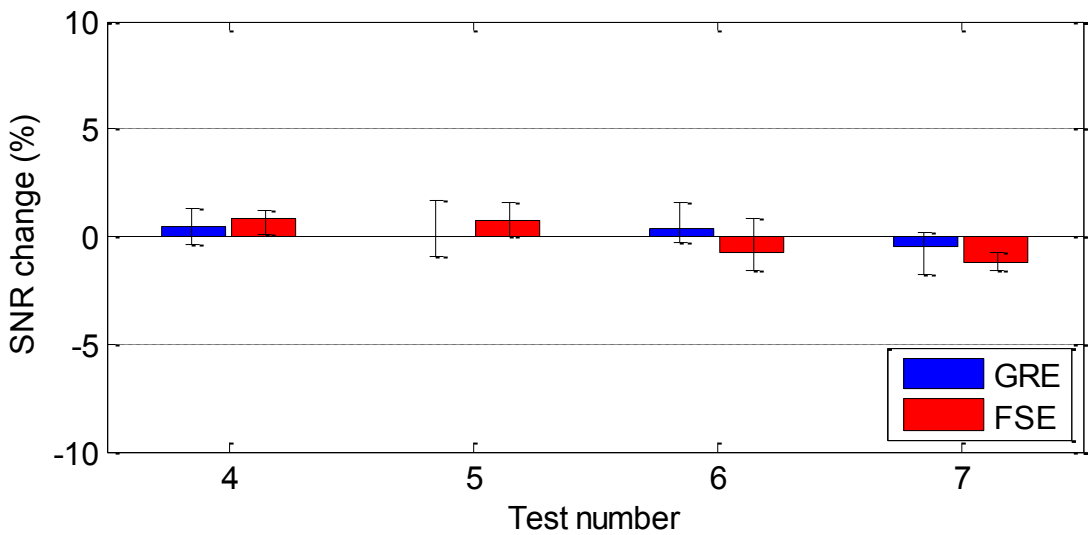

Fig. 6.3.4. Effect on image SNR of moving motor controls and changing power source when a single motor is placed in the scanner isocenter (see Table 6.3.2). Mean SNR plotted, with error bars representing maximum and minimum results.

6.3.4 System Evaluation Results and Discussion

Fig.6.3.3 suggests that the motor either conducts noise from the motor driver into the scanner bore, or acts as a radiative source of noise itself. Because of this, shielding of the motor driver has little effect unless it is combined with cable shielding and motor shielding. If this is done (Test 3), then the motor has no effect on the FSE sequence and reduces image SNR by less than 3% for the GRE sequence even when placed directly in the centre of the imaging volume.

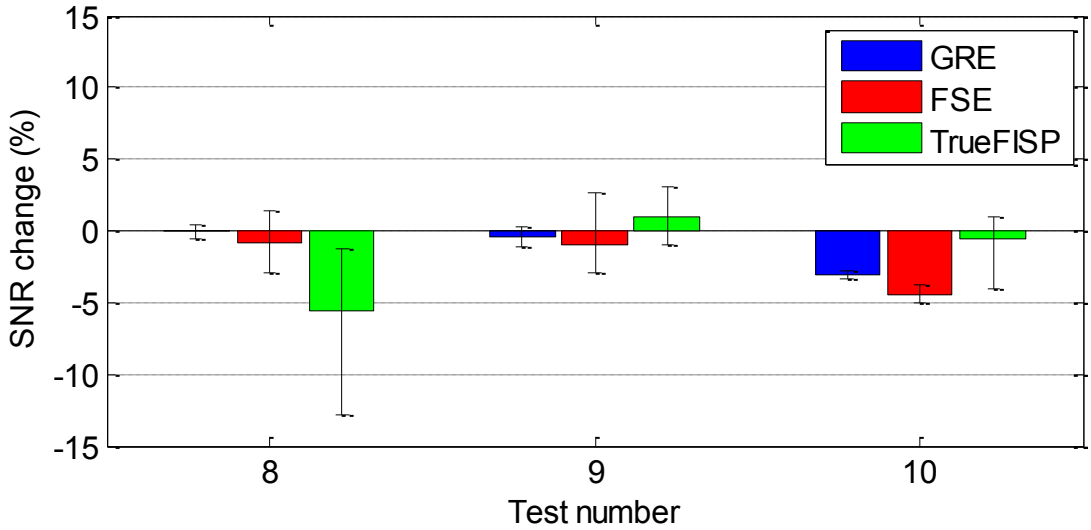

Fig. 6.3.5 Effect on image SNR of changing position of motor controls and battery grounding for complete actuation system (see Table 6.3.2). Mean SNR plotted, with error bars representing maximum and minimum results.

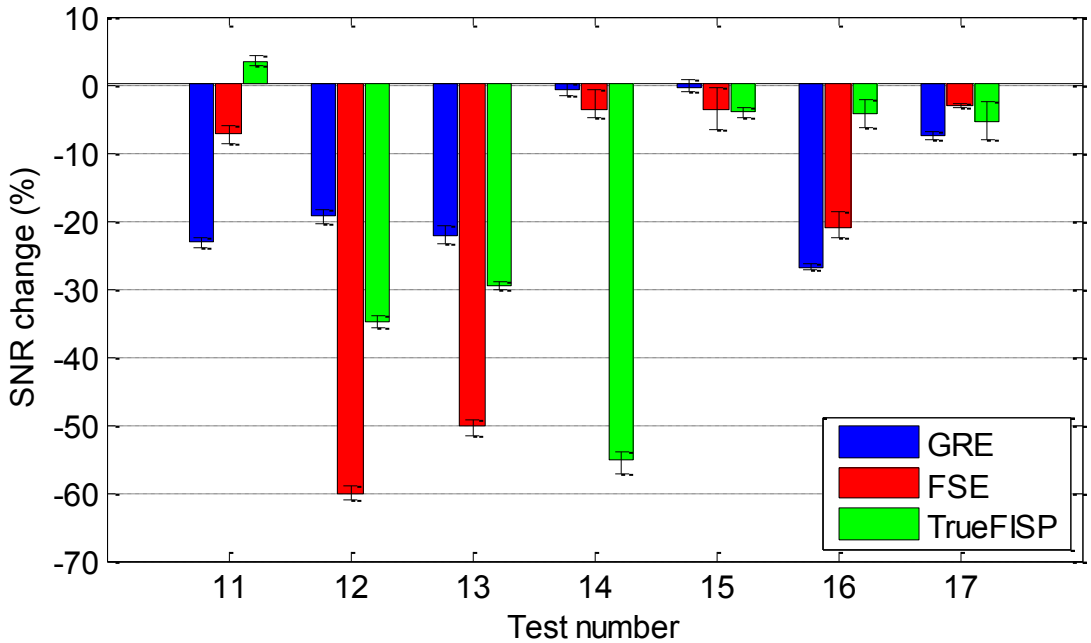

Fig. 6.3.6. Effect on image SNR of changing the shielding, grounding and monitor location of the camera subsystem (see Table 6.3.3). Mean SNR plotted, with error bars representing maximum and minimum results.

When assessed for a single motor, this effect appears to be insensitive to details such as the position of the motor controls and the method used to power the motor. Fig. 6.3.4 demonstrates that the change in image SNR remains below 2% regardless of these details, provided the control cables remain shielded and filtered when passing through the MRI scanner room shield.

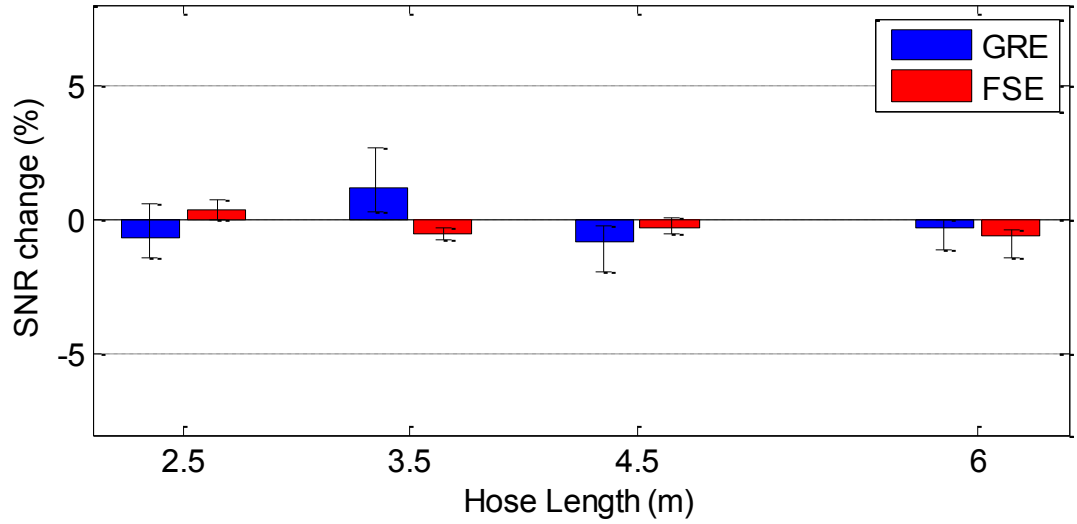

Fig. 6.3.7. Effect on image SNR of increasing clutch hose length and therefore moving the clutch actuation valve away from the scanner isocenter. Mean SNR plotted, with error bars representing maximum and minimum results.

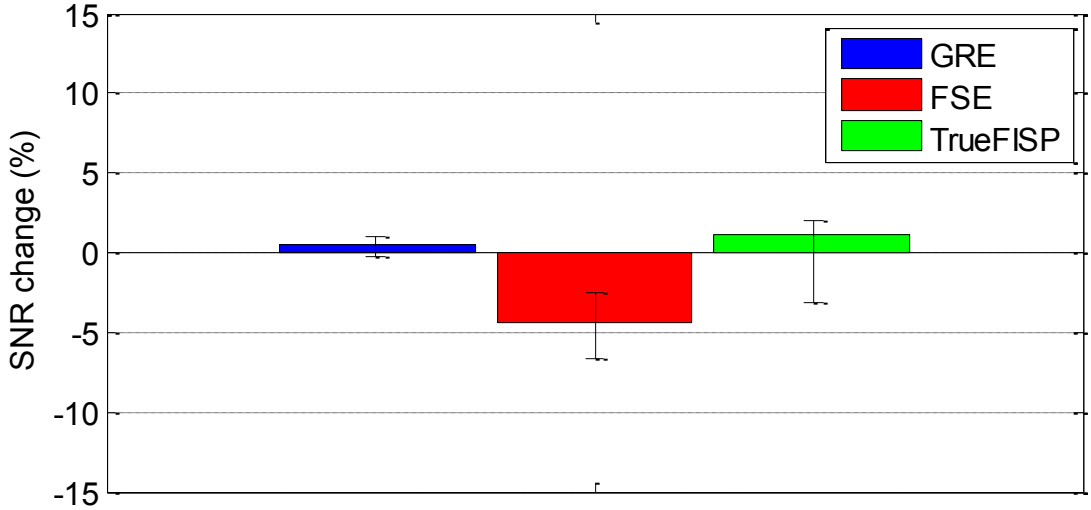

Fig. 6.3.8. Effect on image SNR of complete endoscope actuation system.

However, when the test is scaled up to include the full actuation system, moving the motor controls into the control room causes a greater drop in SNR at 1.5T (GRE and FSE sequences) when compared with a single motor and when compared with the system images acquired at 3T using the TrueFISP sequence (Fig. 6.3.5). The difference between the single motor and system results may be related to the type of filter used on the cable as it connects through the MRI scanner room shield – the greater number of connections on the system cable necessitated the use of a more compact capacitor filter rather than the more effective pi filter (see Section 5.7.3).

As with the motor, the presence of unshielded wires passing from a source of electromagnetic noise into the scanner bore appears to be an issue with the endoscope camera. The introduction of the endoscope camera onto the MRI scanner bed is not in itself enough to cause a significant drop in image SNR for the FSE or TrueFISP sequences (Test 11, Fig. 6.3.6). However, if the camera is connected to the endoscope with it's tip inside the imaging volume then there is a significant drop in image SNR (Test 12). This is despite there being no conductive path between the camera body and the endoscope steering wires (see Section 4.4.1), suggesting that the electromagnetic interference is transmitted through inductive coupling between the camera and steering wires.

Both the camera and motors have external metal casings that are connected to the negative DC supply terminal – under some circumstances these could form electromagnetic shields. The effectiveness of this shielding was investigated in Tests 8 and 9 for the motor and Tests 13 - 15 for the camera. Tests 8 and 9 in Fig. 6.3.46 show that connection of the motor negative DC terminal (and therefore the casing) to the scanner room shield (Ground terminal) has little effect on the SNR of the GRE and FSE images, but serves to degrade the SNR of the TrueFISP images. The same can be seen in Fig. 6.3.6 when comparing Tests 14 and 15 – connection of the camera external casing to ground degrades the TrueFISP image SNR. Test 13 demonstrates that grounding of the camera external casing without an additional external shield is not sufficient to shield the MRI scanner from the camera for any of the image sequences.

These results demonstrate that in order to be fully shielded to prevent electromagnetic interference, the active components of the endoscope remote actuation system on the scanner bed must be covered with an external shield and their power source must be fully isolated from the scanner room shield. The cause of this interference may be the presence of ground loops within the circuit between the camera and scanner room shields, which could be facility dependent – hence the differing interference observed between the image sequences acquired using the 1.5T and 3T MRI scanners.

Once the camera and endoscope were isolated from the MRI scanner, alternative locations for viewing the camera image were evaluated (tests 16 and 17, Fig. 6.3.6). If the operator is to be inside the MRI scanner room then the simplest method for displaying the endoscope video is to set up a monitor inside the room. However, Test 16 demonstrates that even a small battery powered monitor, if unshielded itself, can cause an unacceptable degradation of the MR images. If the camera feed is to the monitor in the control room shield via a filtered connection (see Section 5.7.3) as in Test 17 then the MR image degradation is limited. Most modern MRI facilities have a monitor that is visible from

inside the scanner room and integrated into the scanner system. With the endoscope camera feed accessible from the scanner room such facilities can be utilised.

The effect of on image SNR of activating the clutch solenoid valve during imaging is shown in Fig. 6.3.7. Due to magnetically induced force on the magnetic components of the pneumatic valve, a hose length of less than 2.5 metres could not be used. Compared with the reference image, there was no significant reduction in image SNR due to the presence of the pneumatic valve when it was more than 2.5 metres from the imaging volume – the SNR of all image slices was within 1.2% of the reference image regardless of hose length.

Fig. 6.3.8 demonstrates that when combined, the most effective shielding and filtering solutions for the endoscope actuation system (Test 9) and the camera (Test 17) result in a loss in image SNR of less than 5% compared with reference images. This result is consistent with the sub-system results and is within the performance criteria outlined in Section 6.2.

6.4 Functional Testing

6.4.1 Introduction

The functional performance of the endoscope remote actuation system is dependent on both the technical capacity of the system (such as the available torque and range of motion) as well as the user interface of the system. These factors are heavily dependent on the scenario which the user is presented with and the user's existing abilities.

To account for these factors an assessment tool was developed that enables the technical performance of a user to be objectively measured on a repeatable simulation of biliary cannulation. The assessment tool was validated by comparing the performance of a range of operators with known levels of endoscopic skill, before being used to measure how operators' performance changed when they used the endoscope remote actuation system.

6.4.2 Background

Quantitative assessment of technical skill in medical operations and particularly endoscopy is an expanding field, with many approaches being developed concurrently. Traditionally, skill is defined by surrogate markers of performance such as number of procedures completed, cannulation rate and procedure completion rate. This does not give any detailed information regarding an operator's strengths or weaknesses [Pfau,

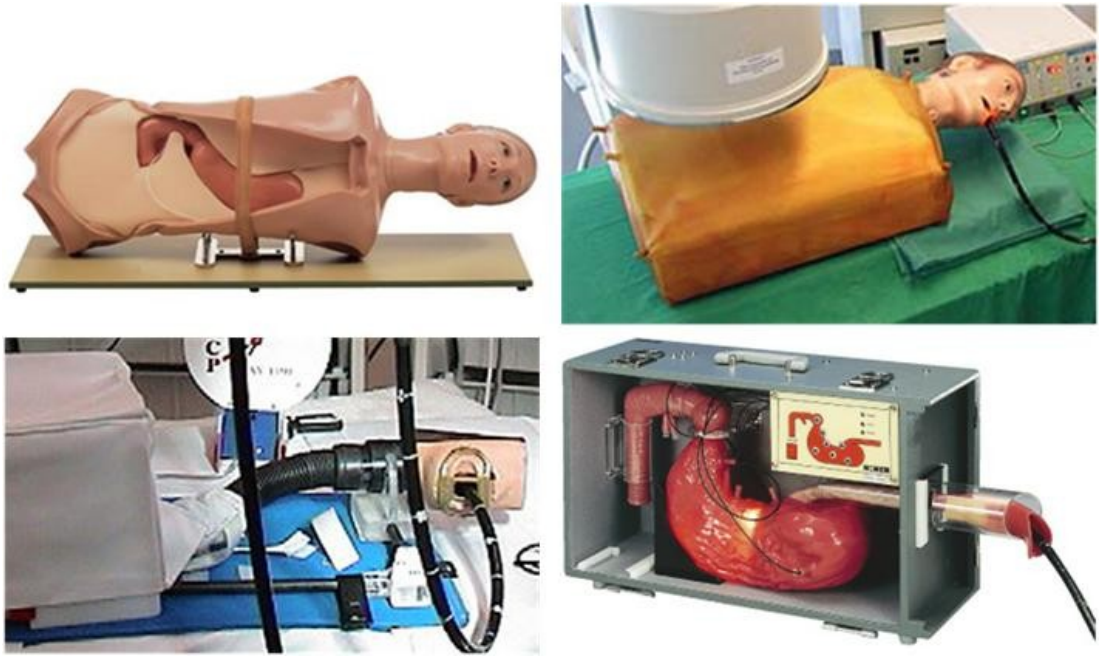

Fig. 6.4.1 ERCP training simulators (clockwise from top left) AC4 OGI Phantom (Adam Rouilly, Kent, UK); Hands-on simulator [Grund, 2012]; ERCP Training Model LM-022 (Koken Ltd, Tokyo, Japan); and ERCP Mechanical Simulator [Leung, 2007]. See also Fig. 6.4.4.

2011] and does not take into account the variation due to patient and case-specific factors.

To provide a more in-depth assessment of endoscopic skill, standardised observational scoring systems have been developed [Memon, 2010; Vassiliou, 2010] which demonstrate good correlation between rating scores and experience. However, despite efforts to provide clear ranking guidelines and remove inter-assessor variability these remain subjective metrics that require oversight and moderation by expert endoscopists. Assessment of skills in a clinical setting will always be subject to patient variation and the difficulty of the cases attempted.

A number of endoscopic simulators have been developed in an effort to provide a repeatable environment to assist with training and skills assessment. Indeed, modern training programs commonly incorporate simulation training into their syllabus [Desilets, 2011; Ende, 2012; Leung, 2011]. Simulators fall into four categories: mechanical models, computer simulations, animal models and harvested organ simulators [Leung, 2011; Memon, 2010; Sedlack, 2003a]. While animal models and harvested organs offer the most realistic endoscopic challenge in terms of visualisation and tactile feedback they can be prohibitively expensive, challenging to work with and prone to the same variability as a clinical setting [Leung, 2011]. Computer simulations offer a variety of repeatable

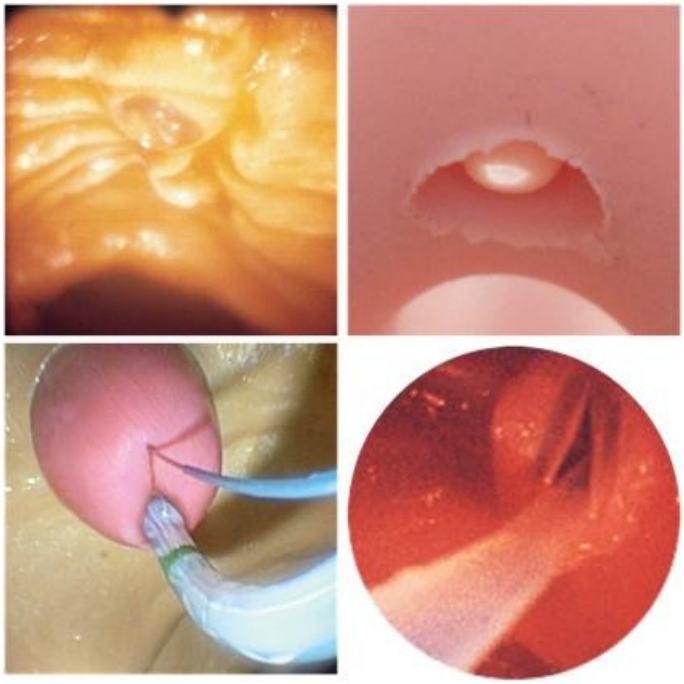

Fig. 6.4.2. Internal views of ERCP training simulators (clockwise from top left) AC4 OGI Phantom (Adam Rouilly, Kent, UK); ERCP Trainer (The Chamberlain Group, MA, USA); ERCP Training Model LM-022 (Koken Ltd, Tokyo, Japan); and Hands-on simulator [Grund, 2012].

scenarios, but they can also be expensive and do not allow standard endoscopic equipment and tools to be used. Some studies have shown that the performance metrics of computer simulations bear little resemblance to clinical performance [Sedlack, 2003b].

Mechanical training simulators available specifically for ERCP focus on two aspects of the procedure: intubation of the patient and cannulation. Intubation of the patient requires the upper GI tract (mouth, oesophagus, stomach) to be reproduced in detail. The upper GI tract has a complex shape and consists of many different tissues, making a realistic mechanical simulation challenging, but a model designed to train operators for this stage of the procedure is produced by Adam Rouilly Ltd. and variations are reported in [Grund, 2012; Leung, 2007].

The ERCP training simulators referenced above all include a model of the papilla and can therefore be used to train operators in the cannulation phase of the procedure. In addition, there are commercially available simulators that do not include realistic upper GI tracts and are only aimed at cannulation training and identification of anatomy (Fig. 6.4.2). All three commercially available simulators have very basic models of the papilla and ampulla, which are rigid and have large, obvious openings through which access is gained to the bile duct. Because of this they only present a limited challenge to cannulate,

even for inexperienced operators. The models developed by Grund et al [Grund, 2012] and Leung et al [Leung, 2007] are intended to address these issues as well as providing a setting for therapeutic training by modelling the papilla with soft rubber parts. However the visual and tactile fidelity of these components is not clear from the published literature.

Studies have shown that an operator's skill in using mechanical models correlates with their experience level, suggesting they can act as a valid tool for assessing clinical skills [Leung, 2011; Plooy, 2012]. As well as being highly repeatable and capable of simulating a range of scenarios, mechanical models enable standard endoscopic equipment to be used during training and are much more cost effective.

Development of objective performance metrics for assessment and certification purposes in the medical profession is ongoing, and has been identified as an area requiring further research [Pfau, 2011]. Studies of training simulators [Leung, 2007; Sedlack, 2003b] have used the time taken to complete various stages of the procedure as an objective measurement of operator skill. This can fail to take account of factors such as the trade-off between speed and accuracy of endoscope control [Parthornratt, 2011], and the potentially dangerous consequences of poorly controlled endoscopic tools. Another study [Plooy, 2012] combined time measurements with a force sensor to measure the peak force applied to the simulator by the operator, penalising operators that risk harming the patient by using excessive force.

In the growing field of kinematic performance assessment electromagnetic position sensors are used to measure dexterity and skill by tracking tool movements. These methods have been applied to simulated image-guided needle insertion [Tabriz, 2011], laparoscopy [Datta, 2002] and colonoscopy [Obstein, 2011]. In all cases the results indicate that kinematic analysis scores generally correlate with experience, while variations from the linear trend suggest that the scores are a measurement of skill and not simply experience. The metrics used for performance assessment are procedure specific and a standardised technique for deriving them for a given procedure does not currently exist.

6.4.3 Study Design

Direct comparisons between operators' performance at a standardised task when using the remote actuation system and when operating manually were used to assess the functional capabilities of the remote actuation system. Operators were asked to perform biliary cannulation of a mechanical simulator and the movements of the duodenoscope tip

Operator Experience Group	Description	Number of Subjects	Mean number of ERCP completed (min,max)
1	Foundation Year Doctor	6	0 (0, 0)
2	Gastrointestinal Registrar	7	20.6 (2, 45)
3	Specialist ERCP Registrar	5	129 (75, 150)
4	ERCP Consultant	3	>200

Table 6.4.1 Categories of study participants.

and catheter were tracked during the procedure using an electromagnetic tracking system.

A kinematic scoring system was derived to enable a quantitative comparison between the electromagnetic tracking system data for each test run. The validity of the mechanical simulator and the scoring system was determined by comparing the performance of a number of operators of known skill levels during their manual attempts of the task. Finally operators' performance scores at the manual task were compared with their score when using the duodenoscope remote actuation system to determine the functional capabilities of the remote actuation system.

A total of 21 volunteers attempted the simulated biliary cannulation task both manually and with the remote actuation system. The subjects were characterised as consultant endoscopists specialising in ERCP (>200 procedures completed, n= 3), senior registrars specialising in ERCP (50-200 procedures completed, n= 3), junior gastroenterology registrars (<50 procedures completed, n= 7) and Foundation year doctors with no endoscopic experience (n= 6, see Table 6.4.1).

Each operator was given a brief explanation of the duodenoscope and training simulator (see below) before the duodenoscope was placed in the simulator at the junction between the plastic and silicone tubing that corresponds to the pylorus. The operator was then asked to attempt to cannulate the bile duct of the model, with the test run being deemed complete when the bile duct was cannulated. Only data from each operator's first manual and first remotely actuated test runs were directly compared, to remove the effect of a learning curve due to familiarity with the specific task. In some cases subjects completed the biliary cannulation simulation more than once with the remote actuation system (see Section 6.4.7). In these cases only the first run was considered for the model validation and remote actuation system comparison, although these results were used to inform the discussion on learning curves below.

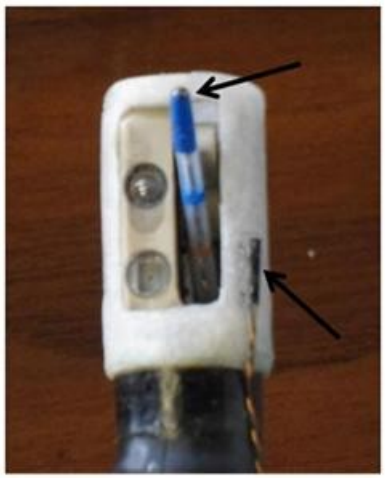

Fig. 6.4.3 Duodenoscope tip showing catheter and tip mounted electromagnetic tracking sensors (arrows).

The cannulation task was performed using the MRI compatible duodenoscope described in Section 4.4.1 and, when used, the remote actuation system was in the unclutched configuration described in Section 5.3. The duodenoscope video feed was visualised on a computer monitor and recorded using a USB video capture card (StarTech, Northampton, UK). During each test run the position of the duodenoscope and catheter tip was recorded at an update rate of 40Hz using an electromagnetic tracking system (Aurora, Northern Digital Inc., Ontario, Canada). The recorded data was analysed using a Matlab script (MathWorks Inc., MA, USA) and was analysed alongside digital video obtained from the endoscope camera.

A 5 DOF tracking coil was mounted at the tip of the catheter in the guidewire channel, with a second on a cap fitted on the outside of the duodenoscope tip (Fig. 6.4.3). The choice of sensor positions reflects the specific procedural challenges experienced during bile duct cannulation. While Obstein et al [Obstein, 2011] used sensors placed along the length of the endoscope to measure flex and curvature during colonoscopy, bile duct cannulation is performed with the duodenoscope in a relatively fixed position opposite the ampulla. Therefore placement of separate sensors on the endoscope tip and catheter during the present study allowed the operator's ability to control the catheter to be separated from their endoscope control.

6.4.4 Biliary Cannulation Simulator

A modified version of a commercially available ERCP simulator (The Chamberlain Group, MA, USA) was used for this study (Fig. 6.4.4). As outlined above, this model is includes only a rudimentary upper GI model. This is appropriate for this study because the

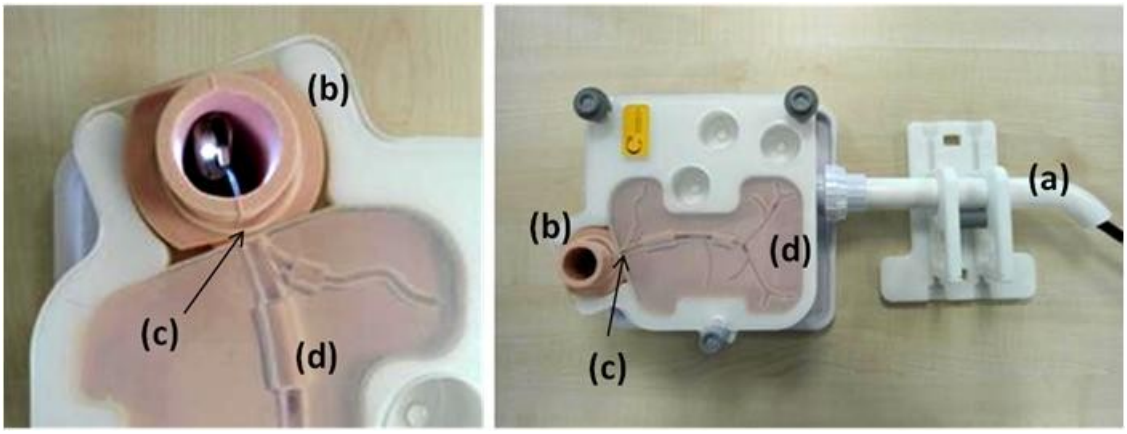

Fig. 6.4.4. ERCP Trainer manufactured by The Chamberlain Group, showing (a) simplified upper GI tract, (b) rubber duodenum part, (c) location of ampulla part and (d) biliary tract.

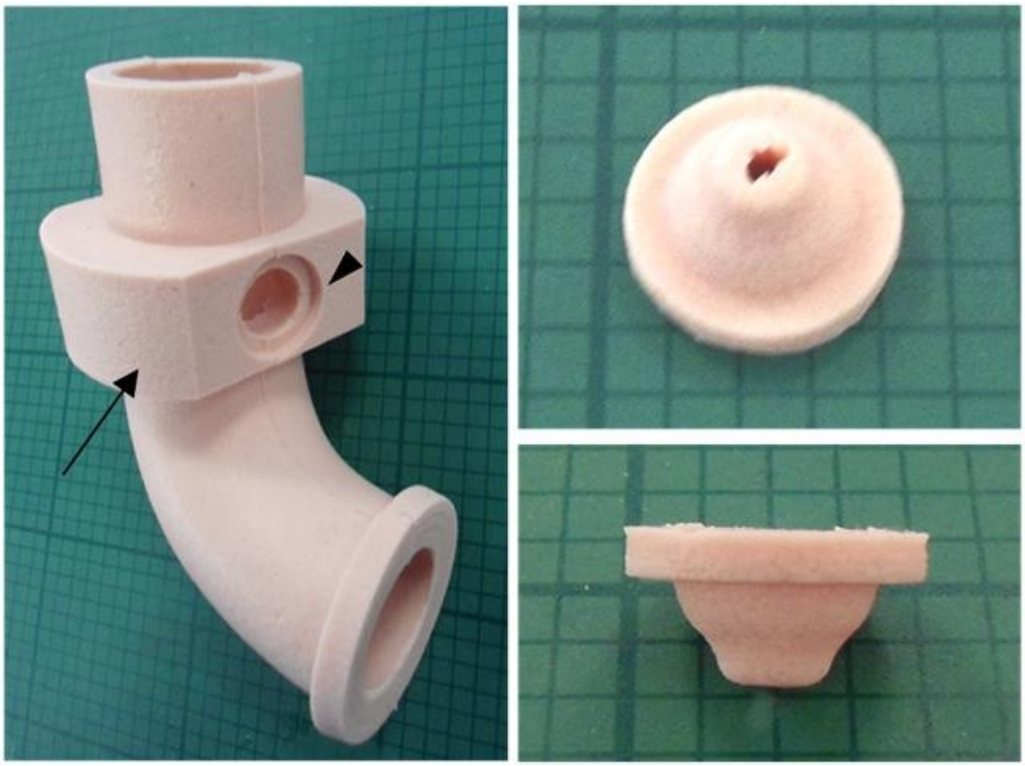

Fig. 6.4.5. Original rubber parts of the ERCP Trainer. Duodenum part shown (l) with recess for ampulla (arrowhead) and collar for locating within simulator frame (arrow). Ampulla part shown from the top (top right) and side (bottom right).

endoscope remote actuation system is designed to be used only for the cannulation phase of the procedure and not for intubation (see Section 4.3).

The simulator consists of a length of plastic tubing (intended to represent the oesophagus and stomach) connected to a rubber representation of the duodenum and biliary tree, between which is a silicone foam ampulla model (Fig. 6.4.5). Preliminary

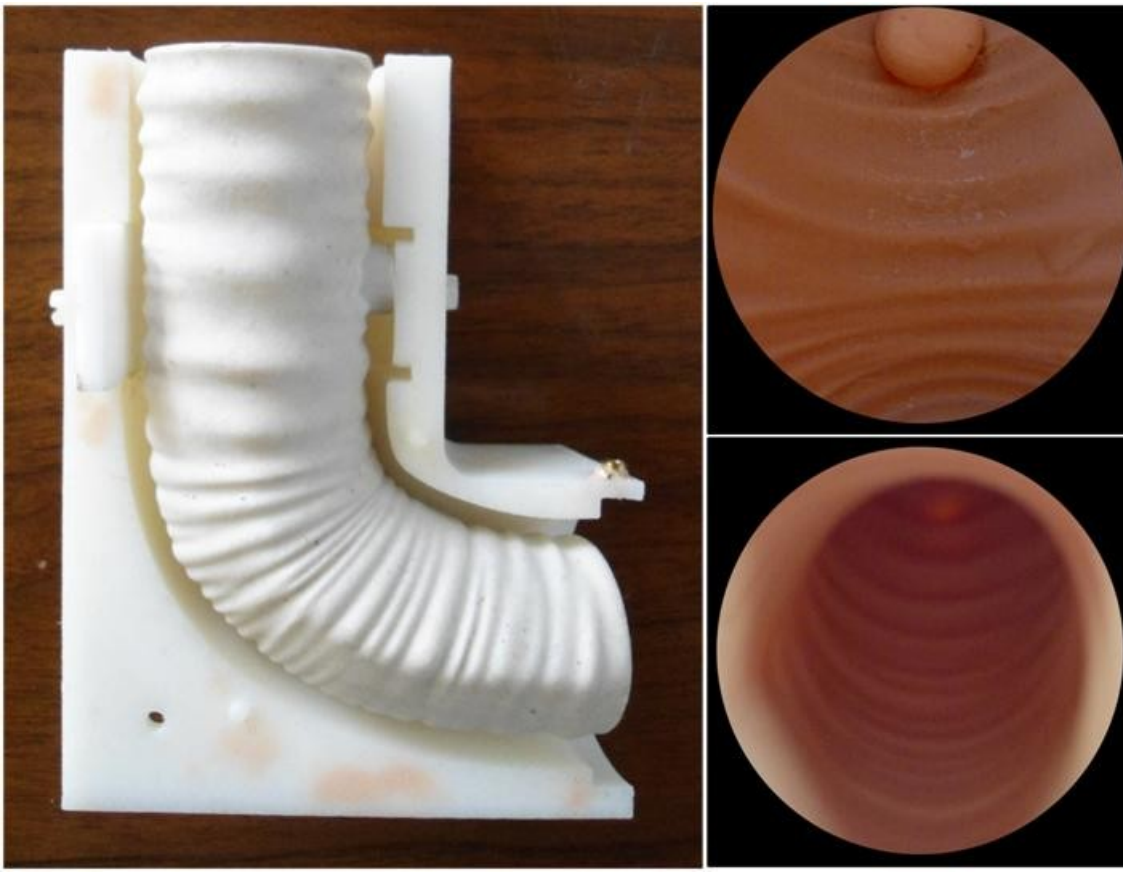

Fig. 6.4.6. Modified duodenum part. Rapid prototyped mould for the duodenum part shown (l), with endoscopic views of the inner surface of the modified duodenum (r). The modified ampulla part can be seen in the top right image.

testing with the simulator indicated a number of areas that needed to be improved in order to make it a realistic challenge of biliary cannulation.

The original duodenum section is made from 5mm thick solid silicone rubber that is moulded around a reinforcement mesh. This construction makes the part extremely durable, but also increases it's stiffness, particularly in the area around the ampulla which includes the collar used to locate the duodenum part in the simulator (Fig. 6.4.5). Because of this the duodenum section acts as a guide to the duodenoscope tip, which simplifies the cannulation task because very little duodenoscope tip steering is required by the operator; advancement of the duodenoscope flexible section without steering is sufficient to position the tip opposite the ampulla. Additional deformation would be desirable to allow the duodenoscope tip to get caught and therefore require a more complex manoeuvring strategy to correctly position the tip without damage to the model, as in the real-life clinical situation.

In addition to this, the internal appearance of the original duodenum part is smooth, with no discernible features other than the separate ampulla part. This is in stark

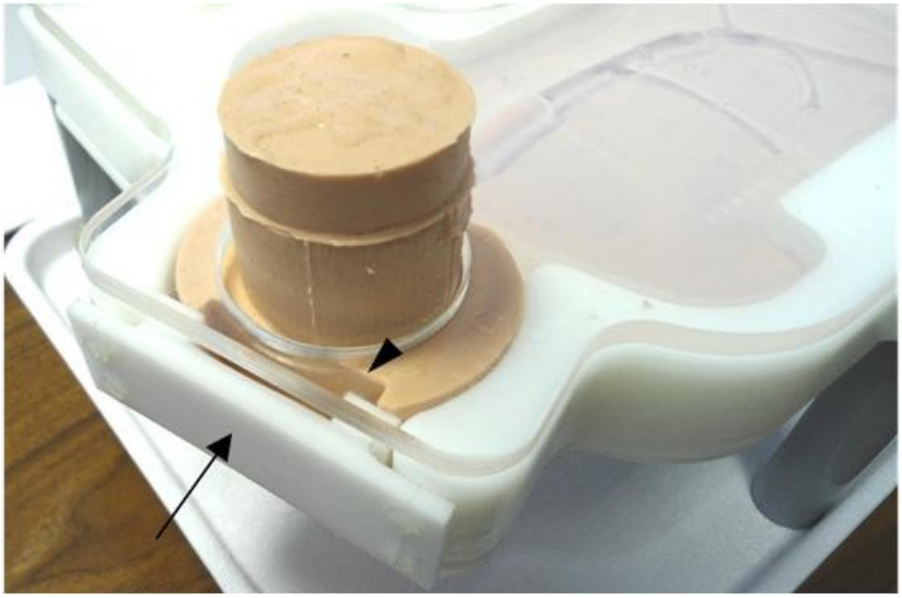

Fig. 6.4.7 Modified duodenum part mounted on training simulator, showing plate to compress duodenum against biliary tract (arrow) and void that allows duodenum wall to remain flexible despite the additional compression force (arrowhead).

contrast to the human duodenum, which has numerous folds and ridges on it's inner surface. These features are used by endoscopists to provide a reference of their orientation and give visual feedback to their movement input, so it is desirable to reproduce them in the simulation.

A modified duodenum part was manufactured to improve on these factors. The part was moulded from solid silicone rubber (Platsil 7315, Mouldife Ltd., Sussex, UK) that was chosen for it's low stiffness (shore hardness 15A). The five-part mould was manufactured using a sintered-powder rapid prototyping process (Z-Printer, 3D Systems, SC, USA), which produces a non-porous mould with good release properties and enables the shape of the mould to be precisely controlled. The shape of the mould was drawn using CAD software (Solidworks, Dassault Systémes, MA, USA), with the inner part lofted from a set of splines with random 2mm deviations from the nominal profile. The rubber is 1.5-3.5mm thick along the unsupported length of the duodenum, and this thickness is maintained in the critical area opposite the papilla by removing some of the locating collar. These changes resulted in a moulded part with realistic appearance due to the ridges on the inner surface (Fig. 6.4.6), while the softer and thinner rubber means that the tactile and mechanical feedback of the part was greatly improved.

The duodenum section is mounted in the training simulator by a collar at the proximal end that fits into a plumbing fitting to hold it against the plastic tubing and a larger collar around the ampulla area (Fig. 6.4.5). The second of these is compressed

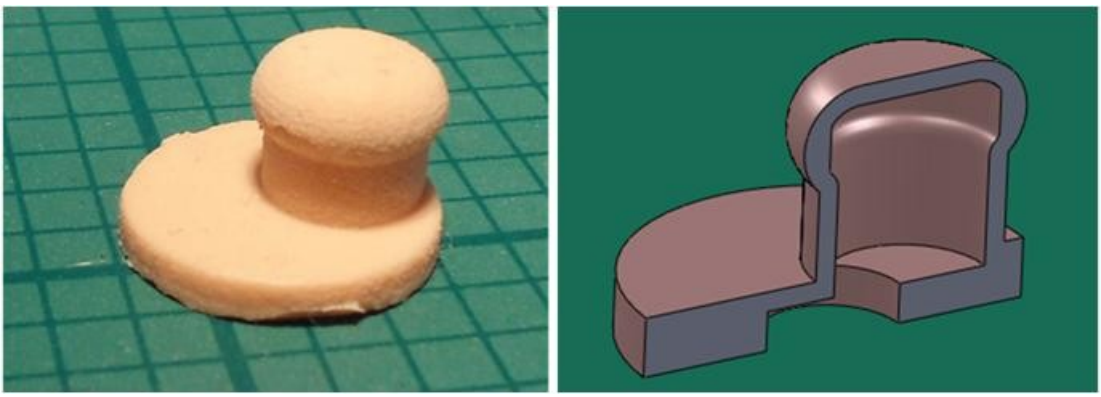

Fig. 6.4.8 Modified ampulla part (l) moulded from silicone rubber and (r) cross sectional view of part CAD model. The hole piercing the top surface of the ampulla is not visible in this image.

inside the plastic frame of the simulator, which pushes it against the ampulla and biliary tree parts. In the original configuration this compression was insufficient, which resulted in the catheter slipping through the gap between parts and not reaching the bile duct after passing through the ampulla. To improve this, an adjustable plastic compression plate was added to the outside of the simulator frame (Fig. 6.4.7) and was shaped to compress the outer collar of the modified duodenum part without supporting the duodenum wall and compromising it's flexibility (see above).

The part of the model that represents the papilla and ampulla also required significant modification. The original part has a very simplistic structure in which the papilla is extremely flat and includes a large hole to represent the opening at the end of the ampulla (Fig. 6.4.5). The combination of the flat, stiff structure and large opening makes the task of cannulating the model relatively easy. Advancing the catheter toward the opening at almost any angle will result in successful access to the bile duct, with the part's stiffness guiding the catheter into the right place.

A modified ampulla part was manufactured to improve the visual, tactile and mechanical feedback of the model and increase the difficulty of the cannulation task. As with the duodenum part, the modified ampulla was made from silicone rubber (Platsil 7315, Mouldlife Litd., Sussex, UK) using a rapid prototyped mould.

The recess on the duodenum part into which the ampulla part locates was moved upward and the papilla made longer so it protrudes into the duodenum lumen. The protruding section of the modified papilla is hollow and has walls that are an average of 1mm thick. The end of the hollow section adjacent to the bile duct part has a narrow opening that is offset from the opening on the outer wall of the papilla (Fig. 6.4.8). Instead of moulding a hole into the outer wall of the papilla to cannulate through, the outer wall is

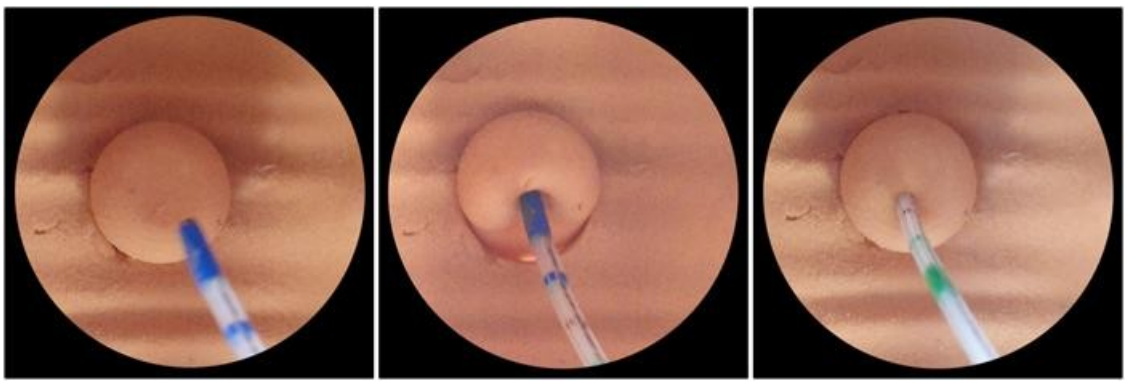

Fig. 6.4.9. Endoscopic image series showing cannulation of the modified ampulla part: (l) catheter is advanced towards papilla, (m) incorrect catheter positioning results in papilla deforming and catheter failing to access the ampulla, and (r) catheter cannulated correctly through the papilla into the ampulla.

pierced by a needle before assembly into the model. This piercing deforms enough to allow the catheter to pass through it during cannulation, but is very hard to see on the duodenoscope optical image.

These changes result in a requirement for the endoscopist to introduce the catheter into the papilla from above, which from the endoscopic perspective appears as between 10 and 12 o'clock. This is similar to the approach recommended during ERCP training, as outlined in Section 4.2. Incorrect approach angles result in the catheter being stuck inside the hollow ampulla section, or being guided towards the pancreatic duct. The hollow thin-walled structure of the papilla and indistinct opening mean that the papilla surface must be probed in the correct place in order to cannulate. Probing with the catheter in the wrong place causes the papilla to collapse and results in the catheter getting stuck before passing into the bile duct (Fig. 6.4.9), as in the real clinical situation.

In summary, the modifications made to the simulator result in the task of biliary cannulation being both more difficult and more realistic. The flexibility of the duodenum and ampulla parts combined with the hollow ampulla section mean that the duodenoscope and catheter must be positioned correctly in order to successfully cannulate the simulator. The inner surface of the duodenum and protruding ampulla provide a realistic visual environment for the endoscopist allowing the experienced operators to use their skills in a more familiar context.

6.4.5 Kinematic Performance Analysis

The electromagnetic tracking system consists of a magnetic field generator unit, sensor interface units and a system control unit. The system records the position and angle of

#	Parameter Name	Calculation Method	Rationale
1	Number of ampulla contacts	Sensor position data analysed to find points coinciding with prior measurements of the ampulla position. Confirmed with analysis of the duodenoscope video.	Probing of the delicate ampulla and papilla can result in inflammation and tissue damage. A more skilled operator is assumed to seek to minimise these contacts.
2	Total distance travelled	Sum of the Pythagorean distances (in mm) between consecutive datapoints for the duodenoscope tip and catheter sensors.	A shorter distance travelled suggests the operator can accurately guide the endoscope tip and catheter to the desired location.
3	Time taken to cannulate	Test started when the proximal end of the duodenum was passed by the endoscope tip sensor, and ended when the catheter sensor passed through the distal face of the ampulla part (Fig. 6.3.11).	A faster cannulation is desirable for patient safety, while completing the task in a shorter time suggests greater operator skill.
4	Trajectory corrections per second	Change in the angle of endoscope heading is measured by calculating the dot product of two successive velocity unit vectors. A trajectory correction is defined as a change in heading angle greater than the timeseries mean plus standard deviation.	Fewer trajectory corrections suggest greater control over the endoscope and catheter. The inclusion of this parameter enables the two cases shown in Fig. 6.4.12 to be distinguished.
5	Mean speed	The average of the Pythagorean length of each velocity vector (see above) for the duration of the test.	In feedback controlled tasks skilled operators will tend to work at greater average speeds due to their greater confidence and skill [Parthornratt, 2011].
6	Time spent planning	Timeseries points that represented a velocity of less than 2mm/s were assumed to represent a lack of control inputs. This is expressed as a percentage of the total number of datapoints.	Operators that are familiar with the equipment were assumed to spend less time considering their next move and a lower percentage of their time planning.

Table 6.4.2. Parameters used to assess operator performance.

sensors placed within the range of the magnetic field generator at 40Hz. The ERCP training simulator was placed on top of the field generator unit with locating tabs mounted on the bottom of the simulator base to ensure repeatable positioning of the simulator relative to the field generator coordinate system (Fig. 6.4.10).

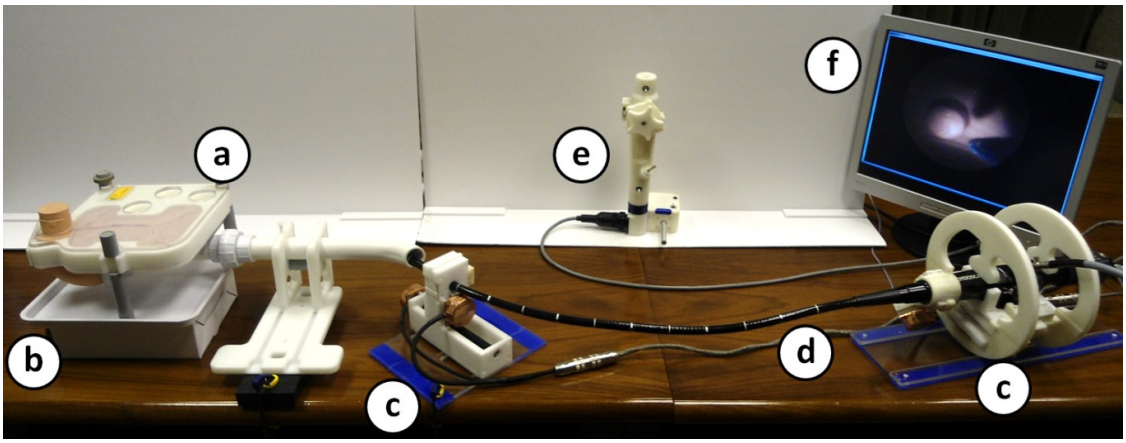

Fig. 6.4.10. Experimental setup showing (a) training simulator, (b) electromagnetic field generator, (c) remote actuator modules, (d) duodenoscope, (e) remote actuation system user interface and (f) monitor for duodenoscope video visualisation.

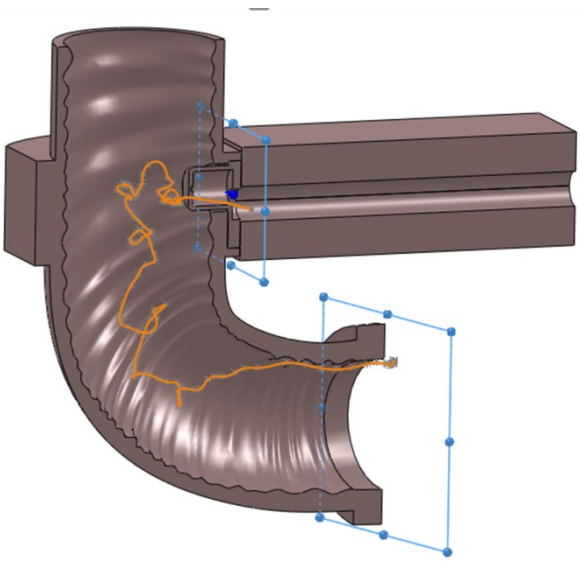

Fig. 6.4.11. CAD model of modified ERCP training simulator with a trace of the catheter electromagnetic tracking sensor (orange) and planes designating test start and end (blue).

The timeseries recorded from the catheter and duodenoscope tip sensors (Fig. 6.4.11) for each test run were filtered using a 2nd order low-pass Buttterworth filter with a cut-off frequency of 10 Hz to smooth out sensor noise. Missing data points due to errors with the tracking system were filled in using a linear interpolation between existing points.

A performance score was calculated (Z) representing endoscopic technical skill based on the tracking system data acquired during each test run. The score is a sum of 6 parameters, each intended to characterise a different aspect of endoscopic skill (Table 6.4.2) using the principle that an expert is faster and more error free at performing tasks

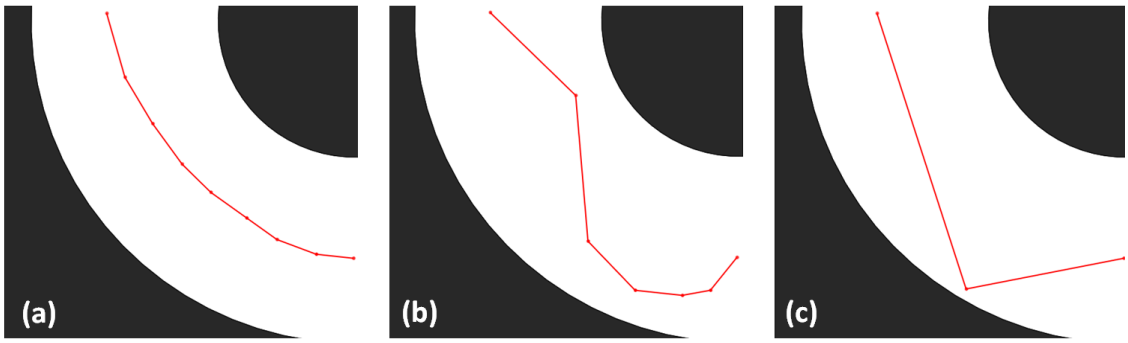

Fig. 6.4.12. Example 2D trajectories to illustrate scoring system. Trajectory (a) covers the least distance and has zero corrections so will score the highest. Trajectories (b) and (c) cover the same distance, but because trajectory (c) has a major correction it will score less than trajectory (b).

compared with novices [Ericsson, 2006]. To calculate a user's score, the value recorded for a user in a given parameter $i\,(X_i)$ is first normalised using the following formula:

$$Q_i = \frac{X_i - \check{X}_i}{\hat{X}_i - \check{X}_i}$$

(Eq. 6.1)

Where the upper and lower values of X_i ($\hat{X}_i$ and $\check{X}_i$ respectively) used to normalise the measurement are derived from the experimental data using maximum and minimum measured values offset by 50%. The normalised measurement (Q_i) is then used to calculate the user score for parameter $i\,(Y_i)$, using to following formula:

$$Y_i = \log_2\left[1 + \frac{1}{Q_i}\right]$$

(Eq. 6.2)

P_i is then used to calculate the operator performance score:

$$Z = \sum [Y_1 + Y_2 + \ldots \mathrm{Y}_6]$$

(Eq. 6.3)

The $\log_2$ format of (Eq. 6.2) is consistent with Fitt's law, which governs motor skills in a feedback controlled task [Parthornratt, 2011]. For all parameters except mean speed, a lower X_i measurement recorded generates an exponentially higher Y_i score, with a higher score representing increased endoscopic skill. Significance was measured by using the

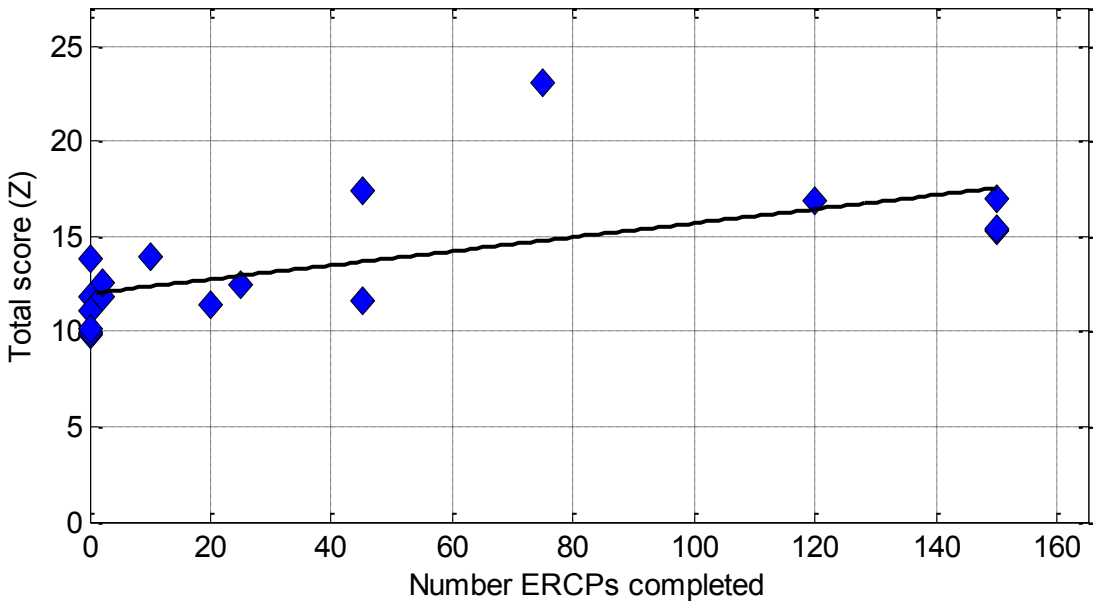

Fig. 6.4.13. Total performance score (Z) plotted against number of ERCPs completed for operators in experience categories 1, 2 and 3. R^2 of trendline = 0.396.

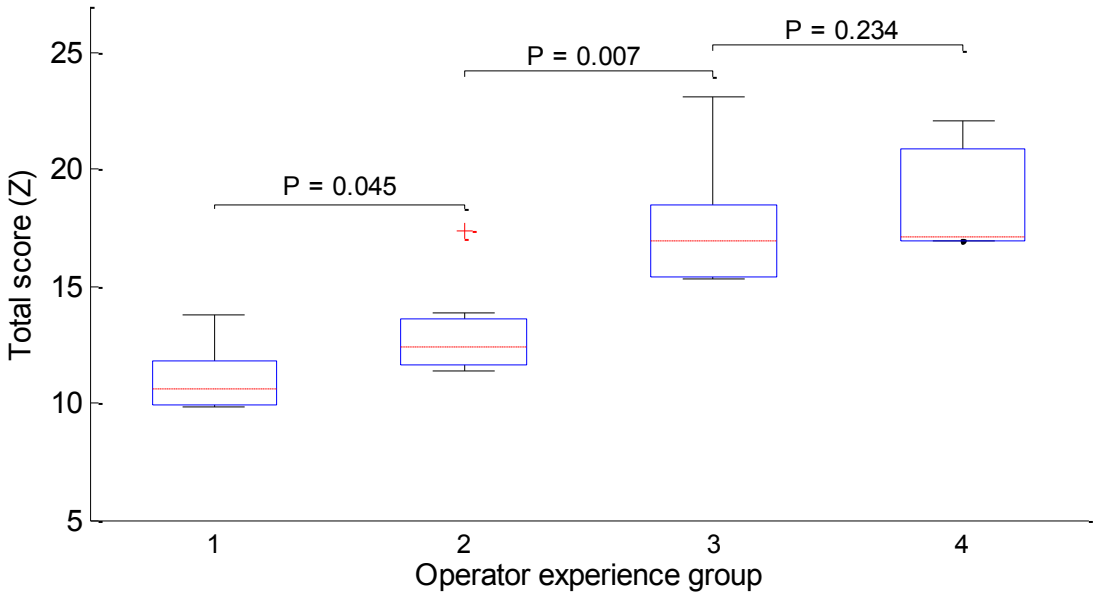

Fig. 6.4.14. Total performance score (Z)plotted against operator experience category, with significance values (P) displayed.

student's T-Test (one tailed, significance level $P \leq 0.05$), while correlation was measured using linear regression models.

Operator Experience Group	Number ERCPs Completed	Ampulla contacts	Total distance travelled	Time taken to cannulate	Trajectory corrections per second	Mean speed	Time spent planning	Total Score
1	0	8 (2.1)	5313 (2.0)	432 (1.4)	0.758 (1.5)	5.96 (1.3)	54.6% (1.5)	9.8
	0	9 (1.9)	1563 (3.7)	212 (2.2)	0.754 (1.5)	4.3 (1.1)	61.3% (1.4)	11.8
	0	6 (2.4)	1214 (4.0)	135 (2.8)	0.573 (1.9)	4.87 (1.2)	53.8% (1.5)	13.8
	0	17 (1.3)	2733 (2.9)	219 (2.2)	0.690 (1.6)	7.66 (1.5)	45.3% (1.7)	11.1
	0	10 (1.8)	3332 (2.6)	483 (1.3)	0.708 (1.6)	3.66 (1.1)	52.5% (1.5)	9.9
	0	15 (1.4)	9699 (1.4)	426 (1.4)	0.684 (1.6)	10.4 5(2.2)	34.5% (2.0)	10.1
2	2	3 (3.2)	4001 (2.4)	382 (1.6)	0.700 (1.6)	6.11 (1.3)	42.4% (1.7)	11.8
	2	5 (2.6)	4258 (2.3)	335 (1.7)	0.563 (2.0)	6.12 (1.3)	21.2% (2.7)	12.6
	10	5 (2.6)	10749 (1.3)	464 (1.4)	0.651 (1.7)	9.48 (1.9)	8.4% (5.0)	13.9
	20	7 (2.2)	6378 (1.8)	373 (1.6)	0.659 (1.7)	7.14 (1.4)	22.2% (2.6)	11.4
	25	10 (1.8)	3888 (2.4)	269 (1.9)	0.395 (2.9)	4.73 (1.2)	31.2% (2.1)	12.4
	45	1 (4.7)	4258 (2.3)	52 (4.4)	0.563 (2.0)	6.12 (1.3)	21.2% (2.7)	17.4
	45	7 (2.2)	3762 (2.4)	270 (1.9)	0.756 (1.5)	7.59 (1.5)	34.2% (2.0)	11.6
3	75	1 (4.7)	280 (7.4)	24 (6.5)	0.728 (1.5)	6.53 (1.4)	48.3% (1.6)	23.1
	120	2 (3.8)	884 (4.6)	66 (3.9)	0.695 (1.6)	6.98 (1.4)	47.6% (1.6)	16.9
	150	6 (2.4)	1410 (3.8)	86 (3.5)	0.652 (1.7)	8.21 (1.6)	27.8% (2.3)	15.3
	150	4 (2.9)	561 (5.4)	77 (3.7)	0.558 (2.0)	4.81 (1.2)	40% (1.8)	17.0
	150	3 (3.2)	782 (4.8)	110 (3.1)	0.697 (1.6)	4.41 (1.1)	53.3% (1.5)	15.4
4	>200	4 (2.9)	687 (5.0)	64 (4.0)	0.606 (1.8)	5.66 (1.3)	32.4% (2.1)	17.1
	>200	2 (3.8)	646 (5.2)	35 (5.3)	0.679 (1.6)	12.41 (3.3)	19.1% (2.9)	22.1
	>200	6 (2.4)	1108 (4.2)	57 (4.2)	0.642 (1.7)	9.69 (1.9)	25.6% (2.4)	16.9

Table 6.4.3. Results for each subject (manual test). Measured values for each parameter are displayed, with the score given to that measurement in brackets. The final column is the sum of the six score parameters.

6.4.6 Training Simulator Validation

6.4.6.1 Manual Test Results

All test subjects successfully cannulated the bile duct when performing the simulated task using the duodenoscope manually. Table 6.4.3 shows the measured values and score components for all 21 test subjects arranged by experience level.

Fig. 6.4.13 shows the performance score of each individual participant from experience groups 1, 2 and 3 plotted against number of ERCPs performed. The linear regression line shows a positive correlation between score and number of cases completed, although the coefficient of correlation (R^2) is low due to the presence of significant outliers from all three experience groups. The median performance scores (Z) for each of the four experience groups along with the interquartile ranges and significance values are shown in Fig. 6.4.14. These results show that with greater than 95% confidence groups 1, 2 and 3 are separate populations; however there is not a significant difference between groups 3 and 4.

Fig. 6.4.15 and Fig. 6.4.16 show the measured results for each of the 6 parameters used to assess the performance score, plotted against operator experience group. In general the trend of all six parameters is as expected - all parameters other than mean speed decrease with increasing experience. For mean speed, heading corrections per second and time spent planning these trends are particularly weak and approximately linear with low gradients. The distance travelled by the sensors and time taken to cannulate show significant discontinuities between experience groups 2 and 3, while the number of ampulla contacts has a significant fall after experience group 1 and a slight upturn for experience group 4.

6.4.6.2 Discussion

ERCP is a complex procedure that requires many skills including endoscopic control, familiarity with fluoroscopy, recognition of pathology and the ability to correctly implement treatments (see Section 4.2). In the context of the duodenoscope remote actuation system, a key skill that needs to be assessed is the ability of the operator to manoeuvre the duodenoscope during the challenging cannulation phase. The results presented above suggest that the biliary cannulation mechanical simulator combined with kinematic analysis is a method capable of providing this information.

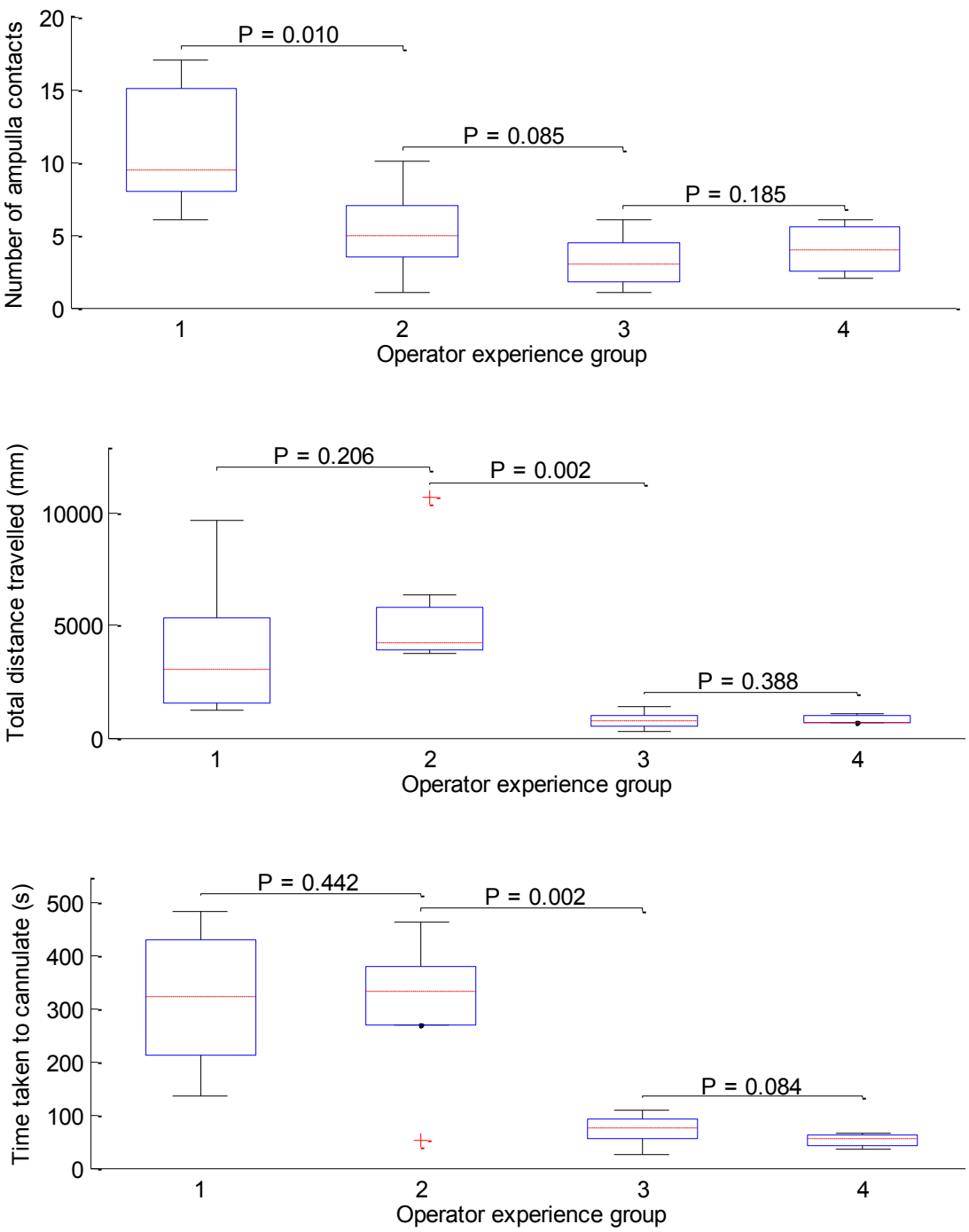

Fig. 6.4.15. Box plots showing measured values plotted against operator experience category for parameters 1, 2 and 3 (top, middle and bottom respectively).

Fig. 6.4.15 and Fig. 6.4.16 show that individually each of the six performance criteria outlined in Table 6.4.2 do not correlate consistently with experience, however when the scores are combined significant trends emerge (Fig. 6.4.14). One reason for this is the choice of scoring parameters, which enables the contribution of different skills and techniques to be assessed. For example the three trajectories shown in Fig. 6.4.12 are clearly different. Trajectory (a) describes a path that covers a short distance with no

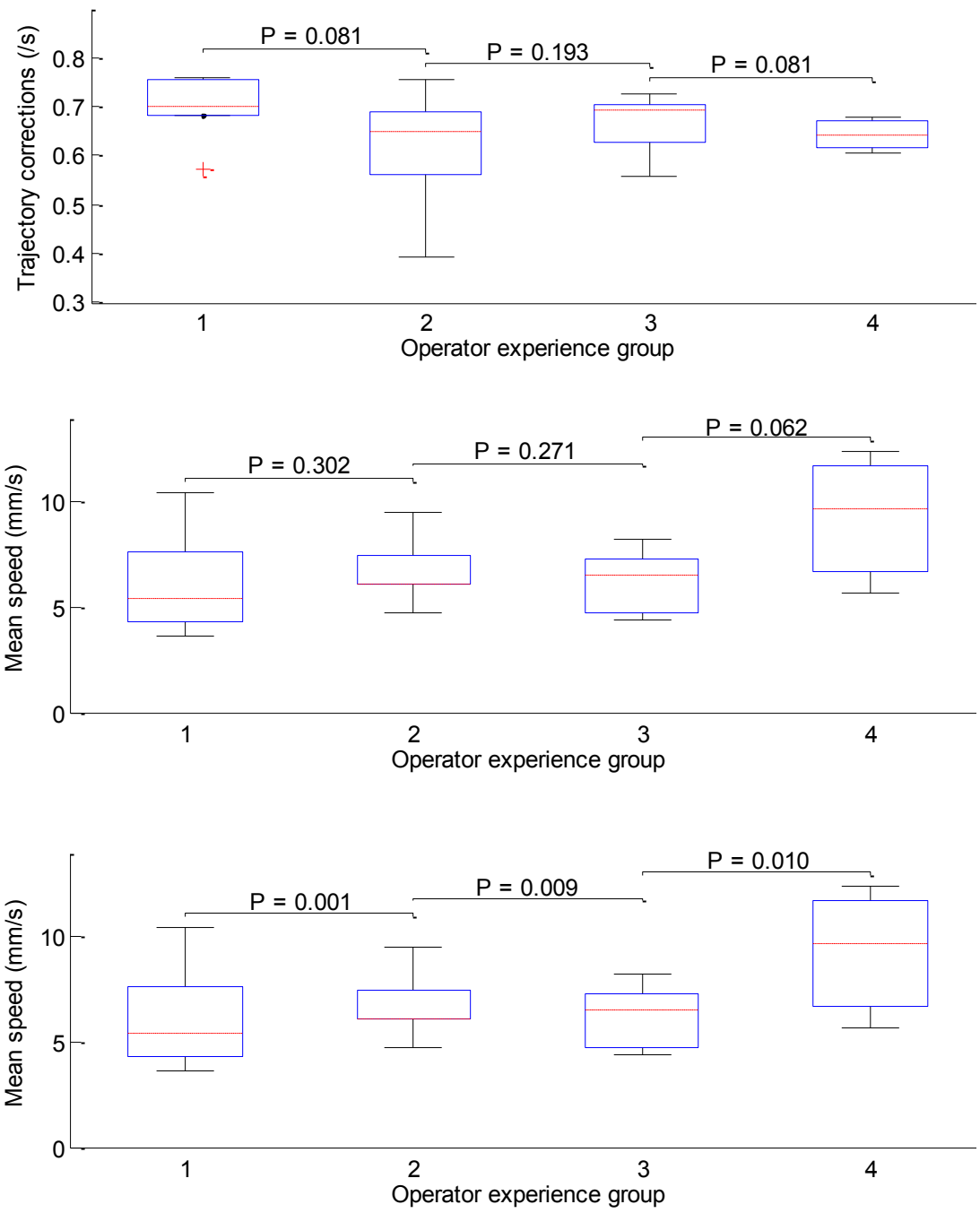

Fig. 6.4.16. Box plots showing measured values plotted against operator experience category for parameters 4, 5 and 6 (top, middle and bottom respectively).

major heading changes, while trajectories (b) and (c) cover the same distance as each other but include a different number of trajectory corrections. Trajectory (a) has the highest score, while the inclusion of a trajectory correction component to the score allows differentiation between trajectories (b) and (c).

The measurements of cannulation time and distance travelled demonstrate the applicability of Fitts' law to this task, as the expected logarithmic decay in measured values with increasing operator experience is observed. The use of the $\log_2$ term in the

scoring algorithm accounts for this, and results in the linear scoring trends seen in Fig. 6.4.14. Due to the low correlation between operator experience and results for the mean speed and time spent planning parameters (Fig. 6.4.15) it may be appropriate to adjust the relative weighting of the parameters or to remove them from the scoring system altogether, although this was not investigated here.

Although there will be variations between individual operators, in general more experienced operators will demonstrate a greater level of endoscopic technical skill. The fact that there is a significant difference in mean scores between operator experience groups 1, 2 and 3 (Fig. 6.4.14) suggests that the simulated cannulation task and scoring system is a valid way of quantifying this endoscopic skill. A lack of significant difference between the scores of groups 3 and 4 is expected since more experienced trainees are likely to have mastered the technical skills of duodenoscope operation that are measured here. Progression from group 3 to group 4 is achieved by competence in more advanced skills such as treatment and recognition of pathology, which are not assessed in this test.

The presence in the test results of outliers that have higher performance scores than their experience would suggest (Fig. 6.4.13) is predicted by models of learning curves [Ericsson, 2006; Kumar, 2011] and suggests that the scoring system is measuring skill as opposed to simply experience. This means that this work has wider significance to the field of endoscopic training and assessment. The mechanical simulator, method of kinematic analysis and scoring algorithm have the potential to be introduced into the curriculum of training centres to enable trainees' skills to be quantified in greater depth. In addition, with further validation the method could be utilised by professional certification bodies. Limitations of this study and the conclusions drawn from it include a small cohort size, particularly in experience group 4, and the reliance on volunteer participants.

6.4.7 Remote Actuation System Testing

With the biliary cannulation simulator and kinematic scoring system validated as an objective measure of skill, it is possible to quantify the effect that using the duodenoscope remote actuation system has on operators' skill levels. A simulated biliary cannulation with the remote actuation system was performed by each operator (see Table 6.4.1) immediately after the manual test run.

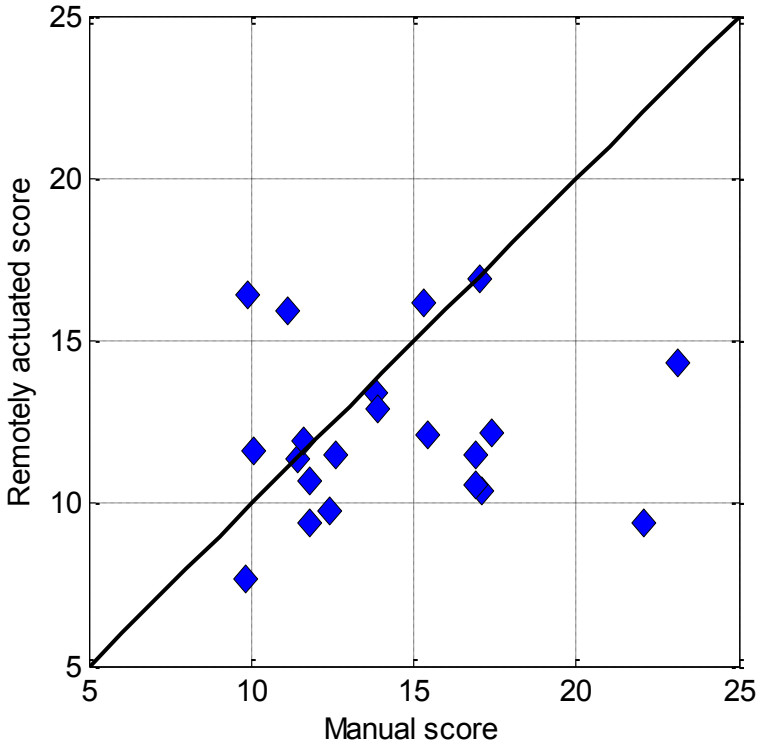

Fig. 6.4.17. Subjects' score for the manually operated test plotted against score for remotely actuated test score. The black line represents an equal score on both tests.

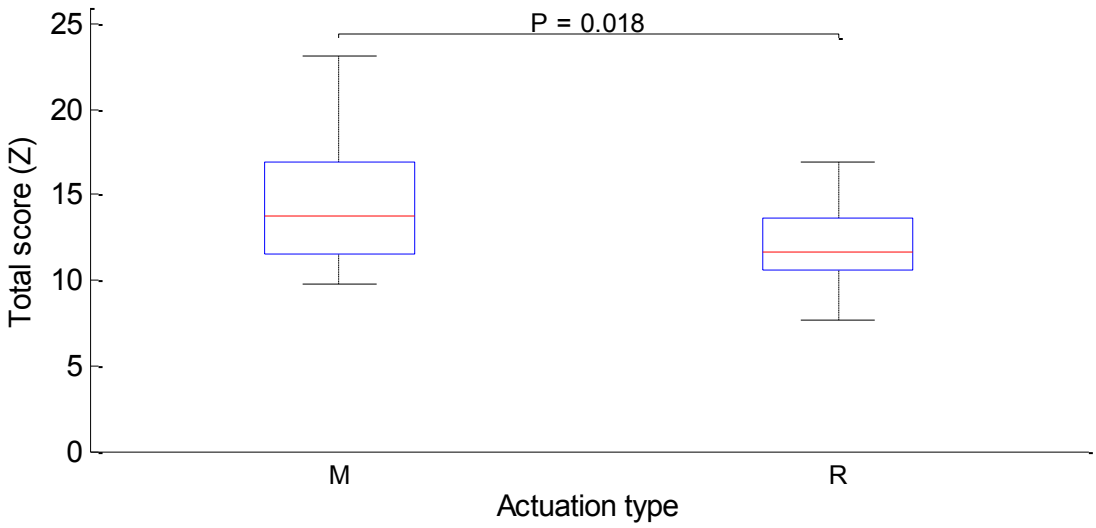

Fig. 6.4.18. Box plot of all operators scores for manually actuated test (M) and remotely actuated test (R).

The learning effect of allowing the operator a second attempt at the biliary cannulation simulator was not corrected for in this study. This was due in part to the number of available participants being limited, which prevented randomisation of the test order. In addition, the exposure to the simulator was brief and any familiarity acquired was anticipated to be less significant than the change of actuation method.

Operator Experience Group	Number ERCPs Completed	Ampulla contacts	Total distance travelled	Time taken to cannulate	Trajectory corrections per second	Mean speed	Time spent planning	Total Score
1	0	25 (1.0)	6362 (1.8)	862 (0.9)	0.722 (1.5)	3.17 (1.0)	58.1% (1.4)	7.7
	0	9 (1.9)	4386 (2.3)	507 (1.3)	0.721 (1.5)	3.98 (1.1)	64.8% (1.3)	9.4
	0	3 (3.2)	897 (4.6)	308 (1.8)	0.643 (1.7)	1.32 (0.9)	75.2% (1.2)	13.4
	0	2 (3.8)	463 (5.9)	133 (2.8)	0.858 (1.3)	1.96 (1.0)	72.4% (1.2)	15.9
	0	1 (4.7)	494 (5.7)	168 (2.5)	0.845 (1.3)	1.97 (1.0)	75.6% (1.2)	16.4
	0	6 (2.4)	1139 (4.1)	434 (1.4)	0.725 (1.5)	1.41 (0.9)	76% (1.2)	11.6
2	2	4 (2.9)	1761 (3.5)	N/A (0.0)	0.573 (1.9)	3.28 (1.1)	63.5% (1.3)	10.7
	25	4 (2.9)	1403 (3.8)	550 (1.2)	0.768 (1.4)	1.72 (1.0)	77.8% (1.1)	11.5
	2	1 (4.7)	843 (4.7)	N/A (0.0)	0.886 (1.3)	1.73 (1.0)	63% (1.3)	12.9
	10	1 (4.7)	5755 (1.9)	524 (1.3)	1.013 (1.1)	0.79 (1.1)	64.7% (1.3)	11.4
	20	8 (2.1)	2454 (3.0)	628 (1.1)	0.762 (1.5)	0.95 (1.0)	72.8% (1.2)	9.8
	40	7 (2.2)	1196 (4.1)	263 (2.0)	0.636 (1.7)	2.16 (1.0)	68.5% (1.2)	12.2
	45	3 (3.2)	858 (4.6)	N/A (0.0)	0.663 (1.7)	2.47 (1.0)	62.7% (1.3)	11.9
3	150	2 (3.8)	822 (4.7)	294 (1.8)	0.65 (1.7)	2.8 (1.0)	64.2% (1.3)	14.3
	150	8 (2.1)	1292 (3.9)	368 (1.6)	0.657 (1.7)	2.02 (1.0)	68.4% (1.2)	11.5
	120	2 (3.8)	581 (5.4)	117 (3.0)	0.66 (1.7)	3.04 (1.0)	63.1% (1.3)	16.2
	75	2 (3.8)	448 (6.0)	110 (3.1)	0.588 (1.9)	2.45 (1.0)	70.3% (1.2)	16.9
	150	8 (2.1)	892 (4.6)	310 (1.8)	0.691 (1.6)	1.69 (1.0)	75.8% (1.2)	12.1
4	>200	10 (1.8)	1712 (3.5)	459 (1.4)	0.727 (1.5)	1.95 (1.0)	76.1% (1.2)	10.4
	>200	8 (2.1)	1509 (3.7)	N/A (0.0)	0.77 (1.4)	2.32 (1.0)	75.6% (1.2)	9.4
	>200	6 (2.4)	1915 (3.4)	618 (1.1)	0.685 (1.6)	1.57 (0.9)	76.7% (1.1)	10.6

Table 6.4.4. Remotely actuated test results for each subject. Measured values for each parameter are displayed, with the score given to that measurement in brackets. The final column is the sum of the six score parameters.

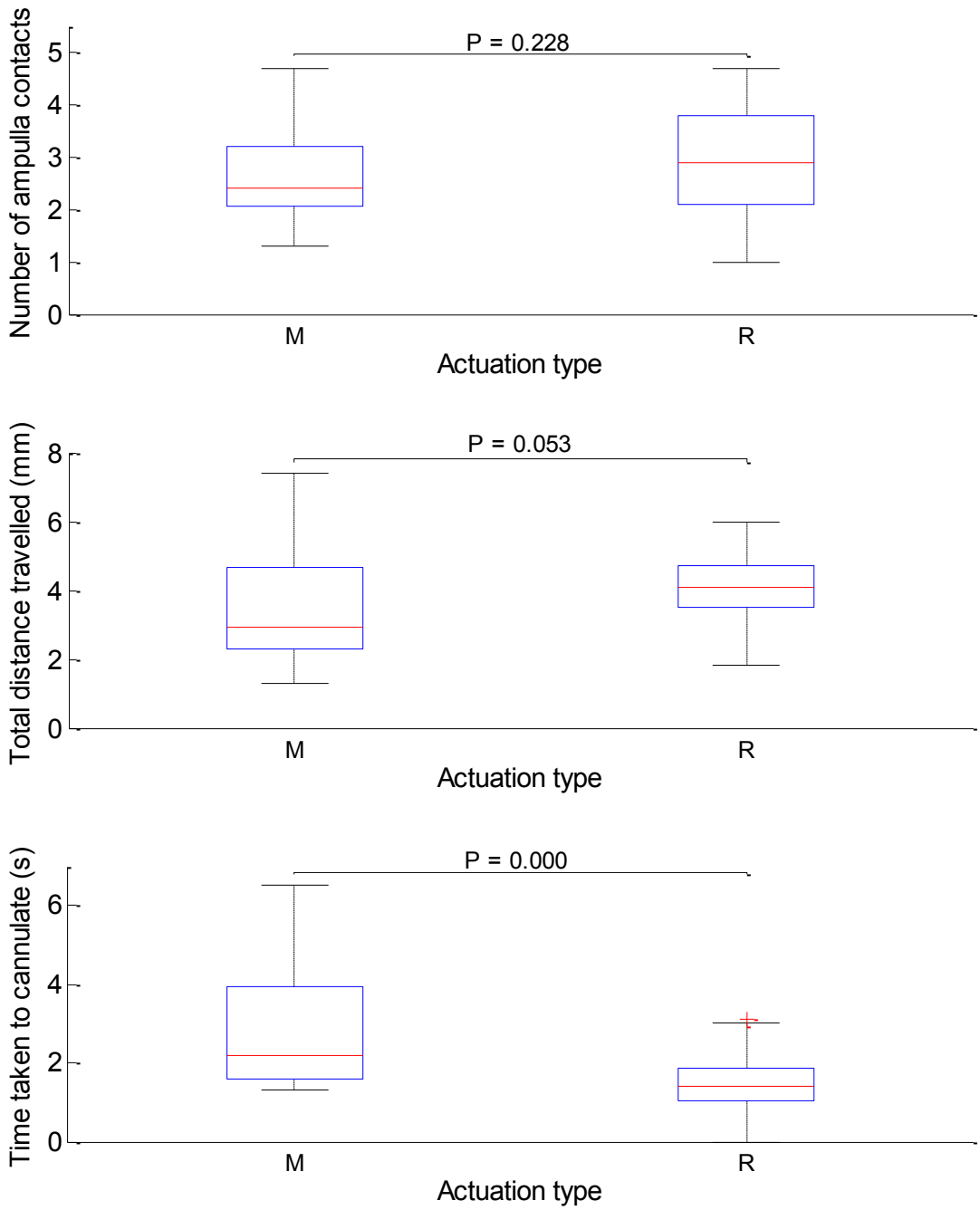

Fig. 6.4.19. Box plots of all operators' scores for parameters 1-3 (top, middle, bottom respectively), separated by manual actuation (M) and remote actuation (R).

6.4.7.1 Results

Four of the operators failed to cannulate the bile duct during the available test time, and were consequently given a score of zero for the 'time taken to cannulate' parameter. Table 6.4.4 shows the measured values and score components for all 21 test subjects arranged by experience level.

Fig. 6.4.17 shows that there is little correlation between an operator's manual and remotely actuated test scores, however the black line shows that only three operators

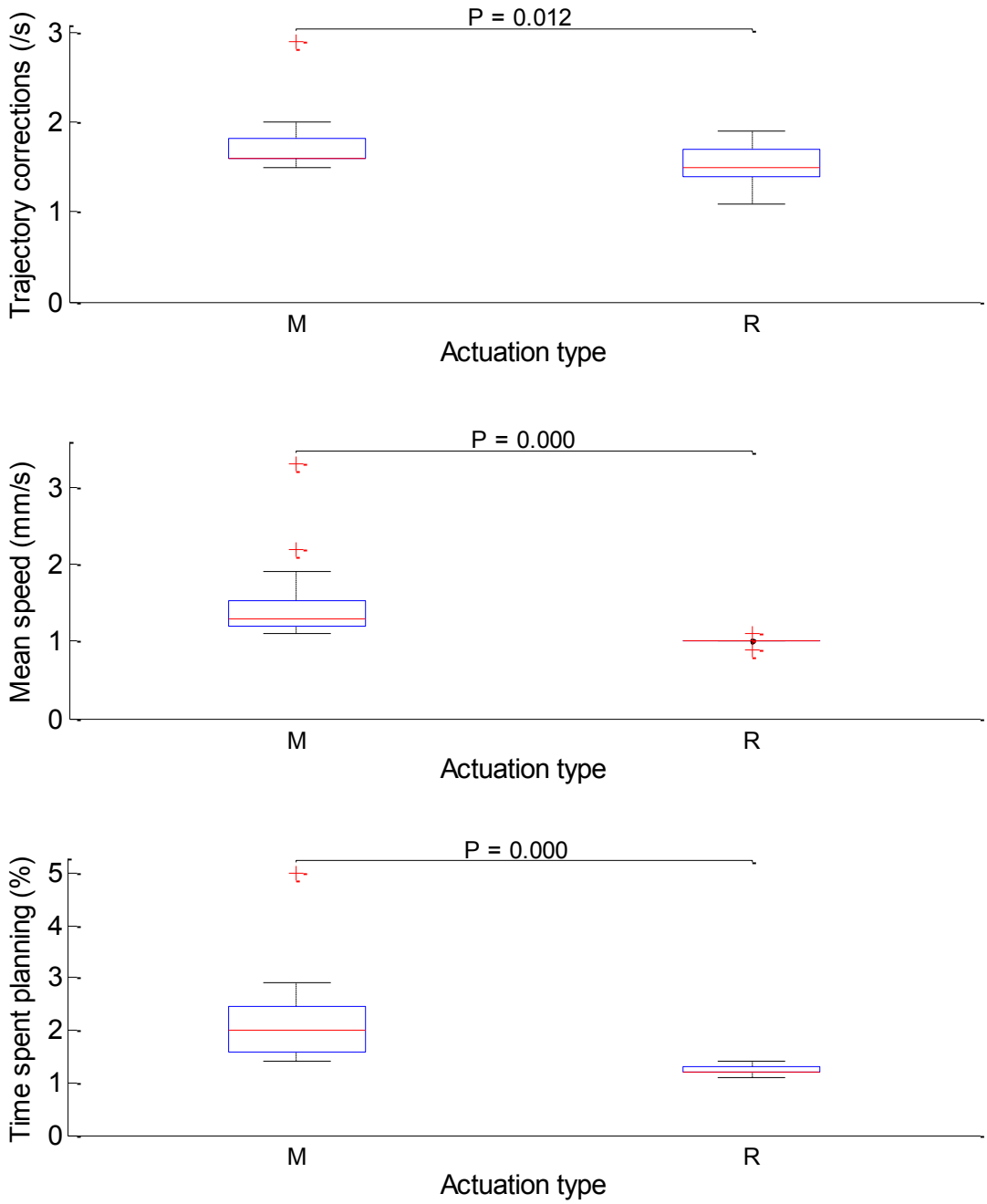

Fig. 6.4.20. Box plots of all operators' scores for parameters 4-6 (top, middle, bottom respectively), separated by manual actuation (M) and remote actuation (R).

scored higher on the remotely actuated task than the manual task. This is confirmed by the box plot Fig. 6.4.18, which suggests that the remotely actuated test scores were lower on average and exhibited a lower interquartile range than the manual test scores.

The scores for each parameter (Fig. 6.4.19 and Fig. 6.4.20) show the overall drop in score is a result of significantly lower scores for planning, mean speed and time taken to cannulate. The planning time and mean speed in particular exhibit very little spread in

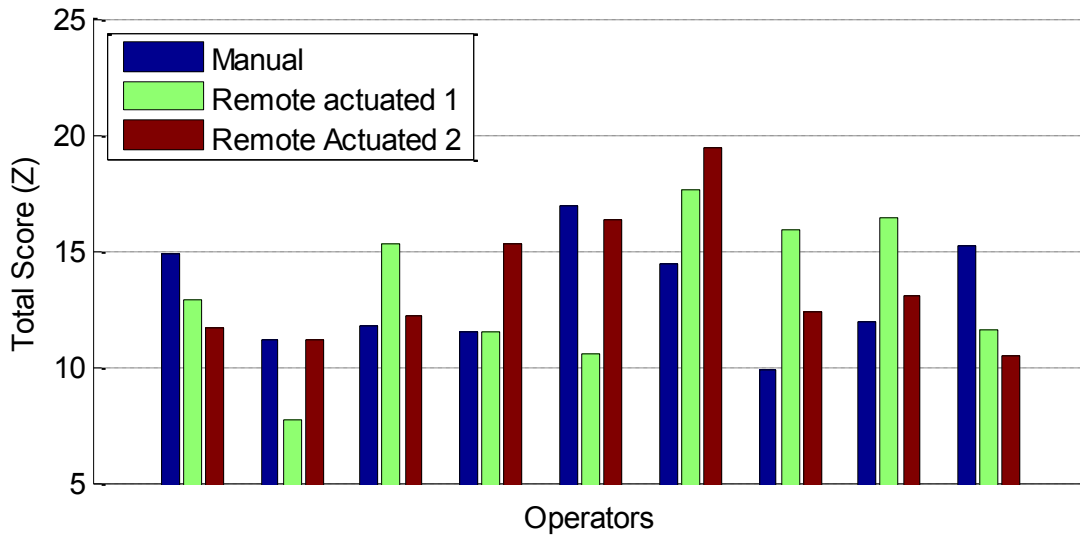

Fig. 6.4.21. Comparison between test runs for operators that completed a second remotely actuated test run.

results. The results using remote actuation have higher median values for the trajectory changes per second, distance travelled and ampulla contacts parameters, although in all three the interquartile range is large.

Due to restrictions on the availability of volunteers, only 9 subjects completed a second test using the remote actuation system (Fig. 6.4.21). The small sample size and limitation of only two tests being completed prohibit any conclusions from being drawn regarding learning curves, although it is noted that the highest score achieved was with the remote actuation system and not manually.

6.4.7.2 Discussion

The results presented here demonstrate the functional capability of the duodenoscope remote actuation system. For the 21 operators that completed both tasks the median operator performance score fell from 14.3 to 11.5 when manual duodenoscope actuation was changed to the remote actuator system. From (Fig. 6.4.14) this is equivalent to the average operator in this study going from a registrar with a medium level of experience to a novice endoscopist.

However, the situation is more complex than a simple drop in the skill level of each operator. Fig. 6.4.17 demonstrates this, by illustrating the lack of correlation between a subject's manual and remotely actuated score. This suggests that the skills that contribute to an operator's performance on the manual task do not translate well to the remotely actuated task and vice versa. Specific training on the use of the remote actuation system may be required to achieve the necessary level of technical skill consistently.

The highest remotely actuated scores achieved are in the region of an experienced registrar or consultant, so clearly the remote actuation system is capable of enabling an operator to achieve a high score on this task, provided they are sufficiently skilled. The limited results available for operators' second attempts at remotely actuated cannulation are inconclusive, but again suggest that high scores for technical skill are achievable, with the highest score on a second attempt being above 18 and firmly in the range of the most skilled operators.

The remote actuation system limits the operators' ability to rapidly manoeuvre the duodenoscope and catheter regardless of their technical skill, due to the limited power and fixed gearing available from the ultrasonic motors (see Section 5.2). This can be seen in the scores recorded for the mean speed and, to a lesser extent, time taken to cannulate parameters (Fig. 6.4.19 and Fig. 6.4.20), and contributes to the lower average score achieved by subjects using the remote actuation system. This is offset by the higher average scores for the distance travelled parameter achieved by the remotely actuated system.

The average score for the planning time parameter was relatively low when the task was attempted using the remote actuation system. The very low interquartile range suggests this is operator independent, as with the mean speed parameter, and may be the result of the actuation system itself. For these tests the planning time was defined as periods when the sensors were not moving and in some cases the sensors did not move despite the operator activating one of the remote actuation system controls.

One cause of this could be backlash, either in the remote actuator system or in the duodenoscope itself. The actuator modules themselves are relatively free of backlash due to the small modulus gears used. However the effect of backlash in the duodenoscope tip steering cables and flexible section is magnified by the use of the speed control rather than position control. When operating manually the backlash of the steering cables is intuitively compensated for by the operator, as they will rapidly turn the control past the region in which the steering cable is slack. Since the actuator modules operate at roughly constant speeds the steering wheel remains in this region for a relatively long time, amplifying the time for which there is no recorded sensor movement.

This is illustrated in Fig. 6.4.22, which was generated by using a microcontroller to record the user inputs during an attempt to cannulate the simulate bile duct using the remote actuation system. Event (a) relates to backlash in the duodenoscope tip steering cables, as this DOF was previously actuated CCW for some period before being reversed. Event (b) relates to a straightening of the duodenoscope flexible section due to a brief reversal of the feed direction. The CCW lobe at event (c) begins with an output movement

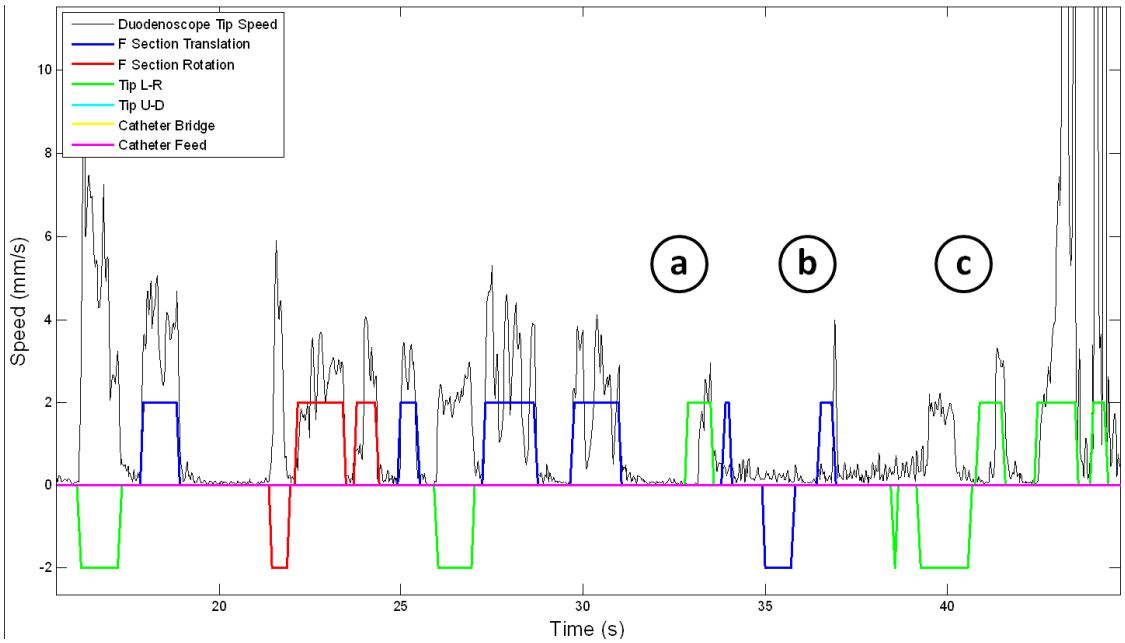

Fig. 6.4.22. Excerpt from a test run to cannulate the simulated bile duct using the remote actuation system. The black line corresponds to the speed of the duodenoscope tip sensor speed. Coloured lines indicate user inputs, with +2 corresponding to the motor rotating clockwise (CW) and –2 corresponding to the motor rotating counter clockwise (CCW).

but the duodenoscope tip stops before the input is stops. This is due to the tip steering control reaching the extent of it's movement.

The increase in the time spent planning parameter during the remotely actuated test could also be related to the user interface of the remote actuation system. Feedback from test subjects highlighted several areas that could be improved, as well as some benefits that the system offers over manual control. The change to speed control from position control required practice, although opinion was divided on which control system was best suited to the task. Speed control has the advantage of enabling very precise movements over a shorter range; however it can be slow and frustrating for larger movements, particularly with the increase in backlash described above.

Most controls on the user interface handle were utilised correctly, however several subjects reported issues with the rod used to control the duodenoscope flexible section degrees of freedom, particularly the more experienced operators. Test observations showed that two techniques are used to manually apply torque to the duodenoscope flexible section: either by grasping it in the right hand and twisting, or by turning the control handle with the left hand and utilising the torsional rigidity of the duodenoscope to transmit this torque along the flexible section. The remote actuation system user interface handle operates in a manner analogous to the first technique only,

but a number of operators struggled to overcome their instinct to use the second technique. This had the effect of increasing frustration levels as well as breaking the operator's concentration as they searched for the control while attempting to coordinate other movements. A modification to the position of the flexible section controls on the user interface handle would improve this issue.

In both the manual and remotely actuated tests the video feed from the duodenoscope tip provides visual feedback to enable the operator to guide the duodenoscope and catheter. However, when operating manually the user has additional tactile feedback from the duodenoscope controls, which are removed by the presence of the remote actuation system. Test subjects experienced this as an issue when control inputs stop causing the duodenoscope to move and therefore do not change the video image. Without knowledge of the position of the duodenoscope controls and tactile feedback from the instrument the user has no way of knowing why the duodenoscope has stopped moving. Instances of this occurred particularly when the tip steering wheels reached the end of their range of travel, and when the catheter was inadvertently retracted into the body of the duodenoscope. This issue could be overcome by the use of haptic feedback sensors on the actuation modules, however the incorporation of MRI compatible haptic feedback into the actuation system is a major challenge and outside the scope of this thesis. Position sensors could also be included in the actuation modules and their outputs displayed to give the operator a reference during the procedure. This development of was not seen to be critical, since the feedback issue did not inhibit this study and could be overcome by giving the test subjects an introduction and a chance to familiarise themselves with the equipment before beginning the test.

An area in which the remote actuation system was reported to provide a positive benefit to duodenoscope handling was the application of a holding torque by the ultrasonic motors. Due to their method of operation these motors cannot be back-driven, which means that once a position has been achieved the operator is not required to use further control inputs to maintain that position. This is in contrast to manual operation of the duodenoscope, during which the operator sometimes struggles to maintain a position of one DOF while actuating another, particularly in the case of the flexible section. The remote actuator system allows the operator to halt and consider their next manoeuvre without danger of losing the desired duodenoscope position.

6.5 Conclusions

Use of the endoscope actuation system, endoscope and camera have been shown to cause a degradation in image SNR of less than 5% when operating inside the MRI scanner during scanning sequences. The robustness of this result has been investigated by exploring the effect of the active devices on three different imaging sequences while changing parameters such as the position of controls, monitors and shielding setups. The precise design of the device shielding outlined in Section 5.7 has been shown to be critical, particularly as it applies to the endoscope camera.

A tool for objective, quantitative measurement of endoscope technical skill has been developed in order to assess the functional performance of the endoscope remote actuation system. This tool consists of a modified biliary cannulation simulator combined with an electromagnetic tracking system to give operators a kinematics-based score for their technical skill. A comparative study involving endoscopists at a range of skill levels confirmed that the assessment tool distinguishes between skilled and unskilled operators.

The remote actuation system was assessed using the objective measurement tool. Operators were able to complete the simulated task and in some cases exhibited considerable skill at manoeuvring the duodenoscope with the remote actuation tool. The average of all operator scores is lower for the remotely actuated test compared with the manual test. However this is not consistent for individual operators and there is no evidence that the remote actuation system prevents the procedure being performed with a high level of technical skill. Limitations of the system due to operator experience, ergonomics and sensors were identified as areas for future development.

Chapter 7

Duodenoscope Tip Tracking in MRI

7.1 Introduction

This chapter describes the development of a method to enable the tip of the duodenoscope and the catheter to be tracked inside the MRI scanner. With this method the MR receiver coils mounted at the tips of the tools can be used as active tracking coils, which enables more information to be provided to the endoscopist during the cannulation phase of the procedure, while also facilitating the application of direct motion compensation during the acquisition of high quality diagnostic MRI using the internal receiver coils, as discussed in Section 2.2.3.

7.2 Background

In order for the MRI guided endoscopy system described in this thesis to function optimally, it is important to be able to determine the location of the interventional tool relative to the intra-operative images. This enables the operator to interpret the intra-operative images correctly and determine the required procedural steps to move the tool towards the desired target. This is quantitatively investigated in Chapter 8.

In addition, precise high-speed tracking of the duodenoscope tip and catheter will enable high-quality images of the surrounding anatomy to be acquired without motion artefacts. Navigator imaging sequences for motion compensation (see Section 2.2.3) are available to provide information about the movement of the diaphragm; however studies [Bilgin, 2009; Brandner, 2006] have shown that each abdominal organ moves differently under respiratory motion. The flexible duodenum and bile duct which are only loosely connected to the diaphragm will experience this phenomenon, particularly with the presence of the duodenoscope inside the duodenum. Instead of generating a complex and empirical motion correction model based on the diaphragm motion [McClelland, 2013], an accurate and rapid measurement of the duodenum and catheter positions can be used to perform motion compensation during the MR image acquisition sequence.

In order to provide these benefits to the procedure a coil location method must be able to accurately determine the position of the coil. Improved accuracy is always desirable, but at a minimum the method must be able to determine the position of the coil within the MRI slice thickness (typically 5mm), while the coil angle must be known to an accuracy of $\pm 10°$ to position it within a single slice. In addition, because a typical respiratory cycle takes around 4 seconds to complete [Clifford, 2002], a high update rate is required in order to provide sufficient information to apply motion correction to acquired images.

Passive device tracking from images is used by some interventional MRI systems (see Section 3.4), but it suffers from a very slow update rate due to the need to acquire and process image data. It is also highly dependent on the contrast between the device and surrounding tissue, and for this reason passive tracking generally involves a high contrast marker being mounted on the interventional tool to aid the tracking algorithm. However, there is no area available on the duodenoscope tip or catheter to mount such a marker (see Section 4.4.1), making this approach subject to potential instability in addition to the speed limitation.

Active device tracking is characterised by a faster update rate and inherently more robust performance than passive device tracking; it is preferred for the majority of flexible interventional MRI tools reported in the literature (see Section 3.4). Active device tracking coils are typically small solenoids, which have a limited spatial sensitivity and contain a quantity of MR signal producing material in the centre. These two design features mean that the signal acquired from the coil is a single, well defined peak with a high SNR, making determination of the centre of the coil computationally simple. The orientation of the device is determined from the location of several coils rigidly mounted on the device.

As noted above, the duodenoscope tip and catheter do not have space available for additional tracking coils. Furthermore, such a coil on the device could interfere with the tip imaging coils. The work presented in this section was undertaken to explore whether the existing duodenoscope and catheter tip imaging coils can be used as active tracking coils to determine the location of the devices within the MRI scanner coordinate system. An experiment based around the duodenoscope tip imaging coil is described along with the development of an algorithm for processing the tracking signals and determining the location and orientation of the coil.

7.3 Materials and Methods

7.3.1 Coil Position Measurement Method

The standard procedure for active MR tracking is to obtain a signal using a series of one-dimensional (1D) MR projections and then determine the location of the tracking coil by determining the location at which the peaks of orthogonal projections intersect [Dumoulin, 1997]. This procedure has been adapted to the case where an MR imaging coil is mounted at the duodenoscope tip.

The 1D projections are acquired by using a RF pulse to excite a large volume (500mm^3) within the centre of the MRI scanner and then applying a frequency encoding gradient in a single direction during signal acquisition (Fig. 7.3.1). Each point on the projection acquired therefore corresponds to the signal received from a plane orthogonal to the direction of the frequency encoding gradient (Fig. 7.3.2).

The signal acquired by an MR receiver coil is a function of it's spatial sensitivity and the composition of objects within that space. The tip imaging coils are designed to have a large spatial sensitivity to MR signals, which enables them to acquire images with a clinically useful field of view. Therefore the 1D projection exhibits a broad series of peaks instead of the single sharply defined peak seen in most active tracking systems. The magnitude of the peak increases significantly close to the centre of the coil. The tracking method presented here utilises this feature, and assumes that the geometrical centre of the broad peak on the 1D projection corresponds to the centre of the coil (Fig. 7.3.3).

The algorithm to detect the edges of the peak is based on a method used in the field of spectroscopic peak detection. These applications are characterised by the requirement for rapid processing of large datasets, the presence of peaks of varying width against a noisy background and a need for the position of the peak to be accurately detected [Yang, 2009]. First, a continuous wavelet transform (CWT) is applied to the projection using the function:

$$y(t) = \frac{1}{\sqrt{|a|}} \int_{-\infty}^{\infty} x(t)\psi * \left[\frac{t-b}{a}\right] dt$$

(Eq. 7.1)

Where *x(t)* is the original projection, *a* is a scaling parameter and *b* is the position parameter. The symbol $*$ denotes the complex conjugate of the two functions. ψ is the mother wavelet function, defined in this case as the Mexican Hat function (Fig. 7.3.4):

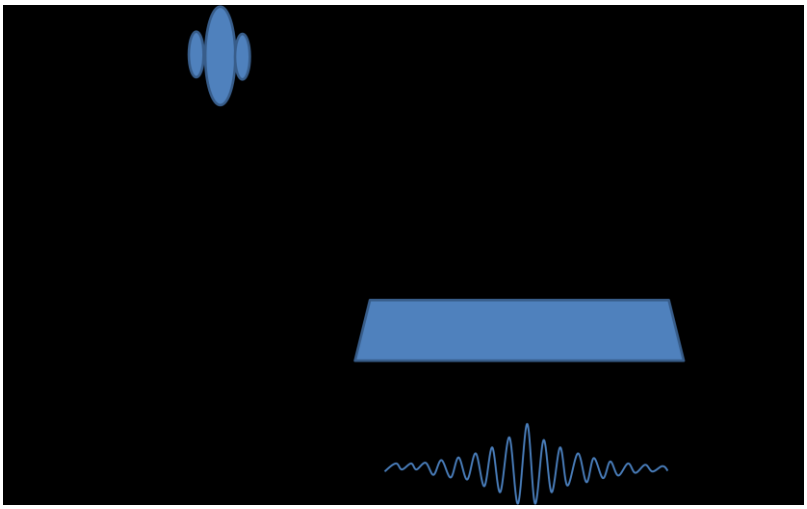

Fig. 7.3.1. Simplified timing diagram of the MRI sequence used to acquire 1D projections. No magnetic gradient is applied during RF excitation and there is no phase encoding. The only gradient applied is frequency encoding (in this case in the Z direction) during scanner ADC signal acquisition.

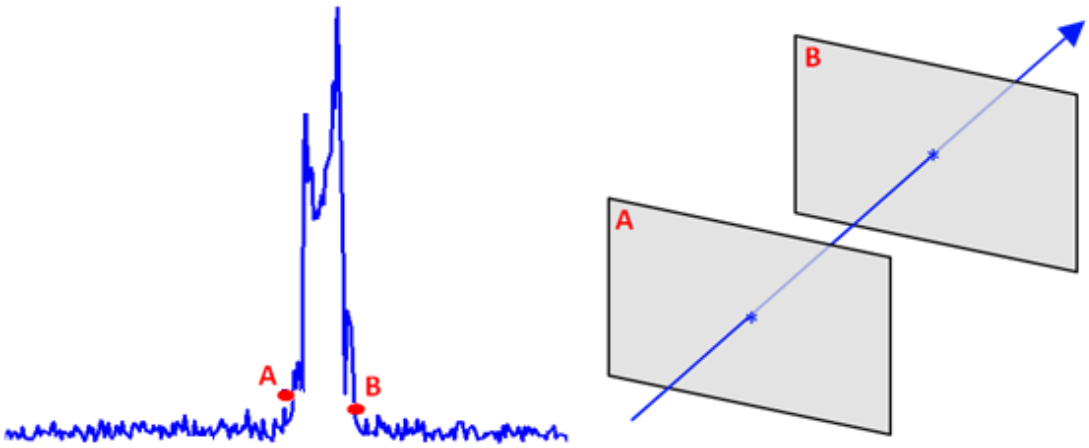

Fig. 7.3.2. Each point on the 1D projection (left) corresponds to the sum of the signal acquired from a plane orthogonal to the projection direction (right).

$$\psi(t) = \frac{2}{\sqrt{3}\pi^{\frac{1}{4}}}(1 - t^2)e^{\frac{-t^2}{2}}$$

(Eq. 7.2)

The CWT (Eq. 7.2) expresses the level of similarity between the original projection and the wavelet function as a coefficient. By continuously adjusting the scale function from 0-100% of the projection length and the position (b) of the transform, a map of coefficients can be generated. The nature of the 1D projection means that the CWT will exhibit a region of high similarity at a small scale at a position corresponding to the centre of the

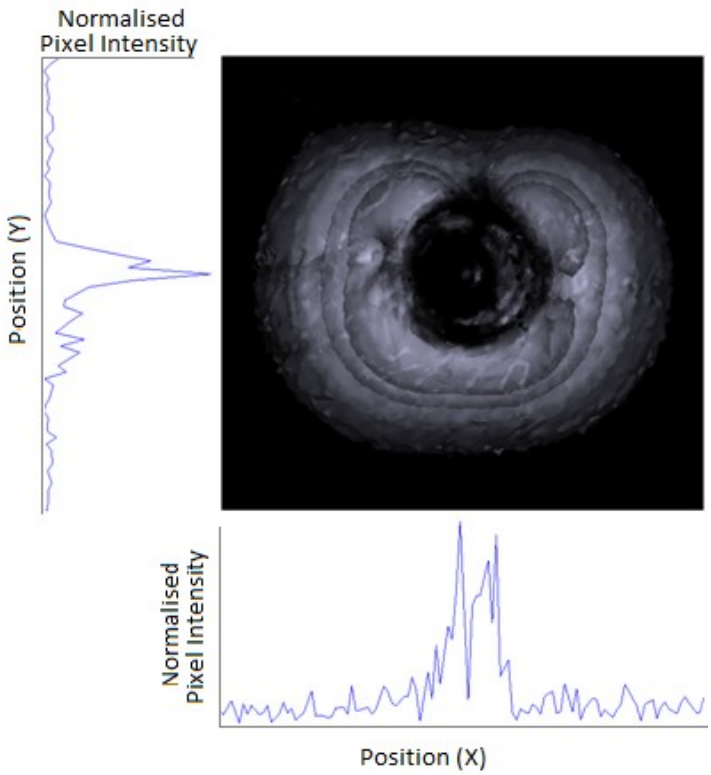

Fig. 7.3.3. Axial image of the tip coil immersed in water shown in top right. Peaks on the 1D projections (blue lines) correspond to the centre of the coil, which is dark on the image due to the plastic mandrel.

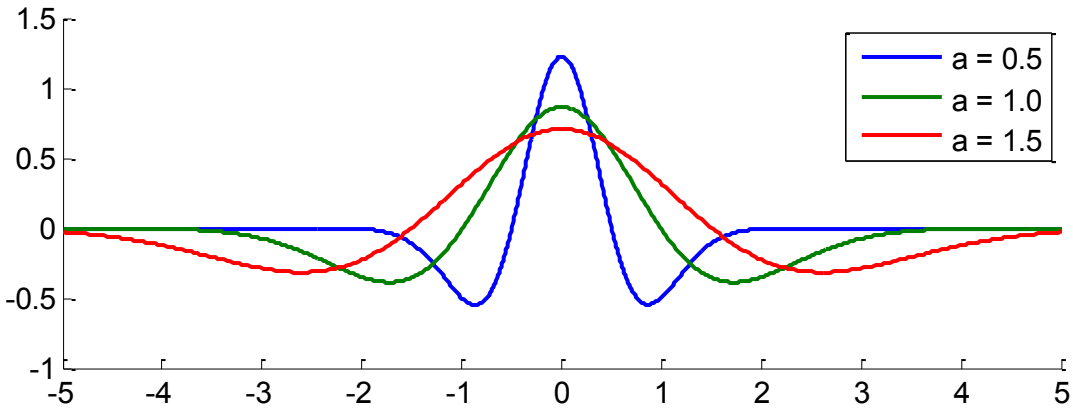

Fig. 7.3.4. Mexican Hat wavelet at position b = 0 and scales a = 0.5, 1.0 and 1.5.

MRI signal peak, while there is an expanding region of similarity at larger scales due to background noise (Fig. 7.3.5).

The CWT coefficient map is used to filter out all background noise by first isolating the coefficient peak corresponding to the peak and setting all coefficients that lie outside that peak to zero. The coefficients at different scales are then added together to generate a cumulative coefficient distribution across the width of the projection. The original projection is then multiplied by this distribution to generate a filtered projection (Fig.

7.3.5). The position of the edge of the peak in the filtered projection is defined as the point at which the projection rises above the filtered projection mean, which accounts for the small shoulder peaks generated by the Mexican Hat wavelet function.

The position of the peak edge on each projection and the direction of the projection define the centre and normal vector (respectively) of a plane in 3D space that corresponds to the edge of the coil's spatial sensitivity. To determine the cuboid-shaped volume surrounding the coil defined by the projections, three orthogonal 1D projections are generated and used to define 6 such planes; two parallel planes for each projection. The 8 points of intersection between these planes are calculated by solving the following equation:

$$\boldsymbol{x} = (|\boldsymbol{n_1}\ \boldsymbol{n_2}\ \boldsymbol{n_3}|)^{-1}[(\boldsymbol{x_1} \cdot \boldsymbol{n_1})(\boldsymbol{n_2} \times \boldsymbol{n_3}) + (\boldsymbol{x_2} \cdot \boldsymbol{n_2})(\boldsymbol{n_3} \times \boldsymbol{n_1}) + (\boldsymbol{x_3} \cdot \boldsymbol{n_3})(\boldsymbol{n_1} \times \boldsymbol{n_2})]$$

(Eq. 7.3)

Where $\boldsymbol{x}$ is the point of intersection between any three planes, $\boldsymbol{x_k}$ and $\boldsymbol{n_k}$ are the peak edge locations in MRI coordinates and projection unit vectors respectively. $|\boldsymbol{n_1}\ \boldsymbol{n_2}\ \boldsymbol{n_3}|$ is the determinant of the matrix formed by writing the three projection unit vectors side by side. This term will be zero if any of the planes are parallel [Weisstein, 2013c]. The mean of these points is the centre of the region of high signal, which aligns with the centre of the coil. In order to improve the robustness of the method additional sets of orthogonal projections can be acquired and the mean of all results used.

One advantage of using a larger coil with a large spatial susceptibility is that information about the peak width can be used to calculate the device orientation. The duodenoscope tip coil is longer than it is wide and therefore has a region of spatial sensitivity that is longer than it is wide. This is reflected in the peaks detected from the 1D projections, which are wider when they align with the long axis of the coil.

By calculating the principal axes of the volume defined by the edges of the peaks it is possible to determine the long axis of the coil. The principal axes are calculated by first determining the moment of inertia tensor ($\boldsymbol{I}$) of the points within the volume [Weisstein, 2013b]:

$$\boldsymbol{I} = \sum_{i=1}^{N} \boldsymbol{x_i^2}$$

(Eq. 7.4)

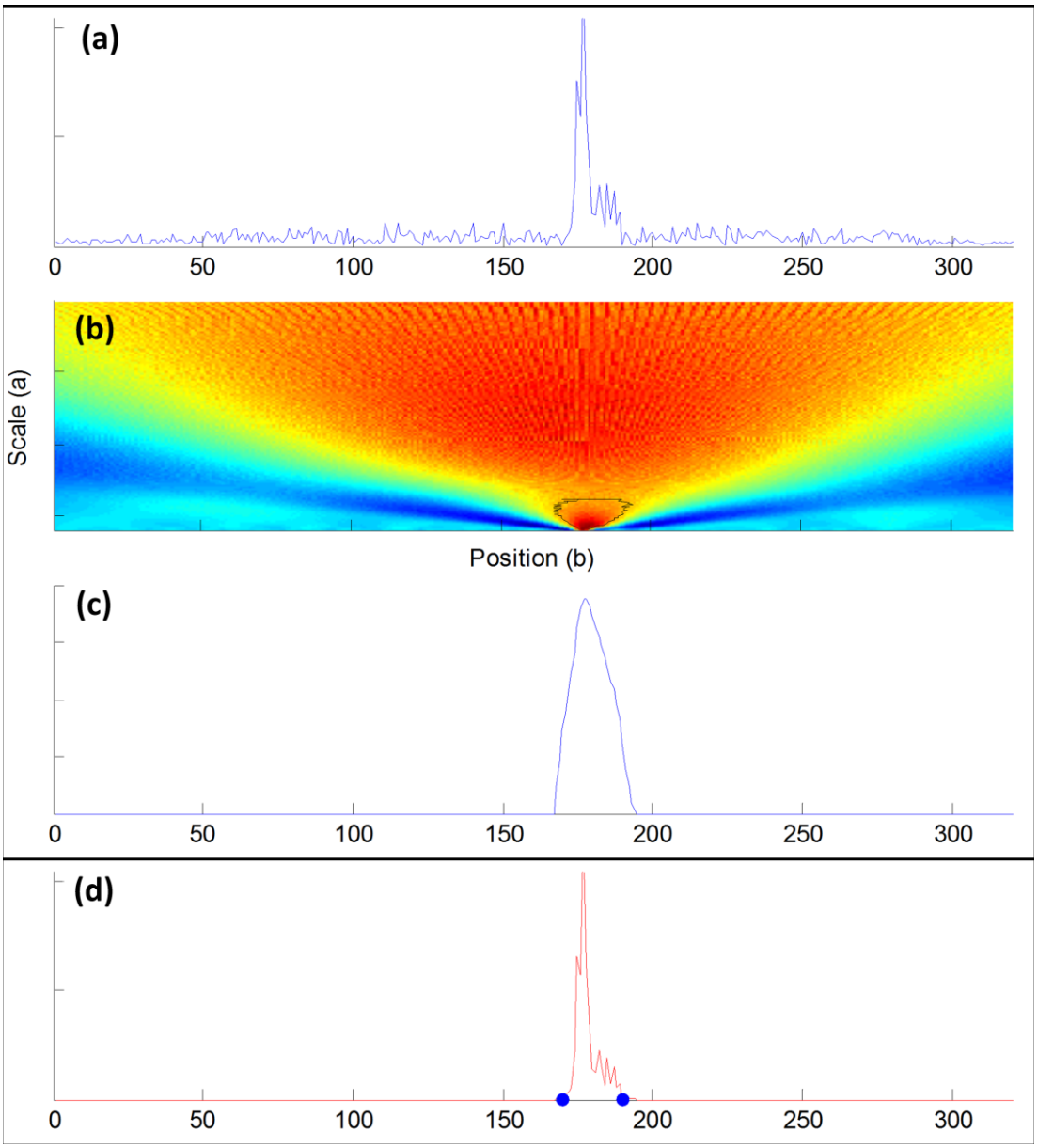

Fig. 7.3.5 Procedure for smoothing 1D projection, showing the original projection (a). This is followed by a coefficient map of the CWT function applied to projection (Eq. 7.1), with an outline around the coefficient peak at low wavelet scales due to the projection peak (b). The sum of the coefficients in the highlighted peak is shown in (c), which is then multiplied by the original projection to produce a smoothed result (d). It is then simple to determine the edges of the filtered peak (blue dots).

Where $\boldsymbol{x_i}$ is the vector from point i to the median of all points. The eigenvectors of the moment of inertia tensor are calculated to determine the principal axes of the volume, and the longest eigenvector should correspond to the long axis of the duodenoscope tip coil.

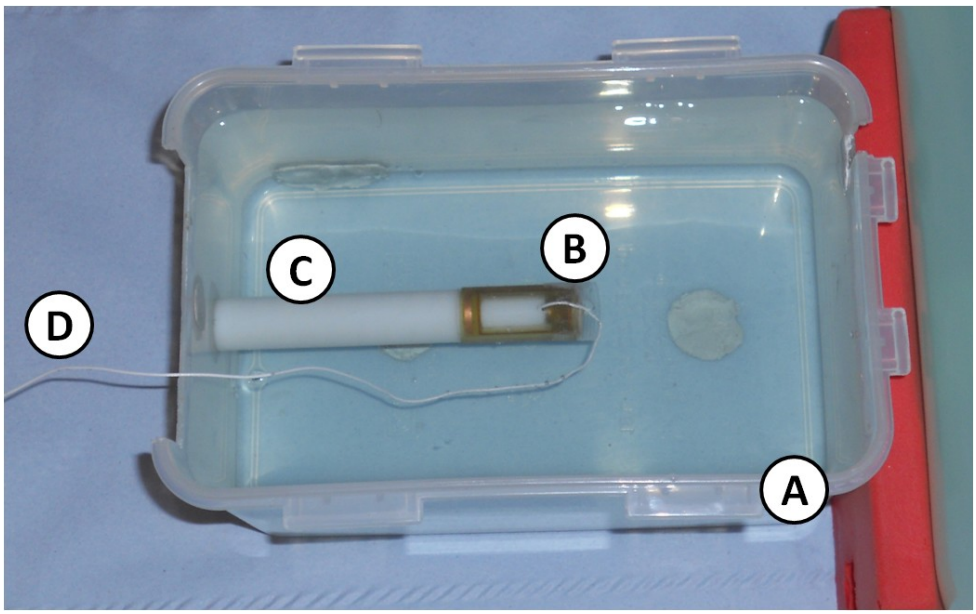

Fig. 7.3.6. Experimental setup, showing (a) plastic container filled with liquid, (b) duodenoscope tip coil, (c) plastic mandrel to rigidly mount the tip coil and (d) coil connection to MRI scanner.

7.3.2 Experimental Procedure

The sequence described in Fig. 7.3.1 was set to run on a 1.5 T clinical scanner (Siemens Verio) with a field of view of 500mm and a matrix size of 320 pixels. The measurement procedure outlined above was programmed into a Matlab script (MathWorks Inc., MA, USA) running on a stand-alone workstation (Intel QuadCore processor @ 2.66GHz, 3.4GB RAM) running Microsoft Windows XP. The workstation was connected to the MRI scanner and the raw scan data was transferred as it was acquired by the MRI scanner. The MR projection data was processed offline to enable a range of calculation scenarios to be explored.

The duodenoscope tip coil was placed on a plastic mandrel to simulate the duodenoscope tip with the mandrel mounted horizontally inside a plastic container. The plastic container was filled with liquid to provide a source of signal surrounding the receiver coil (Fig. 7.3.6).

The position detection calculation described above assumes that the coil is the centre of the signal producing region. In the idealised case, where the coil is surrounded by a homogenous liquid, this is clearly a valid assumption. However if there is a systematic perturbation from the idealised case, for example a large signal void on one side of the coil, then this assumption may not be correct. Plastic blocks and a sheet of air-filled packing material were placed next to and around the coil in order to vary the signal

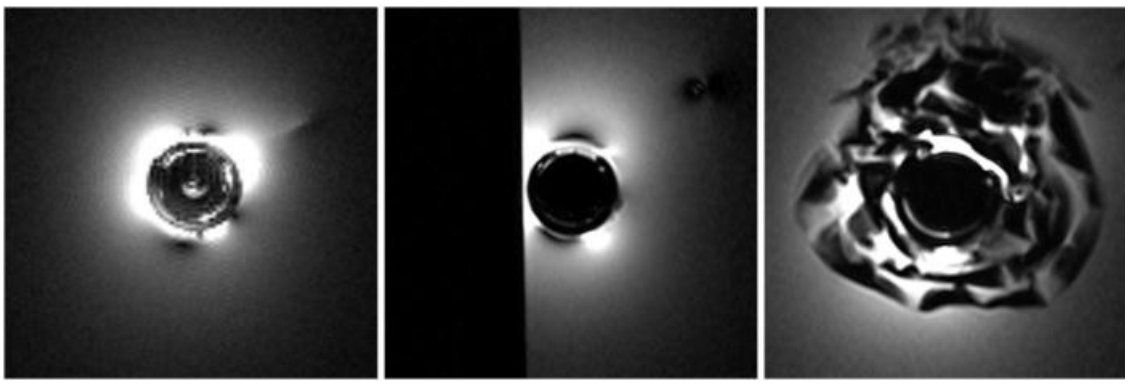

Fig. 7.3.7. Axial MRI of duodenoscope tip coil showing alternative signal loading cases (SLC): Case 1 (left) idealised with coil surrounded by liquid; Case 2 (centre) plastic block placed adjacent to coil and; Case 3 (right) coil wrapped in air-filled plastic packing material.

Projection Number	X Component	Y Component	Z Component
1	1	0	0
2	0	1	0
3	0	0	1
4	0.707	0.707	0
5	0.707	0	0.707
6	0	0.707	0.707
7	0.707	-0.707	0
8	-0.707	0	0.707
9	0	-0.707	0.707

Table 7.3.1. List of X, Y and Z components of the projection unit vectors.

Orthogonal Set	Projection 1	Projection 2	Projection 3
A	1	2	3
B	1	6	9
C	2	5	8
D	3	4	7

Table 7.3.2. List of orthogonal projection sets.

loading surrounding the coil and to provide a more clinically realistic signal distribution case (Fig. 7.3.7).

The plastic container was placed at a variety of locations in the MRI scanner and data acquired. The angle of the coil to the scanner Z axis was varied from 0 to 60° and the position varied by ±20mm. At each extreme of location and position data was acquired for each of the three signal loading cases (SLCs, see Fig. 7.3.7), for a total of 13 test points. At each test point, 1D projections in each of the directions listed in Table 7.3.1 were acquired, enabling four orthogonal sets of projections to be compiled (Table 7.3.2). Each

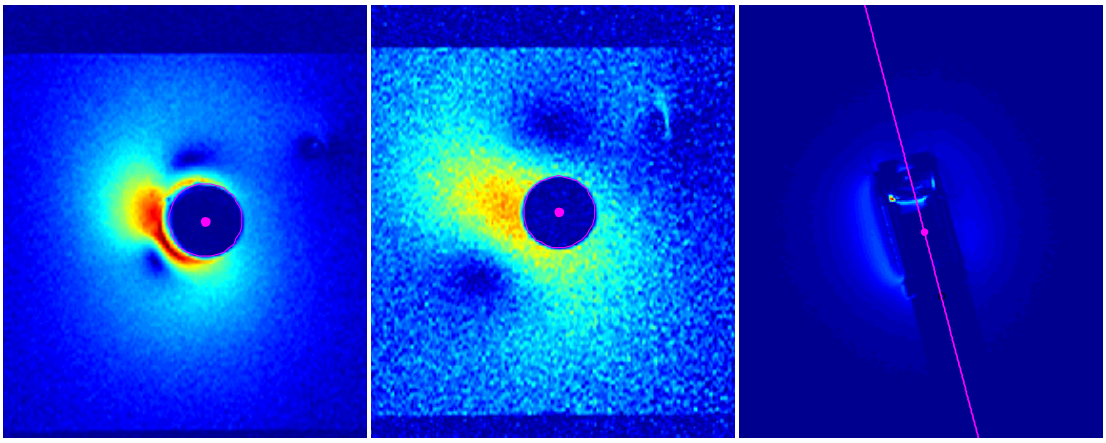

Fig. 7.3.8. Reference method of measuring the true coil position and orientation. Axial image slices (left and centre) were processed to determine the centre of the image void due to the coil mandrel (magenta dot). The centre of the coil was then defined as a distance from the tip of the coil along this axis using a coronal image slice (right).

projection was acquired 10 times at each test point, to enable the repeatability of the detection method to be determined.

At each test point the true location and orientation of the coil in the MRI scanner coordinate system was determined by acquiring high quality image sets in both the coronal and axial planes. These images were then processed using a Matlab script to locate the signal void corresponding to the mandrel that the coil was mounted on and to transform the image feature into a set of MRI coordinates (Fig. 7.3.8).

7.4 Results

The magnitude of the position and angular error between the coil detection method and the actual position of the coil is shown for each of the 13 test points in Fig. 7.4.1. The results are plotted as a function of the angle between the coil long axis and the MRI scanner Z axis. Results for the three different signal loading cases are identified. The error bars represent the standard deviation of the 10 repeat results acquired at that test point.

The magnitude of the position measurement error does not exhibit a consistent trend in relation to changes in the coil angle relative to the MRI scanner, nor due to the different signal loading cases. The error is below 12.7mm for all test points. By contrast, the angular measurement error appears to rise and experiences greater variability with increasing coil angle. This effect is most pronounced for the two non-ideal signal loading cases.

The measurement error between the coil detection method and the actual coil position is separated into errors in the coil X, Y and Z directions and errors in the MRI

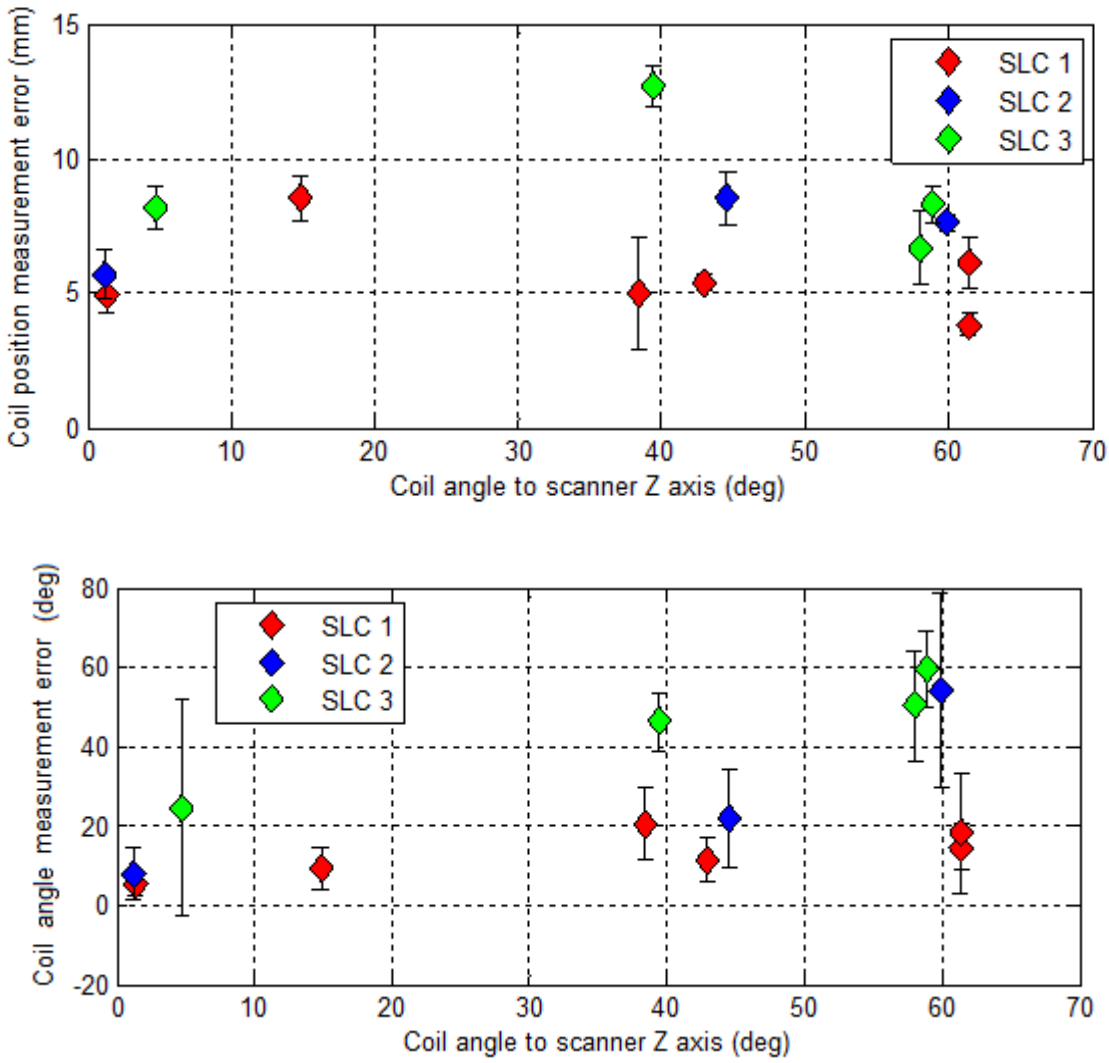

Fig. 7.4.1. Magnitude of coil measurement errors plotted against angle between coil and MRI scanner Z axis, with alternative signal loading cases (SLC) identified. Showing position error (top) and angular error (bottom).

scanner X, Y and Z directions in Fig. 7.4.2 and Fig. 7.4.3 respectively. The error in the Z direction of the coil coordinate system (along the long axis) is consistently negative and greater than the error in either of the coil X or Y directions. The error in the coil X axis (horizontal and parallel to the coil short axis) appears to approach zero as the coil is rotated relative to the MRI scanner Z axis. The errors in the scanner coordinate system are consistent relative to the change in coil angle and signal loading case, with the magnitude of the Y direction error low compared with the X and Z directions.

Fig. 7.4.4 shows the magnitude of the position measurement error when the measured position of the coil is offset by 2mm in the coil X direction and by 4.5mm in the coil Z direction.

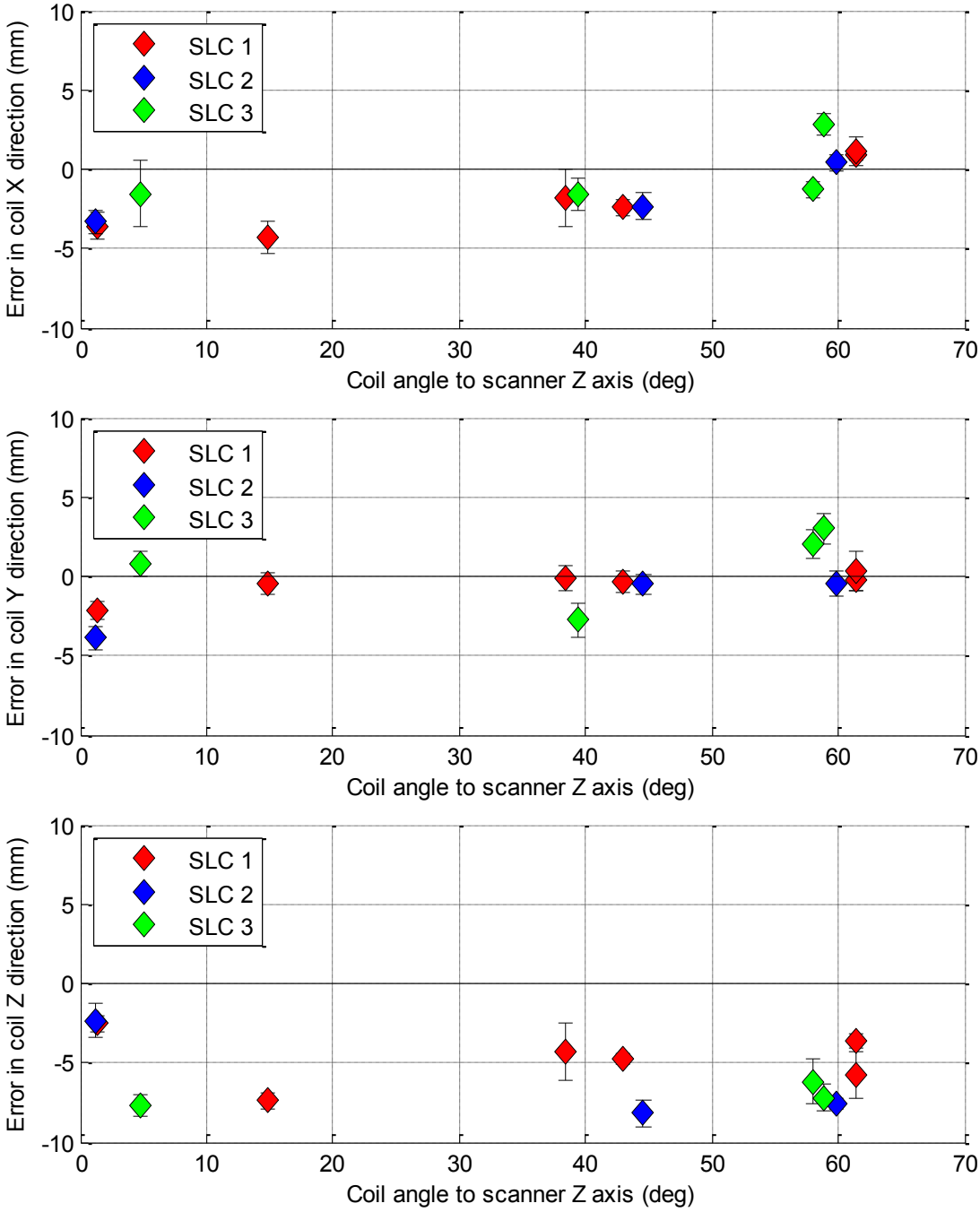

Fig. 7.4.2. Position measurment error in the X, Y and Z axes of the coil coordinate system (top, middle and bottom respectively) as a function of coil angle to MRI scanner Z axis, with separate signal loading cases (SLC) identified.

The Matlab script implementing the coil measurement procedure was executed on a standalone workstation as described above. Once initial variables were declared the script took 200-205 ms to calculate the coil position and orientation from a set of 9 projections for a maximum update rate of approximately 5Hz. The MRI sequence used to

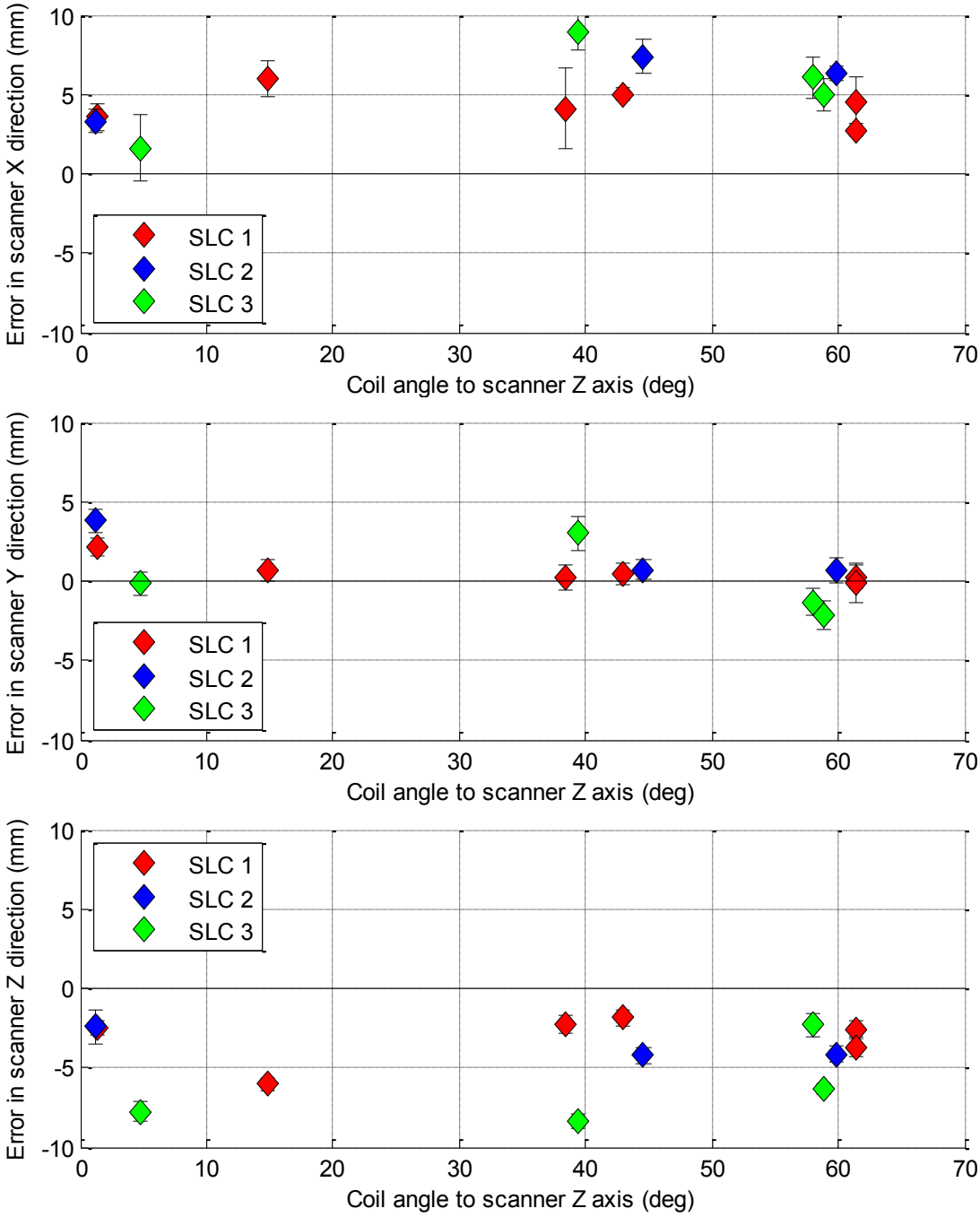

Fig. 7.4.3. Position measurment error in the X, Y and Z axes of the scanner coordinate system (top, middle and bottom respectively) as a function of coil angle to MRI scanner Z axis, with separate signal loading cases (SLC) identified.

acquire the 9 projections required for each calculation took approximately 10ms to complete.

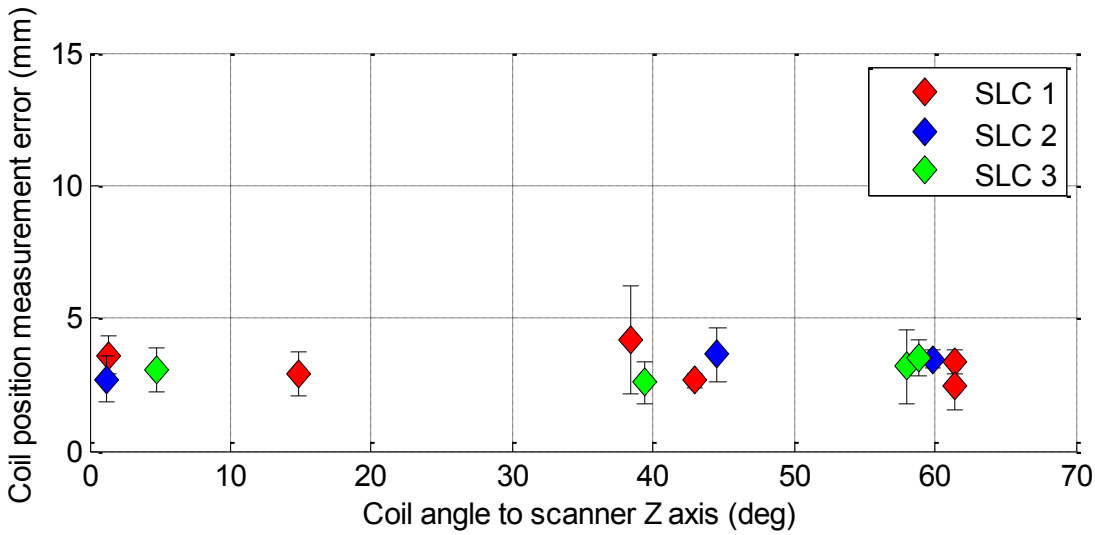

Fig. 7.4.4 Magnitude of coil measurement errors (as Fig. 7.4.1 top) with a fixed offset of 4.9mm and 2mm applied to all results in the scanner Z and X directions respectively.

7.5 Discussion

The results presented here demonstrate a method that enables an instrument-mounted MR receiver coil designed for imaging to be used for position and orientation tracking to facilitate the MRI-guided ERCP procedure.

The magnitude of the uncorrected position error varies from 3.8 to 12.7mm. However, Fig. 7.4.3 demonstrates that this includes consistent errors in both the scanner X and Z directions. If these offsets are corrected for then the magnitude of the position measurement error falls to between 2.4 and 4.2mm (Fig. 7.4.4). This is within the desired range of accuracy and appears to be independent of signal loading as well as being consistent across a range of coil positions and angles.

The magnitude of the corrected coil measurement error is close to the pixel width of the projections (1.6mm), which means it could be reduced further by improving the projection resolution. The accuracy of the method could also be improved by increasing the number of projections. Presently the 9 projections form three orthogonal sets: additional sets would reduce the impact of anomalous peak detection results, and may enable a more accurate measurement of the coil position to be made.

Fig. 7.5.1 shows a single axial image of the coil aligned with the MRI scanner X direction and shows a comparison between the corresponding 1D projection and the sum of the signal from the image set in the same direction. This shows how the shape of the 1D projection compares with the position of the coil as calculated from the image. The cause

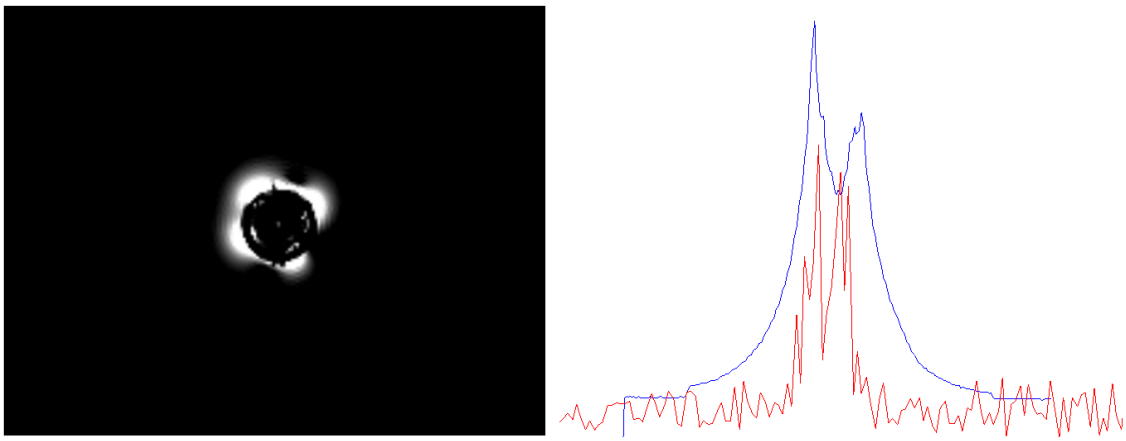

Fig. 7.5.1. Axial image of coil (left) showing four evenly spaced radial signal lobes. These cause the signal sum (right, blue) and projection (red) to exhibit a distinctive peak pattern, which is clearly lower and more truncated on the right of the projection.

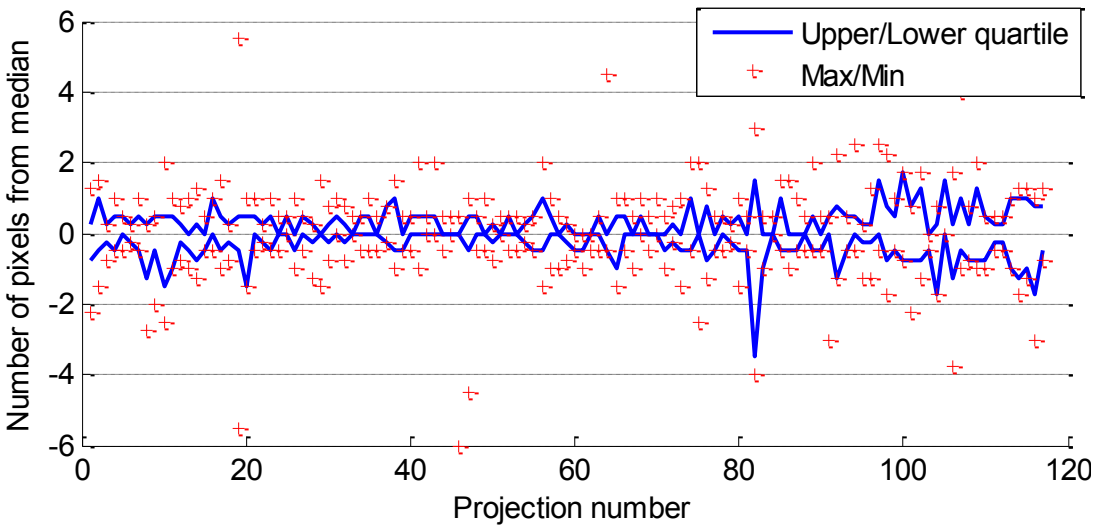

Fig. 7.5.2. The 9 projections were all acquired at each of 13 test points. These 117 projections were each repeated 10 times. This chart shows the interquartile range, maximum and minimum peak centre measurements for each projection set, normalised to the median of the projection set measurement.

of the offset in the coil X direction is evident when the shape of the images generated from the coil is analysed. The saddle shape of the coil causes four lobes of high signal, equally spaced around the radius of the coil. Due to manufacturing inconsistencies, these lobes are not of equal intensity and when the 1D projection sequence is run this causes a distinct weighting of the peak from one side to the other.

A similar effect is evident in the coil Z direction, where there is a significant peak of signal due to the presence of water inside the window cut out for the duodenoscope camera and tooling channel. This does not correspond perfectly with the geometric centre of the coil and causes the peak to be weighted towards the tip of the coil. This effect could

be the cause of the consistent offset in results described above. An alternative explanation is a small imperfection in the main magnetic field or gradient fields of the MRI scanner, as described by Dumoulin et al [Dumoulin, 1997]. Further data would need to be acquired to fully determine the cause of this offset.

Analysis of repeated measurements from the same test point suggests that the peak detection method is capable of calculating the coil position consistently. Fig. 7.5.2 shows that the inter-quartile range between measurements from repeated projections is less than 4 pixels in all measured cases except for one. Furthermore, the presence of signal perturbations surrounding the coil causes much less of an issue with locating the coil than anticipated. Despite significant visual differences in the images generated for each of these three cases (Fig. 7.3.7), the centre of the projection peak remains consistent relative to the coil centre.

An advantage of the CWT filtering algorithm is that it is capable of detecting the low SNR peaks that are present at the edge of the projection peak in loading cases 2 and 3. Thresholding or low pass filtering of these projections may remove these peaks and make the coil location method more susceptible to signal perturbations. However, one advantage that simpler filtering methods have is that they are less computationally intense to complete. The CWT filtering of the 9 projections accounts for around 160ms of the 200ms taken to execute the coil location script and is therefore the limiting factor which determines the measurement update rate. Despite these limitations, the method as implemented achieves and update rate of 5 Hz, which would result in over 20 datapoints for each respiratory cycle and is sufficient for motion compensation.

While the performance of the coil position measurement method is adequate, it's capacity to determine the orientation of the coil is less impressive. The mean angular error rises as high as 60° for the non-homogenous signal loading cases when the coil is at a significant angle to the MRI scanner. The orientation detection method assumes that the width of the projection peak reduces as the projection aligns with the long axis of the coil. Fig. 7.5.3 shows that this is not reliably the case for the measured data, which means that, despite there being some correlation, the calculation of the long axis by the algorithm is unstable and over-sensitive to very slight changes in peak width and position.

A more sophisticated method of coil orientation detection must be developed in order to overcome this issue. This could utilise information that can be gathered from the shape of the 1D projection peak, rather than just utilising it's position and width. Fig. 7.5.1 shows that the radial lobes of high signal cause a pattern of high and low peaks in the 1D projection. This pattern of peaks changes depending on the relative orientations of the

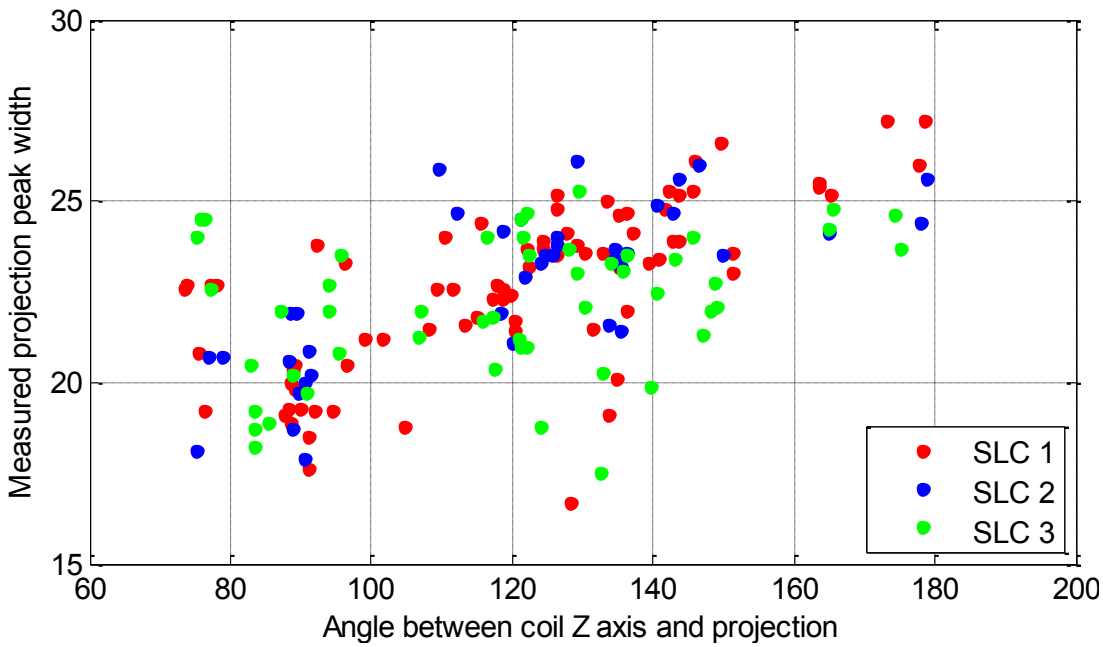

Fig. 7.5.3. Variation in measured projection peak width as a function of the angle between projection and coil Z axis. Only a weak correlation is observed, which contributes to the instability of the coil orientation detection method.

projection and coil and with more investigation this information could be utilised to determine the coil orientation.

The results presented here were acquired using the duodenoscope tip coil only, but the method is applicable to other similar imaging microcoils. In particular it should be well suited to the catheter coil used in the MRI-guided ERCP system, as this coil is much smaller in diameter and has a larger aspect ratio. The narrower diameter will reduce the average peak width and make the method more accurate and less sensitive to signal perturbations, while the larger aspect ratio should improve the coil orientation calculation method.

This experiment demonstrates the feasibility of device tracking using device-mounted microcoils designed for imaging. Much more data is required to fully characterise this method and explore it's use in clinical situations, particularly in relation to the coil orientation calculation method. More data is also required to establish the repeatability of the method used to calibrate the offset applied to the coil position measurement. In it's current form the method described here is clearly capable of providing sufficiently accurate and timely coil position data to the MRI-guided ERCP system.

7.6 Conclusions

A novel method of using the imaging coil mounted at the tip of the duodenoscope to track the movement of the duodenoscope tip is demonstrated in this chapter. This method is shown to be capable of locating the tip consistently to an accuracy of 4.2 mm over a range of coil position and signal loading cases. Further developments to improve the accuracy of the position measurement and enable measurement of the coil orientation are suggested. Improved computational efficiency would in crease the measurement update rate from it's presnt value of 5 Hz, although the present update rate of the method is sufficient for motion correction.

Intra-operative MRI for cannulation guidance relies on an accurate measure of the position of the duodenoscope and catheter tip during the procedure. This dependence is investigated further in Chapter 8.

Chapter 8

System Concept Testing

8.1 Introduction

Test data presented in Chapter 6 demonstrated that the remote actuation system developed in Chapter 5 enables the use of the MRI compatible duodenoscope and internal MR receiver coils during a clinical procedure. The work described in this chapter explores the potential for the duodenoscope, coils and actuation system to be combined to improve the clinical outcomes of the standard fluoroscopic guided ERCP procedure. The objective was to quantitatively assess the benefit to biliary cannulation that MRI guidance provides compared with fluoroscopic guidance.

8.2 Background

Cannulation failures frequently occur due to the use of an incorrect approach angle when introducing the catheter to the duodenal papilla (see Section 4.2). Incorrect approach angles can result in complete cannulation failure, biliary perforation or inadvertent cannulation of the pancreatic duct [Chutkan, 2006]. The ideal procedure is to point the tip of the catheter directly at the duodenal papilla and position the tip of the duodenoscope so it is aligned with the bile duct. However, whilst the papilla and catheter tip are visible on the duodenoscope video, there is generally a lack of information regarding the angle of the bile duct during the ERCP procedure, making the ideal procedure challenging to achieve.

Fluoroscopic images are 2 dimensional projections that can be acquired in real-time, although due to radiation exposure limits frames are usually updated intermittently on the request of the endoscopist. These intra-operative fluoroscopic images can show the patient anatomy and endoscopic tools during the cannulation phase of the procedure.

Fluoroscopic imaging is limited by a lack of image contrast between soft tissue structures. Typically the biliary system is either extremely indistinct or invisible on fluoroscopic images until contrast medium has been injected into the bile duct (Fig.8.2.1), which is performed once cannulation has already been attempted and some level of

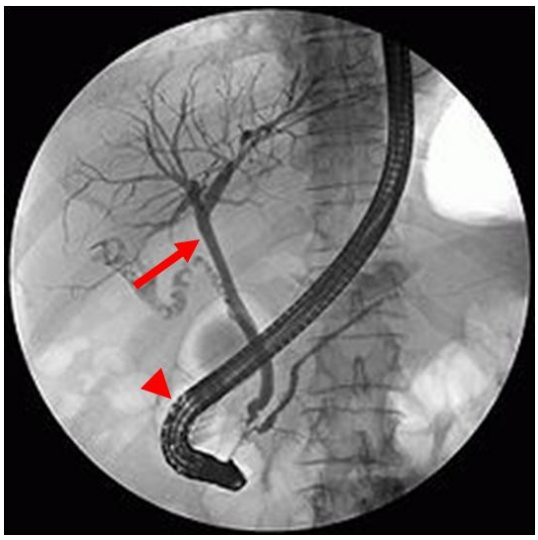

Fig.8.2.1. Fluoroscopic image acquired during ERCP after the injection of contrast medium. The duodenoscope (arrowhead) and biliary tree (arrow) are indicated.

biliary access gained. If the bile duct is perforated or pancreatic duct cannulated by this initial attempt and contrast medium is directly injected there is a risk of serious complications [Anderson, 2012].

Information about the 3 dimensional alignments of anatomic structures and endoscopic tools remains limited even after contrast medium has been injected. As a 2D projection image, the relative alignment of two objects can be deduced by moving one of them by a known amount relative to the static object and imaging plane, but this is a time consuming and challenging process requiring considerable skill and experience. This is particularly true when the object moved is the endoscope tip, which responds paradoxically and inconsistently to user inputs.

An alternative technique is to initially insert a thin guidewire with a flexible tip through the papilla. This can be advanced 'blind' into the biliary system with a lower risk of perforation and complications [Petersen, 2007]. The guidewire is visible on fluoroscopic images, and using their clinical experience endoscopists can identify whether the bile duct or pancreatic duct has been accessed. Once the wire is in the bile duct, a catheter can be introduced to the same location by sliding it over the wire. However, if the pancreatic duct has been accessed in error, the endoscopist must repeat the guidewire insertion and will have gained little information about the correct approach angle. Repeated failed attempts at cannulation risk inflaming the papilla and inhibiting further attempts.

Intraoperative MRI has the capacity to overcome the issues surrounding cannulation guidance due to the image characteristics. The level of image contrast

between soft tissues can be tuned by adjusting imaging sequence parameters (see Section 2.2), which means that the duct anatomy can be visualised without the need for a blind injection of contrast medium or guidewire insertion. Another significant benefit of MRI is the capability to acquire cross-sectional 2D images that display only the anatomy within a thin slice. With careful definition of the slice plane and acquisition of multiple adjacent slices it is possible to determine the relative orientation of objects in 3D space, enabling the endoscopist to align the catheter to the bile duct correctly. The main limitation of MRI for this application is the speed of image acquisition. This limits the rate at which guidance images can be refreshed and can also result in image artefacts as a result of the anatomy moving due to respiration during the image sequence (see Section 2.2.3).

The test presented in this section aims to quantitatively evaluate the benefit to biliary cannulation that MRI guidance can provide compared with fluoroscopy. The endoscopist was presented with a simulated situation analogous to the ERCP procedure immediately prior to biliary cannulation and attempted to align the catheter with a tube representing the bile duct. The alignment error between the catheter and bile duct was compared for a variety of guidance images.

8.3 Materials and Methods

The test was performed using a rig designed to replicate the ERCP procedure in terms of the relative positions of the duodenoscope and anatomic structures from the point of view of the endoscopist (Fig. 8.3.1). The distal end of the duodenoscope flexible section is held in a clamp that allows it to slide and rotate whilst being held at a constant position relative to the duodenum plate. The duodenoscope tip is free to steer both left-right and up-down, while the catheter is positioned with approximately 15mm protruding from the duodenoscope tip. The catheter was not advanced or retracted during the test, but the catheter steering bridge was available to assist the endoscopist with alignment. The duodenoscope was actuated using the duodenoscope remote actuation system described in Section 5.3.

The side of the duodenum plate facing the duodenoscope is featureless apart from a small drilled hole which represents the duodenal papilla. The other side of the duodenum plate has a socket into which a 4mm diameter tube is located to represent the bile duct. The distal end of the bile duct tube is held by a plate that contains 32 holes drilled at different angles and locations. These enable the angle between the bile duct and the duodenum plate to be adjusted. The duodenum plate obscures the bile duct tube from

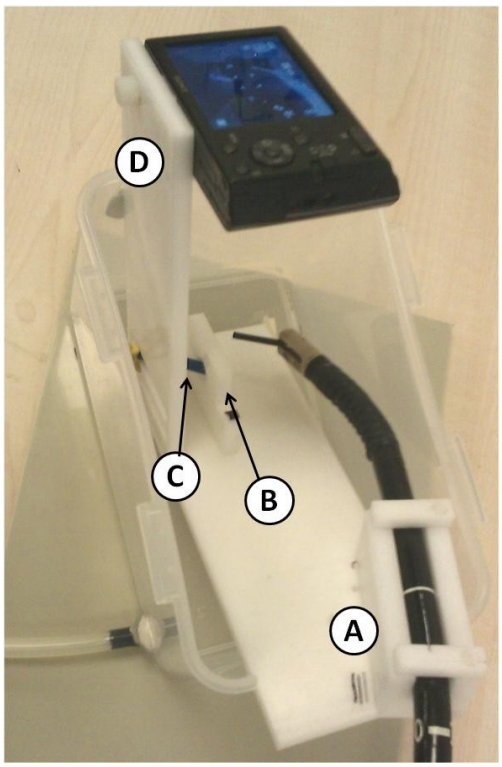

Fig. 8.3.1. Biliary cannulation test rig, showing (A) duodenoscope clamp, (B) duodenum plate, (C) bile duct tube and (D) digital camera and mounting arm.

the duodenoscope, so the endoscopist is unable to determine the angle of the bile duct from the duodenoscope video feed.

As well as the duodenoscope video, guidance images of the rig and duodenoscope position were provided to the endoscopist. Fluoroscopic imaging was simulated by a digital video camera mounted on an arm at an oblique angle to the test rig (Fig.8.3.2). The video stream was visible to the endoscopist in real-time. The nature of fluoroscopic images as 2 dimensional (2D) projections was replicated by designing the test rig without structures between the region of interest (consisting of the duodenoscope and bile duct) and the digital video camera. The low contrast between soft tissue structures was simulated by manufacturing all support components out of white or clear plastic and draping the rig surrounds with white material. The tube used to represent the bile duct was either clear or opaque tube, which simulated the injection or otherwise of fluoroscopic contrast medium (Fig.8.3.2).

MR guidance images were acquired using a 1.5T clinical scanner (Siemens Verio) and the duodenoscope tip receiver coil described in Section 4.4.2.1. The test rig was placed inside a liquid-filled plastic container and adjacent to a cuboid phantom in order to generate MR signal (Fig. 8.3.3). During the test the endoscopist was able to view the duodenoscope video and MR images on monitors in the scanner control room.

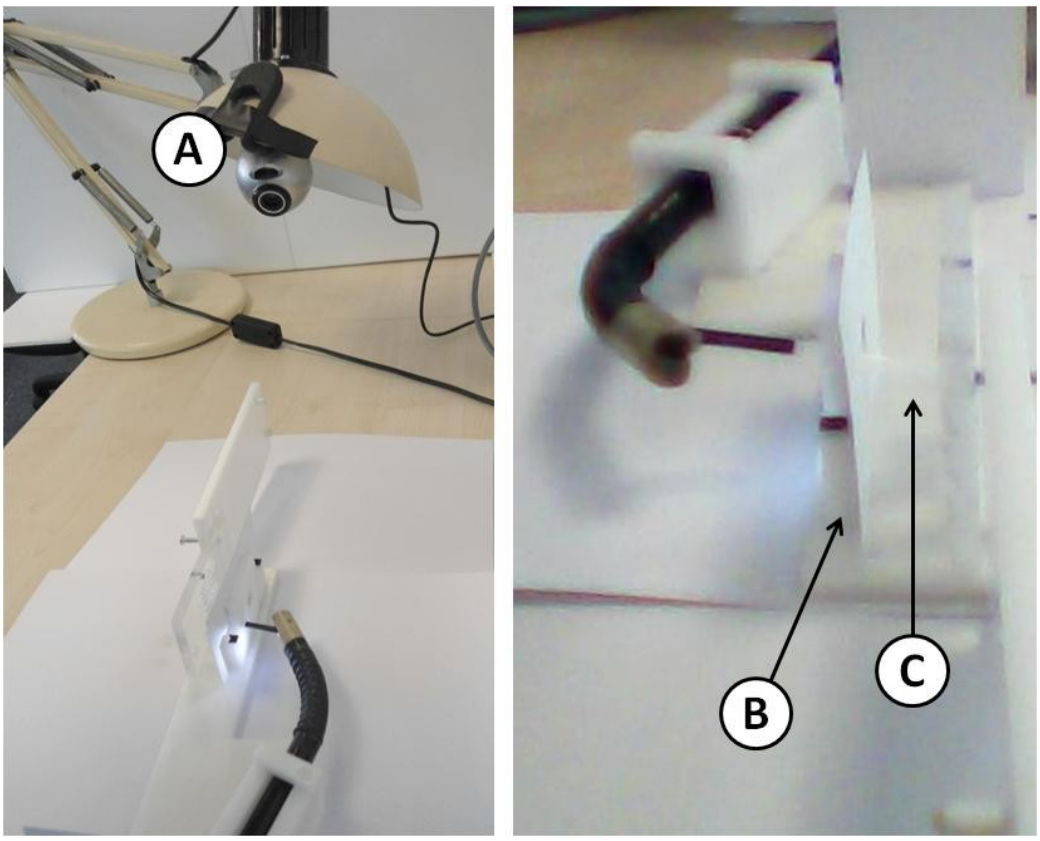

Fig.8.3.2. Setup for simulated fluoroscopic guided test runs (l) and simulated fluoroscopic guidance image (r). Showing (A) digital camera mounted on repositionable arm, (B) duodenum plate and (C) clear bile duct tube.

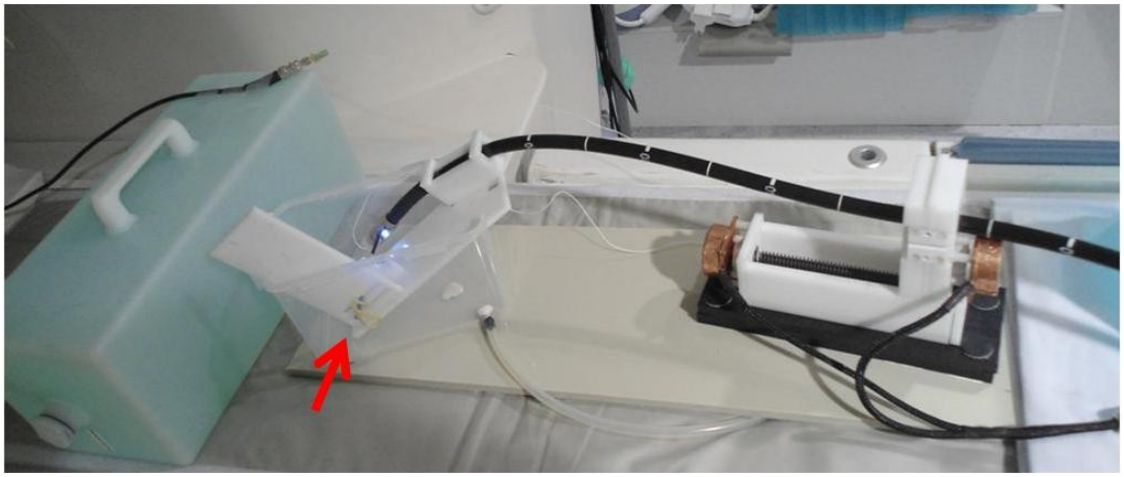

Fig. 8.3.3. Setup for MRI guided test runs, with test rig immersed in liquid-filled plastic container (arrow).

The test setup results in the simulated guidance images having inverted contrast compared to a clinical image. In a clinical image of the biliary region a T2-weighted sequence is used to produce bright fluid-filled structures (bile duct), grey tissue structures (duodenum wall) and dark plastic or air-filled regions (duodenum,

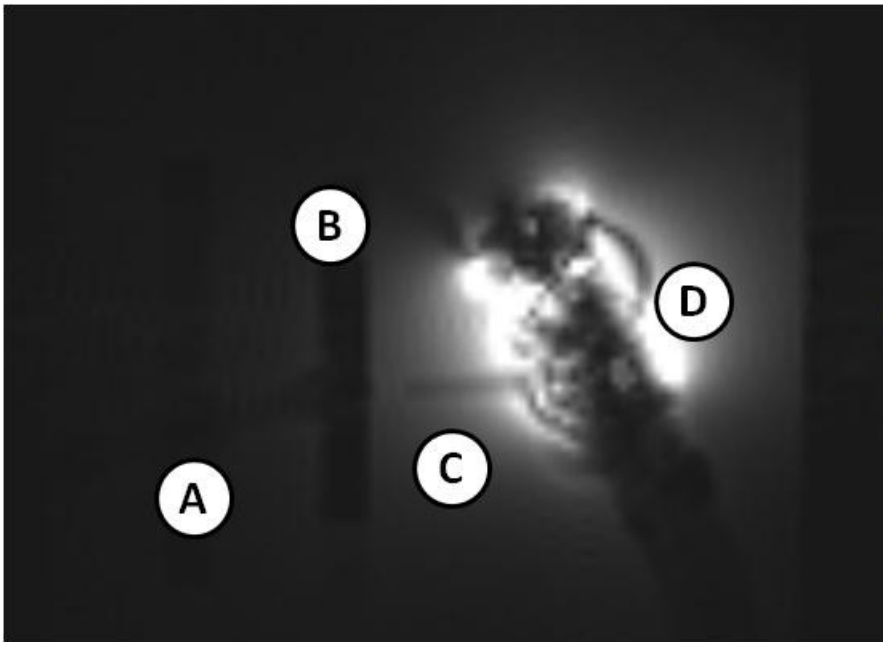

Fig. 8.3.4. MRI guidance image showing (A) bile duct tube, (B) duodenum plate, (C) catheter and (D) duodenum with imaging coil.

duodenoscope). In the simulated image, the bile duct, duodenoscope and duodenum wall are dark while the surrounding areas are fluid filled and appear bright. In both cases the bile duct is clearly visible on the MR images.

In order to provide guidance images in the correct plane, 20 image slices encompassing the entire test rig were acquired before each test run using a balanced steady-state with free precession sequence (bSSFP, TR = 20ms, TE = 5ms, slice thickness = 8mm, FOV = 280x280mm, matrix size 192x192, acquisition time = 1m48s). These were used to define an image plane that included the bile duct tube. During the test run, guidance images were acquired in this plane or adjacent to it when requested by the endoscopist.

The guidance images were acquired using a True Fast Imaging with Steady State Precession sequence (TrueFISP, TR = 4.2ms, TE = 2.1ms, slice thickness = 5mm, FOV = 150x150mm, matrix size 128x128), which resulted in low resolution, low SNR images acquired in approximately 1s (Fig. 8.3.4). The bile duct tube, duodenoscope and duodenum wall are visible on the image despite the poor overall quality. The test was performed with the region of interest static within the MRI scanner, and the image acquisition and quality was limited to simulate the effect of respiratory motion.

A single endoscopist performed all test runs in this experiment, to remove the effect of variability between operators and their level of familiarity with the test setup.

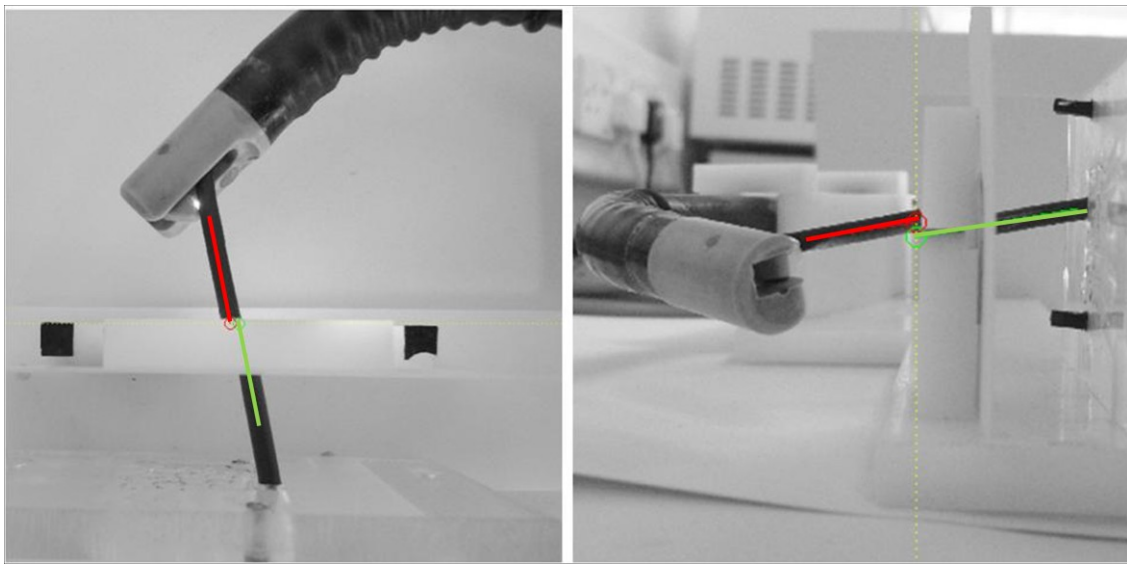

Fig. 8.3.5. Positions of bile duct and catheter after a test run, as recorded using the vertical (left) and horizontal (right) camera mount. The central axis of the catheter (red) and bile duct (green) has been displayed. The black features on the duodenum plate on either side of the bile duct are used to determine the image scale.

The duodenoscope video was available to the endoscopist on all test runs, while each run was performed with only one of the following forms of guidance images:

1. No guidance images
2. Simulated fluoroscopic images with a low contrast, clear bile duct tube (L/C)
3. Simulated fluoroscopic images with a high contrast, opaque bile duct tube (H/C)
4. MRI guidance images

Each test run began with the bile duct being moved to an angle while the endoscopist was blinded to it's new location. The endoscopist then manoeuvred the duodenoscope and catheter until they were satisfied that the catheter was both pointing directly at the papilla and aligned with the bile duct. The test was repeated 60 times in total, with each form of guidance imaging used 15 times.

Once the test run was completed, the positions of the bile duct and catheter were recorded using a digital camera mounted on a stand rigidly attached to the test rig frame. The camera mount enabled images to be acquired in two orthogonal planes, at a fixed orientation and position relative to the duodenum plate. Image processing software (MathWorks Inc., MA, USA) was used to determine the position and orientation of the catheter relative to the bile duct on each image (Fig. 8.3.5). The scale of each image was determined by measuring the distance between two features mounted on the duodenum plate of the test rig. These features are close to the region of interest in the image and at

the same distance from the camera as the papilla feature, in order to reduce the effect of perspective and image distortion due to the camera lens.

The success of the test run was quantified in terms of the angular error between the central axis of the catheter and bile duct, as well as the linear distance between the projection of their ends onto the duodenum plate. These parameters were recorded from both camera images for each test run. The angular and linear results are not assumed to be normally distributed so Levene's test was used to assess the equality of variances between different sets of results [Weisstein, 2013a], with a significance criteria set at $P \leq 0.05$.

8.4 Results

Fig. 8.4.1 shows the distribution of angular alignment errors between the catheter and bile duct for each of the four types of guidance image. The magnitude of the mean angular error is below 5° for all guidance methods apart from the vertical image on the high contrast fluoroscopy test, which exhibits a higher number of large (~40°) errors. The errors for the unguided test range from -45° to 40° and are distributed approximately evenly across the range, while the errors for both fluoroscopic guided tests are clustered more closely around the mean.

Outlying results for both fluoroscopic guided tests (particularly in the vertical image) mean that the range of results stays high at -35° to 30° for the low contrast and -25° to 45° for the high contrast test. The MRI guided test has a much lower range of -10° to 10° with no outlying large errors. In the vertical image the MRI guidance angular errors are clustered closely around the mean, while in the horizontal image they are distributed more evenly across the range.

Table 8.4.1 shows that the variances of the angular errors of the fluoroscopic guided tests are not significantly different to the unguided test in the vertical images ($P > 0.05$). However, there is a significant difference between the same tests in the horizontal images. The high and low contrast fluoroscopic guided test angular errors are not significantly different from each other in either the vertical ($P = 0.4497$) or horizontal ($P = 0.4787$) images. The MRI guided angular error variances are significantly different from all other tests except when compared with the high contrast fluoroscopic guided test in the horizontal image.

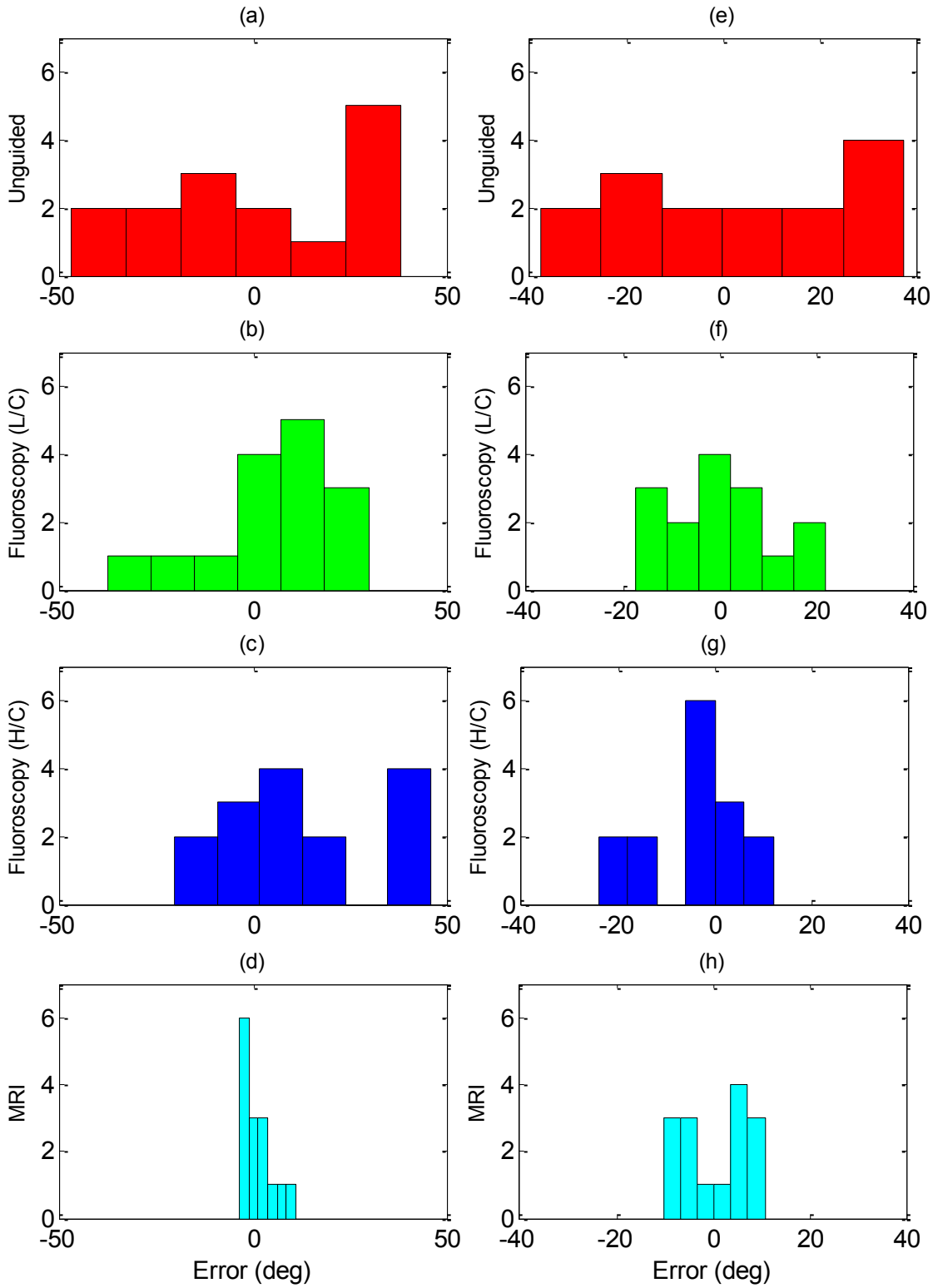

Fig. 8.4.1. Histograms showing angular alignment errors measured with different guidance image types. Plots (a)-(d) show results measured using the vertical digital camera mount, while plots (e)-(h) show results measured using the horizontal digital camera mount.

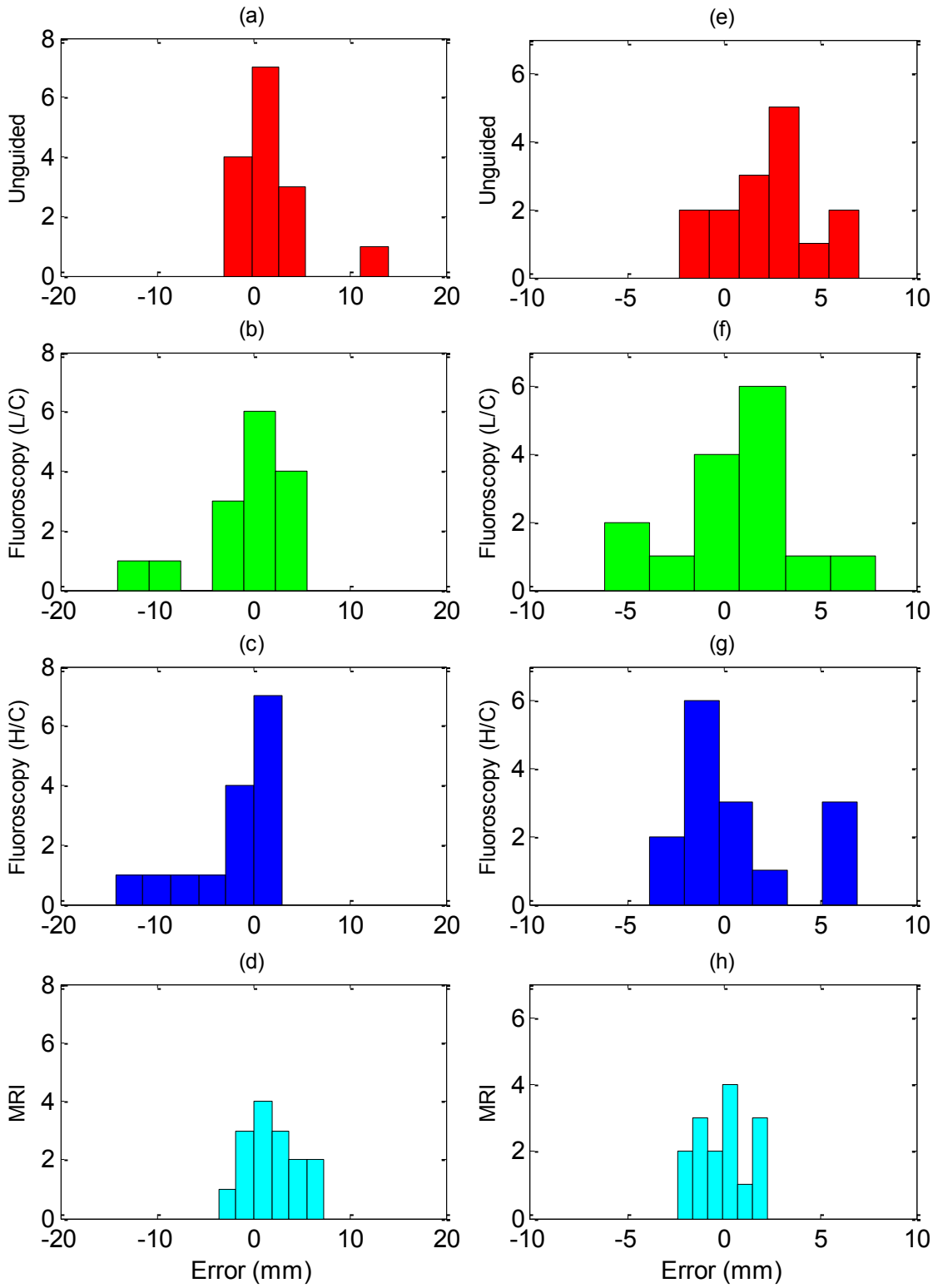

Fig. 8.4.2. Histograms showing linear alignment errors measured with different guidance image types. Plots (a)-(d) show results measured using the vertical digital camera mount, while plots (e)-(h) show results measured using the horizontal digital camera mount.

	Unguided		Fluoroscopy (L/C)		Fluoroscopy (H/C)		MRI	
Unguided	-	-	0.065	0.001	0.172	0.000	0.001	0.000
Fluoroscopy (L/C)	0.065	0.001	-	-	0.450	0.479	0.041	0.035
Fluoroscopy (H/C)	0.172	0.000	0.450	0.479	-	-	0.001	0.124
MRI	0.001	0.000	0.041	0.035	0.001	0.124	-	-

Table 8.4.1. P values calculated using Levene's test to assess the differences in variance between two sets of angular alignment errors. Each cell shows the P value for the vertical digital camera mount results followed by the P value for the horizontal digital camera mount results. Significant (P <= 0.05) results are highlighted red.

	Unguided		Fluoroscopy (L/C)		Fluoroscopy (H/C)		MRI	
Unguided	-	-	0.381	0.241	0.506	0.409	0.577	0.064
Fluoroscopy (L/C)	0.381	0.241	-	-	0.788	0.621	0.127	0.032
Fluoroscopy (H/C)	0.506	0.409	0.788	0.621	-	-	0.163	0.028
MRI	0.577	0.064	0.127	0.032	0.163	0.028	-	-

Table 8.4.2. P values calculated using Levene's test to assess the differences in variance between two sets of linear alignment errors. Each cell shows the P value for the vertical digital camera mount results followed by the P value for the horizontal digital camera mount results. Significant (P <= 0.05) results are highlighted red.

The linear alignment errors between the tip of the catheter and papilla for all tests are shown in Fig. 8.4.2. The magnitude of the mean error in all tests is low (<2mm), but in contrast to the angular error all tests exhibit a range of less than 20mm and there is some clustering around the mean. Outlying linear errors of >|10|mm are seen only in the vertical images for the unguided and both fluoroscopic guided tests. Table 8.4.2 shows

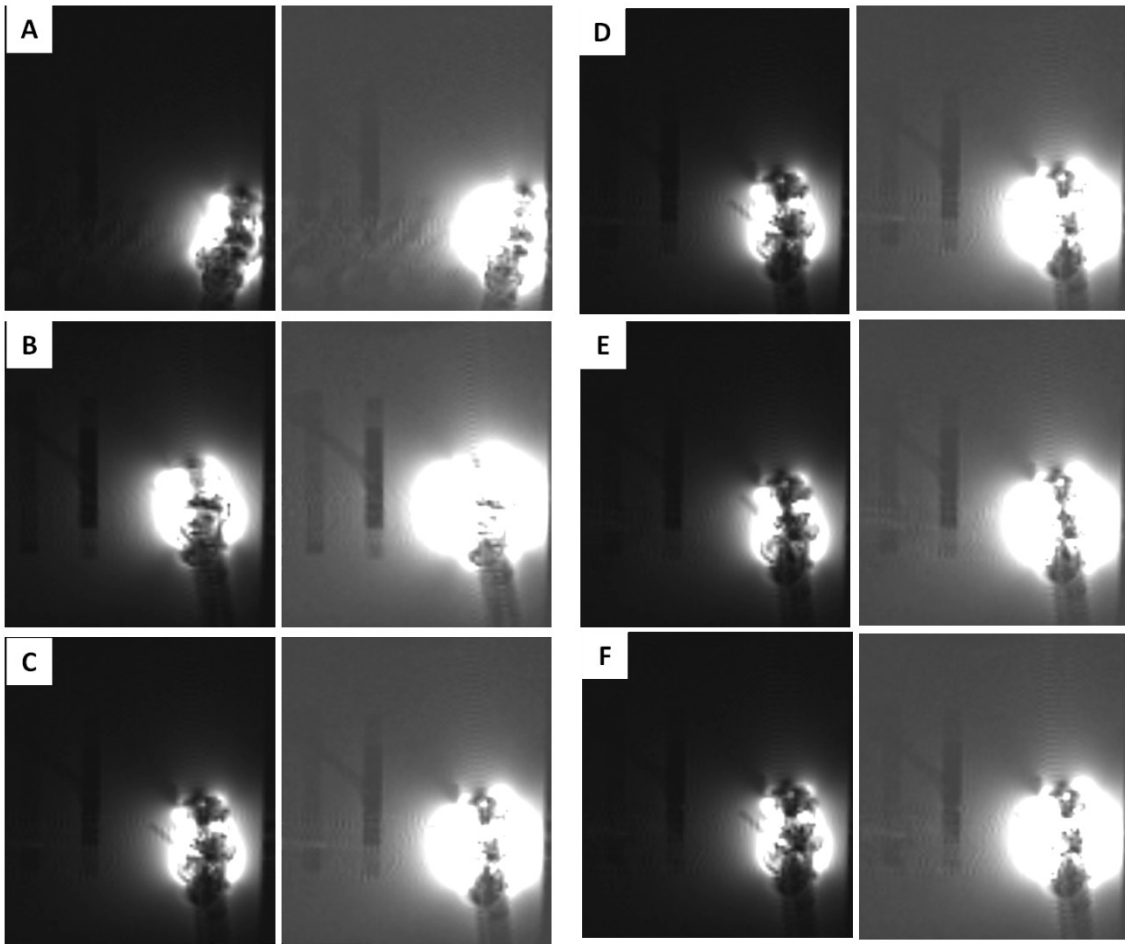

Fig. 8.5.1. MRI guidance series, with the six images (A-F) displayed in the order that they were acquired during the alignment test. On the left the image is displayed with increased contrast (WC = 240, WW = 560) to visualise the catheter, while the right image display is brighter (WC = 80, WW = 220) to visualise the bile duct.

that the only significant differences in linear error variance are between the horizontal MRI guided and fluoroscopic guided tests. All other P values are >0.05 and are therefore not considered significant.

8.5 Discussion

The experiment presented here was designed to provide a qualitative evaluation of the benefit of providing an endoscopist with intra-operative MR images instead of fluoroscopic images during biliary cannulation. While the test setup only approximates the clinical situation, the results presented here suggest that the MRI significantly outperforms the fluoroscopic images. The angular alignment error between the bile duct and catheter is significantly reduced when MRI guidance is used compared with simulated high or low contrast fluoroscopic imaging.

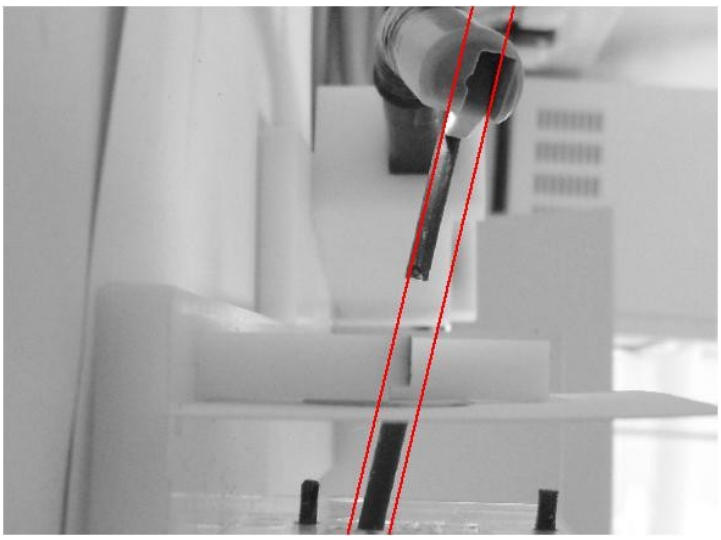

Fig. 8.5.2. Image acquired from the horizontal camera mount showing the position of the MR guidance image slice (red lines). The thickness of the catheter means that it can remain within the slice despite a significant misalignment.

Fig. 8.5.1 shows a sequence of images taken during a test run to illustrate the MRI guidance provided to the operator. The image slice was positioned to so that the bile duct lies along the plane. The in-plane angle of the bile duct can be directly observed and it is a simple matter to position the catheter at the same angle (Fig. 8.5.1 C - F). If the out-of-plane angle of the catheter is different from the bile duct then the catheter disappears from the image slice (Fig. 8.5.1 A, B), which can be noted and corrected by the operator when it occurs to prevent any large angular alignment errors.

This can be contrasted with the fluoroscopic guidance images (Fig.8.3.2) in which there are no reference planes and it is therefore not possible to determine the relative alignment of the objects in three dimensions. Increasing the contrast between the bile duct and surrounding tissue in the fluoroscopic guidance images does not improve the level of guidance, since the limitation is the nature of the image projection, rather than the definition of structures within the image. However, the data suggest that fluoroscopic guidance is an improvement over no guidance as the operator has some information regarding the bile duct angle even though there is no way of contextualising this information.

Due to the design of the camera mount on the test rig, the vertical camera images are approximate to the MR guidance image plane while the horizontal camera images are approximately orthogonal to the MR image plane. The in-plane (approximately vertical image) errors are clustered around the mean while the out of plane (approximately horizontal image) errors are more dispersed (Fig. 8.4.1). The horizontal image shown in

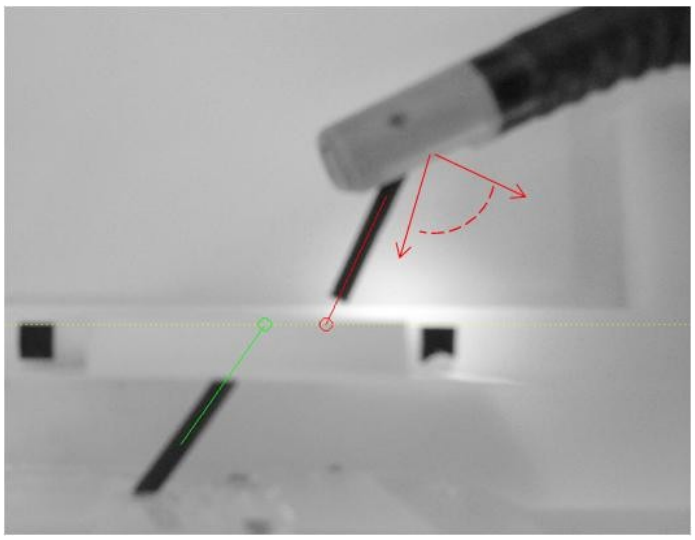

Fig. 8.5.3. Image acquired from the vertical camera mount showing the direction and limits of the duodenoscope camera lens (red lines). In this position, the operator is unable to see the catheter tip or the papilla.

Fig. 8.5.2 demonstrates how the MR image slice thickness causes this effect. The operator is only aware if the catheter moves out of the slice, but once the catheter is in the slice there is no further information available and the errors are distributed randomly. This effect can be minimised by using a thinner image slice, but this will result in a lower image SNR.

In all tests the linear alignment errors between the tip of the catheter and the bile duct were in most cases very low, due to the guidance provided by the duodenoscope video camera. The exceptions to this occurred when the bile duct was placed at an extreme angle without MRI guidance. In order to align the catheter with an extreme bile duct angle the duodenoscope tip must be positioned such that the tip of the catheter and the papilla are no longer visible to the duodenoscope camera (Fig. 8.5.3). As with the angular alignment, the fluoroscopic images do not provide enough information to enable the operator to perform the linear alignment without the duodenoscope camera. This is not an issue with MRI guidance, since the tip of the catheter and papilla are visible on the MR image at all times.

This test was intended to approximate the significant features of the clinical challenge of biliary cannulation, but clearly there are many simplifications that have been made. One area that would require attention for the clinical procedure would be the potential inclusion of an MR visible catheter. In this simulation the MR image contrast was inverted - the catheter was visible as a void in the water-filled container while in the clinical situation the catheter would be surrounded by air, and would have to contain a

signal-producing material in order to be visible. An alternative would be to incorporate a visualisation of the duodenoscope tip coil tracking system, which with development could provide the endoscopist with information about the angle and position of the catheter and duodenoscope tip (Chapter 7).

The quality and clarity of the MR guidance images is another area which would change in a clinical situation. The SNR of the guidance images will be lower due to noise produced by the body, and the anatomic structures will be prone to motion and deformation. Motion artefacts can further degrade the quality of MRI to the extent that the anatomy of interest cannot be visualised. Motion compensation strategies such as image gating and retrospective reconstruction could be used (see Section 2.2.3) to overcome this, with the consequence of significantly extending the image acquisition time. In this simulation the guidance image acquisition time was restricted to cause a reduction in image quality, but in vivo testing is required to determine how accurate this approximation was.

Finally, the benefit of MRI guidance over fluoroscopic guidance may appear greater in this simulation compared with the clinical situation, due to the range of bile duct angles evaluated. As noted in Section 4.2, operators are trained to approach the papilla from a certain direction, as this corresponds to the most common bile duct angle. While clearly this is not correct for all patients, the success rate exhibited for fluoroscopic guidance is higher than suggested by this test due to some consistency between patients. However, in those cases in which the biliary anatomy differs from the majority, this experiment has demonstrated that MRI guidance will offer a significant improvement in cannulation success.

8.6 Conclusions

The MRI guided biliary cannulation procedure relies on both the previously presented endoscope actuation system and the real-time tracking method. The intra-operative tracking images must be aligned with the biliary system, and in order to provide guidance the operator must be able to both contextualise the images relative to the tool and anatomy positions.

The use of guidance images for cannulation was assessed in a simulated clinical situation in this chapter. The MRI-guided system was shown to reduce the angular alignment error between the catheter and bile duct compared with simulated fluoroscopic guidance. This demonstrates that the MRI guided ECRP system presented in this thesis can improve clinical procedure outcomes.

Chapter 9

Conclusions and Future Work

This chapter provides a summary of the research presented in this thesis followed by a discussion of the conclusions that can be drawn from these studies and an outline of further work that would build on this research.

9.1 Summary of Thesis

The motivation and objectives of this thesis are outlined in Chapter 1. The benefits of the use of intra-operative MRI for the guidance of interventional procedures were identified and the opportunity to improve patient outcomes by combining the techniques of intra-operative MRI and flexible endoscopy was described. The technique of MRI and the challenges associated with it are described in Chapter 2, in particular MRI compatibility and the issues of motion during image acquisition.

A variety of interventional MRI systems have been developed by researchers and are categorised in Chapter 3 in terms of the actuation, sensing and device tracking methods utilised. There is no consensus as to the optimal system configuration; instead, the system is dependent on the challenges posed by specific medical procedures. MRI compatible endoscopes have been developed but MRI guided endoscopy does not appear to have been attempted previously.

The technical challenges posed by traditional MRI and endoscopic interventions of the biliary system are identified in Chapter 4, followed by the development of a procedure and system outline to enable MRI guided ERCP. The system relies on an MRI compatible duodenoscope and catheter with intraluminal imaging coils mounted at their tips, which are described in this chapter.

The prototype endoscope remote actuation system is presented in Chapter 5, including the user interface, EMI shielding design and control electronics along with the design features of each actuator module explained in detail. In addition the design, development and testing of a miniature pneumatic clutch was presented, which enables the endoscope actuation modules to rely on significantly fewer motors.

Chapter 6 covered testing of the remote actuation system performance in two broad areas. Firstly the MRI compatibility of the system was investigated, beginning with

component-level testing and building up to complete system testing. This was followed by a study of the functional capacity of the endoscope remote actuation system to perform biliary cannulation.

In order to assess this, an objective measure of an operator's technical skill at completing a simulated biliary cannulation task was developed and validated. The performance of operators using the remote actuation system was then compared to their performance when operating manually.

The development and preliminary testing of a method of tracking the position of the intra-luminal MR receiver coils using the MRI scanner is described in Chapter 7. This includes a procedure for acquiring 1D MR projections, filtering the signals and determining the coil location and orientation, as well as experimental results using the duodenoscope tip coil.

Finally, a test to investigate the potential of the complete MRI-guided ERCP system to improve the clinical outcomes of biliary endoscopy is presented in Chapter 8. The ability of the operator to align the bile duct and catheter using MRI guidance and fluoroscopic guidance was quantitatively compared in a simulated environment.

9.2 Contributions

Overall the objectives outlined in Chapter 1 have been met; a system that allows the duodenoscope to be operated while it is inside the scanner bore has been developed and the system performance demonstrated. A method of tracking the position of the duodenoscope tip using the MRI scanner and the intra-luminal imaging coil has been developed and shown to provide acceptable position measurements. Finally, the clinical benefits of MRI-guided endoscopy were demonstrated by showing the improvement that MRI guidance can provide when compared with fluoroscopic guidance.

Two further areas of interest that lie outside the scope of the original objectives were identified and explored in this thesis. The miniature pneumatic clutch presented in Chapter 5 enables the cost of interventional MRI systems to be significantly reduced by removing the need for multiple costly MRI compatible motors. In addition to this, the tool for objectively assessing endoscopic skill using a mechanical simulator developed in Chapter 6 has applications in the fields of endoscopic training and certification.

9.2.1 Endoscope Remote Actuation System

The endoscope remote actuation system has some specific requirements associated with it, which were described in Chapter 4. The design of this sub-system enables all 6 of the duodenoscope DOF to be actuated remotely from outside the scanner bore. The system is

capable of achieving the force and torque specifications measured during the duodenoscope characterisation test. The USR-30-NM motors are not capable of achieving the specified power targets for three duodenoscope DOF due to their limited rotation speed compared with the high speeds that manual actuation is capable of reaching. However, the slower movements are beneficial for the fine movements required during the critical cannulation phase.

The endoscope remote actuation system is capable of docking onto the duodenoscope during the procedure with minimal interruption of the workflow. The positioning of each module is flexible to enable patients of different sizes to be accommodated and to allow the docking process to begin at different stages of the procedure. The duodenoscope can be released from the system with just three movements, enabling the operator to rapidly revert to manual operation in an emergency.

The MRI compatibility of the actuation system was extensively tested at both 1.5T and 3T with three different imaging sequences. The system with the duodenoscope camera and motors in operation was shown to reduce the image SNR by less than 5% for all image sequences. Experiments demonstrated that this performance was achieved by the construction of an external electromagnetic shield around the active components and the removal of any common grounding between the active components and the MRI scanner shield. No susceptibility artefacts from the endoscope remote actuation system were visible due to it's location out of the imaging volume.

Functional testing of the system demonstrated that operators are capable of completing a simulated biliary cannulation task with minimal loss of technical performance. Individual operators varied in the degree to which they translated their existing skills to the remote actuation system, but the results demonstrated that the system was capable of enabling high performance scores to be achieved.

This is understood to be the first example of the use of the hybrid (manual and remotely actuated) mode of operation in a system for MRI guided endoscopy. This remote actuation system could be utilised in the wider field of endoscopy with small modifications, while there are other clinical specialities which may benefit from the demonstrated hybrid mode of operation.

9.2.2 Duodenoscope tip tracking

The tracking method presented in Chapter 7 enables the position of the MR receiver coils at the tip of the duodenoscope and catheter to be measured using the MRI scanner. Testing with the duodenoscope tip coil showed that, with an appropriate calibration, the

position of the coil was measured to within 4.5mm of it's true position over a range of positions, orientations and signal loading cases. The requirement for a calibration offset to the measured position may be due to the MR receiver coil not producing a symmetrical signal. The coil position measurement method takes approximately 200ms to complete, for an update rate of 5Hz.

The use of the presented method to measure the orientation of the duodenoscope tip coil was less successful than the position measurement. The assumption that a 1D projection along the long axis of the coil would have a wider peak was not correct for many of the test points, which resulted in an inaccurate and unstable measurement of the coil orientation.

Active microcoils have previously been used to track the position of tools within MRI, but published research has focused on the use of small solenoid microcoils which are only suitable for tracking. The research presented in this thesis demonstrates for the first time that accurate tracking is possible using imaging coils. This enables devices with smaller form factors to be constructed and is of particular benefit for applications such as endoscopy where space is particularly limited.

9.2.3 MRI-guided ERCP System and Procedure

The MRI-guided ERCP system presented in this thesis is designed to enable a clinically viable diagnostic and interventional procedure to be performed. Procedural workflow is facilitated by the use of the endoscope remote actuation system, a critical aspect of which is the facility to rapidly exchange between manual and remote actuation. This enables phases of the procedure that do not require remote actuation to be performed manually with standard techniques, before the remote actuation system is introduced for the guided section of the procedure. This feature overcomes the issues experienced by previous attempts at MRI endoscopy (not having access to the endoscope controls during MRI scanning) as well as the issues experienced with robotic endoscope systems that do not enable manual intubation.

In addition to this, the benefit of real-time MRI guidance compared with fluoroscopic guidance has been quantitatively demonstrated. In a simulated biliary cannulation task the MRI guidance provided a greater level of information regarding the relative orientations of the bile duct and catheter, which meant that the operator was able to more accurately align the catheter. This result provides an important indication that the clinical motivation of improving the technical success rate of the ERCP procedure is achievable.

9.2.4 Other Research

Two other activities within this research project have resulted in promising developments, which are summarised in this section. The first of these is the miniature pneumatic clutch which was designed to enhance the prototype endoscope remote actuation system. The clutch precludes the use of two parallel DOF at the same time, but it reduces the system cost and weight by enabling redundant parallel actuators to be removed from the actuation modules and replaced by a single motor with several clutches.

The performance of the endoscope remote actuation system was tested using an objective endoscopic technical skill assessment tool, developed within this project. The tool consisted of a mechanical simulator that was modified to make it specifically a challenge of biliary cannulation. The position of the duodenoscope tip and catheter was recorded during the test run by an electromagnetic tracking system. The data for this recording was then analysed to develop a scoring system that was capable of distinguishing between operators' endoscopic performance. Analysis of results from participants with a wide range of endoscopic skill showed that the performance score derived from the data was a good indicator of skill level.

This assessment tool has the potential to be very valuable in the field of endoscopic training and assessment. The repeatable mechanical simulator and objective data recording mean that consistent data can be obtained, either to compare trainees against a certification standard or to chart the development of a trainee as they progress through the curriculum.

9.3 Future Work

9.3.1 Endoscope Remote Actuation System

Aspects of the endoscope remote actuation system were identified as suitable for further research during functional testing. The user interface for 5 of the 6 DOF performed well, with users reporting a smooth transition from their experience of manual endoscopes. However, many users struggled with the endoscope flexible section rotational control due to it's location and the prevalence of torque steering as a technique among ERCP trained endoscopists. An alternative configuration with the control mounted on a base unit and connected to the main interface handle would make the location of the

control more intuitive and enable the handle to be turned to induce endoscope flexible section rotation.

The use of position and force sensors is a further area in which the endoscope remote actuation system and user interface could be developed. Whilst the MRI guidance removes some of the need for sensor feedback, during testing users reported that an indication of the position of the tip steering wheels and catheter feed would enable them to contextualise the duodenoscope video image more easily. This could be achieved by incorporating position sensors on the left hand and catheter feed actuation modules and providing a visual indication of the steering wheel position to the user alongside the video screen.

Full haptic feedback would be challenging to implement in the MRI environment, but the catheter feed module in particular would benefit from an indication of the force being applied by the actuator module. The force experienced by the tip of the catheter will change significantly during cannulation and during exploration of the bile duct; if this information could be communicated to the operator it would make this stage of the procedure easier and safer.

The capability of the system to be cleaned and sterilized between repeated procedures is an aspect of the remote actuation system that was not addressed. Testing of the prototype in mechanical simulators did not require this, but as testing is expanded to in vitro and in vivo studies (see below) the actuation system will need to be sterilized. This could be achieved by adopting the method described by Ruiter et al [Ruiter, 2012], who incorporated a removable sterile interface part between the endoscope and actuation module.

9.3.2 Duodenoscope tip tracking

The duodenoscope tip coil position measurement method presented is far from optimised and there is significant scope for improving both it's performance and speed. A larger study is required to optimise the measurement accuracy by adjusting the 1D projection resolution, the number of projections used and the relative orientations of the projections. In addition, there is potential to reduce the time that the processing algorithm takes to complete by optimising the coding and investigating faster methods of smoothing the projection signal.

Further work should also be performed to determine the sensitivity of the coil position measurement method to surrounding sources of signal. The results presented in this thesis involved three distinct signal loading cases and found that the method was

insensitive to the loading case. However, each case was based upon the coil being immersed in liquid in a simulated environment. Using the tracking method to measure the position of the coil when surrounded by ex vivo biological tissues would be an important step towards clinical validation of the method.

Several possibilities exist for improvement of the coil orientation calculation. The present method only takes into account the width of the 1D projection peaks. Each measured peak contains a variety of features, such as equally spaced double peaks or clear weighting of peaks to one side. By collecting additional data and analysing the pattern of these peaks relative to the coil orientation it may be possible to determine the coil orientation relative to the projections.

Another strategy for determining the coil orientation could involve a two stage process whereby the position of the coil is calculated first and then that information is used to define a further set of projections of a limited volume near the coil.

The coil position detection method is suitable for any imaging microcoil, and should become more accurate as the size of the coil is reduced. For the development of the MRI-guided ERCP system this should be confirmed by testing with the catheter microcoil. If the position of both coils can be tracked independently using this method then it will be possible to perform motion correction of the bile duct and duodenum separately, as well as providing more information to the endoscopist regarding the state of the endoscope.

9.3.3 MRI-guided ERCP System and Procedure

Further work on the MRI-guided ERCP system must focus on a strategy for working towards in vivo trials and clinical approval. The full MRI-guided ERCP procedure is a complex one and the system currently has many features and sub-systems that are not clinically approved, such as the endoscope remote actuator and the intra-luminal imaging coils. One approach to overcome this would be to run clinical trials of individual sub-systems or components which have relatively limited clinical objectives, but also contribute to the system approval as a whole.

For example, in vivo testing of the intra-luminal MR receiver coils in the rectum or upper oesophagus has been proposed [Syms, In Press]. The advantage of this approach is that it does not rely on the flexible endoscope and actuation system to position the coils correctly since they are only inserted a short distance into the lumen. Because of this the ethical approval process is more straightforward and diagnostic images could be generated which demonstrate the value of the coils.

Similarly, the endoscope remote actuation system could be used initially during a standard fluoroscopic guided procedure to demonstrate it's capacity to assist with ERCP and investigate the benefits of remote endoscope control. This would avoid the need to obtain approval for the MRI-based sections of the system simultaneously. Other approaches could be to perform studies in cadavers or animal models prior to in vivo testing.

As discussed above, the sterilization issue of the remote actuation system is an important first step to obtaining approval for these limited trials. A study of system failure modes and the development of safety override systems would also need to be performed before such studies could be undertaken.

9.3.4 Other Research

The miniature pneumatic clutch presented in Chapter 5 is not limited to this application and could improve any interventional MRI system based on ultrasonic motors in the same manner. Further work could focus on different designs of the clutch to produce versions that engage when there is no pneumatic pressure ('normally on') or variants which lock in position when the pneumatic pressure is removed. These designs would further widen the range of clutch applications.

Further validation work of the endoscope performance assessment tool will need to be undertaken to confirm the preliminary results before it is adopted more widely. Similar studies with much larger numbers of participants will be needed along with a direct, long term comparison with existing methods of technical skill assessment. With more data it may also be possible to identify more detailed characteristics regarding endoscope skill than those currently assessed, such as particular techniques used or the relative use of different endoscope degrees of freedom. Such information could be used to tailor training programs as well as identify more optimised endoscopic techniques.

9.4 Publications to Date

This research has resulted in the following publication:

- North, O. J., Ristic, M., Wadsworth, C. A., Young, I. R. and Taylor-Robinson, S. D. (2012). Design and evaluation of endoscope remote actuator for MRI-guided Endoscopic Retrograde Cholangio-Pancreatography (ERCP). IEEE International Conference on Biomedical Robotics and Biomechatronics. Rome: 787-792.

The following publications have been submitted for peer review:

- Ralphs, S., North, O. J., Taylor-Robinson, S. D., Ristic, M., Kelly, N. I. C., and Lambert, N. A. Objective Assessment of Endoscopic Skill using Kinematic Analysis of an ERCP Training Simulation. Gastrointestinal Endoscopy.

Bibliography

[Abbott, 2007] Abbott, D. J., Becke, C., Rothstein, R. I. and Peine, W. J. (2007). Design of an Endoluminal NOTES Robotic System. *International Conference on Intelligent Robots and Systems*. San Diego, USA, IEEE: 410-416.

[Ahmad, 2009] Ahmad, M. M., Syms, R. R. A., Young, I. R., Mathew, B., Casperz, W., Taylor-Robinson, S. D., Wadsworth, C. A. and Gedroyc, W. M. W. (2009). Catheter-based flexible microcoil RF detectors for internal magnetic resonance imaging. *Journal of Micromechanics and Microengineering* 19(7).

[Ahmad, 2008] Ahmad, M. M., Syms, R. R. A., Young, I. R., Matthew, B., Casperz, W., Taylor-Robinson, S. and Gedroyc, W. (2008). Flexible Microcoils for Magnetic Resonance Imaging of the Bile Duct. *19th MicroMechanics Europe Workshop*. Aachen, Germany: 275-278.

[Allemann, 2009] Allemann, P., Ott, L., Asakuma, M., Masson, N., Perretta, S., Dallemagne, B., Coumaros, D., Mathelin, M. D., Soler, L. and Marescaux, J. (2009). Joystick Interfaces Are Not Suitable for Robotized Endoscope Applied to NOTES. *Surgical Innovation* 16(2): 111-116.

[Anastasiadis, 2006] Anastasiadis, A. G., Lichy, M. P., Nagele, U., Kuczyk, M. A., Merseburger, A. S., Hennenlotter, J., Corvin, S., Sievert, K.-D., Claussen, C. D., Stenzl, A. and Schlemmer, H.-P. (2006). MRI-Guided Biopsy of the Prostate Increases Diagnostic Performance in Men with Elevated or Increasing PSA Levels after Previous Negative TRUS Biopsies. *European Urology* 50(4): 738-749.

[Anderson, 2012] Anderson, M., Fisher, L., Jain, R., Evans, J., Appalaneni, V., Ben-Menachem, T., Cash, B., Decker, G., Early, D., Fanelli, R., Fisher, D., Fukami, N., Hwang, J., Ikenberry, S., Jue, T., Khan, K., Krinsky, M., Malpas, P., Maple, J., Sharaf, R., Shergill, A. and Dominitz, J. (2012). Complications of ERCP. *Gastrointestinal Endoscopy* 75(3): 467-473.

[Andriulli, 2007] Andriulli, A., Loperfido, S., Napolitano, G., Niro, G., Valvano, M. R., Spirito, F., Pilotto, A. and Forlano, R. (2007). Incidence Rates of Post-ERCP Complications: A Systematic Survey of Prospective Studies. *American Journal of Gastroenterology* 102: 1781-1788.

[Arepally, 2004] Arepally, A., Georgiades, C., Hofmann, L. V., Choti, M., Thuluvath, P. and Bluemke, D. A. (2004). Hilar Cholangiocarcinoma: Staging with Intrabiliary MRI. *American Journal of Roentgenology* 183(4): 1071-1074.

[ASTM, 2007] ASTM (2007). Standard Test Method for Evaluation of MR Image Artefacts from Passive Implants. *F 2119-07*. ASTM. West Conshocken, Pa, United States.

[Atkinson, 2011] Atkinson, D. (2011). Motion Compensation Strategies. *19th International Society of Magnetic Resonance in Medicine Conference*. Montreal.

[Barnes, 1987] Barnes, J. R. (1987). *Electronic System Design: Interference and Noise Control Techniques*. Prentice-Hall Inc.,

[Beyersdorff, 2004] Beyersdorff, D., Winkel, A., Hamm, B., Lenk, S., Loening, S. A. and Taupitz, M. (2004). MR Imaging-guided Prostate Biopsy with a Closed MR Unit at 1.5 T: Initial Results. *Radiology* 234(2): 576-581.

[Bilgin, 2009] Bilgin, M., Shaikh, F., Semelka, R. C., Bilgin, S. S., Balci, N. C. and Erdogan, A. (2009). Magnetic resonance imaging of gallbladder and biliary system. *Topics in Magnetic Resonance Imaging* 20(1): 31-42.

[Brandner, 2006] Brandner, E. D., Wu, A., Chen, H., Heron, D., Kalnicki, S., Komanduri, K., Gerszten, K., Burton, S., Ahmed, I. and Shou, Z. (2006). Abdominal organ motion measured using 4D CT. *Oncology Biology Physics* 65(2): 554-560.

[Brown, 2003] Brown, M. A. and Semelka, R. C. (2003). *MRI Basic Principles and Applications*. John Wiley & Sons. Hoboken, NJ, 1st Edition.

[Brujic, 2012] Brujic, D., Galassi, F., Rea, M., Ferreira, P., deSouza, N. and Ristic, M. (2012). Analysis of localisation accuracy of multiple wireless coils in interventional MRI. *9th International Interventional MRI Symposium*. Boston, USA: 62.

[Canes, 2009] Canes, D., Lehman, A. C., Farritor, S. M., Oleynikov, D. and Desai, M. M. (2009). The Future of NOTES Instrumentation: Flexible Robotics and In Vivo Minirobots. *Journal of Endourology* 23(5): 787-792.

[Chen, 2004] Chen, X., Lehman, C. D. and Dee, K. E. (2004). MRI-Guided Breast Biopsy: Clinical Experience with 14-Gauge Stainless Steel Core Biopsy Needle. *American Journal of Roentgenology* 182(4): 1075-1080.

[Chinzei, 1999] Chinzei, K., Kikinis, R. and Jolesz, F. A. (1999). MR Compatibility of Mechatronic Devices: Design Criteria. *Medical Image Computing and Computer-Assisted Intervention* C. Taylor and A. Colchester. Berlin / Heidelburg, Springer. 1679: 1020-1030.

[Christoforou, 2006a] Christoforou, E., Akbudak, E., Ozcan, A., Karanikolas, M. and Tsekos, N. V. (2006a). Performance of interventions with manipulator-driven real-tme MR guidance: implementation and initial in vitro tests. *Magnetic Resonance Imaging* 26(1): 69-77.

[Christoforou, 2006b] Christoforou, E. G., Özcan, A. and Tsekos, N. V. (2006b). Manipulator for Magnetic Resonance Imaging Guided interventions: Design, Prototype and Feasibility. *IEEE International Conference on Robotics and Automation*. Orlando, Florida: 3838-3843.

[Chutkan, 2006] Chutkan, R. K., Ahmad, A. S., Cohen, J., Cruz-Correa, M. R., Desilets, D. J., Dominitz, J. A., Dunkin, B. J., Kantsevoy, S. V., Jr., L. M., Mishra, G., Perdue, D., Petrini, J. L., Pfau, P. R., Savides, T. J., Telford, J. J. and Vargo, J. J. (2006). ERCP core curriculum. *Gastrointestinal Endoscopy* 63(3): 361-376.

[Clifford, 2002] Clifford, M. A., Banovac, F., Levy, E. and Cleary, K. (2002). Assessment of Hepatic Motion Secondary to Respiration for Computer Assisted Interventions. *Computer Aided Surgery* 7: 291-299.

[Corcione, 2005] Corcione, F., Esposito, C., Cuccurullo, D., Stettembre, A., miranda, N., Amato, F., Pirozzi, F. and Caiazzo, P. (2005). Advantages and limits of robot-assisted laparoscopic surgery: preliminary experience. *Surgical Endoscopy* 19(1): 117-119.

[Coutts, 2003] Coutts, G. A., Larkman, D. J., Gilderdale, D. J. and Grantham, A. C. (2003). Endoscope Suitable for Magnetic Resonance Imaging. US 6, 993 B1.

[Datta, 2002] Datta, V., Chang, A., Mackay, S. and Darzi, A. (2002). The relationship between motion analysis and surgical technical assessments. *The American Journal of Surgery* 184(1): 70-73.

[Deshpande, 2003] Deshpande, V. S., Shea, S. M. and Li, D. (2003). Artifact Reduction in True-FISP Imaging of the Coronary Arteries by Adjusting Imaging Frequency. *Magnetic Resonance in Medicine* 49(5): 803-9.

[Desilets, 2011] Desilets, D. J., Banerjee, S., Barth, B. A., Kaul, V., Kethu, S. R., Pedrosa, M. C., Pfau, P. R., Tokar, J. L., Varadarajulu, S., Wang, A., Song, L.-M. W. K. and Rodriguez, S. A. (2011). Endoscopic Simulators. *Gastrointestinal Endoscopy* 73(5): 861-867.

[DeSouza, 1995] DeSouza, N., Gibbons, A. H., Coutts, G. A., Hall, A. S., Puni, R., Calam, J. and Young, I. R. (1995). Magnetic resonance imaging during upper GI endoscopy: technical considerations and clinical feasibility. *Minimally Invasive Therapy and Allied Technologies* 4(5): 277-281.

[DeSouza, 1996] DeSouza, N., Gilderdale, D., Puni, R., Coutts, G. A. and Young, I. R. (1996). A Solid Reusable Endorectal Receiver Coil for Magnetic Resonance Imaging of the Prostate: Design, Use and Comparison with an Inflatable Endorectal Coil. *Journal of Magnetic Resonance Imaging* 6(5): 801-804.

[DiMaio, 2005] DiMaio, S. P., Kacher, D. F., Ellis, R. E., Fichtinger, G., Hata, N., Zientara, G. P., Panych, L. P., Kikinis, R. and Jolesz, F. A. (2005). Needle Artifact Localization in 3T MR Images. *Medicine Meets Virtual Reality 14: Accelerating Change in Healthcare: Next Medical Toolkit*, IOS Press. 119: 120-125.

[Dumoulin, 1997] Dumoulin, C. L. (1997). Active Visualization - MR Tracking. *Interventional Magnetic Resonance Imaging*. J. F. Debatin and G. Adam. Berlin and Heidelberg Springer-Verlag Berlin and Heidelberg GmbH & Co. KG: 65-75.

[Dumoulin, 1993] Dumoulin, C. L., D., D. R., Schenck, J. F. and Souza, S. P. (1993). Tracking System to Follow the Position and Orientation of a Device with Radiofrequency Field Gradients. USPA. 5,211,165.

[Elhawary, 2008a] Elhawary, H. (2008a). MRI compatible mechatronic devices to aid medical diagnosis and intervention Mechanical Engineering, Imperial College, London. PhD Thesis.

[Elhawary, 2008b] Elhawary, H., Tse, Z., Hamed, A., Rea, M., Davies, B. L. and Lamperth, M. U. (2008b). The case for MR-compatible robotics: a review of the state of the art. *The International Journal of Medical Robotics and Computer Assisted Surgery* 4(2): 105-113.

[Elhawary, 2006] Elhawary, H., Zivanovic, A., Rea, M., Davies, B., Besant, C., McRobbie, D., deSouza, N., Young, I. R. and Lamperth, M. (2006). The Feasibility of MR-Image Guided Prostate Biopsy Using Piezoceramic Motors Inside or Near to the Magnet Isocentre. *Medical Image Computing and Computer-Assisted Intervention* R. Larsen, M. Nielson and J. Sporring. Berlin / Heidelburg, Springer: 519-526.

[Ende, 2012] Ende, A., Zopf, Y., Konturek, P., Naegel, A., Hahn, E. G., Matthes, K. and Maiss, J. (2012). Strategies for training in diagnostic upper endoscopy: a prospective, randomized trial. *Gastrointestinal Endoscopy* 75(2): 254-260.

[Ericsson, 2006] Ericsson, K. A., Charness, N., Feltovich, P. J. and Hoffman, R. R., Eds. (2006). *The Cambridge handbook of expertise and expert performance*. New York, Cambridge University Press.

[Feldman, 1997] Feldman, D. R., Kulling, D. P., Hawes, R. H., Kay, C. L., Muckenfuss, V. R., Cotton, P., B., Bohning, D. E. and Young, J. W. R. (1997). MR Endoscopy: Preliminary Experience in Human Trials. *Radiology* 202: 868-870.

[Fichtinger, 2002] Fichtinger, G., Krieger, A., Susil, R. C., Tanacs, A., Whitcomb, L. L. and Atalar, E. (2002). Transrectal Prostate Biopsy Inside Closed MRI Scanner with Remote Actuation, under Real-Time Image Guidance. *Medical Image Computing and Computer-Assisted Intervention*. Berlin / Heidelberg, Springer. 2488: 91-98.

[Fischer, 2008] Fischer, G. S., Iordachita, I. I., Csoma, C., Tokuda, J., Mewes, P. W., Tempany, C. M., Hata, N. and Fichtinger, G. (2008). Pneumatically Operated MRI-Compatible Needle Placement Robot for Prostate Interventions. *IEEE International Conference on Robotics and Automation*. Pasadena, CA, USA, IEEE Xplore: 2489-2495.

[Foutch, 1990] Foutch, P., Kerr, D., Harlan, J., Manne, R., Kummet, T. and Sanowski, R. (1990). Endoscopic retrograde wire-guided brush cytology for diagnosis of patients with malignant obstruction of the bile duct. *American Journal of Gastroenterology* 85(7): 791-5.

[Franco, 2012] Franco, E., Rodriguez y Baena, F. and Ristic, M. (2012). Design and validation of a 2-DOF MRI-Compatible Pneumatic Positioner. *9th International Interventional MRI Symposium*. Boston, USA: 92.

[Gassert, 2008] Gassert, R., Chapuis, D., Bleuler, H. and Burdet, E. (2008). Sensors for Applications in Magnetic Resonance Environments. *IEEE/ASME Transactions on Mechatronics* 13(3): 335-344.

[Gassert, 2006a] Gassert, R., Dovat, L., Lambercy, O., Ruffieux, L., Chapuis, D., Ganesh, G., Burdet, E. and Bleuler, H. (2006a). *A 2-DOF fMR-compatible haptic interface to investigate the neural control of arm movements*. IEEE International Conference on Robotics and Automation, Orlando, Florida, IEEE.

[Gassert, 2006b] Gassert, R., Yamamoto, A., Chapuis, D., Dovat, L., Bleuler, H. and Burdet, E. (2006b). Actuation Methods for Applications in MR Environments. *Concepts in Magnetic Resonance Part B: Magnetic Resonance Engineering* 29B(4): 191-209.

[Gilderdale, 1999] Gilderdale, D. J., deSouza, N. M., Coutts, G. A., Chui, M. K., Larkman, D. J., Williams, A. D. and Young, I. R. (1999). Design and use of internal receiver coils for magnetic resonance imaging. *British Journal of Radioloy* 72: 1141-1151.

[Gilderdale, 2003] Gilderdale, D. J., Williams, A. D., Umakant, D. and M. deSouza, N. (2003). An Inductively-Coupled, Detachable Receiver Coil System for Use With Magnetic Resonance Compatible Endoscopes. *Journal of Magnetic Reosnance Imaging* 18(1): 131-135.

[Goldenberg, 2010] Goldenberg, A. A., Trachtenberg, J., Yi, Y., Weersink, R., Sussman, M. S., Haider, M., Ma, L. and Kucharczyk, W. (2010). MRI-Guided Robot-Assisted Prostatic Interventions. *Robotica* 28: 215-234.

[Gross, 2001] Gross, P., Kitney, R. I., Claesen, S. and Halls, J. M. (2001). MR-compatible endoscopy and tracking for image-guided surgery. *Computer Assisted Radiology and Surgery* 1230: 1076-1082.

[Grund, 2012] Grund, K. E., Ingenpaß, R., Durst, F., Schweizer, U., Vietz, M. and Aurich, V. (2012). New Hands-on Simulator for Realistic Training of Diagnostic and Therapeutic ERCP (Neuartiges Hands-on-Phantom für das realistische Training der gesamten diagnostischen und therapeutischen ERCP). *Endoskopie heute* 25(1): 14-17.

[Haker, 2005] Haker, S. J., Mulkern, R. V., Roebuck, J. R., Barnes, A. S., DiMaio, S., Hata, N. and Tempany, C. M. C. (2005). Magnetic Resonance-guided Prostate Interventions. *Topical Magnetic Resonance Imaging* 16(5): 355-368.

[Harja, 2007] Harja, J., Tikkanen, J., Sorvoja, H. and Myllyla, R. (2007). Magnetic resonance imaging-compatible, three-degrees-of-freedom joystick for surgical robot. *The International Journal of Medical Robotics and Computer Assisted Surgery* 3(4): 365-371.

[Hashizume, 2007] Hashizume, M. (2007). MRI-guided Laparoscopic and Robotic Surgery for Malignancies. *International Journal of Clinical Oncology* 12(2): 94-98.

[Hempel, 2003] Hempel, E., Fischer, H., Gumb, L., Hohn, T., Krause, H., Voges, U., Breitweiser, H., Gutmann, B., Durke, J., Bock, M. and Melzer, A. (2003). An MRI-compatible surgical robot for precise radiological interventions. *Computer Aided Surgery* 8: 180-191.

[Heye, 2006] Heye, T., Kuntz, C., Dux, M., Encke, J., Palmowski, M., Autschbach, F., Volke, F., Kauffmann, G. W. and Grenacher, L. (2006). New Coil Concept for Endoluminal MR Imaging. *European Radiology* 16: 2401-2409.

[Hill, 1997] Hill, K. O. and Meltz, G. (1997). Fiber Bragg Grating Technology Fundamentals and Overview. *Journal of Lightwave Technology* 15(8): 1263-1276.

[Ichikawa, 2001] Ichikawa, T., Kitahara, F., Araki, T., Nanbu, A., Hori, M., Kumagai, H., Aoki, S. and Fujino, M. (2001). MR endoscopy: Results in Applying to the Upper Gastrointestinal and the Pancreatobiliary Tracts. *Proceedings of the International Society of Magnetic Resonance Medicine* 9: 2043.

[Inui, 1998] Inui, K., Nakazawa, S., Yoshino, J. and Ukai, H. (1998). Endoscopic MRI. *Pancreas* 16(3).

[Ito, 2012] Ito, K., Shimizu, A., Tanabe, M. and Matsunaga, N. (2012). Respiratory variation of the extrahepatic bile duct: evaluation with deep inspiratory and expiratory MRCP. *Magnetic Resonance Imaging* 30(4): 579-582.

[Khan, 2007] Khan, S. A., Miras, A., Pelling, M. and Taylor-Robinson, S. D. (2007). Cholangiocarcinoma and its management. *GUT* 56: 1755-1756.

[Koseki, 2002] Koseki, Y., Washio, T., Chinzei, K. and Iseki, H. (2002). Endoscope Manipulator for Trans-nasal Neurosurgery; Optimised for and Compatible to Vertical Field Open MRI. *Medical Image Computing and Computer-Assisted Intervention — MICCAI 2002*. Berlin / Heidelberg, Springer. 2488/2002: 114-121.

[Krieger, 2010] Krieger, A., Iordachita, I., Song, S.-E., Cho, N. B., Guion, P., Fichtinger, G. and Whitcomb, L. L. (2010). Development and Preliminary Evaluation of an Actuated MRI-Compatible Robotic Device for MRI-Guided Protate Intervention. *Robotics and Automation (ICRA), 2010 IEEE International Conference on*. Anchorage, AK, IEEE Explore: 1066-1073.

[Krieger, 2006] Krieger, A., Metzger, G., Fichtinger, G., Atalar, E. and Whitcomb, L. L. (2006). *A Hybrid Method for 6-DOF Tracking of MRI-Compatible Robotic Interventional Devices*. IEEE International Conference on Robotics and Automation, Orlando, Florida, IEEE Computer Society Press.

[Kulling, 1997] Kulling, D., Feldman, D. R., Kay, C. L., Bohning, D. E., Hoffman, B. J., Velse, A. K. V., Baron, P. L., Lahr, C. J. and Hawes, R. H. (1997). Local staging of anal and distal colorectal tumours with the magnetic resonsance endoscope. *Gastrointestinal Endoscopy* 47(2): 172-178.

[Kumar, 2011] Kumar, R., Jog, A., Malpani, A., Vagvolgyi, B., Yuh, D., Nguyen, H., Hager, G. and Chen, C. C. G. (2011). Assessing system operation skills in robotic surgery trainees. *The International Journal of Medical Robotics and Computer Assisted Surgery* 8(1): 118-124.

[Lambert, 2012] Lambert, N. A., Ristic, M. and DeSouza, N. M. (2012). Design of a Novel Device for MRI Guided Transrectal Prostate Biopsy. *9th International Interventional MRI Symposium*. Boston, USA: 58.

[Lehman, 2002] Lehman, G. A. (2002). What are the determinants of success in utilization of ERCP in the setting of pancreatic and biliary diseases? *Gastrointestinal Endoscopy* 56(6): S291-S293.

[Leung, 2007] Leung, J. W., Lee, J. G., Rojany, M., Wilson, R. and Leung, F. W. (2007). Development of a novel ERCP mechanical simulator. *Gastrointestinal Endoscopy* 65(7): 1056-1062.

[Leung, 2011] Leung, J. W., Wang, D., Hu, B., Lim, B. and Leung, F. W. (2011). A head-to-head hands-on comparison of ERCP mechanical simulator (EMS) and Ex-vivo Porcine Stomach Model (PSM). *Journal of Interventional Gastroenterology* 1(3): 108-113.

[Lu, 1996] Lu, D. S., Lee, H., Farahani, K., Sinha, S. and Lufkin, R. (1996). Biopsy of Hepatic Dome Lesions: Semi-Real-Time Coronal MR Guidance Technique. *American Journal of Roentgenology* 168: 737-739.

[Maeso, 2010] Maeso, S., Reza, M., Mayol, J. A., Blasco, J. A., Guerra, M., Andradas, E. and Plana, M. N. (2010). Efficacy of the Da Vinci Surgical System in Abdominal Sugery Compared with that of Laparoscopy: A Systematic Review and Meta-Analysis. *Annals of Surgery* 252(2): 254-262.

[Maghoo, 1994] Maghoo, M. (1994). A Wavelength Encoded Rotary Displacement Fibre Sensor. *Meas. Sci. Technol* 5: 260-265.

[Magnuson, 1999] Magnuson, T. H., Bender, J. S., Duncan, M. D., Ahrendt, S. A., Harmon, J. W. and Regan, F. (1999). Utility of magnetic resonance cholangiography in the evaluation of biliary obstruction. *Journal of the American College of Surgeons* 189(1): 63-71.

[McClelland, 2013] McClelland, J. R., Hawkes, D. J., Schaeffter, T. and King, A. P. (2013). Respiratory motion models: A review. *Medical Image Analysis* 17(1): 19-42.

[McRobbie, 2007] McRobbie, D., Moore, E., Graves, M. and Prince, M. (2007). *MRI from picture to proton*. Cambridge University Press. Cambridge, 2nd Edition.

[Melzer, 2008] Melzer, A., Gutmann, B., Remmele, T., Wolf, R., Lukoscheck, A., Bock, M., Bardenheuer, H. and Fischer, H. (2008). INNOMOTION for Percutaneous Image-Guided Interventions. *Engineering in Medicine and Biology Magazine*, IEEE. 27: 66-73.

[Memon, 2010] Memon, M. A., Brigden, D., Subramanya, M. S. and Memon, B. (2010). Assessing the surgeon's technical skills: analysis of the available tools. *Academic Medicine* 85(5): 869-880.

[Moche, 2010] Moche, M., Zajonz, D., Kahn, T. and Busse, H. (2010). MRI-guided Procedures in Various Regions of the Body using a Robotic Assistance System in a Closed-Bore Scanner: Preliminary Clinical Experience and Limitations. *Journal of Magnetic Resonance Imaging* 31(4): 964-974.

[Muntener, 2008] Muntener, M., Patriciu, A., Petrisor, D., Schar, M., Ursu, D., Song, D. Y. and Stoianovici, D. (2008). Transperineal Prostate Intervention: Robot for Fully Automated MR Imaging - System Description and Proof of Principle in a Canine Model. *Radiology* 247(2): 543-549.

[Naka, 2012] Naka, S., Murayama, H., Murakami, K., Haque, H. A., Kurumi, Y., Morikawa, S. and Tani, T. (2012). MR-Image Guided Endoscopic surgery - Initial Animal Study. *9th International Interventional MRI Symposium*. Boston, USA: 96.

[NEMA, 2008] NEMA (2008). Determination of Signal-to-Noise Ratio (SNR) in Diagnostic Magnetic Resonance Imaging. *MS 1-2008*. Rosslyn, Va.

[North, 2012] North, O. J., Ristic, M., Wadsworth, C. A., Young, I. R. and Taylor-Robinson, S. D. (2012). Design and evaluation of endoscope remote actuator for MRI-guided Endoscopic Retrograde Cholangio-Pancreatography (ERCP). *IEEE International Conference on Biomedical Robotics and Biomechatronics*. Rome, IEEE Xplore: 787-792.

[Obstein, 2011] Obstein, K. L., Patil, V. D., Jayender, J., Estépar, R. S. J., Spofford, I. S., Lengyel, B. I., Vosburgh, K. G. and Thompson, C. C. (2011). Evaluation of colonoscopy technical skill levels by use of an objective kinematic-based system. *Gastrointestinal Endoscopy* 73(2): 315-321.

[Oliveira, 2007] Oliveira, A. d., Rauschenberg, J., Beyersdorff, D., Semmler, W. and Bock, M. (2007). Automatic Passive Tracking of and Endorectal Prostate Biopsy Device Using Phase-Only Cross-Correlation. *Magnetic Resonance in Medicine* 59(5): 1043-1050.

[Ott, 1976] Ott, H. W. (1976). *Noise Reduction Techniques in Electronic Systems*. John Wiley & Sons. New York; London, 1st Edition.

[Oura, 2006] Oura, M., Kobayashi, Y., Okamoto, J. and Fujie, M. G. (2006). Development of MRI Compatible Versatile Manipulator for Minimally Invasive Surgery. *Biomedical Robotics and Biomechatronics, 2006. BioRob 2006. The First IEEE/RAS-EMBS International Conference on*. Pisa, Italy, IEEE Explore: 176-181.

[Padda, 2010] Padda, M., Siddiqui, U., Aslanian, H., Jamidar, P. (2010). Minor Papilla Sphincterotomy. *DAVE Project - Gastroenterology http://daveproject.org/minor-papilla-sphincterotomy/2010-04-17/* Access date 22/12/2013.

[Parthornratt, 2011] Parthornratt, T., Parkin, R. M. and Jackson, M. (2011). Human Performance index - a generic performance indicator. *Proceedings of the Institution of Mechanical Engineers, Part I: Journal of Systems and Control Engineering* 225(6): 721-734.

[Petersen, 2007] Petersen, B. T., Somogyi, L., Chuttani, R., Croffie, J., DiSario, J., Liu, J., Mishkin, D., Shah, R., Tierney, W. and Song, L. M. W. K. (2007). Guidewires for use in GI Endoscopy. *Gastrointestinal Endoscopy* 65(4): 571-576.

[Pevec, 2011] Pevec, S. and Donlagic, D. (2011). All-fiber, long active length Fabry-Perot strain sensor. *Optics Express* 19(16): 15641-15651.

[Pfau, 2011] Pfau, P. R. (2011). Colonoscopy and kinematics: what is your path length and tip angulation? *Gastrointestinal Endoscopy* 73(2): 322-324.

[Phee, 2009] Phee, S. J., Low, S. C., Huynh, V. A., Kencana, A. P. and Z.L. Sun, K. Y. (2009). Master And Slave Transluminal Endoscopic Robot (MASTER) for Natural Orifice Transluminal Endoscopic Surgery (NOTES). *International Conference of the IEEE Engineering in Medicine and Biology Society*. Minneapolis, USA, IEEE: 1192-1195.

[Plooy, 2012] Plooy, A. M., Hill, A., Horswill, M. S., Cresp, A. S. G., Watson, M. O., Ooi, S.-Y., Riek, S., Wallis, G. M., Burgess-Limerick, R. and Hewett, D. G. (2012). Construct validation of a physical model colonoscopy simulator. *Gastrointestinal Endoscopy* 76(1): 144-150.

[Pondman, 2008] Pondman, K. M., Futterer, J. J., ten Haken, B., Schultze Kool, L. J., Witjes, A. J., Hambrock, T., Macura, K. J. and Barentsz, J. O. (2008). MR-Guided Biopsy of the Prostate: An Overview of Techniques and a Systematic Review. *European Urology* 54(3): 517-527.

[Rahnejat, 2010] Rahnejat, H. (2010). *Tribology and dynamics of engine and powertrain : fundamentals, applications and future trends*. Woodhead. Oxford,

[Rasche, 1997] Rasche, V., Holz, D., Kohler, J., Proska, R. and Roschmann, P. (1997). Catheter Tracking Using Continuous Radial MRI. *Magnetic Resonance in Medicine* 37(6): 963-968.

[Rea, 2010] Rea, M. (2010). Integration and Localisation of Mechatronic Devices into the MRI Environment, Imperial College, London, London. PhD Thesis: 225.

[Rea, 2008] Rea, M., McRobbie, D., Elhawary, H., Tse, Z. T. H., Lamperth, M. and Young, I. R. (2008). Sub-pixel localisation of passive micro-coil fiducial markers in interventional MRI. *Magnetic Resonance Materials in Physics, Biology and Medicine* 22(2): 71-76.

[Rivas, 2002] Rivas, P. A., Nayak, K. S., Scott, G. C., McConnell, M. V., Kerr, A. B., Nishimura, D. G., Pauly, J. M. and Hu, B. S. (2002). In Vivo Real-Time Intravascular MRI. *Journal of Cardiovascular Magnetic Resonance* 4: 223-232.

[Ruiter, 2012] Ruiter, J., Rozeboom, E., van der Voort, M., Bonnema, M. and Broeders, I. (2012). Design and Evaluation of Robotic Steering of a Flexible Endoscope. *4th IEEE International Conference on Biomedical Robotics and Biomechatronics*. Roma, Italy, IEEE: 761-767.

[Schenck, 1996] Schenck, J. F. (1996). The Role of Magnetic Susceptibility in Magnetic Resonance Imaging: MRI Magnetic Compatibility of the first and second kinds. *Medical Physics* 23(6): 815-850.

[Sedlack, 2003a] Sedlack, R., Petersen, B., Binmoeller, K. and Kolars, J. (2003a). A direct comparison of ERCP teaching models. *Gastrointestinal Endoscopy* 57(7): 886-890.

[Sedlack, 2003b] Sedlack, R. E. and Kolars, J. C. (2003b). Validation of a computer-based colonoscopy simulator. *Gastrointestinal Endoscopy* 57(2): 214-218.

[Shang, 2011] Shang, J., Noonan, D. P., Payne, C., Clark, J., Sodergren, M. H., Darzi, A. and Yang, G.-Z. (2011). An Articulated Universal Joint Based Flexible Access Robot for Minimally Invasive Surgery. *International Conference on Robotics and Automation*. Shanghai, China, IEEE: 1147-1152.

[Shergill, 2009] Shergill, A. K., McQuaid, K. R. and Rempel, D. (2009). Ergonomics and GI Endoscopy. *Gastrointestinal Endoscopy* 70(1): 145-153.

[Shinsei, 2005] Shinsei (2005). Ultrasonic Motor General Catalogue. Tokyo, Japan: 1-15.

[Song, 2010] Song, S.-E., Cho, N., Tokuda, J., Hata, N., Tempany, C. M., Fichtinger, G. and Iordachita, I. (2010). Preliminary Evaluation of a MRI-compatible Modular Robotic System for MRI-guided Prostate Interventions. *Biomedical Robotics and Biomechatronics, IEEE RAS & EMBS International Conference on* Tokyo, Japan, IEEE. 2010: 796-801.

[Stoianovici, 2007a] Stoianovici, D., Patriciu, A., Petrisor, D., Mazilu, D. and Kavoussi, L. (2007a). A New Type of Motor: Pneumatic Step Motor. *IEEE/ASME Transactions on Mechatronics* 12(1): 98-106.

[Stoianovici, 2007b] Stoianovici, D., Song, D. Y., Petrisor, D., Ursu, D., Mazilu, D., Muntener, M., Schar, M. and Patriciu, A. (2007b). "MRI Stealth" robot for prostate interventions. *Minimally Invasive Therapy* 16(4): 241-248.

[Su, 2012a] Su, H., Cardona, D. C., Shang, W., Camilo, A., Cole, G. A., Rucker, D. C., Robert J. Webster, I. and Fischer, G. S. (2012a). A MRI-guided concentric tube continuum robot with piezoelectric actuation: A feasibility study. *IEEE International Conference on Robotics and Automation*. Saint Paul, Minnesota, USA, IEEE Xplore: 1939 - 1945.

[Su, 2012b] Su, H., Cole, G. A. and Fischer, G. S. (2012b). High field MRI-compatible needle placement robots for prostate interventions: pneumatic and piezoelectric approaches. *Advances in Robotics and Virtual Reality*. T. Gulrez and A. Hassanien, Springer Belin Heidelbery.

[Su, 2011] Su, H., Zervas, M., Cole, G., Furlong, C. and Fischer, G. (2011). Real-time MRI-guided needle placement robot with integrated fiber optic force sensing. *IEEE International Conference on Robotics and Automation*. Shanghai, China.

[Susil, 2006] Susil, R. C., Menard, C., Krieger, A., Coleman, J. A., Camphausen, K., Choyke, P., Fichtinger, G., Whitcomb, L. L., Coleman, C. N. and Atalar, E. (2006). Transrectal Prostate Biopsy and Fiducial Marker Placement in a Standard 1.5T Magnetic Resonance Imaging Scanner. *The Journal of Urology* 175: 113-120.

[Suzuki, 2007] Suzuki, T., Liao, H., Kobayashi, E. and Sakuma, I. (2007). Ultrasonic Motor Driving Method for EMI-free Image in MR image-guided Surgical Robotic System. *International Conference on Intelligent Robots and Systems 2007*. San Diego, Ca, IEEE: 522-527.

[Swanstrom, 2011] Swanstrom, L. L. (2011). NOTES: Platform Development for a Paradigm Shift in Flexible Endoscopy. *Gastroenterology* 140(4): 1150-1154.

[Syms, In Press] Syms, R. R. A., Young, I. R., Wadsworth, C. A., Taylor-Robinson, S. D. and Rea, M. (In Press). Magnetic Resonance Imaging Duodenoscope. *Transactions of Biomedical Engineering*.

[Tabriz, 2011] Tabriz, D. M., Street, M., Pilgram, T. K. and Duncan, J. R. (2011). Objective Assessment of Operator Performance During Ultrasound-guided Procedures. *International Journal of Computer Assisted Radiology and Surgery* 6(5): 641-652.

[Tan, 2011] Tan, U.-X., Yang, B., Gullapalli, R. and Desai, J. P. (2011). Triaxial MRI-Compatible Fiber-optic Force Sensor. *IEEE Transactions on Robotics* 27(1): 65-74.

[Tse, 2008] Tse, T. H. (2008). Medical Robots for MRI Guided Diagnosis and Therapy. Department of Mechanical Engineering, Imperial College, London. PhD Thesis.

[Tse, 2011] Tse, Z. T. H., Elhawary, H., Montesinos, C. A. F., Rea, M., Young, I. and Lamperth, M. (2011). Testing MR Image Artefacts Generated by Engineering Materials. *Concepts in Magnetic Resonance Part B: Magnetic Resonance Engineering* 39B(2): 109-117.

[Uchino, 1998] Uchino, K. (1998). Piezoelectric Ultrasonic Motors: Overview. *Smart Material Structures* 7: 273-285.

[Vassiliou, 2010] Vassiliou, M. C., Kaneva, P. A., Poulose, B. K., Dunkin, B. J., Marks, J. M., Sadik, R., Sroka, G., Anvari, M., Thaler, K., Adrales, G. L., Hazey, J. W., Lightdale, J. R., Velanovich, V., Swanstrom, L. L., Mellinger, J. D. and Fried, G. M. (2010). Global Assessment of Gastrointestinal Endoscopic Skills (GAGES): a valid measurement tool for technical skills in flexible endoscopy. *Surgical Endoscopy* 24(8): 1834-1841.

[Wadsworth, 2012] Wadsworth, C. A., Lim, A., Taylor-Robinson, S. D. and Khan, S. A. (2012). The risk factors and diagnosis of cholangiocarcinoma. *Hepatology International*.

[Weisstein, 2013a] Weisstein, E. W. (2013a). "ANOVA." *MathWorld - A Wolfram Web Resource* Retrieved 26-07-2013, from mathworld.wolfram.com/ANOVA.html.

[Weisstein, 2013b] Weisstein, E. W. (2013b). "Moment of Inertia." *MathoWorld - A Wolfram web Resource* Retrieved 26-07-2013, from mathworld.wolfram.com/MomentofInertia.html.

[Weisstein, 2013c] Weisstein, E. W. (2013c). "Plane-Plane Intersection." *MathWorld-A Wolfram Web Resource* Retrieved 26-07-13, from mathworld.wolfram.com/plane-planeintersection.html.

[Wendt, 2000] Wendt, M. and Wacker, F. (2000). Visualization, tracking, and navigation of instruments for magnetic resonance imagin-guided endovascular procedures. *Topics in Magnetic Resonance Imaging* 11(3): 163-172.

[Williams, 2007] Williams, E. J., Taylor, S., Fairclough, P., Hamlyn, A., Logan, R. F., Martin, D., Riley, S. A., Veitch, P., Wilkinson, M., Wiliamson, P. R. and Lombard, M. (2007). Are

we meeting the standards set for endoscopy? Results of a large-scale prospective survey of endoscopic retrograde cholangio-pancreatograph practice. *GUT* 56: 821-829.

[Yang, 2009] Yang, C., He, Z. and Yu, W. (2009). Comparison of public peak detection algorithms for MALDI mass spectrometry data analysis. *BMC Bioinformatics* 10(4): 1-13.

[Yeh, 2009] Yeh, B. M., Liu, P. S., Soto, J. A., Corvera, C. A. and Hussain, H. K. (2009). MR imaging and CT of the biliary tract. *Radiographics* 29: 1669-1688.

[Zangos, 2007] Zangos, S., Eichler, K., Thalhammer, A., Schoepf, J. U., Costello, P., Herzog, C., Mack, M. G. and Vogl, T. J. (2007). MR-guided interventions of the prostate gland. *Minimally Invasive Therapy* 16(4): 222-229.

[Zhang, 2002] Zhang, S. H., Wang, D. X., Zhang, Y. R., Wang, Y. H., Wang, Y. G. and Ma, X. P. (2002). The Human machine Interface Implementation for the Robot assisted Endoscopic Surgery System. *Robot and Human Interactive Communication, IEEE Int. Workshop on* Berlin, Germany, IEEE Xplore: 442-447.